Electronic excitations in hybrid perovskites

Dissertation
zur Erlangung des akademischen Grades
doctor rerum naturalium (Dr. rer. nat.)

im Fach: Physik
Spezialisierung: Theoretische Physik

eingereicht an der
Mathematisch-Naturwissenschaftlichen Fakultät
der Humboldt-Universtität zu Berlin

von
M.Sc. Cecilia Vona

Präsidentin der Humboldt-Universität zu Berlin
Prof. Dr. Julia von Blumenthal

Dekanin der Mathematisch-Naturwissenschaftlichen Fakultät
Prof. Dr. Caren Tischendorf

Ich erkläre, dass ich die Dissertation selbständig und nur unter Verwendung der von mir gemäSS ğ 7 Abs. 3 der Promotionsordnung der Mathematisch-Naturwissenschaftlichen Fakultät, veröffentlicht im Amtlichen Mitteilungsblatt der Humboldt-Universität zu Berlin Nr. 42/2018 am 11.07.2018 angegebenen Hilfsmittel angefertigt habe.

Berlin, den 11.01.2025

Cecilia Vona

Mathematisch-Naturwissenschaftliche Fakultät
Insistute für Physik

Electronic excitations in hybrid perovskites

Ph.D. Thesis
by M.Sc. Cecilia Vona

Supervisor: Prof. Dr. Dr. h.c. Claudia Draxl

To Paola, Antonio and Matheus

SUMMARY

Metal halide perovskites are of particular interest as light absorbers in solar-cell devices. More recently, interest has extended to many other optoelectronic applications, such as light-emitting diodes, photodetectors, and lasers. The study of their electronic excitations using theoretical methods presents many challenges. These include the variety of structures that they can form and the large unit-cell sizes they can easily reach. In particular, the organic molecules in hybrid systems can be of different sizes and the octahedra formed by the metal-halide components can exhibit different tilts. These materials exist in both three-dimensional and lower-dimensional structures. Another challenge is the presence of heavy species, which cause large spin-orbit coupling effects that are difficult to treat accurately and efficiently.

This thesis presents a study of electronic excitations in three-dimensional and two-dimensional lead-iodide based perovskites using density-functional theory and methods of many-body perturbation theory. One focus is the search for efficient and accurate methods to compute their band gaps. In this context, we consider different exchange-correlation functionals and their performance as starting points for one-shot *GW* calculations. A special focus is on the hybrid functionals PBE0 and HSE06, including methods for tuning their parameters. In addition, we investigate the effect of replacing the organic molecule with a cesium atom to reduce the size of the two-dimensional systems. After validating this approach for the artificial tetragonal phase of BA_2PbI_4, the same approach is applied to compute the effective masses of its high and low-temperature phases using HSE06.

All these studies are performed with the all-electron full-potential code **`exciting`** using augmented plane waves and local orbitals as basis functions. To achieve the results presented in this work, we realize different implementations. Among them, that of HSE06 is a major step forward in the development of the code. In particular, it allows the accurate study of the electronic structure of many semiconductors, not only halide perovskites, and is the starting point for other implementations based on HSE06.

The presence of significant spin-orbit coupling effects also required new advancements. In this context, we develop a method that uses local orbitals as explicit basis functions in the second variation scheme. The method aims to efficiently treat spin-orbit coupling effects in materials where the traditional second variation treatment fails to do so. In addition, it allows the use of relativistic local orbitals, fundamental to account for the correct asymptotic behavior of relativistic orbitals. Furthermore, we consider spin-orbit coupling also when using hybrid functionals.

ZUSAMMENFASSUNG

Metallhalogenid-Perowskite sind von besonderem Interesse als Lichtabsorber in Solarzellen. In jüngster Zeit hat sich das Interesse auch auf viele andere optoelektronische Anwendungen ausgeweitet, wie z. B. Leuchtdioden, Photodetektoren und Laser. Die Untersuchung ihrer elektronischen Anregungen mit theoretischen Methoden stellt viele Herausforderungen dar. Dazu gehören die Vielfalt der Strukturen, die diese Materialien annehmen können und, verbunden damit, die großen Einheitszellen, die sie leicht erreichen können. Insbesondere können die organischen Moleküle in Hybridsystemen unterschiedlich groß sein, und die von den Metall-Halogenid-Komponenten gebildeten Oktaeder können unterschiedliche Neigungen aufweisen. Diese Materialien existieren sowohl in dreidimensionalen als auch in niederdimensionalen Strukturen. Eine weitere Herausforderung bilden die in dieser Materialklasse vorhandenen schweren Elemente, die starke Spin-Bahn-Wechselwirkung verursachen, welche nur schwer genau und effizient zu behandeln ist.

In dieser Arbeit werden elektronische Anregungen in dreidimensionalen und zweidimensionalen Perowskiten auf Bleijodidbasis mit Hilfe der Dichtefunktionaltheorie und Methoden der Vielteilchenstörungstheorie untersucht. Einen Schwerpunkt bildet die Suche nach effizienten und genauen Methoden zur Berechnung ihrer Bandlücken. In diesem Zusammenhang betrachten wir verschiedene Austausch-Korrelationsfunktionale und deren Leistungsfähigkeit als Ausgangspunkt für One-Shot-*GW* Berechnungen. Ein besonderer Schwerpunkt liegt dabei auf den Hybridfunktionalen PBE0 und HSE06 und Methoden zur Bestimmung ihrer Parameter. Darüber hinaus untersuchen wir, inwieweit die organischen Moleküle durch Cäsiumatome ersetzt werden können, um die Größe der zweidimensionalen Systeme zu reduzieren. Nach der Validierung dieses Ansatzes für die künstliche tetragonale Phase von BA$_2$PbI$_4$ wird derselbe Ansatz angewandt, um die effektiven Massen seiner Hoch- und Tieftemperaturphasen mit HSE06 zu berechnen.

Alle diese Studien werden mit dem *all-electron full-potential* **`exciting`** *code* durchgeführt, der augmentierte ebene Wellen und lokale Orbitale als Basisfunktionen verwendet. Um die in dieser Arbeit vorgestellten Ergebnisse zu erzielen, haben wir verschiedene Methoden implementiert. Die Implementierung von HSE06 ist ein großer Schritt vorwärts für die Entwicklung des Codes. Sie ermöglicht insbesondere die genaue Untersuchung der elektronischen Struktur vieler Halbleiter, nicht nur der Halogenidperowskite, und ist der Ausgangspunkt für andere Implementierungen auf der Grundlage von HSE06.

Das Auftreten signifikanter Spin-Orbit-Kopplungseffekte erforderte ebenfalls Fortschritte. In diesem Zusammenhang haben wir wir eine Methode entwickelt, die lokale Orbitale als explizite Basisfunktionen im *second variation scheme* verwendet.

Die Methode zielt darauf ab, Spin-Orbit-Kopplung in Materialien, bei denen die herkömmliche *second variation scheme* versagt, effizient zu behandeln. Darüber hinaus ermöglicht der neue Zugang die Verwendung relativistischer lokaler Orbitale, was für das korrekte asymptotische Verhalten relativistischer Orbitale von grundlegender Bedeutung ist. Darüber hinaus berücksichtigen wir die Spin-Orbit-Kopplung auch bei der Verwendung von Hybridfunktionalen.

Acknowledgments

Like the most significant journey, this one has been marked by ups and downs that have led me to personal growth. None of this would have been possible without the precious people who have surrounded me and the funding agencies that have supported my research.

To begin with, I would like to express my sincere gratitude to Claudia Draxl, who supervised my doctorate and supported me throughout the process, always believing in me, respecting me, and appreciating my work.

This work would not have been possible without David Egger, Alexey Chernikov, Henry Snaith, and all their group members, who shared with us the extraordinary challenge of studying electronic excitations in 2D perovskites. Special thanks go to Xiangzhou Zhu, who performed crucial calculations for our joint publication.

Thanks should also go to Silvana Botti, Miguel Marques, Pedro Borlido, who helped us validate the implementation of the *density-based mixing* method in `exciting` by providing additional data and engaging in insightful discussions.

I am deeply grateful to Dmitrii Nabok, who co-supervised me during the first year of my PhD and together with Andris Gulans taught me all the best practices for using the `exciting` code effectively. Both of them have always been available to answer my questions and have been a point of reference for me. I thank Sven Lubeck, the person I have collaborated with the most. Our ways of working could not be more different but complementary, leading to a fruitful exchange and growth. I thank Ronaldo Rodrigues Pela, a grateful scientist who taught me that with kindness we can achieve the best results. I thank Pasquale Pavone, who is more than a collaborator, but a guide and a mentor. Hannah Kleine, Wahib Agguone, and Keith Gilmore are other precious internal collaborators, that I must mention for their significant contribution to my scientific work.

Many thanks to all the members who have been part of the solid-state theory group at the Humboldt Universität zu Berlin during these years. Especially the students I worked with, Jessica Richter, Antonio Cillis, Fabian Nemitz, and Seokhyun Hong. Each of them was different, taught me something, and helped me realize how much I enjoy supporting

others to do their best work. I could not have completed this journey without Maria Troppenz, Martin Kuban, Christian Vorwerk, and Ignacio Gonzales, whose contributions went beyond the scientific exchange, as they also became great friends.

Great achievements are never accomplished alone—they are built on the support and belief of others. In this regard, I would like to thank Ana Guilherme Buzanich, who has been a great mentor to me during these years always giving me honest advice. I am extremely grateful to Graziana Oliverio and Melania Vinciarelli who, through psychotherapy, taught me to face difficulties with a growing attitude.

A special thanks to all the friends and people that I met during the path that brought me here today. Especially Ana and Victoria, who made Berlin less gray during these years. Thanks to Danica, my first physics lab buddy and one of my bridesmaids at my wedding eleven years later. I would be remiss not to mention, Camilla and Alessandra, the best part of my time in Trieste. So many great memories, with Caterina and Francesca, my family in Bologna. Thank you to all my friends from my hometown, we have shown ourselves that we are stronger when we face challenges together.

Last but not least, I would like to thank my old and new family, especially my parents Paola and Antonio, and my siblings Nicolò and Barbara, who have always supported me in my choices without ever making me feel alone. Thanks to my husband's family, I immediately felt part of it. Thanks to Matheus, who has always been at my side, first as a friend, then as a partner, and finally as a husband. He always supported me, believed in me, and motivated me. He also taught me the importance of forgiving ourselves when we do not live up to our expectations. Thanks also to Matheus for fulfilling one of my deepest wishes by welcoming our dog Pita into our family. She has taught us to love unconditionally.

My PhD project was supported by several funding agencies: First, I would like to thank the German Research Foundation within the priority program SPP2196 Perovskite Semiconductors project No. 424709454 and the European Community's Horizon 2020 research and innovation program under the Marie Skłodowska-Curie Grant Agreement No. 675867. Partial contribution comes from the European Union's Horizon 2020 research and innovation program under Grant Agreement No. 951786 (NOMAD CoE), and the German Research Foundation, projects 182087777 (CRC HIOS). I benefit from my stay at IPAM and I thank MS1P for a grant to complete my thesis. Lastly, I would like to mention the North-German Supercomputing Alliance (HLRN) for providing computational resources.

Contents

II Method developments and implementations 49

III Applications 95

Appendices 138

Acronyms

APW	Augmented plane waves
BFGS	Broyden–Fletcher–Goldfarb–Shanno
BSE	Bethe-Salpeter equation
BZ	Brillouin zone
CB	Conduction band
CBm	Conduction band minimum
DDH	Dielectric dependent hybrid
DFT	Density functional theory
DM	Density-based mixing
DOS	Density of states
EA	Electron affinity
EXX	Exact-exchange approximation
FV	First variation
GGA	Generalized gradient approximation
gKS	Generalized Kohn-Sham
GWA	*GW* approximation
G_0W_0	One-shot *GW*
HaP	Metal halide perovskite
HEG	Homogeneous electron gas
HF	Hartree-Fock
HK	Hohenberg-Kohn

HT	High-temperature
IAPE	Integral absolute percentage error
IP	Ionization potential
IPA	Independent particle approximation
IPW	Interstitial plane waves
IR	Interstitial region
KS	Kohn-Sham
L	Local/semi-local
LAPW	(Linearized augmented plane waves
(L)APW+LO	(Linearized) augmented plane waves plus local orbitals
LDA	Local density approximation
LFE	Local field effects
LO	Local orbital
LR	Long-range
L(S)DA	Local (spin) density approximation
LT	Low-temperature
MAPE	Mean absolute percentage error
MBPT	Many-body perturbation theory
MLWF	Maximally localized Wannier function
MPB	Mixed product basis
MPI	Message-passing interface
MT	Muffin tin
NL	Non-local
NP	Non perturbative
OMP	Open multi-processing
PAW	Projector augmented wave
PCE	Power conversion efficiency
PDOS	Partial density of states

PW	Plane waves
QE	Quantum ESPRESSO
QP	Quasiparticle
RKS	Relativistic Kohn-Sham
RMSE	Root mean square error
RPA	Random phase approximation
SCF	Self-consistent cycle
SOC	Spin-orbit coupling
SR	Scalar relativistic
sR	Short-range
SV	Second variation
SVLO	Second variation with local orbitals
TDA	Tamm-Dancoff approximation
TMDC	Transition-metal dichalcogenide
VB	Valence band
VBM	Valence band maximum
VDW	Van der Waals
xc	Exchange-correlation
ZORA	Zero order regular approximation?
3D	Three-dimensional
2D	Two-dimensional

CHAPTER 1

Introduction

Metal halide perovskites (HaP) are promising materials for many optoelectronic applications. Initially, they attracted interest as absorber layers in single-junction solar cell devices. In just one decade, these devices went from a power conversion efficiency (PCE) of 14.1% [1] to a PCE of 26.7% [2], which is comparable to that of silicon solar cells [3]. Their optimal performance is attributed to a high carrier mobility with a long diffusion length (μm range) [4, 5], high defect tolerance [6], and low exciton binding energies [7]. They are also easy and cheap to manufacture, as they can be produced using solution processes. Nevertheless, they still present challenges that prevent them from being used in the mass production of solar cell devices. In particular, they are highly unstable under operating conditions, and the most promising compounds contain lead, which is toxic.

In their simplest three-dimensional (3D) form, HaP have the chemical formula ABX_3, where B is a divalent metal cation of the carbon group (B=Ge^{2+}, Sn^{2+} or Pb^{2+}), octahedrally coordinated by the anion X, which is part of the halide group (X=F^-, Cl^-, Br^- and I^-). The cation A is accommodated in the cages between the B-X octahedra. A can be organic, such as methylammonium (MA) and formamidinium (FA), or inorganic, such as Cs^+. Their band gaps can be tuned by varying the divalent cation and the anion, with values ranging from $\sim$ 1.2 eV for Sn-I based compounds to $\sim$ 3.5 eV for Sn-Cl based perovskites [8, 9]. This makes them suitable for many other optoelectronic applications, such as light emitting devices [10, 11], photodetectors [12], and lasers [13, 14]. The cation A is most important for stabilizing the structure. In this context, the Goldschmidt's tolerance factor [15] and a modified version [16], which uses all the ionic radii and/or the oxidation state of A, measure the probability for ABX_3 to stabilize in a perovskite structure. The perovskite structures have different symmetries depending on the octahedral tilts and can be classified as cubic, tetragonal, and orthorhombic lattices. With increasing temperature, higher symmetry structures are favored.

Quasi two-dimensional (2D) HaP have also attracted particular interest in recent years, as they improve the stability of HaP-based photovoltaic cells when mixed with their 3D counterpart [17, 18, 19]. However, the PCE is lower due to the lower carrier mobility and increased exciton binding energy. They are classified into three different structural types, named Ruddlesden-Popper phases, Dion-Jacobson perovskites, and perovskites with alternating cations in the interlayer space [20]. They all have a layered structure with a quantum well nature. The Ruddlesden-Popper type shown in Fig. 1.1 is the only one considered in this work. It has the chemical formula $(RNH_3)_2(A)_{n-1}BX_{3n+1}$ [21]. A, B, and X are the same as described for 3D HaP and form the perovskite layers that behave like potential wells. In each of them, there are n layers of B-X octahedra. RNH_3 are aliphatic or aromatic cations that serve as organic spacers between the perovskite layers and act as insulating layers of the quantum well. For $n = \infty$ the 3D HaP structure is recovered. Single-layer ($n = 1$) quasi-2D compounds exhibit larger band gaps than their 3D counterparts and, due to the 2D confinement and the weak dielectric screening of the organic layer, they have strongly bound exciton states with binding energies in the order of hundreds of meV [22, 23, 24]. As the number of inorganic layers increases, the energy gaps and exciton binding energies decrease and become more similar to those of the 3D compounds, making them suitable for solar-cell devices. The size and type of spacer molecules, which determine the dielectric screening, also influence the binding energies, charge transport, and stability [25, 26]. The combination of these features makes the properties of 2D HaP even more flexible and tunable than their 3D counterparts, making them suitable for many optoelectronic devices such as field-effect transistors [27], light-emitting diodes [28, 29], and hard photodetectors [30, 31]. In the following, we refer to quasi-2D perovskites simply as 2D.

This work presents a study of the electronic excitations in 3D and 2D lead-iodide based perovskites, using ab initio methodologies such as density functional theory (DFT) and many-body perturbation theory (MBPT). The first question we want to answer is whether we can accurately and efficiently predict the band gaps of 3D lead-iodide based

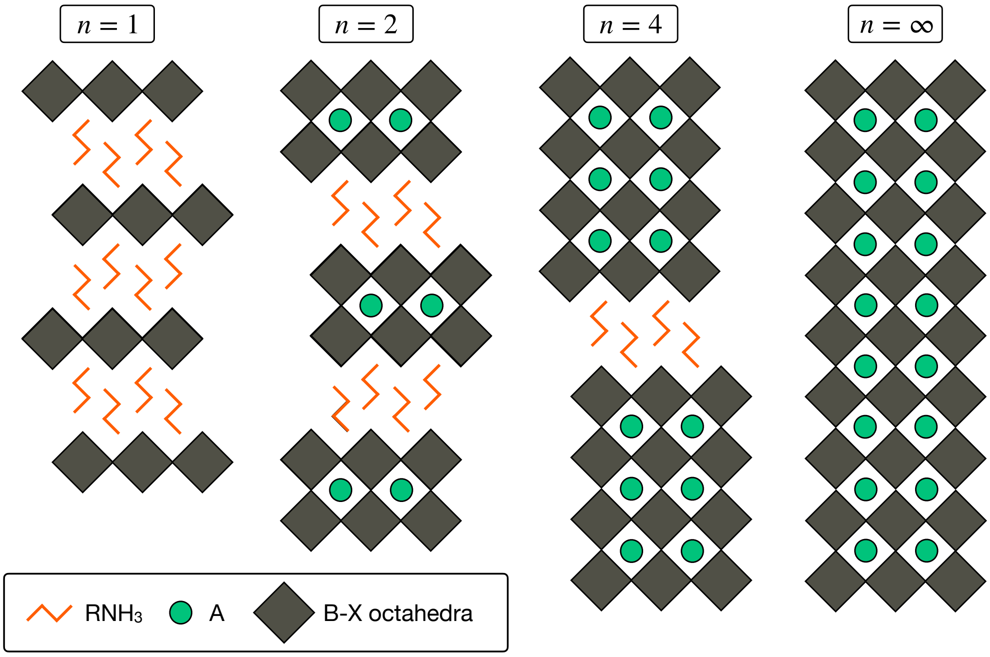

Figure 1.1: Schematic representation of Ruddlesden-Popper type perovskites with the formula $(RNH_3)_2(A)_{n-1}BX_{3n+1}$, where RNH_3 is the organic spacer, A=(Cs^+, MA^+, FA^+), B=(Pb^{2+}, Sn^{2+}), and X=(Cl^-, Br^-, I^-). n is the number of inorganic layers. For $n = \infty$, 3D HaP with the formula ABX_3 are recovered.

perovskites using hybrid exchange-correlation functionals. In this respect, a major focus is on HSE06 [32], which is known to give the best estimates for crystalline semiconductors. To assess its performance, we compare it with other methods, including the hybrid functional PBE0, and one-shot *GW* (G_0W_0) calculations using different functionals as starting points. We also investigate how the parameters that fix the amount of exact exchange contained in the hybrid functionals affect the band-gap values. In this respect, we use different tuning methods, such as the *dielectric dependent hybrid* (DDH) method and the *density-based mixing* (DM) method. These calculations proved to be particularly challenging for the following reasons: i) These materials are characterized by significant spin-orbit coupling (SOC) effects, which strongly reduce the band gaps and are challenging to treat accurately and efficiently. ii) The structures that best compare with the experimental counterparts are those with lower symmetry, with unit cells containing several stoichiometric units and therefore not being suitable as a testbed for such high-level methodologies. iii) When considering hybrid organic-inorganic systems, the unit cells are even bigger. As mentioned above, the organic/inorganic cation is mainly important for the structural stability of the system and affects the electronic excitations near the Fermi energy only indirectly through the structure, which are instead determined by the metal-halide part of the systems. This led us to consider the precursor of lead-iodide-based perovskites, i.e. PbI_2, for a systematic study of the methodologies used.

When considering 2D systems, the study of their electronic excitations with high-level methodologies becomes even more challenging due to the presence of large organic spacers. For example, with the butylammonium molecule (BA = $C_4H_9NH_3^+$), which is among the smallest organic spacers, the experimentally observed structures have unit cells of the order of 150 atoms or more. Therefore, following the logic applied to the 3D perovskites, where the A cation is most important for the structural properties of the systems, we decided to reduce the size of the systems by replacing the organic molecules with Cs atoms. In order to justify this approach, an extensive study of electronic and optical properties is carried out, with particular attention paid to the position of the MA molecules and the Cs atoms. This approach allowed us to calculate the electronic properties, including the effective masses of the two phases of the BA_2PbI_4 system with HSE06. Moreover, this approach allows to isolate the effects of the different components, i.e. the type of organic molecule, the layer distance, the number of the B-X octahedral layers, and the octahedral distortion, on the electronic excitations of the systems.

For this study, we used the **`exciting`** package. As a full-potential all-electron code, using augmented plane wave (APW) and local orbitals (LO) as basis functions, **`exciting`** allows to obtain highly precise results [33, 34]. To perform these studies, we also implemented new features in the code. Among the most important achievements in this context, are the implementation of the hybrid functional HSE06, the evaluation of SOC effects with hybrid functionals, and the development of the *second variation with local orbitals* (SVLO) method for the treatment of SOC effects. Prior to this work, PBE0 was the only hybrid functional implemented, and SOC was treated only for local/semi-local functionals with the conventional *second variation* (SV) method, which turned out to be particularly inefficient for systems such as HaP. The SV method is a two-step procedure where the SOC term is evaluated using as basis functions a subset of the states obtained by diagonalizing the scalar relativistic Hamiltonian, i.e. without including SOC effects. For HaP, we observed that all available states are needed to obtain precise results. We have shown that with the SVLO method, which additionally uses LO as explicit basis functions in the second step, a factor of 3.6 improvement in computational time can be obtained for the orthorhombic phase of $CsPbI_3$ compared to other methods with the same accuracy [35]. Moreover, this method allows us to easily include relativistic LO, which are fundamental for the accurate prediction of SOC effects.

As mentioned above, the cation A, is mainly important for structure stabilization and has no direct influence on the electronic structure of the HaP compounds. Therefore, and because the purely inorganic structures are computationally more accessible, they are often chosen in fundamental studies dedicated to the electronic excitations of 3D HaP [36, 37, 38, 39]. Here, we apply this strategy for the investigation of 3D HaP [35]. We have also taken a step forward by using the precursor of the HaP under study, e.g. PbI_2 for Pb-I-based compounds, as a test bed to determine the best methodology for investigating their electronic excitations. A similar approach is used also for 2D HaP substituting the inorganic spacer with the inorganic cation [40, 41, 42, 43, 44, 45, 46]. In this case, however, the complexity of the systems is higher due to their layered structure. It is therefore important to understand to what extent the simplified structure can be used to study the "true" system and how to choose the position of the inorganic cation replacement.

The thesis is structured in three parts. The first part consists of two chapters that cover all the methods necessary to understand the implementations and results discussed in the rest of the work. In particular, Chapter 2 focuses on the theoretical background, while Chapter 3 describes the `exciting` code. The second part deals with the various implementations that have been achieved in this thesis and that were necessary for the study of the electronic excitation of HaP. Chapter 4 presents the implementation of the hybrid functional HSE06 in `exciting`, and Chapter 5 deals with additional implementations also related to hybrid functionals. These include the incorporation of SOC and the implementation of the DM method, which we use to tune the parameters of the hybrid functionals in Chapter 7. In Chapter 5, we also discuss some optimizations applied to the code to make these calculations feasible even for the more complex HaP studied. Chapter 6 presents the SVLO method and shows its performance for a set of materials that are affected by SOC to different degrees. The third and final part focuses on lead-iodide perovskite compounds. In Chapter 7 the impact of different methodologies on the electronic structure of 3D lead-iodide compounds is studied. The main focus is on hybrid functionals and their parameters. Their influence on the starting point of G_0W_0 calculations is studied. Chapter 8 shifts the focus to 2D HaP, in particular BA_2PbI_4. The initial focus is on several tetragonal BA_2PbI_4 model systems consisting of only 39 atoms. When the BA molecule is replaced by Cs^+, the systems are reduced to only 7 atoms and thus proved to be perfect for studying to which extent the Cs-replaced systems can mimic the hybrid ones. In the following, the approach developed for the model systems is applied to study the electronic properties of the high and low-temperature phases of BA_2PbI_4.

PART I

BACKGROUND

CHAPTER 2

Theoretical background

Materials are quantum mechanical systems made of atomic nuclei and many electrons, whose interactions give rise to a many-body problem. If the nuclei are considered to be fixed, one speaks of the many-electron problem. Its theoretical description from first principles is one of the major challenges in the physics and chemistry communities. In this regard, several methodologies have been developed that allow us to study the properties of materials. Moreover, the combination of these methodologies with the advances in computation provides the opportunity to study materials of increasing complexity. In this chapter, we will address density-functional theory and the *GW* method of many-body perturbation theory, which are among the most popular frameworks for treating the many-electron problem. We will also discuss some common methods for treating optical excitations. All the methods discussed here, are those that we have employed to study the electronic excitations of metal halide perovskites at 0 K.

2.1 The many-body problem

Quantum mechanical systems like atoms, molecules, and crystals, are described, in a time-independent framework, by the electronic (non-relativistic) Schrödinger equation, in which the nuclei are considered to be frozen:

$$\mathcal{H}_{\text{el}}(\{\boldsymbol{r}\};\{\boldsymbol{R}\})\Psi(\{\boldsymbol{r}\};\{\boldsymbol{R}\}) = E(\{\boldsymbol{R}\})\Psi(\{\boldsymbol{r}\};\{\boldsymbol{R}\}). \tag{2.1}$$

This equation describes a system of M nuclei and N electrons, whose sets of coordinates are $\{\boldsymbol{R}\} \equiv \{\boldsymbol{R}_1, \dots, \boldsymbol{R}_M\}$ and $\{\boldsymbol{r}\} \equiv \{\boldsymbol{r}_1, \dots, \boldsymbol{r}_N\}$, respectively. Since the nuclei are frozen, $\{\boldsymbol{R}\}$ are parameters. $\Psi(\{\boldsymbol{r}\};\{\boldsymbol{R}\})$ is the wave function of the electronic many-body state with total energy, E, and $\mathcal{H}_{\text{el}}$ is the electronic Hamiltonian operator. In atomic units ($\hbar = m_e = e = 4\pi/\varepsilon_0 = 1$), $\mathcal{H}_{\text{el}}$ is defined as

$$\mathcal{H}_{el} = -\sum_{i=1}^{N} \frac{\nabla_i^2}{2} + \sum_{i=1}^{N} v_{\text{ext}}(\boldsymbol{r}_i) + \frac{1}{2} \sum_{\substack{i,j=1 \\ i \neq j}}^{N} \frac{1}{|\boldsymbol{r}_i - \boldsymbol{r}_j|} + E_{IJ}. \tag{2.2}$$

The first term of this equation is the kinetic energy operator of the electrons, v_{ext} is the external potential arising from the frozen nuclei interacting with the electrons, and the third term is the operator expressing the electron-electron interaction. E_{IJ} is an additive constant resulting from the (classical) electrostatic interaction between the nuclei, which we will neglect in the following discussion.

Since the electronic wave function, Ψ, in Eq. 2.1, has $3N$ degrees of freedom, the solution of the equation is a high-dimensional problem, for which analytical and numerically exact solutions are possible only for a few simple systems. Over the years several methods have been developed to tackle this many-body problem. DFT is among the most popular approaches to handle Eq. 2.1 for the ground-state and MBPT for computing the properties of the excited states. In particular, the *GW* method within MBPT, provides a robust framework for evaluating excited state properties such as the electronic band gaps. In the following discussion, we will not include the spin degrees of freedom, unless it is specified.

2.2 Density-functional Theory

DFT is a widespread technique used for computing the electronic structure of materials. One reason for this is its relatively low computational cost combined with significant predictive power. Kohn-Sham (KS) DFT [47] is what we often simply refer to as DFT, however, other flavors of it exist, e.g., the generalized Kohn-Sham (gKS) DFT for the treatment of exact exchange and hybrid exchange-correlation (xc) functionals.

2.2.1 Kohn-Sham DFT and its foundations

KS-DFT owes its origins to the theorems of Hohenberg and Kohn (HK) [48] and to the non-interacting auxiliary system introduced by Kohn and Sham, which made its application possible [47].

Hohenberg and Kohn theorems

The HK theorems were proposed by Hohenberg and Kohn in 1964 [48] and later proved in a more rigorous way by Levy [49]. The key quantity is the electron density, which for a given Ψ is:

$$\rho(\boldsymbol{r}) = N \int d\boldsymbol{r}_1, \dots, d\boldsymbol{r}_N |\Psi(\boldsymbol{r}_1, \dots, \boldsymbol{r}_N)|^2. \tag{2.3}$$

For simplicity, the electronic wave function is written explicitly in terms of the electronic coordinates, while the nuclear coordinates are omitted. The first theorem provides a one-to-one correspondence between the external potential, v_{ext}, and the density of the ground-state, ρ_0. As a result, v_{ext} is a unique functional of ρ_0. By fixing the external potential, the Hamiltonian, $\mathcal{H}_{el}$, is completely determined, therefore, the ground-state of the many-body system is a unique functional of ρ_0. Hohenberg and Kohn, for a given external potential, defined the energy functional:

$$E[\rho] = F[\rho] + \int d\boldsymbol{r} \hat{v}_{\text{ext}}(\boldsymbol{r})\rho(\boldsymbol{r}). \tag{2.4}$$

Here, $F[\rho]$ is a universal functional that accounts for the kinetic and electron-electron interaction energy contributions and is valid for any number of particles and any external potential. The second theorem states that the energy functional of the ground-state density, ρ_0, is the ground-state energy, E_0, being $E[\rho_0]$ the minimum energy value.

Kohn-Sham system

In the HK theorems, the functional forms of the kinetic and potential energy of an interacting electron system are not given explicitly, and they are still unknown today (except for the contribution of the classical Coulomb interaction). The KS system simplifies this problem: it consists of an auxiliary system of non-interacting electrons, having the same ground-state electron density, ρ_0, as the fully interacting electron system [47]. The electron density of this system of non-interacting electrons is

$$\rho(\mathbf{r}) = \sum_i^{\mathrm{occ}} |\varphi_i(\mathbf{r})|^2, \tag{2.5}$$

where the single-particle wave functions φ_i are named KS wave functions. Unlike the real interacting system, the kinetic energy of non-interacting particles is known:

$$T_0 = \frac{1}{2}\sum_i^{\mathrm{occ}} \int d\boldsymbol{r} |\nabla\varphi_i(\boldsymbol{r})|^2. \tag{2.6}$$

The total energy functional of Eq. 2.4 can then be rewritten as:

$$E[\rho] = T_0 + \int d\boldsymbol{r}\ \rho(\boldsymbol{r})[v_{ext}(\boldsymbol{r}) + v_{\mathrm{H}}(\boldsymbol{r})] + E_{\mathrm{xc}}[\rho], \tag{2.7}$$

where v_{H} is the Hartree potential arising from the classical Coulomb interaction:

$$v_{\mathrm{H}}(\boldsymbol{r}) = \frac{1}{2}\int d\boldsymbol{r}' \frac{\rho(\boldsymbol{r})}{|\boldsymbol{r} - \boldsymbol{r}'|}. \tag{2.8}$$

The last term E_{xc} is the xc functional, which accounts for all quantum mechanical effects of the interacting electron system. More precisely, it is the difference between the kinetic energy and potential energies of the true many-electron system and those of the auxiliary system, obtained by comparing Eq. 2.4 with Eq. 2.7:

$$E_{\mathrm{xc}}[\rho] = F[\rho] - T_0 - \int d\boldsymbol{r} v_{\mathrm{H}}(\boldsymbol{r}) n(\boldsymbol{r}). \tag{2.9}$$

While the KS formalism is exact for the ground-state, an exact form for the xc functional is unknown. Many different approximations have been developed. They can be divided into local/semi-local approximations, which can be treated within the KS-DFT formalism, and non-local (NL) approximations, for which a generalized form of it is required.

Kohn-Sham equations

For the KS system, the Scrhödinger equation (Eq. 2.2) becomes a set of independent-particle Scrhödinger-like equations, named KS equations:

$$\left[-\frac{1}{2}\nabla^2 + v_{\mathrm{KS}}\right]\varphi_i(\boldsymbol{r}) = \epsilon_i\varphi_i(\boldsymbol{r}), \tag{2.10}$$

where v_{KS} is the KS potential, defined as:

$$v_{\mathrm{KS}}(\boldsymbol{r}) = v_{\mathrm{ext}}(\boldsymbol{r}) + v_{\mathrm{H}}(\boldsymbol{r}) + \frac{\delta E_{\mathrm{xc}}[\rho(\boldsymbol{r})]}{\delta\rho(\boldsymbol{r})}. \tag{2.11}$$

These differential equations are non-linear in the density, ρ, which is computed through the independent particle wave functions φ_i (Eq. 2.5), and must be solved self-consistently. The self-consistent cycle (SCF), works as follows: The first step is the calculation of the KS potential, v_{KS}, employing an initial guess for the density, ρ. Knowing the KS potential, the KS equations can be solved, and the resulting KS wave functions, φ_i, can be used to compute a new density, ρ, which is plugged into the next iteration in order to update the KS potential. The cycle ends when the output density is equal (up to a certain precision) to the density of the previous step of the cycle. Details on how the KS equations (2.10) are solved in DFT codes, especially in the `exciting` package [50], are discussed in Chapter 3.

Exchange-correlation derivative discontinuity

It is important to note that, while the ground-state electron density and the ground-state total energy of the KS system are the same as those of the real interacting system, the eigenvalues of the KS equations have no physical meaning. Interpreting the KS gap as the fundamental gap of the system is fundamentally wrong, since, as described below, they differ by a quantity called xc derivative discontinuity.

The fundamental gap is defined as the difference between the electron affinity (EA), which is the energy required to add an electron, and the ionization potential (IP), which is the energy required to remove an electron:

$$E_{\mathrm{gap}} = \mathrm{EA} - \mathrm{IP} = [E(N+1) - E(N)] - [E(N) - E(N-1)]. \tag{2.12}$$

The energies are the ground-state total energy of systems with N (neutral), $N+1$, and $N-1$ electrons, respectively. From this definition, the following relationship between the fundamental band gap and the KS eigenvalues can be derived [51, 52, 53]:

$$E_{\text{gap}} = \epsilon_{N+1}^{\text{KS}} - \epsilon_{N}^{\text{KS}} + \Delta_{\text{xc}}^{\text{KS}} = E_{\text{gap}}^{\text{KS}} + \Delta_{\text{xc}}^{\text{KS}}, \tag{2.13}$$

where $E_{\text{gap}}^{\text{KS}}$ is the KS gap computed from the difference between the eigenvalue of the lowest unoccupied KS state ($\epsilon_{N+1}^{\text{KS}}$) and that of the highest valence state (ϵ_{N}^{KS}). $\Delta_{\text{xc}}^{\text{KS}}$ is the discontinuity of the derivative of the xc potential with respect to the number of particles. The absence of this term, combined with an error inherent in local/semi-local xc-functional approximations, known as the self-interaction problem, typically leads to an underestimation of band gaps by a factor of 2 [54].

2.2.2 Generalized Kohn-Sham DFT

The gKS scheme was proposed by Seidl and co-workers [54] to improve the evaluation of band gaps compared to what is obtained with local and semi-local functionals while providing accurate values for the total energy. It is a rigorous framework that takes into account the NL nature of the exchange interaction.

The basic idea of gKS is to map the fully interacting system onto a partially interacting one represented by a single Slater determinant, Φ, and having the same ground-state density, ρ_0, as the fully interacting system [55]. The NL energy contributions are functionals of a single Slater determinant, $S[\Phi]$, or, equivalently, of the (spinor) orbitals used to construct it, $S[\{\phi_i\}]$. Examples of it are the kinetic energy of a non-interacting electron system or the Hartree-Fock (HF) like exchange energy. Due to the properties of the Salter determinant, the functional $S[\cdot]$ is invariant under unitary transformations. Moreover, it is associated with an energy density functional $F^S[\rho]$ with $\rho = \sum_i |\phi_i|^2$ by the following relation:

$$F^S[\rho] = \min_{\Phi \to \rho(\boldsymbol{r})} S[\Phi] = \min_{\{\phi_i\} \to \rho(\boldsymbol{r})} S[\{\phi_i\}]. \tag{2.14}$$

The Slater determinant that minimizes $S[\cdot]$ must be found among those yielding the density $\rho(\boldsymbol{r})$. In the gKS DFT, the HK density functional $F[\rho]$, displayed in Eq. 2.4, is replaced by two density functionals:

$$E[\rho] = F^S[\rho] + R^S[\rho] + \int d\boldsymbol{r} v_{\text{ext}}(\boldsymbol{r})\rho(\boldsymbol{r}). \tag{2.15}$$

$F^S[\rho]$, as defined in Eq. 2.14, depends directly on the orbitals of the Slater determinant. $R^S[\rho]$ is the residual contribution from the difference of $F[\rho] - F^S[\rho]$ and depends indirectly on the orbitals through the density, ρ. By employing a Lagrangian procedure to minimize the total energy, one obtains the following single-particle gKS equations:

$$\hat{O}^S[\{\phi_j\}]\phi_i + v_{\text{ext}}(\boldsymbol{r})\phi_i + v_R(\boldsymbol{r})\phi_i(\boldsymbol{r}) = \epsilon_i\phi_i, \tag{2.16}$$

where

$$v_R(\boldsymbol{r}) = \frac{\delta R^S[\rho]}{\delta\rho(\boldsymbol{r})}. \tag{2.17}$$

$\hat{O}^S$ is a non-multiplicative operator, which may depend on the orbitals and the functional $S[\cdot]$, but not explicitly on the potential $(v_{\text{ext}} + v_R)$. As the KS equations (Eq. 2.10), the gKS equations must be solved self-consistently, and the orbitals obtained by their solution give the exact ground-state density, ρ_0, of the fully interacting system. The complete derivation of the gKS and its realization with different functionals, $S[\cdot]$, can be found in Ref. [54]. When we will address hybrid functionals, we will discuss the gKS equations for the specific case.

In their work, Seidl and coworkers [54], also show that the eigenvalues of the gKS equations contain part of the discontinuity. For example, when employing a NL exchange potential, like the HF exact exchange, the gKS band gap is:

$$E_{\text{gap}}^{\text{gKS}} = E_{\text{gap}}^{\text{KS}} + \Delta_{\text{x}}^{\text{KS}}. \tag{2.18}$$

where $\Delta_{\text{x}}^{\text{KS}}$ is the part of the xc derivative discontinuity related to the exchange.

2.2.3 Exchange-correlation functionals

As mentioned above, the exact form of the xc functional is unknown. Therefore, several approximations have been proposed. Based on the quantities used for their construction, e.g., density, density gradient, etc., they are classified into different levels, commonly represented by a Jacob's ladder [56] (Fig. 2.1). The first rung of the ladder uses only the electron density, ρ, hence the name local (spin) density approximation (L(S)DA) [47]. It is computationally most efficient, but it is considered least accurate. By climbing the steps, the approximations include more quantities and are considered more accurate at a price of increased computational cost. This way of representing the xc functionals is convenient, but it is a simplified picture when it comes to how they perform: Depending on the system and the property under investigation, the lower rungs may give comparable results to higher rungs [57, 58, 59, 60]. This is especially true for structural properties, where the first two rungs give fairly accurate results.

In the following section, we will focus on local and semi-local xc-functionals, which are the first three rungs of the ladder. Hybrid functionals, part of the fourth rung (Fig. 2.1), are one of the main topics of this work and are discussed in detail in Section 2.2.3.2. The exact-exchange approximation (EXX, also fourth rung) and the random phase approximation (RPA, fifth rung) are beyond the scope of this thesis and are therefore not discussed further. More details can be found in Ref. [61].

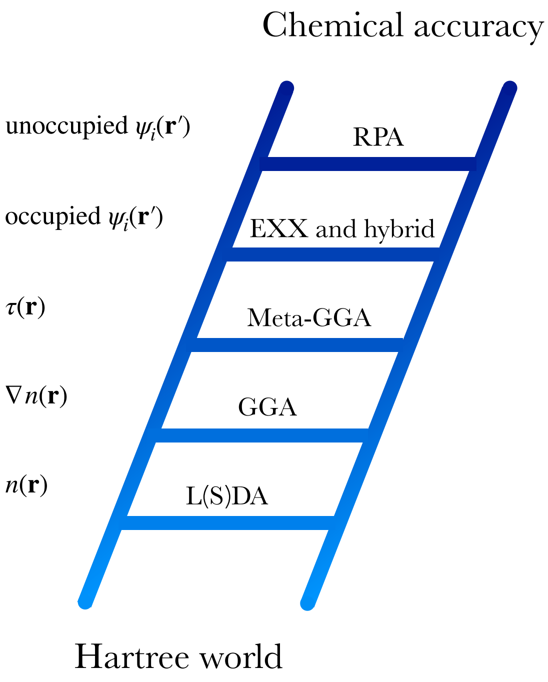

Figure 2.1: Jacob's ladder for the xc-functionals proposed by Perdew and co-workers [56, 61]. In this schematic representation, the last two rungs contain the most popular approximations. They are ordered by the quantities used to construct them (shown on the left side of the ladder). The ladder connects Hartree's world [62], which ignores correlation effects, and the "chemical accuracy", which is the accuracy needed to reliably predict the probability of having a chemical reaction (~0.0434 eV per atom).

2.2.3.1 Local and semi-local exchange-correlation functionals

A general way to write the local/semi-local xc energy functional is [61]:

$$E_{\mathrm{xc}}[\rho_{\uparrow}(\boldsymbol{r}),\rho_{\downarrow}(\mathbf{r})]=\int d\boldsymbol{r}\;\rho(\boldsymbol{r})\varepsilon_{\mathrm{xc}}(\rho_{\uparrow}(\boldsymbol{r}),\rho_{\downarrow}(\boldsymbol{r})),\tag{2.19}$$

where the total electron density $\rho(\boldsymbol{r})$ is given by the sum of the spin-resolved electron densities, $\rho(\boldsymbol{r})=\rho_{\uparrow}(\boldsymbol{r})+\rho_{\downarrow}(\boldsymbol{r})$, $\varepsilon_{\mathrm{xc}}$ is the xc energy per electron, and $\rho\varepsilon_{\mathrm{xc}}$ is the xc energy density. The complexity of the xc energy per electron, $\varepsilon_{\mathrm{xc}}$, and the quantities on which it depends, determine which of the three first rungs the approximation belongs to.

In addition to the missing xc discontinuity, local and semi-local approximations suffer from the so-called self-interaction problem: the Hartree potential in Eq. 2.7-2.8 contains an unphysical self-interaction that is not compensated in this type of xc functionals. Most of the failures of local and semi-local functionals are related to this [63].

Local spin-density approximation

The simplest approximation, at the bottom of Jacob's ladder (Fig. 2.1), is the L(S)DA, which depends only on the local density. This approximation relies on the fact that the electron density in a solid locally resembles that of the homogeneous electron gas (HEG). For unpolarized systems ($\rho_{\uparrow}(\boldsymbol{r})=\rho_{\downarrow}(\boldsymbol{r})$), it is better known as local density approximation (LDA) and the functional form is the following:

$$E_{\mathrm{xc}}^{\mathrm{LDA}}[\rho(\boldsymbol{r})]=\int d\boldsymbol{r}\;\rho(\mathbf{r})\varepsilon_{\mathrm{xc}}^{\mathrm{HEG}}(\rho(\boldsymbol{r})),\tag{2.20}$$

$\varepsilon_{\mathrm{xc}}^{\mathrm{HEG}}$ is the xc energy per particle of the HEG for a given density. This quantity can be split into the exchange and correlation contributions ($\varepsilon_{\mathrm{xc}}^{\mathrm{HEG}}=\varepsilon_{\mathrm{x}}^{\mathrm{HEG}}+\varepsilon_{\mathrm{c}}^{\mathrm{HEG}}$), which are evaluated separately. The exchange has an exact analytical form [64, 65], while the correlation has been accurately computed for different densities by the quantum Monte Carlo method [66, 67, 68]. For ground-state properties such as geometries and vibrational frequencies, this approximation works remarkably well, but the errors in the dissociation energies can reach about 2 eV [69]. The reason for the high predictive power of LDA for structural features is mainly attributed to the fact that, by being constructed from the HEG, it satisfies many exact properties [56, 61].

Generalized gradient approximation

In addition to the density, the generalized gradient approximation (GGA), also depends on the density gradient. It is therefore considered a *semi-local* approximation. For an unpolarized system, GGA functionals have the form:

$$E_{\mathrm{xc}}^{\mathrm{GGA}}[\rho(\boldsymbol{r})] = \int d\boldsymbol{r}\ \rho(\boldsymbol{r})\epsilon_{\mathrm{xc}}^{\mathrm{GGA}}(\rho(\boldsymbol{r}), |\nabla\rho(\boldsymbol{r})|). \tag{2.21}$$

The GGA xc energy density, $\epsilon_{\mathrm{xc}}^{\mathrm{GGA}}$, is defined as follows:

$$\epsilon_{\mathrm{xc}}^{\mathrm{GGA}}(\rho(\boldsymbol{r}), |\nabla\rho(\boldsymbol{r})|) = \epsilon_{\mathrm{x}}^{HEG}(\rho(\boldsymbol{r}))F_{\mathrm{xc}}(\rho(\boldsymbol{r}), |\nabla\rho(\boldsymbol{r})|), \tag{2.22}$$

where $\epsilon_{\mathrm{x}}^{HEG}$ is the (unpolarized) energy of a HEG and F_{xc} is a dimensionless quantity called *enhancement factor*. Many GGA functionals have been proposed over the years [70, 71, 72, 73], which differ in the construction of the enhancement factor F_{xc}. In solid-state physics, the Perdew-Burke-Ernzerhof (PBE) functional [73, 74] is one of the most widely used since it gets rid of the LDA overbinding [56].

Meta-generalized gradient approximation

The last rung, which is considered semi-local is that of the meta-GGA [75, 76, 77, 78]. As shown in Fig. 2.1, it depends on the kinetic energy density,

$$\tau(\boldsymbol{r}) = \frac{1}{2}\sum_{i=1}^{\mathrm{occ}} |\nabla\varphi_i|^2. \tag{2.23}$$

Since $\tau(\boldsymbol{r})$ is only an implicit functional of the density through the orbitals, the evaluation of the xc potential defined as the functional derivative of the xc energy density functional ($v_{xc} = \delta E_{\mathrm{xc}}[\rho]/\delta\rho$), is not straightforward [79]. Once the xc potential has been evaluated, meta-GGA can be treated within KS-DFT, and the computational demand is similar to that of LDA and GGA functionals [56]. Meta-GGA do not solve the self-interaction error problem. The so obtained energy gaps include part of the xc discontinuity, but this is very small [80].

Meta-GGA functionals are currently a hot topic in the DFT community because, depending on the property to study, they can perform better than the more computationally demanding hybrid functionals. An example is the modified Becke–Johnson (mBJ) meta-

GGA [77] which has been shown to outperform HSE06 (see Section 2.2.3.2) for band gaps of solid [59]. Another example is TASK, a more recent meta-GGA [81] tuned towards band-gap prediction [82]. However, since they are not a focus of this work, we will not discuss them further.

2.2.3.2 Hybrid functionals

Hybrid xc-functionals were proposed by Becke in 1993 [83]. They combine a local/semi-local (L) functional with a fraction of NL exact exchange:

$$E_{\mathrm{xc}}^{\mathrm{hyb}} = E_{\mathrm{xc}}^{\mathrm{L}} + \alpha[E_{\mathrm{x}}^{\mathrm{NL}} - E_{\mathrm{x}}^{\mathrm{L}}], \tag{2.24}$$

where

$$E_{\mathrm{x}}^{\mathrm{NL}} = -\frac{1}{2}\sum_{\sigma}\sum_{i,j}^{\mathrm{occ}}\int d\boldsymbol{r}d\boldsymbol{r}'\frac{\varphi_i^{\sigma *}(\boldsymbol{r})\varphi_j^{\sigma}(\boldsymbol{r})\varphi_j^{\sigma *}(\boldsymbol{r}')\varphi_i^{\sigma}(\boldsymbol{r}')}{|\boldsymbol{r}-\boldsymbol{r}'|}. \tag{2.25}$$

Here, σ is the spin and φ_i^{σ} are the KS wave functions. α is called the *mixing parameter.*

The NL exact exchange is analogous to that of HF theory [62, 84]; the difference lies in the single-particle orbitals. In fact, the HF wave function is a Slater determinant of single-particle orbitals, which is antisymmetric and therefore satisfies the Pauli exclusion principle [85]. In HF theory, the exchange term cancels out the extra charge of the Coulomb term and makes the method free of the self-interaction problem. In hybrid functionals, the same is partially true, i.e. to the extent of the fraction of NL exchange. The latter is also responsible for the partial inclusion of the exchange derivative discontinuity (see Eq. 2.16). In addition to this, a part of the success of hybrid functionals in predicting energy gaps of materials is attributed to the error cancellation between the HF method and the local/semi-local xc-functionals: due to the lack of electron correlation, the former highly overestimates gaps while the latter highly underestimate them.

The first hybrid xc functional was named *half-and-half*, since it is composed of half L(S)DA and half NL exact exchange. In order to justify its construction, Becke made use of the adiabatic connection formula [86, 87, 88], which will be discussed below. Using the same idea, many forms of hybrid xc-functionals were quickly developed [89, 90, 91, 92]. The most relevant hybrid functionals for this work are PBE0 [93, 94] and HSE06 [95, 96, 32].

In the case of hybrid functionals, the gKS equations read [55, 97]:

$$h^{\mathrm{L}}(\boldsymbol{r})\varphi_i(\boldsymbol{r}) + \alpha v_{\mathrm{x}}^{\mathrm{NL}}[\{\varphi_j(\boldsymbol{r})\}]\varphi_i(\boldsymbol{r}) = \epsilon_i \varphi_i(\mathbf{r}), \tag{2.26}$$

where h^{L} is the local one-particle Hamiltonian operator,

$$h^{\mathrm{L}}(\boldsymbol{r}) = -\frac{1}{2}\nabla^2 + v_{\mathrm{ext}}(\boldsymbol{r}) + v_{\mathrm{H}}(\boldsymbol{r}) + \frac{\delta}{\delta\rho(\boldsymbol{r})}\left[E_{\mathrm{xc}}^{\mathrm{L}} - \alpha E_{\mathrm{x}}^{\mathrm{L}}\right], \tag{2.27}$$

and $v_{\mathrm{x}}^{\mathrm{NL}}$ the NL exchange operator:

$$v_{\mathrm{x}}^{\mathrm{NL}}[\{\varphi_j(\boldsymbol{r})\}]\varphi_i = -\sum_j^{\mathrm{occ}} \int d\boldsymbol{r}' \frac{\varphi_j(\boldsymbol{r})\varphi_j^*(\boldsymbol{r}')\varphi_i(\boldsymbol{r}')}{|\boldsymbol{r} - \boldsymbol{r}'|}. \tag{2.28}$$

For $\alpha = 0$, the KS equations are recovered.

Adiabatic connection formula

The adiabatic connection formula [86, 87, 88] provides an exact expression to derive xc-functionals. It connects the fully interacting system ($\lambda = 1$) to the non-interacting KS system ($\lambda = 0$) through partially interacting systems ($0 < \lambda < 1$), all having the same density, via the following condition:

$$E_{\mathrm{xc}}[\rho] = \int_0^1 d\lambda \, U_{\mathrm{xc}}^{\lambda}[\rho]. \tag{2.29}$$

$U_{\mathrm{xc}}^{\lambda}$ refers to the potential energy of the xc-functional, while the kinetic energy contribution of the xc-functional arises from the integration over λ. This feature makes the adiabatic connection formalism an excellent tool that has been used as a starting point for the construction of various xc-functionals [98, 99, 100, 101, 102] and as a basis for the determination of parameters of hybrid functionals [83, 103, 104].

PBE0

The form of PBE0 was proposed separately by two groups in 1999 [93, 94]. It combines a fraction of NL exact exchange with PBE as follows:

$$E_{\mathrm{xc}}^{\mathrm{PBE0}} = E_{\mathrm{xc}}^{\mathrm{PBE}} + \alpha(E_{\mathrm{x}}^{\mathrm{NL}} - E_{\mathrm{x}}^{\mathrm{PBE}}), \tag{2.30}$$

where $\alpha = 0.25$. This fraction of exact exchange was proposed by Perdew and coworkers [103] for mixing the NL exchange with a GGA functional. Its value was theoretically justified by making use of the Görling-Levy perturbation theory [105]. PBE0 gives good results for molecular systems and solids. Unlike LDA and GGA, which tend to strongly underestimate the band gaps of all materials, PBE0 significantly overestimates those of small- and medium-gap semiconductors but gives good estimates for large-gap semiconductors and insulators [106, 59, 107]. One reason for this is associated with the overshoot of the long-range (LR) tail of the Coulomb interaction, which is expected to be effectively screened in periodic systems.

HSE06

Heyd and co-workers developed the HSE functional [95] to solve the issue of the Coulomb tail in periodic systems, whose evaluation can be computationally demanding. HSE is a range-separated hybrid functional, in which only a short range (sR) portion of the NL exact exchange is substituted:

$$E_{\mathrm{xc}}^{\mathrm{HSE}} = E_{\mathrm{xc}}^{\mathrm{PBE}} + \alpha[E_{\mathrm{x}}^{\mathrm{NL,sR}}(\omega) - E_{\mathrm{x}}^{\mathrm{PBE,sR}}(\omega)]. \tag{2.31}$$

The NL-sR and the PBE-sR contributions are constructed by splitting the Coulomb operator into a sR and a LR part by making use of the error function and its complement:

$$v(r) = v^{\mathrm{sR}}(r) + v^{\mathrm{LR}}(r) = \frac{\mathrm{erfc}(\omega r)}{r} + \frac{\mathrm{erf}(\omega \mathrm{r})}{r}. \tag{2.32}$$

The amount of the sR contributions is determined by the *screening parameter*, ω. In the first proposed version of HSE (HSE03), the screening parameter had different values for the NL-sR and PBE-sR contributions, i.e. $\omega^{\mathrm{NL}} = 0.106\ \mathrm{a}_0^{-1}$ and $\omega^{\mathrm{PBE}} = 0.189\ \mathrm{a}_0^{-1}$, respectively, [95, 96]. However, for HSE to be exact in the HEG limit, the condition $\omega^{\mathrm{NL}} = \omega^{\mathrm{PBE}}$ must be satisfied. Therefore, a new version of the HSE functional (HSE06) was published in 2006. HSE06 uses as screening parameter $\omega = 0.11\mathrm{a}_0^{-1}$ for both contributions [32]. It excels in the evaluation of small- and medium-gap semiconductors [106, 59, 107] and gives results comparable to PBE0 for the geometry optimization of solid and molecular systems. In the rest of the manuscript, we will use HSE when referring to HSE06.

For certain settings of the HSE parameters, PBE0 and PBE are restored: For $\omega = 0$, Eq. 2.31 becomes equal to the definition of PBE0 (Eq. 2.30), since the error function in Eq. 2.32 and its complement become $\mathrm{erf} = 0$ and $\mathrm{erfc} = 1$, respectively, and the entire Coulomb interaction is contained in the sR part. PBE is recovered for $\omega \to \infty$. In this case, $\mathrm{erf} \to 1$ and $\mathrm{erfc} \to 0$, which means that the NL-sR and PBE-sR contributions in Eq. 2.31 also go to 0. In addition, both HSE and PBE0 recover PBE for $\alpha = 0$.

2.2.3.3 Methods to tune the parameters of hybrid functionals

One way to improve the performance of the hybrid functionals and achieve results comparable to the more computationally intensive *GW* approach is to tune their parameters. There are empirical and non-empirical methods for doing this. In this thesis, we focus on the DDH and the DM methods, both of which are non-empirical and are used in Chapter 7 to determine the optimal hybrid functional parameters of lead-iodide based perovskites.

Dielectric dependent hybrid method

The family of DDH methods is based on the connection between the mixing parameter α and the inverse electronic dielectric constant ε_∞^{-1} [108, 106, 109, 110, 111, 112]. In particular, the method we use in Chapter 7 adopts for the PBE0 mixing parameter the relation $\alpha = \varepsilon_\infty^{-1}$. This is obtained by comparing the self-energy Σ of MBPT with the gKS equation [113, 114, 54]. The evaluation of the dielectric constant is the critical step in this approach, as there are several methods with varying degrees of accuracy and computational complexity. A common method to access the dielectric function is based on linear-response theory in the framework of time-dependent DFT [115, 116], the accuracy of which depends on the choice of the xc-kernel and on the approximation employed to evaluate the response function. The RPA in combination with a local or semi-local starting point performs rather well in evaluating the dielectric constant due to the error cancellation between the typical underestimation of gaps by local and semi-local functionals and the absence of electron-hole interaction in the RPA [117, 112, 118]. Unfortunately, RPA calculations, including local field effects (LFE) as discussed in Section 2.4, can become expensive for complex materials.

Density-based mixing method

As an alternative to the DDH method, Marques and coworkers [106] also proposed the DM method. It can be used to tune the mixing parameters of both PBE0 and HSE. This method is based on a global estimator, $\bar{g}$, which is a function of the quantity $|\nabla\rho|/\rho$. The latter has previously been used to estimate the band gap locally [119] and to construct "local hybrid" functionals [120, 121]. To construct a global estimator, the function of $|\nabla\rho|/\rho$ must be averaged over the unit cell volume V_{cell}. In Ref.[106], the estimator $\bar{g}$ is defined as:

$$\bar{g} = \frac{1}{V_{\text{cell}}} \int_{V_{\text{cell}}} \mathrm{d}\boldsymbol{r} \sqrt{\frac{|\nabla\rho(\boldsymbol{r})|}{\rho(\boldsymbol{r})}}. \tag{2.33}$$

The same global estimator was previously used in the construction of the mBJ meta-GGA functional of Tran and Blaha [77].

From $\bar{g}$, the mixing parameters of PBE0 and HSE are then evaluated as follows:

$$\alpha_{\text{PBE0}} = -1.00778 + 1.10507\ \bar{g}, \tag{2.34}$$

$$\alpha_{\text{HSE}} = 0.121983 + 0.130711\ \bar{g}^4. \tag{2.35}$$

Note that in the case of PBE0, the relation between α and $\bar{g}$ is linear, while in the case of HSE, the fourth power of $\bar{g}$ is calculated to account for screening effects.

An advantage of the DM method is that it can be evaluated at the end of a ground-state calculation performed with a (semi-)local functional, since the functional used was found to have a negligible influence on its value [106]. Moreover, for the set of materials used in Ref. [106], the DM leads to average errors of 14.37 % for PBE0-DM and 10.376 % for HSE-DM, while the PBE0 and HSE values are 29.42% and 16.92%, respectively. For the same set, the PBE0-DDH (dielectric constant evaluated with linear response) shows an average error of 16.53%. In a more recent work [59], the method was applied to a larger set of materials, for which worse performance was found for both PBE0-DM and HSE-DM.

Other versions of the DM method exist. For example, Koller et al. [109] used a different definition for the global estimator $\bar{g}$. Richter [122] determined different relations between $\bar{g}$ and the mixing parameters. Borlido et al. [123] proposed a version designed for interfaces. The original version proposed in Ref. [106], has been implemented in `exciting` as part of this work (Section 5.2).

2.2.4 Relativistic Kohn-Sham DFT

In systems composed of rather heavy elements, the consideration of relativistic effects is fundamental. To treat them, Relativistic Kohn-Sham (RKS) DFT [124, 125] can be used. Its foundation is in the relativistic HK theorem, in which the current density plays the role of the electron density [126]. In addition, the many-body wave function is rewritten as a four-component wave function, ψ, which satisfies the Dirac-KS equation [127, 128]:

$$\begin{bmatrix} v & c\boldsymbol{\sigma}\cdot\boldsymbol{p} \\ c\boldsymbol{\sigma}\cdot\boldsymbol{p} & v-2c^2 \end{bmatrix}\begin{bmatrix}\psi_{\mathrm{L}} \\ \psi_{\mathrm{S}}\end{bmatrix} = \epsilon\begin{bmatrix}\psi_{\mathrm{L}} \\ \psi_{\mathrm{S}}\end{bmatrix}. \tag{2.36}$$

ψ_{L} and ψ_{S} are the large and the small components, respectively, of the four-component wave function, ψ. v is the effective relativistic potential, $\boldsymbol{\sigma}$ is the vector spin operator of the Pauli matrices[1], $\boldsymbol{p}$ is the momentum operator, and c is the speed of light. The solution of Eq. 2.36 is not trivial, and several approaches to treat it have been developed over the years [129, 130]. A computationally advantageous strategy is to consider only the large component and neglect the small one. After a few steps, the resulting equation to solve has the following form [131]:

$$[c\boldsymbol{p}K_{\mathrm{SR}}\cdot\boldsymbol{p} + ic\boldsymbol{\sigma}\cdot\boldsymbol{p}K_{\mathrm{SOC}}\times\boldsymbol{p} + \hat{v}]\Psi_{\mathrm{L}} = \epsilon\Psi_{\mathrm{L}}. \tag{2.38}$$

The first term is the scalar relativistic (SR) kinetic energy term, which is spin-independent. The second term is the SOC term, which, as discussed in more detail at the end of this section, couples the operators of spin and angular momentum. There are several approximations for the operators K_{SR} and K_{SOC} [132, 133, 134]. Here we concentrate on those of K_{SOC}. For example, if $K_{\mathrm{SOC}} \approx 1/2c$, the SOC term in Eq. 2.38 is zero, and the SR Schrödinger equation is obtained:

$$[c\boldsymbol{p}K_{\mathrm{SR}}\cdot\boldsymbol{p} + v]\Psi_{\mathrm{L}} = \epsilon\Psi_{\mathrm{L}}. \tag{2.39}$$

---

[1] The vector spin operator of the Pauli matrices is $\boldsymbol{\sigma} = \{\sigma_x, \sigma_y, \sigma_z\}$, where the Pauli matrices σ_i are defined as:

$$\sigma_x = \begin{bmatrix} 0 & 1 \\ 1 & 0 \end{bmatrix}, \quad \sigma_y = \begin{bmatrix} 0 & -i \\ i & 0 \end{bmatrix}, \quad \sigma_z = \begin{bmatrix} 1 & 0 \\ 0 & -1 \end{bmatrix}. \tag{2.37}$$

This is the equation that the electronic structure theory community solves when performing DFT calculations without considering SOC effects. To include the SOC term, K_{SOC} must be taken at least at first order in $(\epsilon - \hat{v}/c^2)$:

$$K_{\mathrm{SOC}} \approx \frac{1}{2c} - \frac{\epsilon - \hat{v}}{4c^3}, \tag{2.40}$$

which leads to the following relativistic Schrödinger equation:

$$\left[c\boldsymbol{p}K_{\mathrm{SR}} \cdot \boldsymbol{p} + v + \frac{i}{4c^2}\boldsymbol{\sigma} \cdot \boldsymbol{p}v \times \boldsymbol{p}\right]\Psi = [\mathcal{H}_{\mathrm{SR}} + \mathcal{H}_{\mathrm{SOC}}]\Psi = \epsilon\Psi. \tag{2.41}$$

Spin-orbit coupling

SOC is generated by the interaction of the spin of the electrons with the magnetic field induced by their movement around the nuclei:

$$H_{\mathrm{SOC}} = -\boldsymbol{\mu}_{\mathrm{S}} \cdot \boldsymbol{B}_{\mathrm{orbit}} \propto \boldsymbol{S} \cdot \boldsymbol{L}, \tag{2.42}$$

where $\boldsymbol{\mu}_{\mathrm{S}}$ is the spin magnetic momentum, which is proportional to the spin angular momentum $\boldsymbol{S}$, and $\boldsymbol{B}_{\mathrm{orbit}}$ is the induced orbital magnetic field, which is proportional to

$$\boldsymbol{B}_{\mathrm{orbit}} \propto \frac{1}{r}\frac{\partial V(r)}{\partial r}\boldsymbol{L}. \tag{2.43}$$

Here, $\boldsymbol{L}$ is the angular momentum and V is the potential of the electron in the central nuclear field $V = -Z/r$, where Z is the atomic number [135, 136]. Because of this dependence on the nuclear charge, SOC may lead to significant effects in materials containing heavy atoms. It is fundamental to be accounted for to obtain an accurate description of their optoelectronic properties. For example, SOC generates a splitting of the l-degenerate states ($l \neq 0$) and may lead to a lowering of gaps reduction and/or splittings in optical transitions. Other effects include the Rashba and Dresselhaus splitting, which have been studied in both 3D and 2D HaP [137, 138, 139, 140, 141, 142, 143, 144, 145, 146, 147, 148, 44]. When studying optical properties, it is important to keep in mind that the selection rules change due to SOC, because the spin degree of freedom s is no longer a good quantum number, but the total angular momentum j ($|l - s| \leq j \leq l + s$) is.

2.3 Many-body perturbation theory

MBPT is a theoretical and computational framework that makes use of Green's correlation functions to compute electronic excitations [149]. Within MBPT, the *GW* approach and the Bethe-Salpeter equation (BSE) are considered *state-of-the-art* for calculating electronic and optical properties. The *GW* approach uses the one-body Green's function to compute the IP and the EA, while the BSE evaluates optical spectra, electron energy loss spectra, and much more, via the two-body correlation function. In the following, we will focus mainly on *GW*. The BSE is briefly discussed in Section 2.4 together with other methods used to compute optical properties.

2.3.1 One-body Green's function

In the time domain, the one-body Green's function is defined as:

$$G(xt, x't') = -i \langle N | \hat{T}[\hat{\Psi}(xt)\hat{\Psi}^{\dagger}(x't')] | N \rangle , \tag{2.44}$$

where $|N\rangle$ is the ground-state of an N-electron system. $\hat{\Psi}(xt)$ and $\hat{\Psi}^{\dagger}(x't')$, where x combines the three space coordinates, $\boldsymbol{r}$, and the spin, σ, are the annihilation and creation operators in the Heisenberg picture, respectively. $\hat{T}$ is the time-ordering operator, which allows for both the addition and removal of electrons from the systems [149]. For the sake of simplicity, we will omit the spin from now on and consider only the spatial coordinates $\boldsymbol{r}$.

To access the IP and EA, the one-body Green's function in the time domain (Eq. 2.44) must be Fourier transformed into the frequency domain. For an unpolarized system, the equation can be written as:

$$G_1(\boldsymbol{r}, \boldsymbol{r}', \omega) = \lim_{\eta \to 0^+} \sum_s f_s(\boldsymbol{r}) f_s^*(\boldsymbol{r}') \left[\frac{\Theta(\epsilon_s - E_{\mathrm{F}})}{\omega - (\epsilon_s - i\eta)} + \frac{\Theta(E_{\mathrm{F}} - \epsilon_s)}{\omega - (\epsilon_s + i\eta)} \right]. \tag{2.45}$$

This form of G is called spectral or Lehman representation [150, 151, 152]. Θ is the Heaviside step function, which is 0 for negative arguments and 1 for positive arguments. It is employed to have both time orders in one equation. η is needed for the convergence of the Fourier transforms in the frequency domain [149], and E_{F} is the Fermi energy. $f_s(\boldsymbol{r})$ is the transition amplitude from the ground-state $|N\rangle$ to the $N \pm 1$-particle state

$|N \pm 1, s\rangle$:

$$f_s(\boldsymbol{r}) = \begin{cases} \langle N-1, s|\,\hat{\Psi}(\boldsymbol{r})\,|N\rangle & \text{for} \quad \epsilon_s < E_\mathrm{F}, \\ \langle N|\,\hat{\Psi}(\boldsymbol{r})\,|N+1, s\rangle & \text{for} \quad \epsilon_s \geq E_\mathrm{F}. \end{cases} \tag{2.46}$$

$f_s^*(\boldsymbol{r}')$ is its complex conjugate. The connection to the IP and EA (for the state s) is given by the energies ϵ_s, which are the poles of the Lehman representation of G (Eq. 2.45). More specifically, they correspond to the energies required to remove or add an electron to the state s:

$$\epsilon_s = \begin{cases} E(N) - E(N-1, s) = \mathrm{IP}_s & \text{for} \quad \epsilon_s < E_\mathrm{F}, \\ E(N+1, s) - E(N) = \mathrm{EA}_s & \text{for} \quad \epsilon_s \geq E_\mathrm{F}. \end{cases} \tag{2.47}$$

The Lehman representation of G is also suitable for accessing the spectral function:

$$A(\boldsymbol{r}, \boldsymbol{r}', \omega) = \frac{1}{\pi}\mathrm{Im}G(\boldsymbol{r}, \boldsymbol{r}', \omega)\mathrm{sgn}(E_\mathrm{F} - \omega). \tag{2.48}$$

In the case of a finite system, it consists of a series of δ-peaks at the excitation energies ϵ_s, with the weight defined by the product of the respective transition amplitudes f_s [153]:

$$A(\boldsymbol{r}, \boldsymbol{r}', \omega) = \sum_s f_s(\boldsymbol{r}) f_s^*(\boldsymbol{r}')\delta(\omega - \epsilon_s), \tag{2.49}$$

Differently, in the case of an infinite system, it consists of a series of peaks with a Lorenzian shape:

$$A(\boldsymbol{r}, \boldsymbol{r}', \omega) = \sum_s f_s(x) f_s^*(x') \frac{\Gamma_s}{(\omega - \tilde{\epsilon}_s)^2 + \Gamma_s^2}, \tag{2.50}$$

where, $\tilde{\epsilon}_s$ are the energies give the peak positions and $|\Gamma_s|$ the peak widths. The peaks arise from the many-electron interactions and are associated with the formation of *quasiparticles* (QP). A QP behaves like a single particle, whose energy is affected by the interaction with other particles. The *GW* approximation treats quasielectrons, whose energies are affected by the interaction with other electrons. They are complex quantities, i.e. $\epsilon_s^\mathrm{QP} = \tilde{\epsilon}_s + i\Gamma_s$. Their imaginary part is related to the lifetime of the QP ($\tau_s = 2/\Gamma_s$).

2.3.2 *GW* approach

The formulation of the *GW* method is based on the work of Hedin, published in 1965 [154], but, its application to real systems started only 20 years later [155, 156]. Hedin proposed a set of self-consistent coupled integro-differential equations for the one-body Green's function, which overcomes the self-interaction problem and the absence of long-range polarization effects [152]. They read:

$$G(1,2) = G_0(1,2) + \int G_0(1,3)\Sigma(3,4)G(4,2)d(3,4), \tag{2.51}$$

$$\Sigma(1,2) = i\int G(1,4)W(1,3)\Gamma(4,2;3)d(3,4), \tag{2.52}$$

$$W(1,2) = v_c(1,2) + \int v_c(1,3)\chi_0(3,4)W(4,2)d(3,4), \tag{2.53}$$

$$\Gamma(1,2;3) = \delta(1,2)\delta(1,3) + \int \frac{\delta\Sigma(1,2)}{\delta G(4,5)}G(4,6)G(7,5)\Gamma(6,7;3)d(4,5,6,7). \tag{2.54}$$

$$\chi_0(1,2) = -i\int G(1,3)G(4,1)\Gamma(3,4;2)d(3,4), \tag{2.55}$$

For the sake of simplicity in the equations, we have used the notation $1 \equiv (x_1t_1)$, $2 \equiv (x_2t_2)$, etc.. Equation 2.51 defines G and has the form of a *Dyson equation* [157], i.e. an integral equation that relates a bare quantity to its dressed counterpart through a kernel that includes the effects of the coupling [158]. In the case of Eq. 2.51, G_0 is the bare quantity, G is the dressed solution, and the self-energy Σ (Eq. 2.52) is the kernel. Since the dressed quantity G appears on both sides, its definition results in an infinite sum:

$$\begin{aligned} G_0 &= G_0 + G_0\Sigma G \qquad (2.56)\\ &= G_0 + G_0\Sigma G_0 + G_0\Sigma G_0\Sigma G_0 + \cdots . \qquad (2.57)\end{aligned}$$

Equations 2.53-2.54 are also Dyson equations and define the screening W and the vertex correction Γ, respectively. Unlike the HF exchange, which includes only the static screening, W also includes dynamic screening effects and is a key quantity in GW methods. Γ depends on three space-time points and accounts for interactions going beyond those included in W. With Eq. 2.55 one obtains the irreducible polarizability χ_0. The complex interplay between Eqs 2.51-2.55, which makes them extremely difficult to solve, is obvious. This opened the way for the development of several approximations, among which the *GW*-approximation (GWA).

The *GW* approximation

The GWA simplifies Hedin's equations (Eqs 2.51-2.55) by constraining the vertex Γ (Eq. 2.54) to be diagonal in all coordinatesand equal to unity, $\Gamma(1,2;3) = \delta(1,2)\delta(1,3)$. This approximation, known as RPA, leads to the following set of equations, often referred to as GW-RPA [149]:

$$G(1,2) = G_0(1,2) + \int G_0(1,3)\Sigma(3,4)G(4,2)d(3,4), \tag{2.58}$$

$$\Sigma(1,2) = iG(1,2)W(1,2). \tag{2.59}$$

$$W(1,2) = v_c(1,2) + \int v_c(1,3)\chi_0(3,4)W(4,2)d(3,4), \tag{2.60}$$

$$\chi_0(1,2) = -iG(1,2)G(2,1), \tag{2.61}$$

The name *GW* is derived from the form of the self-energy in Eq. 2.59: Unlike in Eq. 2.52, here Σ is defined as the product of G and W. The self-consistent solution of the GWA equation is possible, but is computationally highly demanding and not always satisfactory [158]. Therefore, the one-shot *GW* (G_0W_0) approximation is often preferred.

G_0W_0: quasiparticle equations

The G_0W_0 approximation is used for calculating QP energies. It is considered the first rung of the *GW* methods since it corresponds to the first iteration of the GW-RPA equations (2.58-2.59), where G_0 is computed from the solution of a single-particle equation. In this work, DFT results are used as a starting point. From the Dyson equation for G (Eq. 2.51) one can derive the following effective single-particle eigenvalue equations:

$$\hat{h}(\boldsymbol{r})\varphi_i^{\mathrm{QP}}(\boldsymbol{r}) - \int \mathrm{d}\boldsymbol{r}' v_{\mathrm{xc}}(\boldsymbol{r},\boldsymbol{r}')\varphi_i^{\mathrm{QP}}(\boldsymbol{r}') + \int \mathrm{d}\boldsymbol{r}'\Sigma(\boldsymbol{r},\boldsymbol{r},\epsilon_s^{\mathrm{QP}})\varphi_i^{\mathrm{QP}}(\boldsymbol{r}') = \epsilon_i^{\mathrm{QP}}\varphi_i^{\mathrm{QP}}(\boldsymbol{r}). \tag{2.62}$$

φ_i^{QP} and ϵ_s^{QP} are the QP wave functions and energies, respectively. The former are not computed in the first rung of the GWA. The solution of Eq. 2.62 leads to the following set of QP equations to evaluate the energies:

$$\epsilon_s^{\mathrm{QP}} = \epsilon_s^0 + Z_s \langle\varphi_s^0|\, \Sigma(\epsilon_s^0) - v_{\mathrm{xc}}\, |\varphi_s^0\rangle\,. \tag{2.63}$$

φ_s^0 and ϵ_s^0 are the eigenvectors and eigenvalues, respectively, obtained from the solution of (g)KS-equations with v_{xc} as xc functional. Z_s is the QP re-normalization factor, defined as:

$$Z_s = \left[1 - \frac{d}{d\omega}\langle\varphi_s^0|\, \Sigma(\omega)\, |\varphi_s^0\rangle_{\omega=\epsilon_s^0}\right]^{-1}. \tag{2.64}$$

This quantity varies from 0 to 1 and carries information about the spectral weight of the QP peaks. Values of Z_s between 0.7 and 0.8 are typical for the main peak of insulators, semiconductors, and metals [159, 160] while values of 0.9 are common for molecules [152]. The self-energy in Eqs 2.63-2.64 is usually computed as the sum of the correlation (Σ_c) and exchange (Σ_x) self-energy. The form of the latter is very similar to that of the NL exact exchange potential (Eq. 3.13) of hybrid functionals. The correlation part requires the evaluation of the dynamical screened Coulomb potential, W, which in turn requires the evaluation of the dynamical dielectric tensor. Therefore, the evaluation of W is the most complex and computationally expensive part of the G_0W_0 calculations.

In summary, given Eq. 2.63, the QP energies are evaluated by correcting the DFT eigenenergies. Clearly, even though this method is known to provide a satisfactory solution for the calculation of QP excitations, it has a dependence on the xc functionals used in the underlying DFT calculations [161, 162, 35]. This dependence has been studied mainly for molecules [163, 164, 165, 166, 167]. In Chapter 7, we show results that we have obtained for HaP as published in Ref. [35]. To reduce or eliminate the dependence on the initial starting points, it is necessary to go to higher rungs of the GW method and include some degree of self-consistency [168, 156, 169, 170, 171].

2.4 Optical properties

The optical absorption is described by the imaginary part of the macroscopic dielectric function, $\varepsilon_{\mathrm{M}}(\mathbf{q}, \omega)$, which in solids is related to the microscopic dielectric function in the long wavelength limit ($\mathbf{q} \rightarrow 0$) by the following equation:

$$\varepsilon_{\mathrm{M}}(\omega) = \lim_{\boldsymbol{q}\rightarrow 0}[\varepsilon^{-1}_{\boldsymbol{G}=0,\boldsymbol{G}'=0}(\boldsymbol{q}, \omega)]^{-1}. \tag{2.65}$$

$\varepsilon_{\boldsymbol{G}=0,\boldsymbol{G}'=0}$ is the leading element of the dielectric matrix in reciprocal space:

$$\varepsilon_{\boldsymbol{G},\boldsymbol{G}'}(\boldsymbol{q}; \omega) = \delta_{\boldsymbol{G},\boldsymbol{G}'} + v(\boldsymbol{q}+\boldsymbol{G})\chi_{\boldsymbol{G},\boldsymbol{G}'}(\boldsymbol{q}, \omega), \tag{2.66}$$

where $\boldsymbol{G}$ is a reciprocal lattice vector and $\boldsymbol{q}$ is a vector in the first Brillouin zone (BZ). χ is the response function, which is related to the irreducible polarizability (χ_0) and the bare Coulomb potential by a Dyson equation. If $\varepsilon_{\boldsymbol{G}\boldsymbol{G}'}$ is diagonal in $\boldsymbol{G}$, the macroscopic dielectric function is simply $\varepsilon_{\mathrm{M}} = \lim_{\boldsymbol{q}\rightarrow 0}\varepsilon_{\boldsymbol{G}=0,\boldsymbol{G}'=0}$. If $\varepsilon_{\boldsymbol{G}\boldsymbol{G}'}$ is not diagonal, the dielectric function is defined as in Eq. 2.65, which means that all elements of the matrix contribute to the leading terms of its inverse. In this case, one speaks of *local field effects* (LFE) [149]. By inserting Eq. 2.66 into Eq. 2.65, one obtains the following relation [2]:

$$\varepsilon_{\mathrm{M}}(\omega) = 1 - \lim_{\boldsymbol{q}\to 0}[v(\boldsymbol{q})\chi_{\boldsymbol{G}=0,\boldsymbol{G}'=0}(\boldsymbol{q},\omega))]. \tag{2.67}$$

The method used to evaluate the response function defines the level of approximation, e.g., if the reduced polarizability, χ_0, is computed as in Eq. 2.61, one speaks about RPA. When LFE are neglected, the optical spectrum is computed as:

$$\mathrm{Im}\varepsilon_M(\omega) = \frac{16\pi}{\omega^2}|\langle\varphi_v|\,\hat{\boldsymbol{v}}\,|\varphi_c\rangle|^2\delta(\epsilon_c - \epsilon_v - \omega). \tag{2.68}$$

Here, $\hat{\boldsymbol{v}}$ is the velocity operator, φ_v (φ_c) are the wave functions of the independent particle valence (conduction) states, and ϵ_v (ϵ_c) are their energies. This expression is termed independent-particle approximation (IPA).

Going beyond the RPA, i.e., considering the interaction between electrons and holes, it is convenient to compute the response function from the two-particle correlation function:

$$\chi(1,2) = -iL(1,2,1',2'), \tag{2.69}$$

where

$$L(1,2,1'2') = -G_2(1,2,1',2') + G(1,1')G(2,2'). \tag{2.70}$$

L is a two-body Green's correlation function that carries information about processes involving two particles and their interactions. In the context of optical excitations, where the interacting particles are an electron and a hole, the only possible time orders are $t_1, t_1' \lessgtr t_2, t_2'$. The two-body Green's function is computed by solving the BSE [172] of MBPT. The BSE is considered the *state-of-the-art* method for describing optical spectra, electron energy loss spectra, and much more. The BSE also provides access to quantities such as exciton binding energies, E_{b}. Excitons are QP formed by electron-hole pairs attracted to each other by the Coulomb interaction. E_{b} is the energy difference between the transition energy of the independent particles and that of the excitons.

Another property related to the dielectric functions ε_M is the static dielectric constant, ε_∞, which is the (real) dielectric function evaluated at frequencies tending to infinity.

---

[2] For the optical spectra, it is useful to use a modified response function, $\bar{\chi}$, which sets the long wavelength component ($\boldsymbol{G} = 0$) of the Coulomb potential to zero [158, 149].

CHAPTER 3

The `exciting` code

`exciting` [50] is a full-potential all-electron computer package for performing DFT and MBPT calculations employing augmented plane waves and local orbitals as basis functions. The goal of this chapter is to introduce `exciting` in order to provide a solid background for understanding the new implementations achieved in this work. The main topics include: The basis functions, ground state calculations with hybrid functionals, and the second variation treatment to include SOC effects in non-magnetic systems. A brief description of the methods that we have used to study metal halide perovskites is also given, such as the G_0W_0 approximation, the methods used to evaluate the optical properties, and the Wannier interpolation for band structure and density of states calculations.

3.1 Numerical solution of the Kohn-Sham equation

The KS equations (Eq. 2.10) for periodic systems have the following form:

$$\left[-\frac{1}{2}\nabla^2 + v_{\mathrm{KS}}(\boldsymbol{r})\right]\varphi_{n\boldsymbol{k}}(\boldsymbol{r}) = \epsilon_{n\boldsymbol{k}}\varphi_{n\boldsymbol{k}}(\boldsymbol{r}), \tag{3.1}$$

where n and $\boldsymbol{k}$ are the band index and the Bloch wave number, respectively. v_{KS} is the KS potential (Eq. 2.11), $\epsilon_{n\boldsymbol{k}}$ are the KS eigenenergies, and $\varphi_{n\boldsymbol{k}}(\boldsymbol{r})$ are the KS wave functions.

To solve the KS equations numerically, the KS wave functions are expanded into a basis. Leaving out LO, the expansion in augmented plane-waves is:

$$\varphi_{n\boldsymbol{k}}(\mathbf{r}) = \sum_{\substack{\boldsymbol{G} \\ |\boldsymbol{G}+\boldsymbol{k}|<G_{\max}}} c^{\boldsymbol{k}}_{n\boldsymbol{G}} \phi_{\boldsymbol{G}+\boldsymbol{k}}(\boldsymbol{r}). \tag{3.2}$$

The sum runs over the reciprocal lattice vectors $\boldsymbol{G}$ up to the cutoff $G_{\max}$, which makes the sum finite and determines the number of basis functions, N_{b}. The quality of the basis functions is crucial for a precise solution of the KS equation. In `exciting`, in addition to APW, also LO are employed as basis functions. This applies to valence and semi-core states, while the core states are treated differently, i.e., by solving the four-component Dirac equation. In the next section, the (linearized) augmented plane waves plus local orbitals ((L)APW+LO) methods, which treat APW and LO basis functions, are described in more details.

Given the basis, the Hamiltonian ($H^{\boldsymbol{k}}$) and the overlap ($S^{\boldsymbol{k}}$) matrices are constructed, and the secular equation is solved at each $\boldsymbol{k}$-point:

$$\sum_{\boldsymbol{G}'} H^{\boldsymbol{k}}_{\boldsymbol{G}\boldsymbol{G}'} c^{\boldsymbol{k}}_{n\boldsymbol{G}'} = \epsilon_{n\boldsymbol{k}} \sum_{\boldsymbol{G}'} S^{\boldsymbol{k}}_{\boldsymbol{G}\boldsymbol{G}'} c^{\boldsymbol{k}}_{n\boldsymbol{G}'}. \tag{3.3}$$

Here the sum goes over the number of basis functions, N_{b}, so diagonalizing the Hamiltonian is a problem of $\mathcal{O}(N_{\mathrm{b}}^3)$. The coefficients $c^{\boldsymbol{k}}_{n\boldsymbol{G}}$ are the only variables in the problem. $H_{\boldsymbol{G}\boldsymbol{G}'}$ and $S_{\boldsymbol{G}\boldsymbol{G}'}$ are the matrix elements of the square matrices $H^{\boldsymbol{k}}$ and $S^{\boldsymbol{k}}$ of rank N_{b}. They are defined as:

$$H^{\boldsymbol{k}}_{\boldsymbol{G}\boldsymbol{G}'} = \langle \phi_{\boldsymbol{G}+\boldsymbol{k}} | -\frac{1}{2}\nabla^2 + v_{\mathrm{KS}}(\boldsymbol{r}) | \phi_{\boldsymbol{G}'+\boldsymbol{k}} \rangle, \tag{3.4}$$

and

$$S^{\boldsymbol{k}}_{\boldsymbol{G}\boldsymbol{G}'} = \langle \phi_{\boldsymbol{G}+\boldsymbol{k}} | \phi_{\boldsymbol{G}'+\boldsymbol{k}} \rangle, \tag{3.5}$$

respectively. As mentioned in Section 2.2.1, the KS equation must be solved self-consistently. The diagonalization of Eq. 3.3 is the most time-consuming part of the SCF cycle. Details on the implementation of the SCF cycle in `exciting` are given in Ref. [50].

3.2 (Linearized) augmented plane waves and local orbitals methods

The (L)APW+LO methods are considered the *gold-standard* for condensed matter calculations [173, 34]. A property, common to the entire (L)APW+LO family is the dual-space partition, which is motivated by the different behavior of the wave function and the potential in space: In the vicinity of the nuclei, the wave functions and potentials change rapidly, and are nearly spherical, as those in the atoms. Consequently, atomic-like functions are a natural choice for the basis functions in the spheres around the nuclei, which are called muffin tin (MT) spheres. On the other hand, in the space between the spheres, named interstitial region (IR), the wave functions and the potentials vary smoothly and the plane waves (PW) are considered to be a suitable choice as basis functions. In the following, we will briefly discuss some of the (L)APW+LO numerical schemes that are implemented in `exciting`.

Augmented plane waves

The APW method was proposed by Slater in 1937 [174]. It is relevant because it is the forerunner of the (L)APW+LO methods. The APW basis functions have the following form:

$$\phi^{\mathrm{APW}}_{\boldsymbol{G}+\boldsymbol{k}}(\boldsymbol{r}) = \begin{cases} \sum_{lm} A^{\boldsymbol{G}+\boldsymbol{k}}_{lm\alpha} u_{l\alpha}(r_\alpha) Y_{lm}(\hat{\boldsymbol{r}}_\alpha) & \text{for} \quad r_\alpha \leq R_{\mathrm{MT}}, \\ \frac{1}{\sqrt{\Omega}} e^{i(\boldsymbol{G}+\boldsymbol{k})\cdot\boldsymbol{r}} & \text{for} \quad \boldsymbol{r} \in I. \end{cases} \tag{3.6}$$

In the MT spheres of radius R_{MT}, the basis functions are expanded in terms of spherical harmonics, $Y_{lm}(\hat{\boldsymbol{r}}_\alpha)$, and radial functions, $u_{l\alpha}(r_\alpha)$. The latter are centered on the positions of the atomic nuclei with indices α and coordinates $\boldsymbol{R}_\alpha$, with $\boldsymbol{r}_\alpha \equiv \boldsymbol{r} - \boldsymbol{R}_\alpha$. The expansion coefficients, $A^{\boldsymbol{G}+\boldsymbol{k}}_{lm\alpha}$, are constructed so that each PW in the IR is augmented by the atom-centered functions, and it is continuous at the boundaries of the MT spheres. One of the weaknesses of the APW method is that the radial functions are energy dependent, since they are obtained by solving the radial Schrödinger equation, where the eigenenergies are those of the KS equation. Consequently, the eigenvalue problem in Eq. 3.3 is nonlinear in energy.

Linearized augmented plane-wave method

The linearized augmented plane wave (LAPW) method [175] overcomes the nonlinearity of the APW method. It is based on two main ideas: (*i*) The method uses an energy parameter for each angular momentum l and atomic sphere ($\varepsilon_{l\alpha}$), which is kept fixed during the whole calculation. In this way, the radial functions are obtained for energy parameters $\varepsilon_{l\alpha}$ [176]. (*ii*) In order to reduce the error related to the mismatch between the parameter $\varepsilon_{l\alpha}$ and the "true" energy, the basis functions in the MT not only consist of the radial functions $u_{l\alpha}(r_\alpha;\varepsilon_{l\alpha})$, but also of their energy derivatives $\dot{u}_{l\alpha}(r_\alpha;\varepsilon_{l\alpha})$:

$$\phi^{\mathrm{LAPW,MT}}_{\boldsymbol{G}+\boldsymbol{k}}(\boldsymbol{r}) = \sum_{lm}[A^{\boldsymbol{G}+\boldsymbol{k}}_{lm\alpha}u_{l\alpha}(r_\alpha;\varepsilon_{l\alpha}) + B^{\boldsymbol{G}+\boldsymbol{k}}_{lm\alpha}\dot{u}_{l\alpha}(r_\alpha;\varepsilon_{l\alpha})]Y_{lm}(\hat{\boldsymbol{r}}_\alpha). \tag{3.7}$$

The expansion coefficients $A^{\boldsymbol{G}+\boldsymbol{k}}_{lm\alpha}$ and $B^{\boldsymbol{G}+\boldsymbol{k}}_{lm\alpha}$ ensure that $\phi^{\mathrm{LAPW}}_{\boldsymbol{G}+\boldsymbol{k}}$ and its spatial derivative are continuous at the MT sphere boundaries. The inclusion of the radial function derivatives guarantees an error in the wave functions and energies of the order of $\mathcal{O}(\varepsilon_{l\alpha}-\epsilon)^2$ and $\mathcal{O}(\varepsilon_{l\alpha}-\epsilon)^4$, respectively, where ϵ are the true eigenenergies. Using the energy parameters $\varepsilon_{l\alpha}$ brings its own problems: By having a single energy parameter for all possible l_α, the description of semi-core states is problematic. Moreover, the precision of the calculations depends on the choice of the energy parameters and on how far they are from the "true" values. In the following, we will refer to the basis functions of the form in Eq. 3.6 and Eq. 3.7, both with fixed energy parameters, as APW basis functions.

APW plus local orbitals

The LO, $\phi_\mu(\boldsymbol{r})$, added to the APW basis functions, provide more flexibility trying to get rid of the error due to the energy mismatch and address the problem of semi-core states [177, 178]. Then, the KS wave functions of Eq. 3.2 become:

$$\varphi_{n\boldsymbol{k}}(\boldsymbol{r}) = \sum_{\boldsymbol{G}} c^{\boldsymbol{k}}_{n\boldsymbol{G}}\phi^{\mathrm{APW}}_{\boldsymbol{G}+\boldsymbol{k}}(\boldsymbol{r}) + \sum_{\mu} c^{\boldsymbol{k}}_{n\mu}\phi_\mu(\boldsymbol{r}). \tag{3.8}$$

The LO are zero in the IR, while in the MT spheres, they are linear combinations of radial functions and/or their energy derivatives. In a general form, they can be defined as:

$$\phi_\mu(\boldsymbol{r}) = \delta_{\alpha,\alpha_\mu}\delta_{l,l_\mu}\delta_{m,m_\mu}U_\mu(r_\alpha)Y_{lm}(\hat{r}_\alpha), \tag{3.9}$$

where

$$U_\mu(r_\alpha) = \sum_{\xi} a_{\mu\xi}u^{\nu}_{\alpha\xi l}(r_\alpha;\varepsilon_{\alpha\xi l}). \tag{3.10}$$

The index ξ sums over different radial functions, $u^{\nu}_{\alpha\xi l}$, where $\nu = 0, 1, 2, \ldots$ is the order of the derivative. The derivatives are evaluated at predefined energy parameters ($\varepsilon_{\alpha\xi l}$) which can be representative of the valence or of the semi-core states. The coefficients $a_{\mu\xi}$ are chosen to ensure that they go to zero with zero derivatives at the MT boundaries and that $\int_\Omega |\phi_\mu(\boldsymbol{r})|^2 \mathrm{d}\boldsymbol{r} = 1$. Depending on the purpose, an LO can be obtained by the linear combination of radial functions with the same or different energy parameters and with derivatives of the same or different orders. Again, the radial functions are computed for fixed energy parameters by solving the radial Schrödinger equation.

How to use (L)APW+LO in practice

Due to the dual-space representations of the APW basis functions, the cutoff $G_{\max}$ of Eq. 3.2 alone, is meaningless: The amount of APW functions needed for a converged calculation depends on the sphere sizes. Therefore, it is better to use the dimensionless product $R_{\mathrm{MT}}G_{\max}$ as the convergence parameter. In the case of different atomic species with different R_{MT}, the smallest one is used to determine the number of APW functions through the product $R_{\mathrm{MT}}^{\min}G_{\max}$. Note that the MT spheres must be sufficiently large to accommodate the extension of the core states. The number of LO needed depends on the type of calculation one wants to perform and on the precision one wants to achieve. In addition, the further away the energy parameters are from the true energies, the more LO may be needed [50]. A good initial guess for the energy parameters is to use those of isolated atoms since they are typically not too far from those of the occupied states.

3.3 Hybrid functionals in the (L)APW+LO framework

The implementation of hybrid functionals in `exciting` follows the scheme proposed by Betzinger and coworkers [97] for the PBE0 functional in the FLEUR code. For the evaluation of the NL potentials, it builds on the `exciting` G_0W_0 implementation, based on the FHI$_{\mathrm{GAP}}$ package [179]. The form of the exchange self-energy is indeed very similar to that of the non-local exact exchange (see Section 2.3.2). The scheme is explained here for PBE0 and is the starting point for the implementation of other hybrid functionals, e.g. HSE.

The use of hybrid functionals requires the solution of the gKS equations (Eq. 2.16), which, in a periodic system, take the form:

$$\left[-\frac{1}{2}\nabla^2 + v_{\text{ext}}(\boldsymbol{r}) + v_{\text{H}}(\boldsymbol{r}) + v_{\text{xc}}^{\text{L},\alpha}(\boldsymbol{r})\right]\varphi_{n\boldsymbol{k}}(\mathbf{r}) + \alpha \int v_{\text{x}}^{\text{NL}}(\boldsymbol{r},\boldsymbol{r}')\varphi_{n\boldsymbol{k}}(\boldsymbol{r}')d\boldsymbol{r} = \varepsilon_{n\boldsymbol{k}}\varphi_{n\boldsymbol{k}}(\boldsymbol{r}). \quad (3.11)$$

The local xc potential $v_{\text{xc}}^{\text{L},\alpha}$ corresponds to the last term in Eq. 2.27, i.e.

$$v_{\text{xc}}^{\text{L},\alpha} = \frac{\delta}{\delta\rho}[E_{\text{xc}}^{\text{L}} - \alpha E_{\text{x}}^{\text{L}}]. \quad (3.12)$$

The NL exchange potential is defined as

$$v_{\text{x}}^{\text{NL}}(\boldsymbol{r},\boldsymbol{r}') = -\sum_{n}^{\text{occ.}}\sum_{\boldsymbol{k}'}^{\text{BZ}} \frac{\varphi_{n\boldsymbol{k}'}(\boldsymbol{r})\varphi_{n\boldsymbol{k}'}^{*}(\boldsymbol{r}')}{|\boldsymbol{r}-\boldsymbol{r}'|}. \quad (3.13)$$

By rewriting the gKS equations (Eq. 3.11) in terms of APW+LO basis functions, one obtains the following generalized eigenvalue problem:

$$\sum_{\boldsymbol{G}'}[H_{\boldsymbol{G}\boldsymbol{G}'}^{\text{L},\boldsymbol{k}} + \alpha V_{\text{x},\boldsymbol{G}\boldsymbol{G}'}^{\text{NL},\boldsymbol{k}}]c_{n\boldsymbol{G}'}^{\boldsymbol{k}} = \epsilon_{n\boldsymbol{k}}\sum_{\boldsymbol{G}'} S_{\boldsymbol{G}\boldsymbol{G}'}^{\boldsymbol{k}}c_{n\boldsymbol{G}'}^{\boldsymbol{k}}, \quad (3.14)$$

where $H_{\boldsymbol{G}\boldsymbol{G}'}^{\text{L},\boldsymbol{k}}$ and $V_{\text{x},\boldsymbol{G}\boldsymbol{G}'}^{\text{NL},\boldsymbol{k}}$ are the matrix elements of the local part of the Hamiltonian and the NL potential, respectively. In (L)APW+LO codes it is convenient to compute the NL exact exchange matrix in terms of the KS wave functions and then project it back onto APW+LO basis functions [97]:

$$V_{\text{x,GG}'}^{\text{NL},\boldsymbol{k}} = \sum_{nn'}\left[\sum_{\boldsymbol{G}''}(S_{\boldsymbol{G}\boldsymbol{G}''}^{\boldsymbol{k}})^{*}c_{n\boldsymbol{G}''}^{\boldsymbol{k}}\right]V_{\text{x},nn'}^{\text{NL},\boldsymbol{k}}\left[\sum_{\boldsymbol{G}''}(c_{n'\boldsymbol{G}''}^{\boldsymbol{k}})^{*}S_{\boldsymbol{G}''\boldsymbol{G}'}^{\boldsymbol{k}}\right], \quad (3.15)$$

where $V_{\text{x},nn'}^{\text{NL},\boldsymbol{k}}$ are the NL exact exchange matrix elements in the KS space:

$$V_{\text{x},nn'}^{\text{NL},\boldsymbol{k}} = -\sum_{n''}^{\text{occ}}\sum_{\boldsymbol{k}'}^{\text{BZ}}\int\int \frac{\varphi_{n\boldsymbol{k}}^{*}(\boldsymbol{r})\varphi_{n''\boldsymbol{k}'}(\boldsymbol{r})\varphi_{n''\boldsymbol{k}'}^{*}(\boldsymbol{r}')\varphi_{n'\boldsymbol{k}}(\boldsymbol{r}')}{|\mathbf{r}-\boldsymbol{r}'|}d\boldsymbol{r}d\boldsymbol{r}'. \quad (3.16)$$

The reasons are that (*i*) the NL exchange is small compared to other energy contributions such as the kinetic and the Hartree energies, so the NL exchange can be computed for a subset of KS states limited by the cutoff, $n, n' \leq n_{\text{max}} = N_{\text{occ}} + N_{\text{unocc}}$. N_{occ} is the number of occupied states, which is fixed, and N_{unocc} is that of the unoccupied states, which is a parameter to be converged. (*ii*) If the indices n, n' fall into different representations, the matrix elements of the NL potential are zero. This can be used to reduce the computational effort [97] (not yet implemented in **`exciting`**).

The sum over the index n'' in Eq. 3.16 goes over core and valence/semi-core states. The former require a different treatment that takes advantage of their restriction to the MT spheres and can be considered simple and computationally cheap [180]. For the valence/semicore states, it is convenient to use the mixed-product basis (MPB), which simplifies the six-dimensional integral by decomposing it into a vector-matrix-vector product. Even with these simplifications, the NL exchange potential is the most computationally demanding term of the generalized KS equation (Eq. 3.14). For this reason, it is convenient to solve the gKS problem by constructing a nested self-consistent loop (see Section 3.3.3).

3.3.1 Mixed-product basis

The MPB functions, $\chi_I^{\mathbf{q}}$, are designed to accurately describe the product of two KS wavefunctions:

$$\varphi^*_{n\boldsymbol{k}}(\boldsymbol{r})\varphi_{n'\boldsymbol{k}'}(\boldsymbol{r}) = \sum_I M^I_{nn'}(\boldsymbol{k},\boldsymbol{q})\chi_I^{\boldsymbol{q}}(\boldsymbol{r}), \tag{3.17}$$

where $\boldsymbol{q} \equiv \boldsymbol{k} - \boldsymbol{k}'$ and $M^I_{nn'}(\boldsymbol{k},\boldsymbol{q})$ are the expansion coefficients defined as:

$$M^I_{nn'}(\boldsymbol{k},\boldsymbol{q}) = \int_\Omega [\chi_I^{\boldsymbol{q}}(\boldsymbol{r})\varphi_{n'\boldsymbol{k}'}(\boldsymbol{r})]^*\varphi_{n\boldsymbol{k}}(\boldsymbol{r})d\boldsymbol{r}. \tag{3.18}$$

Like the APW basis functions, they have a different character in the MT and in the IR. The MPB are defined only in one region and zero in the other. In this regard, one can split the MPB as follows:

$$\{\chi_I^{\boldsymbol{q}}(\boldsymbol{r})\} \equiv \{\gamma^{\boldsymbol{q}}_{\alpha NLM}(\boldsymbol{r}), P_i^{\boldsymbol{q}}(\boldsymbol{r})\}, \tag{3.19}$$

where $\gamma^{\boldsymbol{q}}_{\alpha NLM}$ and $P_i^{\boldsymbol{q}}$ are the MPB in the MT sphere of atom α and in the IR, respectively. The former are constructed to be orthonormal and exploit the property that the product of two spherical harmonics can be expanded into a spherical harmonic using the Clebsch–Gordan coefficients:

$$\gamma^{\boldsymbol{q}}_{\alpha NLM}(\boldsymbol{r}) = \mathrm{e}^{i\boldsymbol{q}\cdot\boldsymbol{r}_\alpha}v_{\alpha NL}(r_\alpha)Y_{LM}(\hat{\boldsymbol{r}}_\alpha). \tag{3.20}$$

Here, $v_{\alpha NL}(r_\alpha)$ are the radial functions constructed by the product of the APW+LO radial functions, and N, L, and M are indices combining the quantum numbers of the APW+LO basis functions that are multiplied. The procedure for determining the radial functions $v_{\alpha NL}(r_\alpha)$ is explained in more detail in Ref. [179]. However, it is important to note that only radial functions $u_{l\alpha}$ with $l \leq l_{\max}^{\mathrm{MPB}}$ are used to construct $v_{\alpha NL}(r_\alpha)$. The cutoff $l_{\max}^{\mathrm{MPB}}$ can be controlled by the `exciting` input.

The product of two PW is itself a PW. In the case of P_i^{q}, one speaks of interstitial plane waves (IPW), which are not orthogonal. To obtain a set of orthogonal wave functions the overlap matrix must be diagonalized, and from it the following set of orthonormal basis functions is constructed:

$$P_i^{\boldsymbol{q}}(\boldsymbol{r}) = \frac{1}{\sqrt{\Omega}} \sum_{\boldsymbol{G}} \tilde{S}_{\boldsymbol{G}i} \mathrm{e}^{i(\boldsymbol{q}+\boldsymbol{G})\cdot\boldsymbol{r}} \Theta_I(\boldsymbol{r}), \tag{3.21}$$

where Θ_I is 1 in the IR and 0 in the MT spheres, and $\tilde{S}_{\boldsymbol{G}i}$ is computed from the following relation:

$$\tilde{S}_{\boldsymbol{G}i} = \frac{S_{\boldsymbol{G}i}}{\sqrt{\lambda_i^I}}. \tag{3.22}$$

$S_{\boldsymbol{G}i}$ and λ_i^I are the eigenvectors and the eigenvalues of the overlap matrix, respectively. The size of the MPB in the IR is determined by the cutoff used to truncate the expansion in Eq. 3.21, named $G_{\max}^{\mathrm{MPB}}$, which can also be defined in the `exciting` input.

The implementation of the MPB in `exciting` follows that of Ref. [179]. Additional details can be found in Ref. [181, 182, 97].

3.3.2 Non-local exchange potential

Using the MPB (Eq. 3.17), the matrix elements of the NL exchange potential, defined in Eq. 3.16, can be rewritten as vector-matrix-vector products:

$$V_{\mathrm{x},nn'}^{\mathrm{NL}}(\boldsymbol{k}) = -\sum_{n''}^{\mathrm{occ}} \sum_{\boldsymbol{q}}^{\mathrm{BZ}} \sum_{IJ} [M_{nn''}^I(\boldsymbol{k},\boldsymbol{q})]^* v_{IJ}(\boldsymbol{q}) M_{n''n'}^J(\boldsymbol{k},\boldsymbol{q}), \tag{3.23}$$

where $v_{IJ}(\boldsymbol{q})$ is the bare Coulomb potential defined as

$$v_{IJ}(\boldsymbol{q}) = \int\int \frac{[\chi_I^{\boldsymbol{q}}(\boldsymbol{r})]^* \chi_J^{\boldsymbol{q}}(\boldsymbol{r}')}{|\boldsymbol{r}-\boldsymbol{r}'|} d\boldsymbol{r} d\boldsymbol{r}'. \tag{3.24}$$

In `exciting`, the bare Coulomb potential can be computed in two different ways. The default approach is to compute it directly in the MPB as defined in Eq. 3.24. This method requires the use of non trivial numerical techniques [182, 179]. A simpler approach is to compute the bare Coulomb potential in a PW representation, since the potential is diagonal in it, and the result is simply its Fourier transform:

$$v^{\mathrm{PW}}(\boldsymbol{q}+\boldsymbol{G}) = \frac{4\pi}{|\boldsymbol{q}+\boldsymbol{G}|^2}\delta_{\boldsymbol{G}\boldsymbol{G}'}. \tag{3.25}$$

To include this expression in Eq. 3.23, the following overlap integral between the PW basis and the MPB must be computed:

$$\mathcal{W}^I_{\boldsymbol{G}} = \frac{1}{\sqrt{\Omega}}\int_\Omega \mathrm{d}\boldsymbol{r}[\chi^{\boldsymbol{q}}_I(\boldsymbol{r})]^* \mathrm{e}^{i(\boldsymbol{q}+\boldsymbol{G})\cdot\boldsymbol{r}}. \tag{3.26}$$

In this way, Eq. 3.23 can be rewritten as:

$$V^{\mathrm{NL}}_{\mathrm{x},nn'}(\boldsymbol{k}) = -\sum_{n''}^{\mathrm{occ}}\sum_{\boldsymbol{q}}^{\mathrm{BZ}}\sum_{IJ}\sum_{\boldsymbol{G}}[\mathcal{W}^I_{\boldsymbol{G}} M^I_{nn''}(\boldsymbol{k},\boldsymbol{q})]^* v^{\mathrm{PW}}(\boldsymbol{q}+\boldsymbol{G})\mathcal{W}^J_{\boldsymbol{G}} M^J_{n''n'}(\boldsymbol{k},\boldsymbol{q}). \tag{3.27}$$

From Eq. 3.25 it is easy to see that for $\boldsymbol{q}+\boldsymbol{G} \to 0$ the bare Coulomb potential diverges. A special treatment is applied to this term, which is discussed in Refs. [182, 179].

Equation 3.23 can be additionally contracted by first computing

$$\tilde{M}^I_{nn''}(\boldsymbol{k},\boldsymbol{q}) = \sum_P v^{1/2}_{IP}(\boldsymbol{q}) M^P_{nn'}(\boldsymbol{k},\boldsymbol{q}) \tag{3.28}$$

and then inserting it into Eq. 3.23:

$$V^{\mathrm{NL}}_{\mathrm{x},nn'}(\boldsymbol{k}) = -\sum_{n''}^{\mathrm{occ}}\sum_{\boldsymbol{q}}^{\mathrm{BZ}}\sum_{IJ}[\tilde{M}^I_{nn''}(\boldsymbol{k},\boldsymbol{q})]^* \tilde{M}^J_{n''n'}(\boldsymbol{k},\boldsymbol{q}). \tag{3.29}$$

Since the form of the NL exact exchange resembles that of the exchange self-energy, many routines involved in its implementation overlap with those used in *GW*.

3.3.3 Nested self-consistent cycle

The evaluation of the NL exact exchange potential is the computationally most intensive part of hybrid functional calculations. The use of a nested loop greatly reduces the number of times the NL potential must be evaluated. For example, for silicon, a reduction from 29 to 8 times was observed [97].

The implementation in **`exciting`** is sketched in Fig. 3.1. It consists of an outer and an inner loop preceded by an SCF calculation employing PBE as the xc functional. This preliminary SCF is necessary to obtain the KS wave functions to construct the MPB, $\{\chi_I^{\mathbf{q}}\}$ (second block). In the outer loop, the NL potential is updated: first, it is computed in the KS space as explained in Section 3.3.2, and then it is projected onto the APW+LO space (Eq. 3.15). In the inner loop, the generalized KS equations (Eq. 3.11) are solved by the same procedure as for the KS equations, but by keeping the NL potential fixed and updating the L part of the Hamiltonian at each SCF step. The nested loop ends when the difference between the charge densities of the last two outer steps is within the desired

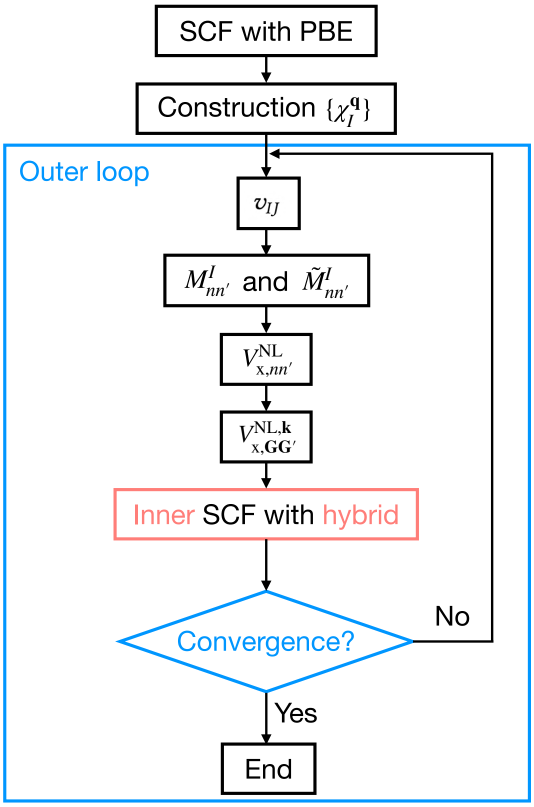

Figure 3.1: Scheme of the nested loop of hybrid functionals. The outer loop is highlighted by the light blue rectangle, while the inner loop is represented by the pink block. Before entering the outer loop, a preliminary SCF calculation is performed using PBE, and the MPB functions ($\{\chi_I^{\mathbf{q}}\}$) are constructed. The blocks in the outer loop indicate the evaluation of the bare Coulomb potential, v_{IJ}, the MPB coefficients $M^I_{nn'}$ and $\tilde{M}^I_{nn'}$, and the NL potential matrix elements in KS space ($V^{\mathrm{NL}}_{\mathrm{x},nn'}$) and in APW+LO space ($V^{\mathrm{NL},\mathbf{k}}_{\mathrm{x},\mathbf{GG}'}$).

convergence criteria. The convergence check is performed immediately after the inner SCF. The evaluation of the MBP coefficients ($\tilde{M}^{I}_{nn'}$), part of the second block of the outer loop, is the computationally most demanding part of the calculation.

3.4 Treatment of spin-orbit coupling

When SOC is considered, the following two-component KS equations must be solved:

$$\sum_{\sigma'=1}^{2}[\delta_{\sigma\sigma'}\mathcal{H}^{\sigma}_{\mathrm{SR}} + \mathcal{H}^{\sigma\sigma'}_{\mathrm{SOC}}]\varphi^{\sigma'}_{n\boldsymbol{k}}(\boldsymbol{r}) = \varepsilon_{i\boldsymbol{k}}\varphi^{\sigma}_{n\boldsymbol{k}}(\boldsymbol{r})\,. \tag{3.30}$$

The first term is the SR Hamiltonian as discussed in Section 2.2.4, and the second term is the SOC Hamiltonian, which in this work is treated only in the MT spheres within the *zero order regular approximation* (ZORA) [133, 134]:

$$\mathcal{H}_{\mathrm{SOC}} = \frac{\alpha_{\mathrm{fs}}^{2}}{[2-\alpha_{\mathrm{fs}}^{2}\tilde{v}_{\mathrm{KS}}(r)]^{2}}\frac{1}{r}\frac{\partial v_{\mathrm{KS}}(r)}{\partial r}\boldsymbol{\sigma}\cdot\boldsymbol{L}. \tag{3.31}$$

Here α_{fs} is the fine structure constant and v_{KS} is the spherical KS potential. Due to the coupling of the two spins, σ, σ', the solution of these equations is computationally demanding. To reduce the computational effort, the SV treatment [183, 173] is often used to solve Eq. 3.30. The direct solution of Eq. 3.30 is what we refer to as *non-perturbative treatment* (NP)[1].

3.4.1 Non perturbative treatment

Equation 3.30 in matrix form becomes:

$$\sum_{\sigma'=1}^{2}\sum_{\boldsymbol{G}'}H^{\sigma\sigma'\boldsymbol{k}}_{\boldsymbol{G}\boldsymbol{G}'}c^{\sigma'\boldsymbol{k}}_{n\boldsymbol{G}'} = \epsilon_{n\boldsymbol{k}}\sum_{\sigma'=1}^{2}\sum_{\boldsymbol{G}'}S^{\sigma\sigma'\mathrm{k}}_{\boldsymbol{G}\boldsymbol{G}'}c^{\sigma'\boldsymbol{k}}_{n\boldsymbol{G}'}. \tag{3.32}$$

where $H^{\sigma\sigma'\boldsymbol{k}}_{\boldsymbol{G}\boldsymbol{G}'}$ are the matrix element of the complete Hamiltonian, $\mathcal{H} = \mathcal{H}_{\mathrm{SR}} + \mathcal{H}_{\mathrm{SOC}}$. Its solution is equivalent to the solution of Eq. 3.3, with the additional evaluation of the SOC matrix elements. However, due to the spin, in Eq. 3.32 the vector of the coefficients is twice as large ($2N_{\mathrm{b}}$), the Hamiltonian matrix is four times as large ($4N_{\mathrm{b}}^{2}$), and the

---

[1] The non-perturbative treatment, implemented in `exciting` by Andris Gulans [184], has not yet been released. In this implementation, the SOC is also evaluated in the IR. However, this aspect is not discussed in the manuscript.

diagonalization of the Hamiltonian, which scales as N^3, is a problem eight times as large ($8N_\mathrm{b}^3$).

3.4.2 Second variation treatment

Considering SOC as a perturbation leads to the inclusion of the SOC term as a correction to the SR solution. The method is a two-step procedure: First, the SR equation is diagonalized (Eq. 3.3), which is the reason why the SR solution is often referred to as *first variation* (FV). A subset of the computed FV eigenvectors and eigenfunctions is then used to construct the total Hamiltonian matrix element. In particular, a fraction of the FV eigenvectors is employed as basis functions for the SV wave function:

$$\varphi_{n\boldsymbol{k}}^{\mathrm{SV}}(\boldsymbol{r}) = \sum_{n'=1}^{N_\mathrm{b}^{\mathrm{SV}}} \sum_{\sigma'=1}^{2} C_{\boldsymbol{k}n'\sigma'}^{n} \varphi_{n'\boldsymbol{k}}^{\sigma',\mathrm{FV}}(\boldsymbol{r}). \tag{3.33}$$

Here the coefficients are $C_{\boldsymbol{k}m\sigma'}^{n} = \tilde{c}_{\boldsymbol{k}m}^{n} \chi_{\sigma'}$ with $\chi_{\sigma'}$ being the spin state associated with σ'. The FV wave functions $\varphi_{n'\boldsymbol{k}}^{\sigma',\mathrm{FV}}$ are expanded in the APW+LO as in Eq. 3.8. In the first sum, the number of SV basis functions ($N_\mathrm{b}^{\mathrm{SV}}$), and thus the number of FV eigenvectors used as basis functions, includes all the valence/semicore states (N_{occ}) plus a number of unoccupied states determined by a cutoff:

$$N_\mathrm{b}^{\mathrm{SV}} = N_{\mathrm{occ}} + N_{\mathrm{unocc}}. \tag{3.34}$$

This number is a convergence parameter to be determined based on the desired precision. The matrix elements of the total Hamiltonian are then computed as

$$H_{\boldsymbol{k}nn'}^{\sigma\sigma'} = \delta_{\sigma\sigma'}\delta_{nn'}\varepsilon_{n\boldsymbol{k}}^{\sigma,\mathrm{FV}} + \langle \varphi_{n\boldsymbol{k}}^{\sigma,\mathrm{FV}} | \, H_{\mathrm{SOC}}^{\sigma\sigma'} \, | \varphi_{n'\boldsymbol{k}}^{\sigma',\mathrm{FV}} \rangle \,, \tag{3.35}$$

where $\varepsilon_{n\boldsymbol{k}}^{\sigma,\mathrm{FV}}$ are the eigenvalues of the SR eigenvalue problem (Eq. 3.3). Since the FV eigenvectors are KS wave functions, the overlap matrix is diagonal and the eigenvalue problem to be solved is the following:

$$\sum_{\sigma''n''} H_{\boldsymbol{k}n'n''}^{\sigma'\sigma''} C_{\boldsymbol{k}n''\sigma''}^{n} = \varepsilon_{n\boldsymbol{k}}^{\mathrm{SV}} C_{\boldsymbol{k}n'\sigma'}^{n}. \tag{3.36}$$

In `exciting`, this procedure is repeated self-consistently until convergence is reached.

The solution of Eq. 3.30 via the SV scales as $(N_\mathrm{b}^\mathrm{FV})^3 + (2N_\mathrm{b}^\mathrm{SV})^3$. Here, we added the superscript FV in the number of APW+LO basis functions, N_b^FV, in order to better distinguish them from the SV basis functions, N_b^SV. This method is convenient only when a few low-lying KS bands are needed for a precise description of the SOC effects ($N_\mathrm{b}^\mathrm{SV} \ll N_\mathrm{b}^\mathrm{FV}$). As we will discuss in Chapter 6, this is not always the case.

3.5 One-shot *GW* calculations

The implementation of the one-shot *GW* approximation in `exciting` follows Refs. [179, 33]. In this implementation, the KS eigenvalues $\epsilon_{n\boldsymbol{k}}^\mathrm{KS}$ are used as zero-order approximations of the QP eigenenergies, which are computed as:

$$\epsilon_{n\boldsymbol{k}}^\mathrm{QP} = \epsilon_{n\boldsymbol{k}}^\mathrm{KS} + Z_{n\boldsymbol{k}} \left[\Re\Sigma_{\mathrm{nk}}^\mathrm{c}(\epsilon_{n\boldsymbol{k}}^\mathrm{KS}) + \Sigma_{n\boldsymbol{k}}^\mathrm{x} - v_{n\boldsymbol{k}}^\mathrm{xc} \right]. \tag{3.37}$$

Here, $\Re\Sigma_{n\boldsymbol{k}}^\mathrm{c}$ and $\Sigma_{n\boldsymbol{k}}^\mathrm{x}$ are the (real) correlation and the exchange part of the self-energy, respectively, and $v_{n\boldsymbol{k}}^\mathrm{xc}$ are the diagonal matrix elements of the xc functional obtained from the self-consistent solution of the KS equations. The QP renormalization factor $Z_{n\boldsymbol{k}}$, which results from the energy dependence of the correlation self-energy, is computed as:

$$Z_{n\boldsymbol{k}} = \left[1 - \left(\frac{\partial}{\partial\omega} \Re\Sigma_{n\boldsymbol{k}}^\mathrm{c}(\omega) \right)_{\omega=\epsilon_{n\boldsymbol{k}}^\mathrm{KS}} \right]^{-1}. \tag{3.38}$$

The correlation and exchange parts of the self-energy are computed in matrix form by making use of the MPB functions (Section 3.3.1). The calculation of the exchange parts is very similar to that of the NL exact exchange potential, $V_{\mathrm{x},nn'}^\mathrm{NL}$ (Eq. 3.3.2), except that the exchange self-energy matrix is diagonal in the band index n, n'. Calculating the correlation part is more complex and computationally demanding. To compute it, the dielectric function and the polarizability within the RPA are evaluated first. Because of the poles of the Green's function and the screened Coulomb potential, it is convenient to compute the polarizability, the screened Coulomb potential, and the correlation self-energy in the imaginary frequency space. The correlation self-energy is then obtained by solving an integral over the imaginary frequency space, which contains a smooth function and can be solved in different ways. The default one in `exciting` is the double Gauss–Legendre quadrature [185, 186]. Jiang and co-workers [179] showed that with this approach only a few imaginary frequency points are needed for convergence. The resulting correlation self-energy is then analytically continued onto the real frequency space. Again, there are several approaches. The default one in **`exciting`** is the Pade approximation [187, 188]. It is important to keep in mind that this method can give unphysical renormalization factors $Z_{n\mathbf{k}}$ for states far from the Fermi energy [179].

Since the self-energy is a NL quantity, both $\boldsymbol{k}$-mesh and a $\boldsymbol{q}$-mesh must be set in the input. In **`exciting`**, they must be the same. As in the case of hybrid xc-functionals, the number of empty states is an important convergence parameter. Quantities that require attention are those related to the MPB (Section 3.3.1), the imaginary frequency grid used in the double Gauss–Legendre quadrature scheme, and the real space grid used for the analytical continuation. In addition, LO for unoccupied states are often necessary [33]. When performing G_0W_0 on top of local/semi-local functionals (already converged), a single ground state step is performed as a starting point. It allows the parameters in the DFT and the GW calculation to be different. Contrarily, in the case of hybrid functionals, the DFT and GW parameters must be the same.

G_0W_0 calculations with SOC are carried out on top of a ground-state calculation including SOC in a two-step procedure: (*i*) The FV eigenvalues and eigenvectors are used to evaluate the QP eigenenergies omitting SOC by solving Eq. 3.37. (*ii*) The SV Hamiltonian matrix elements (Eq. 3.35) are constructed by using the QP eigenenergies evaluated in the previous step. The QP eigenenergies with SOC are then obtained by solving the SV eigenvalue equation (Eq. 6.4). This method is considered sufficient for many materials where SOC does not generate a band inversion [189, 35].

3.6 Calculation of optical properties

The methods used to evaluate the optical properties in Chapters 7 and 8 are the RPA without and including LFE. The former will be referred to as IPA. In Appendix C.3, some calculations are based on the BSE including SOC.

To compute the optical spectra within the IPA, the first step is to calculate the matrix elements of the momentum operator, which for a local Hamiltonian, is equal to the matrix element of the velocity operator (Eq. 2.68). The result is then used to determine the dielectric tensor. Due to the finite size of the simulated system, the resulting optical spectrum is formed by a series of δ peaks with different oscillator strengths. To simulate the infinite system, a Lorentzian broadening is applied, with its width being an input parameter.

For computing the dielectric functions at infinite frequency (ε_∞) within the RPA including LFE, it is convenient to use the time-dependent DFT framework of `exciting`. Important parameters, in this case, are the number of unoccupied states and the LFE cutoff for computing the irreducible polarizability (χ_0). The LFE cutoff ($G_{\max}$) defines the limit $|G + q|,|G' + q| < G_{\max}$ when calculating $\chi_{\boldsymbol{GG}'}(\boldsymbol{q})$ (Eq. 2.66).

When performing a BSE calculation, the first step is to construct the BSE Hamiltonian. Within the Tamm–Dancoff approximation (TDA), the BSE Hamiltonian is composed of three terms: the first term is diagonal and corresponds to the transition energies of the independent particles; the second is the exchange term and evaluates the repulsive interaction between electrons and holes; the third term accounts for the attractive screened Coulomb interaction. In order to compute the latter, the screening has to be calculated, making it the most computationally demanding part. All the parameters important for the RPA calculations just discussed are also important for the BSE.

3.7 Maximally localized Wannier functions interpolation

Maximally localized Wannier functions (MLWF) are a powerful tool widely used in condensed matter physics [190, 191]. The interpolation scheme based on MLWF provides access to both single-particle eigenvalues and eigenfunctions at any reciprocal-space point and can be used for computing properties such as band structures and densities of states (DOS). In `exciting`, the Wannier interpolation method is typically employed when computing these properties with hybrid functionals and G_0W_0, since it is more efficient than evaluating the eigenvalues at each $\boldsymbol{k}$-point via the diagonalizing of the Hamiltonian or using the GW approximation. It also requires fewer $\boldsymbol{k}$-points than other interpolation methods such as the Fourier interpolation.

To use this interpolation method, the first step is to construct the MLWF. This is the computationally most intensive part. There are several methods for constructing the MLWF, depending on the type of bands to be described. For example, the method used for a group of isolated bands, as typical for occupied bands of insulators and semiconductors, is different from that used for bands that cannot be disentangled from other bands, as typical for conduction bands and metals. In addition, the $\boldsymbol{k}$-mesh affects the construction of the MLWF. Once they are constructed, one can obtain a Bloch function at any arbitrary reciprocal space point, which is used to build a new Hamiltonian matrix that is much smaller than the original KS Hamiltonian. More information about the MLWF and the Wannier interpolation method and their implementation in **`exciting`** can be found in Ref. [192].

Part II

Method developments and implementations

CHAPTER 4

The HSE functional in `exciting`

The HSE functional is considered the best hybrid functional for computing the electronic properties of small and medium gap semiconductors, such as HaP. It is also a better starting point for G_0W_0 calculations compared to local/semi-local functionals. For this reason, as part of this work, the HSE functional has been implemented in the `exciting` code. The implementation and its validation are discussed in this chapter.

4.1 Implementation

The HSE functional is defined in Eq. 2.31. The version of HSE implemented in `exciting` is that of 2006, called HSE06 [32], where the screening parameter ω is $0.11 a_0^{-1}$ and set to be the same for the NL potential and the PBE exchange (see Section 2.2.3.2 and Eq. 2.31). Note that the value of ω can be changed in the `exciting` input, but it is not possible to have two different values like in HSE03 [95, 96].

Our implementation is based on the work of Schlipf and coworkers [193, 194], where the xc potential, described in Section 2.2.3.2, is computed as follows:

$$v_{\mathrm{xc}}^{\mathrm{HSE}} = v_{\mathrm{xc}}^{\mathrm{PBE}} - \alpha v_{\mathrm{x}}^{\mathrm{PBE,sR}}(\omega) + \alpha(v_{\mathrm{x}}^{\mathrm{NL}} - v_{\mathrm{x}}^{\mathrm{NL,LR}}(\omega)). \tag{4.1}$$

Here $v_{\mathrm{xc}}^{\mathrm{PBE}}$ and $v_{\mathrm{x}}^{\mathrm{PBE,sR}}$ are the functional derivatives of $E_{\mathrm{xc}}^{\mathrm{PBE}}$ and $E_{\mathrm{xc}}^{\mathrm{PBE,sR}}$, respectively. The parentheses contain the NL-sR potential, which is calculated by subtracting the LR part from the total NL exact exchange potential. The PBE-sR and the NL-LR potentials were the only missing pieces in the code. To obtain the PBE-sR potential, we included the screened exchange-hole formulation of PBE [195, 95, 196], which we refer to as ωPBEh (Section 4.1.1). The scheme used to compute the NL-sR is slightly different from that of Schlipf and coworkers (Section 4.1.2).

4.1.1 Screened exchange-hole formulation of PBE

The ωPBEh functional is employed to compute the PBE-sR [195, 95, 196]. It is constructed starting from the exchange-hole formulation of PBE [197], which we will distinguish from the most common form of PBE [73] by calling it PBEh. Its enhancement factor $F_{\mathrm{x}}^{\mathrm{PBE}h}$ is defined as an integral over the exchange-hole, $J^{\mathrm{PBE}h}(s,y)$:

$$F_{\mathrm{x}}^{\mathrm{PBE}h} = -\frac{8}{9}\int_0^{\infty} dy\ yJ^{\mathrm{PBE}h}(s,y). \tag{4.2}$$

Here s is the reduced density gradient, and y is the reduced interelectronic separation, which are defined as $s = |\nabla\rho|/2k_{\mathrm{F}}\rho$ and $y = k_{\mathrm{F}}|\mathbf{r}-\mathbf{r}'|$, respectively. k_{F} is the Fermi wave vector, which in a 3D crystal is $k_{\mathrm{F}} = (3\pi^2\rho)^{1/3}$. The screened exchange-hole is obtained by multiplying the PBE exchange-hole by the complementary error function, as follows:

$$J^{\omega\mathrm{PBE}h}(\rho,s,y) = J^{\mathrm{PBE}h}(s,y)\mathrm{erfc}\Big(\frac{\omega y}{k_{\mathrm{F}}}\Big). \tag{4.3}$$

If $\omega = 0$, PBEh is recovered. The explicit forms of $J^{\mathrm{PBE}h}(s,y)$ and $J^{\omega\mathrm{PBE}h}(\rho,s,y)$ are complex, so they are omitted here. The one of $J^{\mathrm{PBE}h}(s,y)$ can be found in Ref. [197]. Several forms of ωPBEh have been proposed. We have implemented the revised screened exchange-hole formulation of Ref. [196].

Background

In Section 2.2.3, we gave a brief overview of the different local/semi-local functionals. Here, we will focus only on the ingredients necessary to understand the implementation of ωPBEh in `exciting`.

Considering only the exchange part of PBE, Eq. 2.21 becomes

$$E_{\mathrm{x}}^{\mathrm{PBE}}[\rho(\boldsymbol{r})] = \int d\boldsymbol{r}\rho(\boldsymbol{r})\varepsilon_{\mathrm{x}}^{\mathrm{PBE}}(\rho(\boldsymbol{r}),s(\boldsymbol{r})) = \int d\boldsymbol{r}\rho(\boldsymbol{r})\varepsilon_{\mathrm{x}}^{\mathrm{LDA}}(\rho(\boldsymbol{r}))F_{\mathrm{x}}^{\mathrm{PBE}}(s(\boldsymbol{r})), \tag{4.4}$$

where $\varepsilon_{\mathrm{x}}^{\mathrm{LDA}}$ is the LDA energy density ($\varepsilon_{\mathrm{x}}^{\mathrm{LDA}} = 3/4(3\rho/\pi)^{1/3}$). The PBE exchange potential is obtained from its functional derivative as follows:

$$v_{\mathrm{x}}^{\mathrm{PBE}} = \frac{\delta E_{\mathrm{x}}^{\mathrm{PBE}}[\rho(\boldsymbol{r})]}{\delta\rho(\boldsymbol{r})} = \frac{\partial\varepsilon_{\mathrm{x}}^{\mathrm{PBE}}}{\partial\rho(\boldsymbol{r})} + \nabla\cdot\frac{\partial\varepsilon_{\mathrm{x}}^{\mathrm{PBE}}}{\partial\nabla\rho(\boldsymbol{r})}. \tag{4.5}$$

The PBE enhancement factor has a simple form for which an analytical expression of the divergence in Eq. 4.5 can be derived[1]. In the cases of PBEh and ωPBEh, this is not possible, and the divergence must be computed numerically.

Implementation

We adopted three routines from the Quantum ESPRESSO (QE) code [198, 199] (allowed by the GNU license [200]) and applied a few modifications to make them compatible with the **exciting** code. The routines are `gga_x_wpbeh`, `wpbeh_analy_erfc_approx_grad` and `expint` (renamed in **exciting**). They output the exchange energy density ($\varepsilon_{\mathrm{x}}^{\mathrm{PBE}}$in Eq. 4.4) and two terms needed to calculate the exchange potential (Eq. 4.5):

$$v_{\mathrm{x},1} = \frac{\partial\varepsilon_{\mathrm{x}}}{\partial\rho} \quad\text{and}\quad v_{\mathrm{x},2} = \frac{\partial\varepsilon_{\mathrm{x}}}{\partial\nabla\rho}\frac{1}{|\nabla\rho|}. \tag{4.9}$$

Due to the dual nature of the APW+LO basis (see Section 3.2) the real space grids are defined differently in the MT and the IR. However, the quantities $\varepsilon_{\mathrm{x}}^{\mathrm{PBE}}$, $v_{\mathrm{x},1}$ and $v_{\mathrm{x},2}$ depend on the real space vector $\boldsymbol{r}$ only through $\rho(\boldsymbol{r})$, $s(\boldsymbol{r})$, and $y(|\boldsymbol{r}-\boldsymbol{r}'|)$, which are given as input to the routine that computes them together with the screening parameter ω. On the other hand, the divergence of $v_{\mathrm{x},2}|\nabla n|$ (second term in Eq. 4.5) must be evaluated

---

[1] Perdew and coworkers [73] defined the PBE enhancement factor as:

$$F_{\mathrm{x}}^{\mathrm{PBE}}(s(\boldsymbol{r})) = 1 + \kappa\left(1 - \frac{1}{1+\frac{\mu s^2}{\kappa}}\right), \tag{4.6}$$

where s is the reduced density gradient and κ=0.804 and μ=0.2195. Given this definition of $F_{\mathrm{x}}^{\mathrm{PBE}}$, the expression for the exchange potential can be determined analytically:

$$v_{\mathrm{x}} = \epsilon_{\mathrm{x}}^{\mathrm{LDA}}\left[\frac{4}{3}F_{\mathrm{x}}^{\mathrm{PBE}} - q\left(s^{-1}\frac{dF_{\mathrm{x}}^{\mathrm{PBE}}}{ds}\right) - \left(u - \frac{4}{3}s^3\right)\frac{d}{ds}\left(s^{-1}\frac{dF_{\mathrm{x}}^{\mathrm{PBE}}}{ds}\right)\right]. \tag{4.7}$$

u and q are defined as

$$u = \frac{\nabla\rho\cdot\nabla|\nabla\rho|}{2k_{\mathrm{F}}^3\rho^2} \quad\text{and}\quad q = \frac{\nabla^2\rho}{4k_{\mathrm{F}}\rho}, \tag{4.8}$$

respectively. Some of the terms in s, u and q, such as the density gradient, are computed numerically.

differently in the MT and in the IR.

4.1.2 Screened non-local exact exchange

In `exciting`, the NL-sR potential is computed as:

$$V^{\mathrm{NL,sR}}_{\mathrm{x},nn'}(\boldsymbol{k}) = -\sum_{n''}^{\mathrm{occ}} \sum_{\boldsymbol{q}}^{\mathrm{BZ}} \sum_{IJ} [M^{I}_{nn''}(\boldsymbol{k},\boldsymbol{q})]^{*} v^{\mathrm{sR}}_{IJ}(\boldsymbol{q};\omega) M^{J}_{n''n'}(\boldsymbol{k},\boldsymbol{q}), \tag{4.10}$$

where the sR Coulomb potential is obtained by subtracting the LR part from the bare Coulomb contribution:

$$v^{\mathrm{sR}}_{IJ}(\omega) = v_{IJ} - v^{\mathrm{LR}}_{IJ}(\omega). \tag{4.11}$$

The missing elements for the implementation of HSE were the evaluation of the LR Coulomb potential, v^{LR}_{IJ}, and the NL-sR potential for the limit $\boldsymbol{q} + \boldsymbol{G} \rightarrow 0$, which is treated separately.

Long-range Coulomb potential

To compute the LR Coulomb potential (v^{LR}_{IJ}, we followed the approach of Ref. [193, 194] by using plane waves normalized to the unit-cell volume ($\zeta_{\boldsymbol{q}+\boldsymbol{G}}(\boldsymbol{r}) = \mathrm{e}^{i(\boldsymbol{q}+\boldsymbol{G})\cdot\boldsymbol{r}} / \sqrt{\Omega}$) and not the MPB. The main reason for this is that the form of the LR Coulomb potential in the MPB would be very complicated, and its contribution is small compared to the total Coulomb potential.

The LR Coulomb kernel is defined as follows:

$$v^{\mathrm{LR}}(|\boldsymbol{r} - \boldsymbol{r}'|;\omega) = \frac{\mathrm{erf}(\omega|\boldsymbol{r} - \boldsymbol{r}'|)}{|\boldsymbol{r} - \boldsymbol{r}'|}. \tag{4.12}$$

Its Fourier transform, which is diagonal and known analytically, is given by

$$v^{\mathrm{LR,PW}}(\boldsymbol{q} + \boldsymbol{G};\omega) = \langle \zeta_{\boldsymbol{q}+\boldsymbol{G}'} | \, v^{\mathrm{LR}} \, | \zeta_{\boldsymbol{q}+\boldsymbol{G}} \rangle = \frac{4\pi}{|\boldsymbol{q} + \boldsymbol{G}|^{2}} \mathrm{e}^{-|\boldsymbol{q}+\boldsymbol{G}|^{2}/4\omega^{2}} \delta_{\boldsymbol{G}\boldsymbol{G}'}. \tag{4.13}$$

To insert it into Eq. 4.10-4.11, it must be multiplied from the left and from the right by the overlap integral between the PW basis and the MPB ($\mathcal{W}^{I}_{\boldsymbol{G}}$, defined in Eq. 3.26):

$$v^{\mathrm{LR}}_{IJ}(\boldsymbol{q};\omega) = \sum_{\boldsymbol{G}} \mathcal{W}^{I*}_{\boldsymbol{G}} v^{\mathrm{LR,PW}}(\boldsymbol{q} + \boldsymbol{G};\omega) \mathcal{W}^{J}_{\boldsymbol{G}}. \tag{4.14}$$

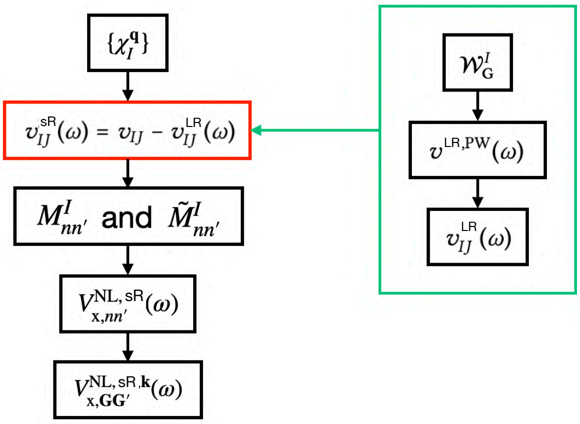

Figure 4.1: Scheme showing how the screened NL exact exchange potential is computed in the **exciting** code. The changes made to the existing code are highlighted: In the red block, which replaces that of the bare Coulomb potential (v_{IJ}) in Fig. 3.1, the sR Coulomb potential is computed. The steps to compute the LR Coulomb kernel, which is subtracted from the bare Coulomb potential to obtain v_{IJ}^{sR}, are shown in the green rectangle.

Once v_{IJ}^{LR} is calculated (green rectangle in Fig. 4.1), it is subtracted from the bare Coulomb potential (red block) to obtain the sR Coulomb potential (Eq. 4.11), which is then used in Eq. 4.10 to compute the NL-sR potential.

Evaluation of the screened Coulomb potential for $\boldsymbol{q} + \boldsymbol{G} \to 0$

The bare Coulomb potential (Eqs. 3.24-3.25) and the LR Coulomb potential (Eq. 4.13) have a divergent behavior for $\boldsymbol{q} + \boldsymbol{G} \to 0$. However, by combining the two terms, the limit for $\boldsymbol{q} + \boldsymbol{G} \to 0$ becomes finite, and the singular term (label s) turns into:

$$v^{\mathrm{s}}(\omega) = \lim_{\boldsymbol{q}+\boldsymbol{G}\to 0} \frac{4\pi}{|\boldsymbol{q}+\boldsymbol{G}|^2}\left(1 - \mathrm{e}^{-|\boldsymbol{q}+\boldsymbol{G}|^2/4\omega^2}\right) \tag{4.15}$$

To compute the limit, in Ref. [193, 194] the exponential was expanded into a Taylor series up to the second order:

$$v^{\mathrm{s}}(\omega) = \frac{4\pi}{|\boldsymbol{q}+\boldsymbol{G}|^2}\left(1 - 1 + \frac{|\mathrm{q}+\mathrm{G}|^2}{4\omega^2} - \cdots\right) = \frac{\pi}{\omega^2}. \tag{4.16}$$

Since for $\omega \to 0$ the singularity term in Eq. 4.16 diverges, this method fails if one wants to employ values of ω approaching the limit. In this respect, we have implemented in **exciting** an alternative method, suggested by Dmitrii Nabok, which does not have this issue.

We made use of the isotropic averaging method, which is based on the following concepts: (*i*) Each quantity involving the Coulomb potential is defined as an integral over the BZ:

$$F(\boldsymbol{k}) = \frac{1}{\Omega_{\mathrm{BZ}}} \int_{\mathrm{BZ}} \mathrm{d}\boldsymbol{q} f(\boldsymbol{k}, \boldsymbol{q}) v(\boldsymbol{q}). \tag{4.17}$$

Here Ω_{BZ} is the BZ volume, and $f(\boldsymbol{k}, \boldsymbol{q})$ is a general function. (*ii*) Numerically this integral is computed as a sum over $\boldsymbol{k}$-points:

$$F(\boldsymbol{k}) = \frac{1}{N_{\boldsymbol{q}}} \sum_{\boldsymbol{q}} f(\boldsymbol{k}, \boldsymbol{q}) v(\boldsymbol{q}). \tag{4.18}$$

(*iii*) To obtain a precise description of the singular term, a dense $\boldsymbol{q}$-point sampling in the vicinity of the Γ-point would be required, resulting in a slow $\boldsymbol{q}$-point convergence. Instead, in this approach, the integral in Eq. 4.17 can be calculated analytically in a sphere of volume $V_{\boldsymbol{k}}$ around the Γ point, treating the function $f(\boldsymbol{k}, \boldsymbol{q})$ as a constant ($f(\boldsymbol{k}, \boldsymbol{q}) \approx f(\boldsymbol{k}, 0)$ for $\boldsymbol{q} \to 0$). $V_{\boldsymbol{k}}$ is determined by the number of $\boldsymbol{k}$-points employed in the calculation ($V_{\boldsymbol{k}} = \Omega_{BZ}/N_{\boldsymbol{k}}$). For the screened Coulomb potential, one ends up with

$$I_{\mathrm{s}} = \frac{1}{V_{\boldsymbol{k}}} \int_{V_{\boldsymbol{k}}} \mathrm{d}\boldsymbol{q} \frac{4\pi}{|\boldsymbol{q}+\boldsymbol{G}|^2} \left(1 - \mathrm{e}^{-|\boldsymbol{q}+\boldsymbol{G}|^2/4\omega^2}\right), \tag{4.19}$$

which in spherical coordinates is:

$$I_{\mathrm{s}} = \frac{16\pi^2}{V_{\boldsymbol{k}}} \int_0^{R_{\boldsymbol{k}}} \mathrm{d}q \left(1 - \mathrm{e}^{-|\boldsymbol{q}+\boldsymbol{G}|^2/4\omega^2}\right). \tag{4.20}$$

$R_{\boldsymbol{k}}$ is the radius of the sphere of volume $V_{\boldsymbol{k}}$:

$$R_{\boldsymbol{k}} = \left(\frac{3\Omega_{\mathrm{BZ}}}{4\pi N_{\mathrm{k}}}\right)^{1/3}. \tag{4.21}$$

The exact solution of the integral in Eq. 4.20 gives following result:

$$I_{\mathrm{s}} = \frac{16\pi^2}{V_{\boldsymbol{k}}} \left(R_{\boldsymbol{k}} - \sqrt{\pi\omega^2} \mathrm{erf}\left(\sqrt{\frac{1}{4\omega^2}} R_{\boldsymbol{k}}\right)\right). \tag{4.22}$$

The difference between the two methods is shown in Fig. 4.2. It can be seen that for $\omega \to 0$ the Taylor expansion method diverges, while the exact solution of the integral

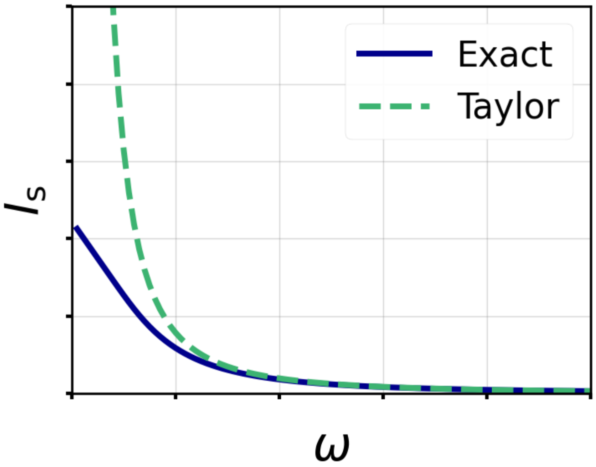

Figure 4.2: Integral of the singular term of the screened Coulomb potential I_s as a function of the screening parameter ω for bulk Si. Shown are the exact solution of the integral (Eq. 4.22, blue solid line) and the Taylor expansion up to the second order of the singular term (Eq. 4.16, green dashed line).

gives a finite value, satisfying the exact limit. For larger values of ω the two methods are equivalent. Note that by Taylor expanding the argument of the integral in Eq. 4.20 up to the second order in the limit $\boldsymbol{q} + \boldsymbol{G} \to 0$, Eq. 4.16 is recovered.

The value of ω at which the Taylor expansion method starts to fail is difficult to determine, since it depends on the number of $\boldsymbol{k}$-points and the system size (see Eq. 4.22). In addition, increasing the number of $\boldsymbol{k}$-points reduces the weight associated with Γ and thus the influence of the method used to evaluate the singular term. Note that the implementation as it is, is only valid for 3D systems.

4.2 Validation and extra features

The validation of the HSE implementation in the `exciting` code, is done in two steps: The first is the validation of ωPBEh, using its property of being equivalent to PBEh for $\omega = 0$. In the second step, we focus on the validation of the HSE functional itself. In this section, we also analyze additional features of the HSE functional as implemented in `exciting`.

4.2.1 Validation of the implementation of the screened exchange-hole formulation of PBE

To validate our implementation of ωPBE*h*, we compare its results for $\omega = 0$ with those of two different implementations of PBE: In the first, the exchange potential is computed solving Eq. 4.7. This is the default method in **`exciting`**, and so we named it PBE-**`exciting`**. The second version evaluates v_x^{PBE} solving Eq. 4.5 after calculating $v_{x,1}$ and $v_{x,2}$ (Eq. 4.9). This is the method used in QE, so we named it PBE-QE. Note that ωPBE*h*($\omega = 0$) is equivalent to PBE*h* [197], which is not the same as PBE, although very similar: The enhancement factor $F_x(s)$ of ωPBE*h* was determined by fitting it to the enhancement factor of PBE [73], aiming for an error within 0.5% [197] for values of $s \leq 6.5$. Therefore, when comparing ωPBE*h*($\omega = 0$) with PBE-**`exciting`** and PBE-QE, good agreement can be expected, but not identical results. All tests were done for silicon[2].

Enhancement factor

The tests start with the enhancement factor, comparing the results of ωPBE*h*($\omega = 0$) with those of PBE-**`exciting`**. Note that for the enhancement factor, using PBE-**`exciting`** or PBE-QE is equivalent, so we will simply refer to it as PBE. We use the electron density from the atomic species and its reduced gradient and consider a single $\boldsymbol{k}$-point (Γ). In

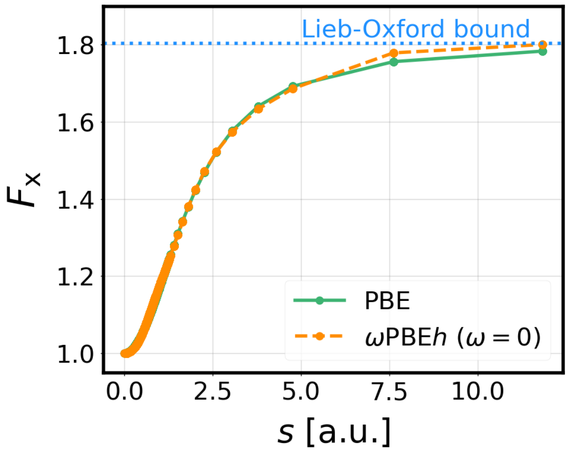

Figure 4.3: Enhancement factor computed with the PBE (green solid line) and with the ωPBE*h* functional with $\omega = 0$ (orange dashed line), plotted with respect to the reduced gradient, s. The horizontal light blue dotted line shows the Lieb-Oxford bound ($F_x \leq 1.804$).

---

[2] Computational details: We used the **`exciting`** default species files, a lattice constant of 5.43Å [201], and $G_{\max}R_{\mathrm{MT}} = 7$.

Fig. 4.3, the enhancement factors, F_x, computed with the two functional models, are plotted with respect to the reduced gradient, s. The two lines almost overlap for $s < 6$ a.u., while for higher values the deviation becomes visibly larger. Unlike PBE, PBEh, and thus ωPBE$h(\omega = 0)$, does not naturally respect the Lieb-Oxford limit ($F_\mathrm{x} \leq 1.804$). To overcome this problem, the reduced gradient is smoothly rescaled for values higher than $s > 8.3$ a.u. by the following equation:

$$s_\mathrm{new} = 8.572844 - \frac{18.796223}{s^2}. \tag{4.23}$$

This explains the larger deviation between the two models for the higher values of s in Fig. 4.3. Considering the integral absolute percentage error (IAPE)[3] for $s \leq 6$ a.u. this is 0.2%, which is within the limit used to fit the enhancement factor of PBEh to that of PBE, which is 0.5% [197].

Exchange potential

To test the exchange potential, we compare the values obtained by employing PBE-**`exciting`**, PBE-QE, and ωPBEh for $\omega = 0$. Here, the use of PBE-QE allows us to verify that the divergence of $v_{\mathrm{x},2}|\nabla n|$ is correctly implemented. Again, we use the density constructed from the atomic species and only one $\boldsymbol{k}$-point.

In the upper panels of Fig. 4.4, the exchange potentials in the MT sphere, v_x^MT, computed with the three different versions of PBE are compared. On the left, the potential is plotted with respect to N_MT, which is the number of grid points in the MT sphere. It can be observed that the ωPBEh potential near the nucleus differs significantly from both PBE potentials, which are in good agreement with each other. The deviations can be better seen by looking at the difference, $\Delta v_\mathrm{x}^\mathrm{MT}$, which are shown in upper-right panel for ωPBEh and PBE-QE using PBE-**`exciting`** as a reference. Near the nucleus, Δv_x of ωPBEh reaches a peak of 5×10^2 a.u. and the mean absolute percentage error (MAPE)[4] is 6%. For PBE-QE, the difference is not visible on this scale, and the MAPE is only 3×10^{-2}%.

---

[3] $\mathrm{IAPE} = 100 \times \frac{\int_{x_0}^{x_1} |Y_\mathrm{r} - Y_\mathrm{a}| \, \mathrm{d}x}{\int_{x_0}^{x_1} Y_\mathrm{r} \, \mathrm{d}x}$,
where Y_r are the reference values and Y_a are the actual values. When computing the IAPE, the integrals are evaluated using the trapezoidal rule (from the `numpy` library in `python`).

[4] $\mathrm{MAPE} = \frac{100}{N} \sum_i \left| \frac{Y_{\mathrm{r},i} - Y_{\mathrm{a},i}}{Y_{\mathrm{r},i}} \right|$,
where N is the number of points considered, $Y_{\mathrm{r},i}$ are the reference values, and $Y_{\mathrm{a},i}$ are the actual values.

The same analysis is performed for the IR (lower panels). The exchange potential against the number of G-vectors on the left does not show much difference between the three methods. However, as in the MT region, $\Delta v_{\mathrm{x}}^{\mathrm{IR}}$ of ωPBEh is considerably larger than that of PBE-QE (lower-right panel): the MAPE of the two methods, using PBE-`exciting` as the reference, is 1.6% and 2×10^{-2}, respectively.

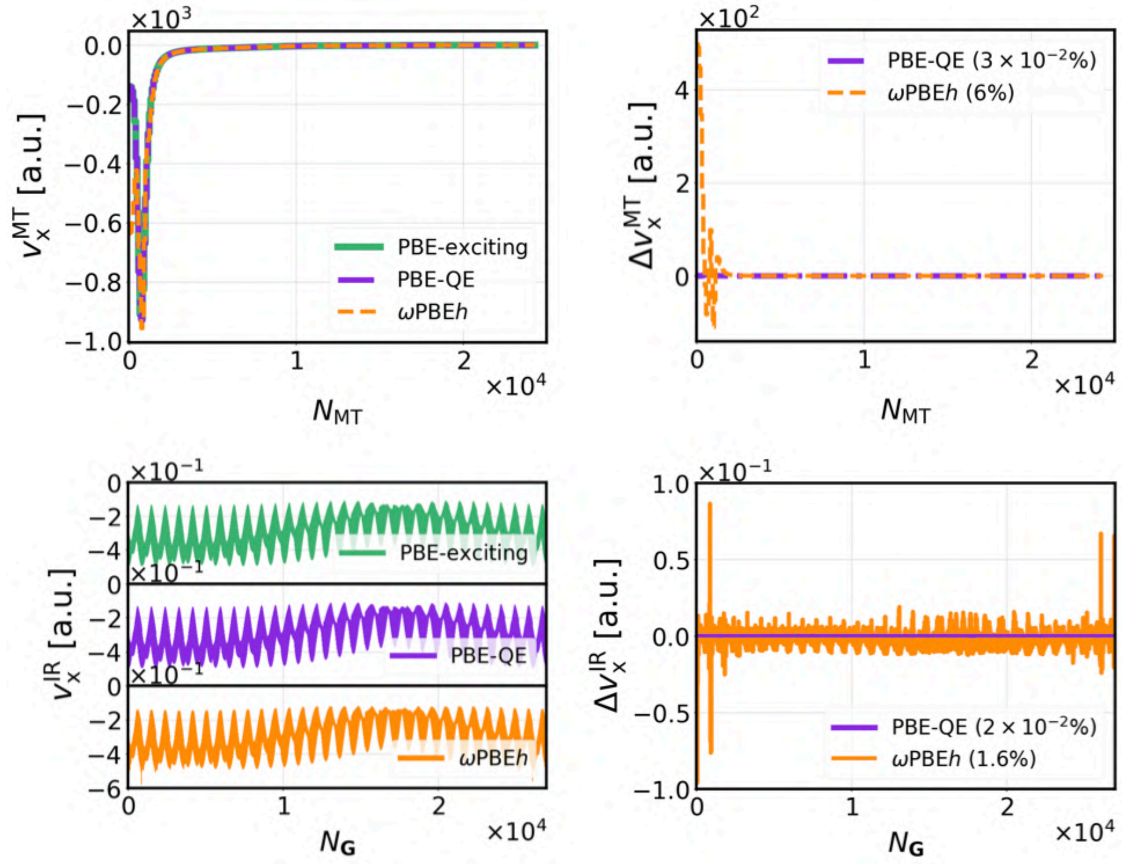

Figure 4.4: Exchange potential in the MT sphere (top panels) and in the IR (bottom panels) computed with PBE-`exciting` (green line), PBE-QE (purple line), and ωPBEh (orange line). In the left panels, v_{x} is plotted against the number of MT grid points (N_{MT}) and in the IR against the number of $\boldsymbol{G}$-vectors (N_{G}). The left panels show differences between potential, Δv_{x}, taking PBE-`exciting` as a reference. The MAPE are shown in parenthesis.

The use of PBE-QE shows that the differences between the ωPBEh exchange potential and that of PBE-`exciting`, are inherited by the differences in the enhancement factor, and the numerical evaluation of $\nabla \cdot (v_{\mathrm{x}}^2 |\nabla n|)$ is correctly computed in both the MT and the IR. One can conclude that ωPBEh and therefore PBE-sR, is correctly implemented in the code, and the differences observed with PBE-`exciting` and PBE-QE are related to the different definitions of the enhancement factor.

4.2.2 Validation of the implementation of HSE

To validate the implementation of the HSE functionals in **`exciting`**, we consider the electronic properties of six different materials, also examined in Refs. [97, 193, 202]. The convergence parameters used are shown in Appendix A.1.

Transition energies

The focus here is to show that the transition energies between the highest valence band (VB) and the lowest conduction band (CB) at Γ, Γ → X, and Γ → L, computed with our HSE implementation, are comparable to those obtained by other codes. For a more meaningful comparison, the same is done for PBE and PBE0.

In Table 4.1, the energies computed with **`exciting`** are compared with those from the literature. These are in particular results obtained with the FLEUR code, which, like **`exciting`**, uses APW+LO as basis functions [97, 193] and VASP [203, 202, 204] that is based on the projector augmented wave (PAW) formalism. The column PBE-FLEUR shows two different sets of results from Refs. [97] and [193], respectively. If a unique number is given, it means that the values of the two sets coincide. Overall, our PBE energies and the PBE-VASP values are in better agreement with Ref. [193]: The average absolute difference between **`exciting`** and Ref. [97] (Ref. [193]) is 36 meV (19 meV). Concerning the comparison with the VASP results, the average absolute difference for Ref. [97] (Ref. [193]) is 51 meV (11 meV). Because of this, only the PBE-FLEUR values from Ref. [193] (column c) are considered in the following.

The transition energies computed with HSE are between those obtained with PBE and PBE0, as expected (Section 2.2.3.2). The differences between the HSE-**`exciting`** results compared to FLEUR and VASP are comparable to those observed for PBE with average absolute differences of 18 meV, 26 meV, and 23 meV between **`exciting`** and FLEUR, **`exciting`** and VASP, and FLEUR and VASP, respectively. For PBE0, the agreement between the three methods is slightly worse: The average absolute differences are 43 meV, 35 meV, and 52 meV, between **`exciting`** and FLEUR, **`exciting`** and VASP, and FLEUR and VASP, respectively. The average absolute difference between the PBE FLEUR data

Table 4.1: Transition energies between the highest VB and the lowest CB at Γ, Γ → X, and Γ → L, where X=(0.5 0.5 0) and L=(0.5 0 0), computed with PBE, PBE0, and HSE. The computational parameters for our calculations are given in Table A.1. The FLEUR results are taken from Refs. [97, 193], the VASP results from Refs. [202, 204].

	Trans.	This work			FLEUR			VASP^{a}		
		PBE	PBE0	HSE	PBE$^{b/c}$	PBE0^{b}	HSE^{c}	PBE	PBE0	HSE
Si	E_{Γ}	2.56	3.98	3.32	2.56	3.96	3.32	2.57	3.97	3.32
	$E_{\Gamma\to X}$	0.71	1.94	1.29	0.71	1.93	1.29	0.71	1.93	1.29
	$E_{\Gamma\to L}$	1.53	2.88	2.24	1.54	2.87	2.24	1.54	2.88	2.24
C	E_{Γ}	5.61	7.73	7.00	5.64/5.60	7.74	6.98	5.59	7.69	6.97
	$E_{\Gamma\to X}$	4.77	6.69	5.93	4.79/4.75	6.69	5.90	4.76	6.66	5.91
	$E_{\Gamma\to L}$	8.49	10.81	10.05	8.58/8.46	10.88	10.02	8.46	10.77	10.02
GaAs	E_{Γ}	0.54	1.98	1.45	0.55/0.54	2.02	1.43	0.56	2.01	1.45
	$E_{\Gamma\to X}$	1.46	2.66	2.04	1.47	2.69	2.06	1.46	2.67	2.02
	$E_{\Gamma\to L}$	1.01	2.36	1.77	1.01	2.38	1.78	1.02	2.37	1.76
MgO	E_{Γ}	4.74	7.22	6.48	4.84/4.77	7.31	6.49	4.75	7.24	6.50
	$E_{\Gamma\to X}$	9.14	11.62	10.86	9.15/9.14	11.63	10.86	9.15	11.67	10.92
	$E_{\Gamma\to L}$	7.91	10.45	9.69	8.01/7.93	10.51	9.69	7.91	10.38	9.64
NaCl	E_{Γ}	5.11	7.22	6.49	5.08/5.20	7.13	6.57	5.20	7.26	6.55
	$E_{\Gamma\to X}$	7.52	9.77	9.01	7.39/7.58	9.59	9.05	7.60	9.66	8.95
	$E_{\Gamma\to L}$	7.27	9.37	8.63	7.29/7.30	9.33	8.66	7.32	9.41	8.67
Ar	E_{Γ}	8.70	11.14	10.36	8.71/8.70	11.15	10.36	8.68	11.09	10.34

^{a} [202, 204], ^{b} [97], ^{c} [193]

from Ref. [97] and ours is 17 meV greater than the average absolute difference between the PBE FLEUR data from Ref. [193] and ours. When the same comparison is made with PBE VASP results, instead of ours, the difference amount to 40 meV. Because of this, it is possible that by using the same setting of Ref. [193] the agreement will improve also for PBE0.

Looking at the different materials, for Si the three codes agree within 20 meV for all functionals. Also for C, GaAs, and Ar the agreement is good with the differences being within 40 meV except for a few PBE0 calculations where the differences between FLEUR and VASP, e.g. a difference of 110 meV is observed for C at Γ → L, and a difference of 50 meV is observed for Ar at Γ. The worst agreement is found for NaCl and MgO: In the case of NaCl, the differences range from 180 meV at Γ → X between `exciting` and FLEUR for PBE0 to 10 meV at Γ → L between FLEUR and VASP for HSE, with an average of 61 meV. The worst agreement for HSE is observed for NaCl between `exciting` and FLEUR, with a difference of 80 meV at Γ. For MgO, the largest difference is 130 meV between FLEUR and VASP for the transition energy at Γ → L computed with PBE0.

In Appendix A.1, we additionally discuss the comparison between our results and those from Ref. [205], also evaluated with `exciting` for PBE and PBE0.

Band structure and DOS

Here we compare, for the same set of materials, the band structure and DOS obtained by PBE, PBE0, and HSE. For a better comparison, we made use of MLWF interpolation for all functionals (Section 3.7). In some cases, the accurate construction of the MLWF, required larger $\boldsymbol{k}$-meshes than those used in Table 4.1 (see Appendix A.1).

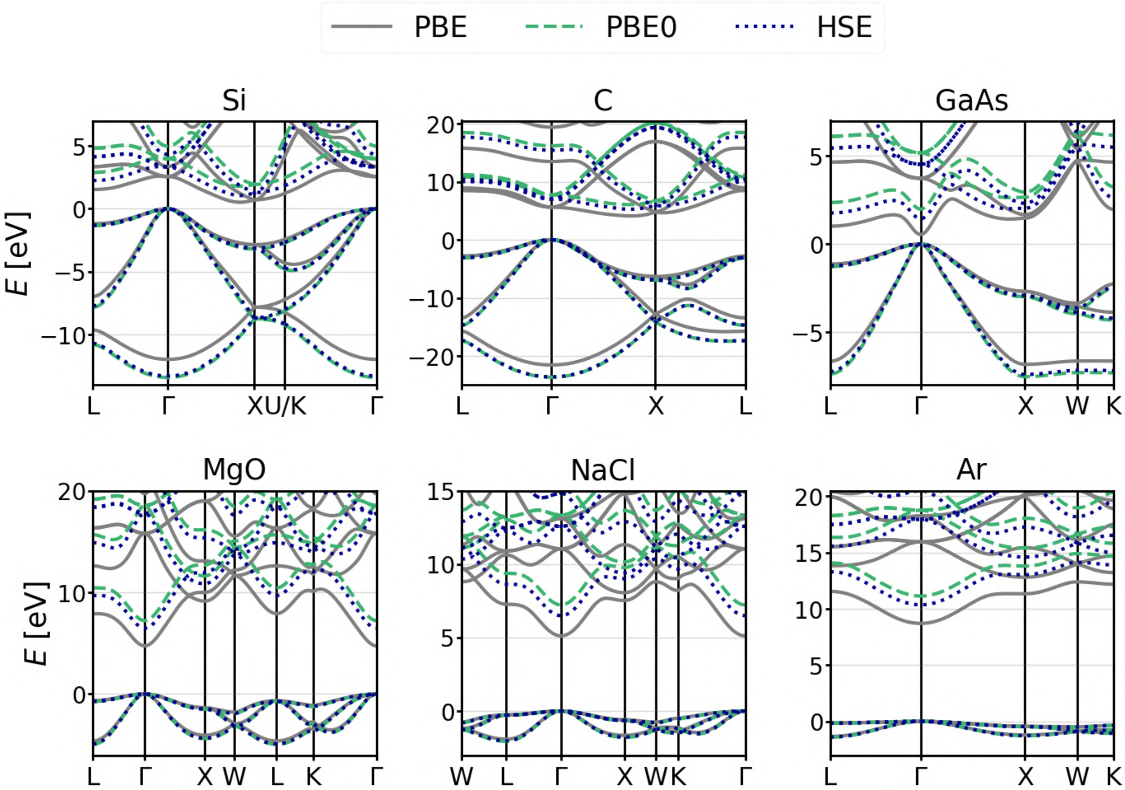

Figure 4.5: Band structure of Si, C, GaAs, MgO, NaCl, and Ar computed by PBE (solid-gray lines), PBE0 (dashed-green lines), and HSE (dotted-blue lines). In all cases, the valence band maximum (VBM) is used as energy zero.

The band structure (Fig. 4.5) and the DOS (Fig. 4.5) of all investigated materials show a similar overall structure for the three different functionals. The main effect of PBE0 and HSE is the expected opening of the gaps. A major effect is observed for Si, C, and

GaAs: in these cases, the plot includes valence states below -5 eV, for which the band dispersion and consequently the DOS of PBE0 and HSE deviate significantly from those of PBE. On the other hand, the PBE0 and HSE results almost overlap for all the occupied states considered.

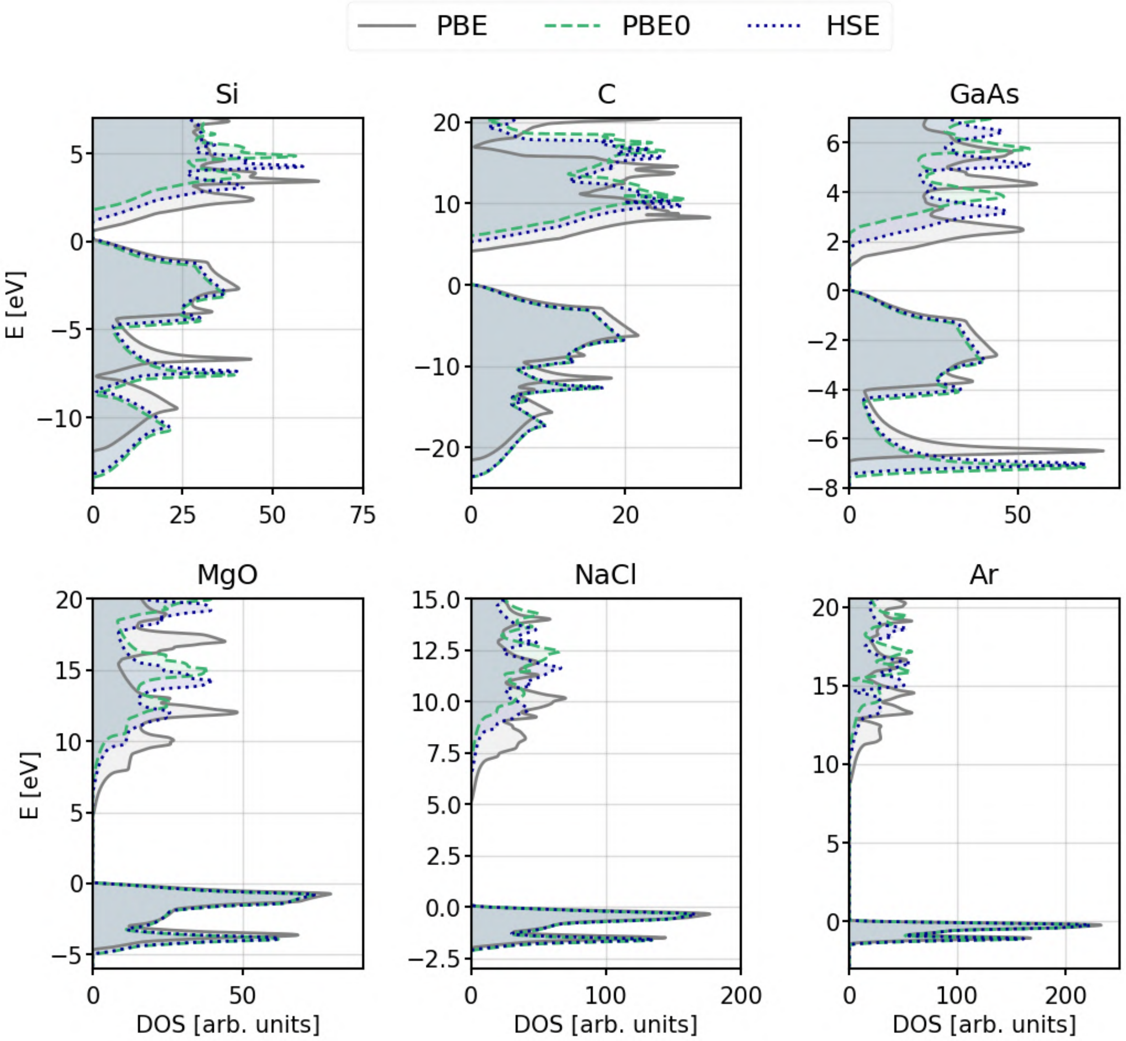

Figure 4.6: DOS of Si, C, GaAs, MgO, and NaCl obtained by PBE (solid-gray lines), PBE0 (dashed-green lines), and HSE (dotted-blue lines). As for the band structure in Fig. 4.5, the results are aligned at the VBM.

From the analysis of the electronic properties, including the comparison of transition energies with those of other codes, we consider the implementation of HSE in `exciting` to be reliable and stable.

4.2.3 k-mesh convergence

In `exciting`, HSE shows a faster convergence with the number of $\boldsymbol{k}$-points compared to PBE0, which makes it computationally less demanding. In Fig. 4.7, the $\boldsymbol{k}$-mesh convergence of the transition energies between the highest VB and the lowest CB at Γ (E_Γ) is monitored for PBE, PBE0, and HSE. Overall, the convergence of PBE0 is slower than that of PBE and HSE for all materials except for Ar. Aiming for a precision of 10 meV, a $4 \times 4 \times 4$ $\boldsymbol{k}$-mesh is found to be sufficient for all three functionals. Otherwise, the $\boldsymbol{k}$-mesh suitable for PBE0 is slightly higher than that for HSE. An exception is GaAs, for which PBE0 requires a $12 \times 12 \times 12$ $\boldsymbol{k}$-mesh, while for HSE an $8 \times 8 \times 8$ $\boldsymbol{k}$-mesh is sufficient. In Fig. 4.7 the convergence of HSE looks slower than that of PBE, but considering the convergence criteria of 10 meV, in addition to Ar, Si, and NaCl also require the same mesh as for PBE. In Appendix A.1, the same analysis is performed for $E_{\Gamma\rightarrow X}$ (Fig. A.1) $E_{\Gamma\rightarrow L}$ (Fig. A.2). Overall, all the tests show a slower $\boldsymbol{k}$-mesh convergence of PBE0 compared to HSE.

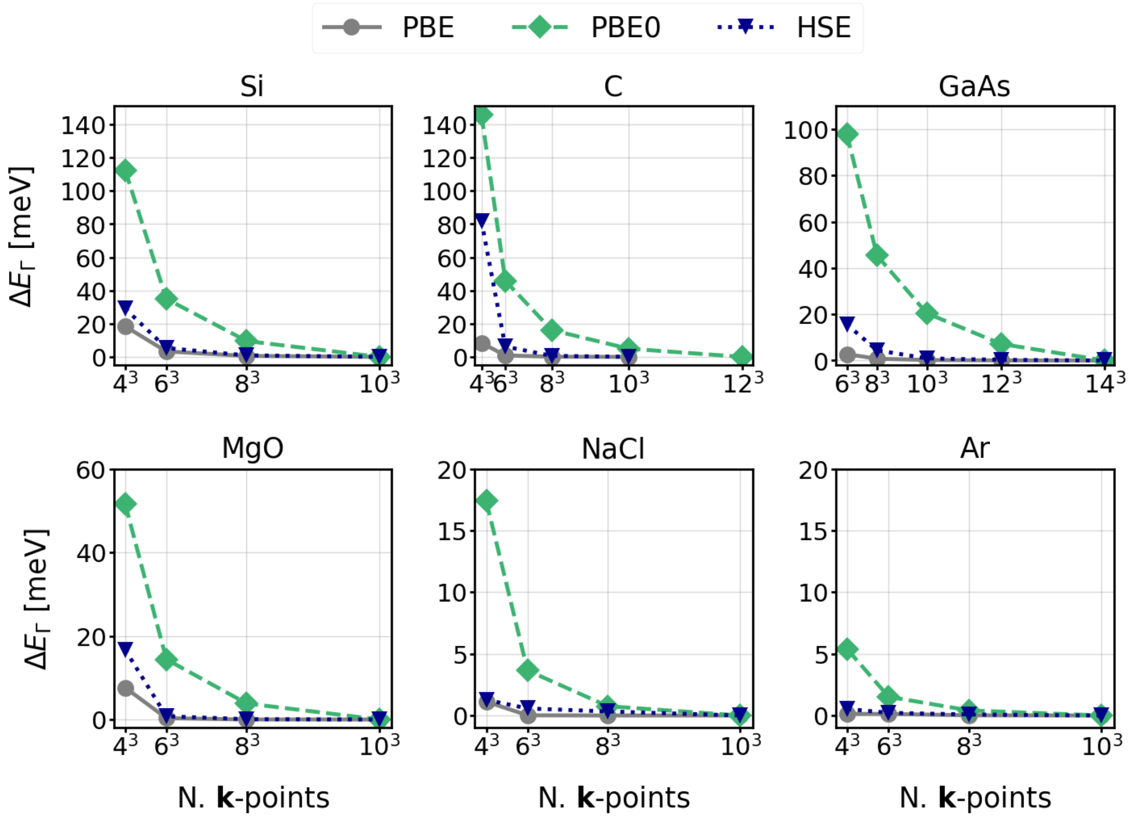

Figure 4.7: Energy differences E_Γ evaluated for the largest $\boldsymbol{k}$-mesh and the $\boldsymbol{k}$-mesh shown in the x-axis. The corresponding energy values are listed in Table A.2.

4.2.4 Treatment of the screened Coulomb potential for $\mathrm{q} + \mathrm{G} \rightarrow 0$

In the calculations discussed so far, we used the Taylor expansion to treat the singular term (see Section 4.1.2). The focus here is to investigate the limits of the Taylor expansion approach for different values of ω and different $\boldsymbol{k}$-meshes. We will also compare its performance with the approach that solves the integral in Eq. 4.22 exactly, which below we will refer to as the "Exact" treatment. The materials used for this analysis are Si, GaAs, Ar, and $\mathrm{PbI_2}$[5].

A major difference between the two methods is that the calculation of the singular integral in the "Exact" treatment (I_E) explicitly depends on the system size and on the number of $\boldsymbol{k}$-points in addition to the screening parameter ω (see Eq. 4.22). In contrast, when the Taylor expansion is used (I_T), the result depends only on ω (Eq. 4.16). Therefore, in Table 4.3, a single value of I_T is given for each ω. For $\omega \geq 0.11\ a_0^{-1}$, the dependence on the method used to compute the integral is minimal for all material and $\boldsymbol{k}$-meshes, while for $\omega = 0.03\ a_0^{-1}$ and $\omega = 0.05\ a_0^{-1}$ the I_T is remarkably larger than I_E. By increasing the number of $\boldsymbol{k}$-points, the difference between them decreases for all materials, and for a sufficiently large $\boldsymbol{k}$-mesh, it is expected to become minimal.

The discrepancies between I_T and I_E for $\omega < 0.11\ a_0^{-1}$ leads to differences in the transition energies between the highest VB and the lowest CB, which are plottedFig. 4.8. For all materials, the deviation between the two methods decreases with larger $\boldsymbol{k}$-meshes, as the values of the integral become closer and the weight associated with the Γ-point is reduced. Considering HSE to be converged with a 6 × 6 × 6 mesh for Si, a 4 × 4 × 4 mesh for Ar, and a 3 × 3 × 2 mesh for $\mathrm{PbI_2}$ (see Appendices A.1 and B.1), the Taylor expansion treatment for $\omega = 0.03\ a_0^{-1}$ yields results that are far from the expected value. On the other hand, for the "Exact" treatment, increasing the mesh, the differences are hardly visible. Note that, for $\omega \leq 0.11\ a_0^{-1}$, the small differences observed between the curves obtained with the "Exact" treatment are due to $\boldsymbol{k}$-meshes being smaller than those considered converged for HSE. In Appendix A.4, the corresponding values of the transition energies are shown, which allow for a more quantitative assessment of the numerical precision. Overall, for the converged $\boldsymbol{k}$-meshes, for $\omega = 0.03\ a_0^{-1}$ the "Exact" treatment gives results within ~20 meV for Si, GaAs, and $\mathrm{PbI_2}$, while for Ar larger meshes are needed to obtain the same precision. The precision of the Taylor expansion method for the same $\boldsymbol{k}$-grids ranges from ~200 meV for GaAs to ~1100 meV for $\mathrm{PbI_2}$. For $\omega = 0.11$

---

[5] Computational details: for Si, GaAs, and Ar see Appendix A.1 and for $\mathrm{PbI_2}$ see Appendix B.1.

Table 4.2: Integral of the singular term computed with the Taylor expansion (Eq. 4.16) and the "Exact" treatment (Eq. 4.22) for Si, GaAs, Ar,and PbI_2 and for different $\boldsymbol{k}$-meshes. The first row shows the values of the screening parameter ω for which the integrals are computed, the second row the values of the Taylor integral (I_T), which are independent of the material and the $\boldsymbol{k}$-mesh.

ω	0.03	0.05	0.11	0.15	0.20
I_T	3490.66	1256.64	259.64	139.63	78.54
$\boldsymbol{k}$-mesh	Si - I_E				
4x4x4	1074.31	716.00	226.82	129.66	75.30
6x6x6	1793.31	952.15	244.16	135.05	77.08
8x8x8	2308.87	1068.57	250.75	137.02	77.71
$\boldsymbol{k}$-mesh	GaAs - I_E				
4x4x4	1136.75	741.65	229.05	130.37	75.54
6x6x6	1866.49	970.65	245.28	135.39	77.18
8x8x8	2372.89	1081.10	251.40	137.22	77.77
$\boldsymbol{k}$-mesh	Ar - I_E				
4x4x4	1023.78	694.28	224.84	129.03	75.09
6x6x6	1731.95	936.04	243.17	134.75	76.98
8x8x8	2253.88	1057.52	250.16	136.85	77.65
$\boldsymbol{k}$-mesh	PbI_2 - I_E				
3x3x2	1010.42	688.40	224.29	128.85	75.03
6x6x4	2238.84	1054.44	250.00	136.80	77.64
9x9x6	2818.49	1159.64	255.28	138.36	78.14

Table 4.3: Integral of the singular term computed with the Taylor expansion (Eq. 4.16) and the "Exact" treatment (Eq. 4.22)and . The first row shows the values of the screening parameter ω for which the integrals are computed, the second raw the values of the Taylor integral (I_T), which are independent of the material and the $\boldsymbol{k}$-mesh.

a_0^{-1}, the difference between the two methods is $\leq$ 2 meV for Si, GaAs and Ar, and 15 meV for PbI_2. From these observations, it can be concluded that the two methods are comparable for $\omega \geq 0.11\ a_0^{-1}$, while the exact treatment is more suitable for smaller values of ω. Whichever method is used, for small ω, it is recommended to verify that the chosen $\boldsymbol{k}$-mesh is sufficient.

4.3 Conclusions

In this chapter, the implementation and validation of the HSE functional in `exciting` has been shown. Three main steps were required, corresponding to the implementation of ωPBEh, the screened NL exact exchange, and its special treatment in the limit $\mathbf{G} + \mathbf{q} \rightarrow 0$. For the latter, two methods have been implemented. What we named "Ex-

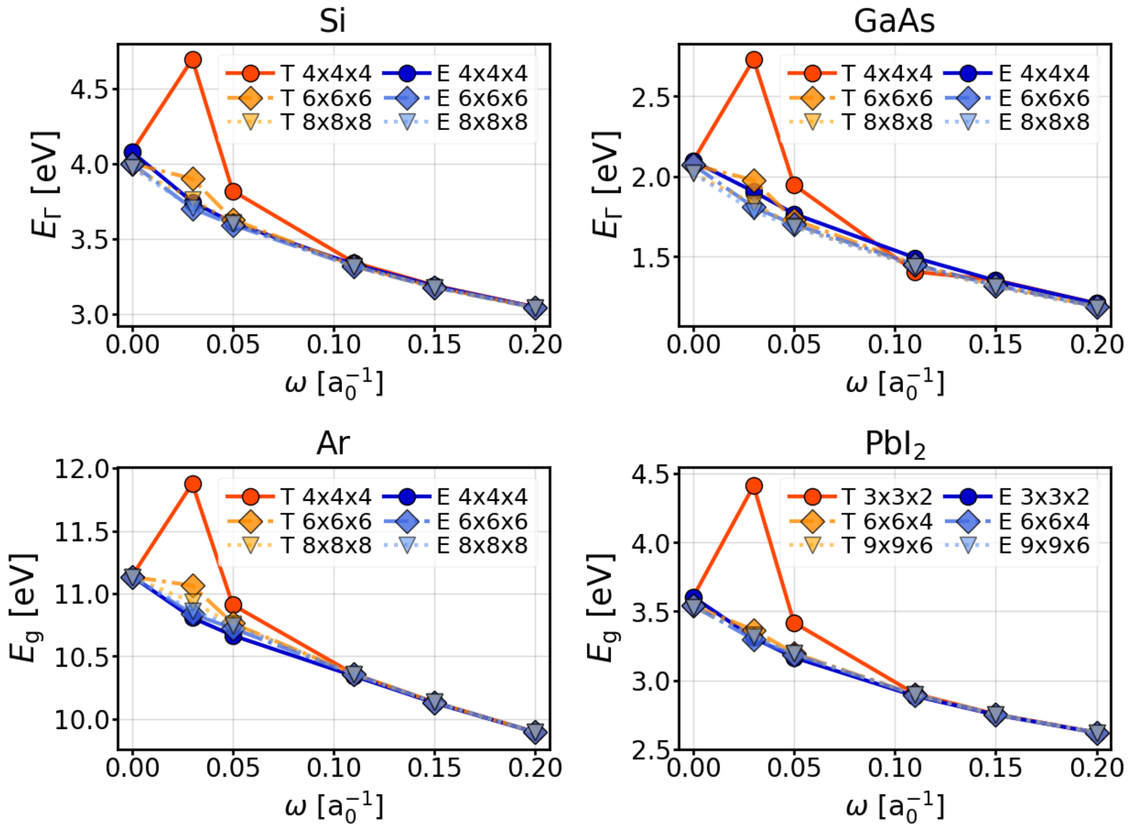

Figure 4.8: HSE transition energies between the highest VB and the lowest CB at Γ (E_Γ) of Si and GaAs (top) and band gap (E_g) of Ar and PbI2 (bottom), obtained by the Taylor expansion (T) and the "Exact" method (E) for treating the screened Coulomb potential for $\boldsymbol{q}+\boldsymbol{G} \to 0$. The values are computed with different $\boldsymbol{k}$-meshes (shown in the legend) and are plotted with respect to the screening parameter ω. The points at $\omega = 0$ are computed with PBE0. The mixing parameter α is 0.25 in all cases.

act" treatment is fundamental for $\omega \leq 0.11$ a_0^{-1}. Overall, our HSE results showed excellent agreement with other codes [202, 204, 193]. The level of agreement is comparable to that observed for PBE and PBE0. Also, the tests performed for the electronic properties showed the correct trend between the functionals.

CHAPTER 5

Hybrid functionals: Additional implementations

The implementations discussed in this chapter are the inclusion of SOC in the hybrid scheme, the implementation of the DM method, and the optimization of the evaluation of the NL exact exchange. They are fundamental for the study of complex materials such as HaP.

5.1 Spin-orbit coupling in hybrid functionals

This section focuses on extending the SOC treatment to hybrid xc functionals (HYB+SOC).

Implementation

As described in Section 3.3.3, a hybrid functional calculation consists of a nested loop, preceded by a PBE SCF cycle (see Fig. 3.1). In our implementation, we include the evaluation of SOC in the preliminary PBE SCF and the inner SCF cycles, while it is not considered in the evaluation of the NL potential. Therefore, SOC only concerns the magenta blocks in Fig. 5.1, where it is treated self-consistently via the SV method as discussed in Section 3.4.2[1]. The SOC operator ($\mathcal{H}_{\text{SOC}}$) is treated within ZORA (Eq. 3.31), which requires the gradient of the radial KS potential. For the NL potentials, this gradient is non-trivial to compute, so the effective potential in the inner cycle is replaced by

---

[1] Only the SV method was implemented in the code when I carried out this work.

a modified one, where PBE entirely accounts for the xc contribution:

$$\tilde{v}_{\text{KS}} = v_{\text{ext}} + v_{\text{H}} + v_{\text{xc}}^{\text{PBE}}. \tag{5.1}$$

The resulting SOC coupling operator is:

$$\mathcal{H}_{\text{SOC}}^{\text{hyb}} = \frac{\alpha_{\text{fs}}^2}{[2 - \alpha_{\text{fs}}^2 \tilde{v}_{\text{KS}}(r)]^2} \frac{1}{r} \frac{\partial \tilde{v}_{\text{KS}}(r)}{\partial r} \tilde{\boldsymbol{\sigma}} \cdot \mathbf{L}. \tag{5.2}$$

The use of $\tilde{v}_{\text{KS}}$ is possible because the impact of the xc functional on it is minimal [131, 206].

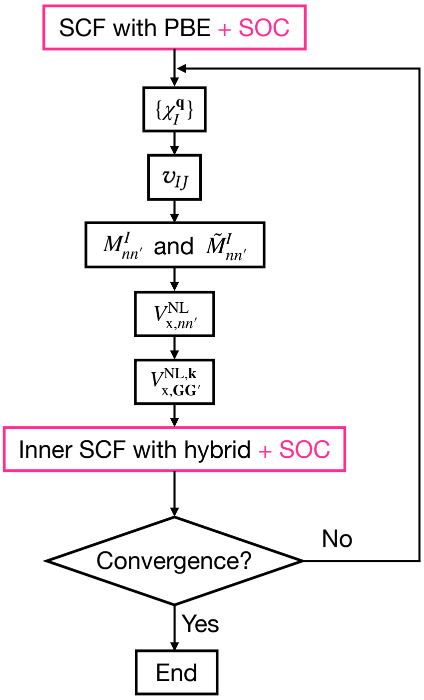

Figure 5.1: Nested-loop of the hybrid functional including SOC. The modifications to the cycle without SOC (Fig. 3.1) are inside the magenta blocks.

Validation

For the validation of HYB+SOC, we chose Si, Xe, MoS_2, and PbI_2. SOC effects of different magnitudes characterize them. The convergence parameters are given in Appendix B.1. Xe, MoS_2, and PbI_2 are also used in Chapter 6 to validate the *second variation with local-orbital approach*. There, the effects of SOC in these materials are discussed in more detail. In general, hybrid functionals are expected to cause only minor changes in SOC effects obtained with semi-local functional. As shown by Huhn and coworkers [131], who tested the impact of different functionals in 103 compounds, SOC effects at the PBE and HSE levels show differences in band gaps and SOC splittings below 60 meV. This result confirms previous work [207].

Figure 5.2 shows the band structures calculated using PBE with and without SOC. One can appreciate the different magnitudes of the SOC effects among the materials. In Si (upper left panel), δ_{SOC} is of the order of 10^{-2} eV and only visible when zooming in as shown on the right: the SOC leads to a split (δ_{SOC}) of the highest VB at Γ, which goes from a six-fold to a four-fold degenerate state (disregarding spin). $\mathrm{MoS_2}$ (lower-right panel) also exhibits small, but non-negligible effects. At the PBE level, SOC induces a splitting of the valence band maximum (VBM) at K of the order of 0.15 eV (Table 5.1). In Xe (upper-right panel) and $\mathrm{PbI_2}$ (lower-right panel), the effects are massive: In Xe, SOC causes the VBM at Γ to split and closes the gap by about 0.43 eV. In $\mathrm{PbI_2}$, SOC generates a split in the second CB and several splits in the valence bands. Another effect in this case is that the first CB and the second CB move further apart. The PBE band gap decreases by 0.69 eV.

The energy gap values with and without SOC ($E_{\mathrm{g}}^{\mathrm{SR}}$ and $E_{\mathrm{g}}^{\mathrm{SOC}}$), their differences ($\Delta E_{\mathrm{g}} = E_{\mathrm{g}}^{\mathrm{SR}} - E_{\mathrm{g}}^{\mathrm{SOC}}$), and the SOC splittings (δ_{SOC}), obtained with the PBE, PBE0, and HSE are listed in Table 5.1. Note that for Si, the transition energy between the highest VB and the lowest CB at Γ is considered instead of the gap. For all materials, SOC closes the gap with all functionals, as expected. Interestingly, the magnitude of the effects decreases slightly as the gaps open up by the hybrid functionals: ΔE_{g} and δ_{SOC} obtained with PBE are equal to or slightly larger than those calculated with HSE, which are equal or slightly larger than those of PBE0. The only exception is $\delta_{\mathrm{SOC}}^{2}$ in $\mathrm{PbI_2}$, where the SOC effects with HSE are slightly smaller than those with PBE0, but the difference is within 10 meV. Overall, the differences between ΔE_{g} of PBE and PBE0 are within 10 meV in Si, $\mathrm{MoS_2}$ and Xe, while it is 60 meV in $\mathrm{PbI_2}$. In Si and $\mathrm{MoS_2}$, the same trend is observed also for the SOC splitting. In contrast, in Xe δ_{SOC} computed with PBE is about 50 meV higher than the values obtained with PBE0 and HSE. In $\mathrm{PbI_2}$, the effects of the functionals are different for $\delta_{\mathrm{SOC}}^{1}$ and $\delta_{\mathrm{SOC}}^{2}$: $\delta_{\mathrm{SOC}}^{1}$ of PBE is about 40-50 meV greater than that obtained with the hybrid functionals, while the $\delta_{\mathrm{SOC}}^{2}$ values are all within 10 meV. For the materials considered, 40 meV is the largest difference observed between PBE and HSE, and it is

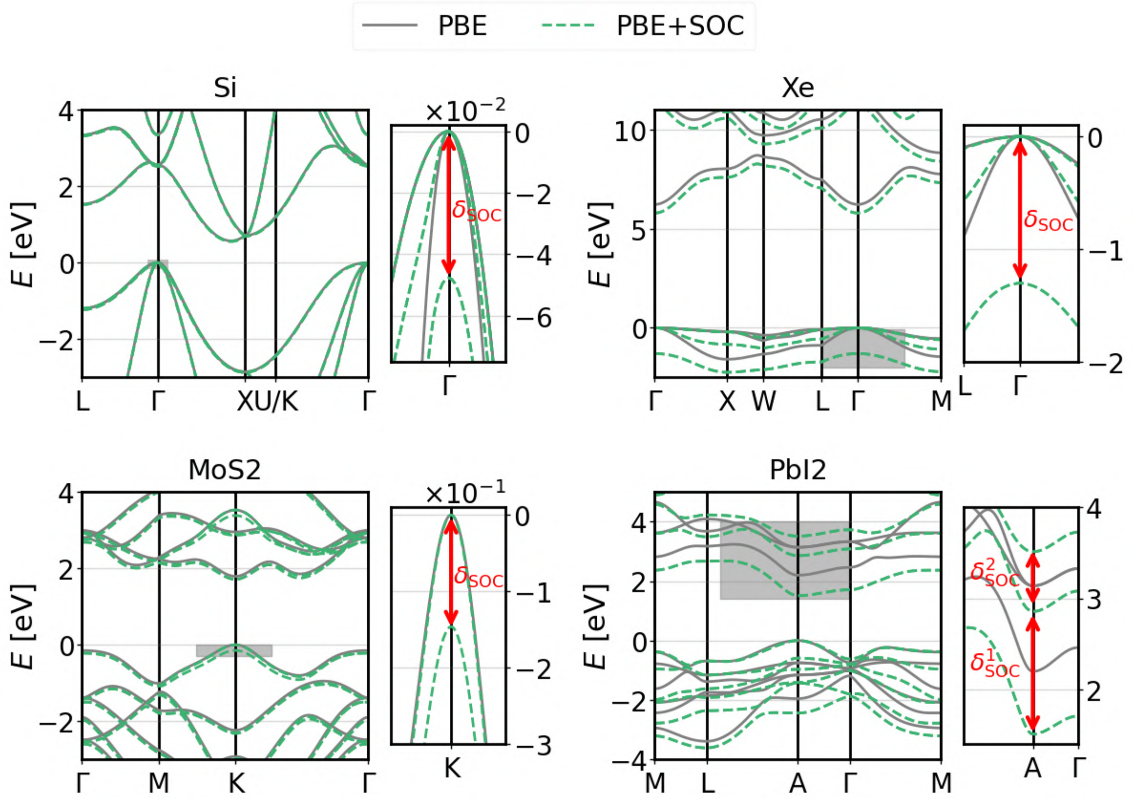

Figure 5.2: Band structures of Si, Xe, MoS2, and PbI2 computed with PBE with (green dashed lines) and without SOC (solid gray lines). The gray rectangles mark the zoomed area in the smaller panels to the right of each band structure. The SOC splittings, $\delta_{\rm SOC}$, (see also Table 5.1) are marked by the red arrows. The VBM is set to 0.

observed for the compound containing Pb, which is the heaviest atom.

Overall, we can conclude that the results are in agreement with those of Huhn and coworkers [131] and that the implementation of HYB+SOC in **`exciting`** is reliable.

5.2 Density-based mixing method

In the implementation of the DM method, described in Section 2.2.3.3, the main part is the evaluation of the quantity $\bar{g}$ (Eq. 2.33). The ingredients for its calculation are the electron density and its gradient. Due to the double-space partitioning of the **`exciting`** code, these quantities are computed differently in the MT and in the IR.

Table 5.1: Energy gaps and SOC splittings of Si, Xe, MoS_2, and PbI_2, computed with PBE, PBE0, and HSE. For each material, the first value is the SR energy gap (E_g^{SR}), followed by the gap calculated with SOC (E_g^{SOC}). For Si, the indirect gap, $E_{\Gamma\to\Gamma}$ is considered. The third value is the difference between the SR and the SOC gap ($\Delta E_g = E_g^{SR} - E_g^{SOC}$), and the last value corresponds to the SOC splitting (δ_{SOC}), highlighted in Fig. 5.2. For PbI_2, two SOC splittings are considered (δ^1_{SOC} and δ^2_{SOC}).

Functional	Si				Xe			
	$E^{SR}_{\Gamma\to\Gamma}$	$E^{SOC}_{\Gamma\to\Gamma}$	$\Delta E_{\Gamma\to\Gamma}$	δ_{SOC}	E^{SR}_{gap}	E^{SOC}_{gap}	ΔE_{gap}	δ_{SOC}
PBE	2.56	2.52	0.04	0.05	6.22	5.79	0.43	1.30
PBE0	3.98	3.95	0.03	0.04	8.13	7.70	0.43	1.25
HSE	3.32	3.29	0.03	0.04	7.40	6.97	0.43	1.25

Functional	MoS_2				PbI_2				
	E^{SR}_g	E^{SOC}_g	ΔE_g	δ_{SOC}	E^{SR}_g	E^{SOC}_g	ΔE_g	δ^1_{SOC}	δ^2_{SOC}
PBE	1.79	1.71	0.08	0.15	2.20	1.51	0.69	1.35	0.65
PBE0	2.91	2.83	0.08	0.14	3.54	2.91	0.63	1.30	0.65
HSE	2.27	2.19	0.08	0.14	2.91	2.26	0.65	1.31	0.64

Evaluation of $\bar{g}$

To validate our implementation, we compare $\bar{g}$ with a subset of the values from Ref. [106], which were kindly provided by the authors. They are computed with the VASP code [203], hence referred to as VASP results. All $\bar{g}$ in Table 5.2 are computed from the PBE ground-state density[2]. The energy gaps obtained with **`exciting`** with PBE, PBE0, and HSE are based on the same $\boldsymbol{k}$-mesh and $R_{MT}G_{max}$ as used in Sections 4.2.2- 5.1 (Tables A.1-B.1). For LiF and ZnO we used a $4 \times 4 \times 4$ $\boldsymbol{k}$-mesh for PBE and HSE and a $6 \times 6 \times 6$ $\boldsymbol{k}$-mesh for PBE0. For LiF (ZnO) the $R_{MT}G_{max}$ value is 9 (7), and the number of unoccupied states is 100 (500). For the calculation of $\bar{g}$ and the corresponding DM energy gaps, the $\boldsymbol{k}$-meshes are the same as those used for PBE0.

Comparing $\bar{g}$ computed with the two codes, the values obtained by **`exciting`** are bigger, except for Ar, for which the two codes agree up to the second digit. The root mean square error (RMSE)[3] of the **`exciting`** results compared to those of VASP is 0.06 $a_0^{-1/2}$; the largest difference is observed for MgO ($\sim$ $0.1 a_0^{-1/2}$). Due to these differences, the mixing parameters α^{PBE0}_{DM} and α^{HSE}_{DM} obtained from Eq. 2.34 and Eq. 2.34, respectively, differ

---

[2] The authors of Ref. [106] have verified that values of $\bar{g}$ computed from the PBE ground-state density are comparable with those computed from a ground-state density obtained with hybrid functionals.

[3] RMSE = $\sqrt{\frac{\sum_{i=1}^{N}(Y_{r,i}-Y_{a,i})}{N}}$, where N is the number of points, $Y_{r,i}$ are the reference values, and $Y_{a,i}$ the actual values.

Table 5.2: $\bar{g}$ and DM mixing parameters for PBE0 and HSE obtained with `exciting` and compared with the corresponding VASP results from Ref. [106]. $\alpha_{\mathrm{DM}}^{\mathrm{PBE0}}$ and $\alpha_{\mathrm{DM}}^{\mathrm{HSE}}$ are evaluated with the DM model of Ref. [106] (Eq: 2.34-2.35).

Material	Si	C	GaAs	MgO	Ar	Xe	LiF	ZnO
				`exciting`				
$\bar{g}$ [$a_0^{-1/2}$]	1.0483	1.1900	1.1554	1.2677	1.3143	1.2102	1.3638	1.2939
$\alpha_{\mathrm{DM}}^{\mathrm{PBE0}}$	0.1507	0.3072	0.2690	0.3931	0.4446	0.3295	0.4993	0.4220
$\alpha_{\mathrm{DM}}^{\mathrm{HSE}}$	0.2799	0.3841	0.3549	0.4595	0.5120	0.4026	0.5742	0.4883
				VASP				
$\bar{g}$ [$a_0^{-1/2}$]	0.9988	1.1173	1.0602	1.1689	1.3158	1.1823	1.3334	1.2729
$\alpha_{\mathrm{DM}}^{\mathrm{PBE0}}$	0.096	0.227	0.163	0.284	0.446	0.299	0.466	0.399
$\alpha_{\mathrm{DM}}^{\mathrm{HSE}}$	0.242	0.325	0.287	0.366	0.514	0.377	0.535	0.465

from those of Ref. [106] (see Table 5.2). The RMSE of $\alpha_{\mathrm{DM}}^{\mathrm{PBE0}}$ is 0.07 while that of $\alpha_{\mathrm{DM}}^{\mathrm{HSE}}$ is 0.05. These differences, in turn, are reflected in the energy gaps computed with $\alpha_{\mathrm{DM}}^{\mathrm{PBE0}}$ and $\alpha_{\mathrm{DM}}^{\mathrm{HSE}}$. In particular, the RMSE of the gaps is 0.5 eV for PBE0 and 0.3 eV for HSE (see PBE0-DM and HSE-DM rows in Table 5.3). The discrepancy is to be attributed mainly to the differences observed in $\bar{g}$, since the RMSE for PBE, PBE0, and HSE (both with $\alpha = 0.25$) gaps are only 0.04 eV, 0.05 eV, and 0.03 eV, respectively.

The differences observed between the `exciting` and VASP results are significant. However, by discussing with the authors of Ref. [106, 123], who in Ref. [123] computed $\bar{g}$ with QE, we realized that there are also significant differences between the results of VASP and QE. This means that the quantity $\bar{g}$ is highly sensitive to the methodology and the code used, and suggests to remodel the DM method for an all-electron code like `exciting`. This is the subject of Appendix B.2.

5.3 Optimization of the implementation

For the study of medium to large systems, the implementation of hybrid functionals has revealed some bottlenecks. After identifying them, Dmitrii Nabok applied a few improvements to the code, which we tested. In particular, we modified the message-passing interface (MPI) parallelization scheme and we reduced the memory consumption by splitting the calculation of the NL potential (Eq. 3.23) into blocks.

Table 5.3: Energy gaps calculated with different xc functionals and mixing parameters. The PBE0-DM and HSE-DM gaps are evaluated using $\alpha_{\mathrm{DM}}^{\mathrm{PBE0}}$ and $\alpha_{\mathrm{DM}}^{\mathrm{HSE}}$, respectively, given in Table 5.2. The VASP values are from Ref. [106]. The last column shows the MAPE using the experimental gaps as a reference. The indirect gaps obtained with `exciting` are evaluated using MLWF interpolation for denser sampling of the reciprocal space.

Material	Si	C	GaAs	MgO	Ar	Xe	LiF	ZnO	MAPE
Exp.	1.17	5.48	1.52	7.83	14.20	9.80	14.20	3.44	-
`exciting`									
PBE	0.58	4.15	0.54	4.74	8.70	6.22	9.19	0.93	45.27
PBE0	1.79	6.06	1.98	7.22	11.14	8.13	12.27	3.28	19.81
PBE0-DM	1.29	6.50	2.10	8.70	13.06	8.74	15.42	5.03	19.02
HSE	1.14	5.30	1.45	6.48	10.36	7.40	11.52	2.59	15.32
HSE-DM	1.21	5.94	1.86	8.01	12.14	8.13	14.62	4.32	12.13
VASP									
PBE	0.59	4.17	0.63	4.77	8.65	6.25	9.24	0.90	44.40
PBE0	1.78	6.06	2.09	7.27	11.06	8.10	12.26	3.26	20.72
PBE0-DM	1.07	5.92	1.56	7.67	12.98	8.48	14.99	4.90	11.41
HSE	1.16	5.33	1.47	6.53	10.31	7.39	11.53	2.57	14.94
HSE-DM	1.21	5.71	1.61	7.41	12.11	7.99	14.28	4.26	9.56

New MPI parallelization scheme

The NL exact exchange in Eq. 3.29 depends on both $\boldsymbol{k}$ and $\boldsymbol{q}$-points. In `exciting`, this is implemented as two loops, one over the symmetry-reduced $\boldsymbol{k}$-points and the other over the $\boldsymbol{q}$-points. Up to `exciting` Nitrogen, the MPI processes were distributed only over the reduced $\boldsymbol{k}$-points, both in the NL potential and in the inner SCF cycle. The positive aspect of this scheme is the low waste of computational resources due to the uniformity of the parallelization, but the time spent in the inner SCF is negligible compared to that needed for the NL potential. For this reason, we opted for a non-homogeneous MPI parallelization, where the NL potential is evaluated by distributing each $\boldsymbol{k}$-$\boldsymbol{q}$ pair to different MPI processes.

Memory redistribution

For medium-large size systems, such as some of the materials studied in this work, the large size of the MPB coefficients $M_{nn'}^{I}$ and $\tilde{M}_{nn'}^{I}$ is a memory bottleneck. In `exciting`, they are defined as complex arrays of size $\mathrm{MPB_s} \times N_{\mathrm{occ}} \times (N_{\mathrm{occ}} + N_{\mathrm{unocc}})$, where $\mathrm{MPB_s}$ is the size of the MPB. To overcome this problem, the sum over the occupied states in Eq. 3.29

can be split into different blocks and Eq. 3.29 can be rewritten as follows:

$$V^{\mathrm{NL}}_{\mathrm{x},nn'}(\mathbf{k}) = -\sum_{b}^{N_{\mathrm{blk}}} \sum_{n_b=1+(b-1)\mathrm{S_b}}^{b\mathrm{S_b}} \sum_{\mathbf{q}}^{\mathrm{BZ}} \sum_{IJ} [\tilde{M}^{I}_{nn_b}(\boldsymbol{k},\boldsymbol{q})]^{*} \tilde{M}^{J}_{n_b n'}(\boldsymbol{k},\boldsymbol{q}). \tag{5.3}$$

Here, N_{blk} is the number of blocks of size S_{b}, b is the index of the block and n_b is the index of the occupied state within the block b. With this approach the size of the $\tilde{M}^{I}_{nn'}$ is reduced to $\mathrm{MPB_s} \times S_{\mathrm{b}} \times (N_{\mathrm{occ}} + N_{\mathrm{empty}})$. To benefit from this method, one needs to change the size of the blocks in the `exciting` input. Although this solves the memory bottleneck problem, it is not optimal, since during the evaluation of the MBP coefficients, some quantities related to the IPW are recomputed for each block. Therefore, for a large number of blocks, a significant increase in computational time is observed.

Note that the performance of the new parallelization scheme and the block distribution depend on the parameters and the system size, so benchmarks are always advisable. An example of their performance for $\mathrm{PbI_2}$ is discussed in Appendix B.3.

5.4 Conclusions

The implementation of the HSE functional (Chapter 4) combined with the implementations discussed here, i.e. HYB+SOC, the DM method, and the code optimization, allows the evaluation of the electronic structure of complex medium-size systems with higher accuracy compared to local and semi-local functionals. An example is HaP, which are characterized by large SOC effects. For this type of systems, the DM showed very promising results, as we will discuss in Chapter. 6. The new MPI scheme turned out to be very useful for speeding up the calculations, and the blocking method allows access to the properties of medium-size systems at the hybrid level, which was not possible before. The largest system for which the implementations have been used so far is the 2D perovskite $\mathrm{BA_2PbI_4}$ consisting of 156 atoms [208]. In addition, HSE turned out to be an excellent starting point for G_0W_0 calculations of several semiconductors [209, 35, 210].

Besides the works cited here, the implementation of the HSE functional in `exciting` is a great step forward for the advancement of the code, e.g., it served as a starting point for the inclusion of hybrid functionals in real-time time-dependent DFT carried out by Antonio Cillis during his master's thesis [211]. Moreover, Fabian Nemitz is extending the hybrid implementation to magnetic systems.

CHAPTER 6

Second variation with local orbitals

In materials with strong SOC, the conventional second variation approach exhibits poor efficiency because it requires a number of basis functions comparable to the number of first variation KS wave functions. Aiming to reduce the effort, together with Sven Lubeck, we developed and implemented in the `exciting` code a new method, named *second variation with local orbitals*, which uses LO as explicit second variation basis functions. In fact, SOC contributes mainly to the region around the nuclei. Hannah Kleine has extended the method to relativistic LO. Part of the description follows Ref. [212] closely. The chapter concludes with a brief discussion of ongoing projects related to this work.

6.1 Introduction

The ultimate goal of this work is to study electronic excitations of HaP, where SOC is of crucial importance. $CsPbI_3$ and its precursor PbI_2 show a slow convergence of the SV method (discussed in Section 3.4.2) with respect to the number of KS wave functions. The example of $CsPbI_3$ is shown in Fig. 6.1, where the convergence of the total energy is plotted with respect to the number of unoccupied KS states. For a clearer visualization, the y-axis shows the energy difference ΔE_{tot}, which is obtained by subtracting the total energy obtained with the NP treatment (Section 3.4.1) from the total energy calculated

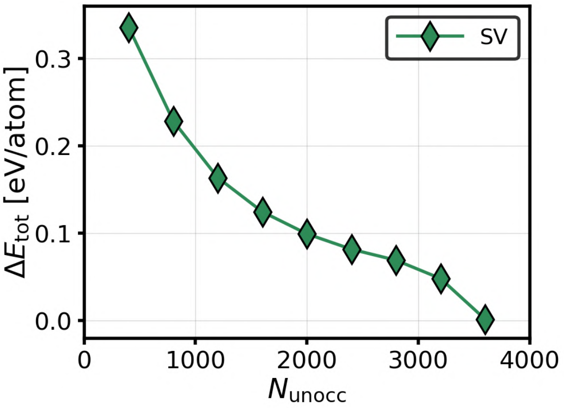

Figure 6.1: Convergence behavior of the total energy of the orthorhombic phase of $CsPbI_3$ with the number of unoccupied KS states (N_{unocc}) computed using the SV method. The y-axis shows the difference to the reference energy computed with the NP treatment.

using SV and the number of unoccupied KS states given in the x-axis. Note that the number of occupied states is fixed. Convergence is reached only when all empty KS bands are included in the calculation. This slow convergence behavior also limits the use of higher-level methodologies, e.g. hybrid functionals, G_0W_0, and BSE, which also require a significant number of unoccupied states, but hardly all the states available. The poor efficiency of the SV method [213, 214] for this class of materials was the motivation for the development of the SVLO method.

Another important aspect when considering SOC within the (L)APW+LO method is that SR and fully relativistic orbitals have different asymptotic behavior at small distances from the nuclei. The latter cannot be described in terms of SR functions [173, 213]. In particular, SOC introduces a splitting within the p states into $p_{1/2}$ orbitals, whose radial part diverges, and $p_{3/2}$ orbitals, whose radial part goes to zero. Singh proposed to include LO constructed using radial functions with $l = 1$ and $j = 1/2$ in the SV step [173], and Kunes and coworkers applied it to study the electronic structure of fcc Th [215]. This motivated the extension of the SVLO method to j-resolved LO, that we refered to as *Dirac type* LO (Section 6.3), done by Hannah Kleine in her bachelor thesis [216]. In the following, the SVLO approach is explained, and its performance is demonstrated and validated via band structure and total energy calculations for Xe, MoS_2, PbI_2, γ-$CsPbI_3$, and Bi_2Te_3. The implementation in the `exciting` code was done together with Sven Lubeck, the validation was mainly done by me in collaboration with Hannah Kleine.

6.2 Second variation with local orbitals as explicit basis functions

The SVLO method is an extension of the conventional SV approach (described in Section 3.4.2). In this new approach, LO are used as explicit basis functions, and the SVLO wave functions are expanded as follows:

$$\varphi_{a\boldsymbol{k}}^{\mathrm{SVLO}}(\boldsymbol{r}) = \sum_{\sigma'=1}^{2} \Big[\sum_{n'=1}^{N_{\mathrm{b}}^{\mathrm{SV}}} C_{an'\sigma'}^{\boldsymbol{k}} \bar{\varphi}_{n'\boldsymbol{k}}^{\sigma'\mathrm{FV}}(\boldsymbol{r}) + \sum_{\mu=1}^{N_{\mathrm{LO}}} C_{a\mu\sigma'}^{\boldsymbol{k}} \phi_{\mu}^{\sigma'}(\boldsymbol{r}) \Big], \tag{6.1}$$

where $\bar{\varphi}_{n'\boldsymbol{k}}^{\sigma'\mathrm{FV}}$ is a modified FV wave function defined as:

$$\bar{\varphi}_{n'\boldsymbol{k}}^{\sigma'\mathrm{FV}}(\boldsymbol{r}) = \sum_{\boldsymbol{G}} c_{n\boldsymbol{G}}^{\boldsymbol{k}\sigma} \phi_{\boldsymbol{G}+\boldsymbol{k}}^{\mathrm{APW}}(\boldsymbol{r}). \tag{6.2}$$

Compared to Eq. 3.33, in Eq. 6.1 there is additionally a sum over the total number of LO, therefore the number of the basis functions is given by:

$$N_{\mathrm{b}}^{\mathrm{SVLO}} = N_{\mathrm{b}}^{\mathrm{SV}} + N_{\mathrm{LO}} = N_{\mathrm{occ}} + N_{\mathrm{unocc}} + N_{\mathrm{LO}}. \tag{6.3}$$

Since N_{occ} and N_{LO} are predetermined, N_{unocc} is the only convergence parameter. A minor drawback of the SVLO method is that since the new basis functions are not orthonormal, the overlap matrix must also be evaluated, and the generalized eigenvalue problem must be solved:

$$\sum_{\sigma''n''} H_{\boldsymbol{k}n'n''}^{\sigma\sigma'} C_{an''\sigma''}^{\boldsymbol{k}} = \varepsilon_{a\boldsymbol{k}}^{\mathrm{SV}} \sum_{\sigma''n''} S_{\boldsymbol{k}n'n''}^{\sigma'\sigma''} C_{an''\sigma''}^{\boldsymbol{k}}. \tag{6.4}$$

The SVLO method is computationally convenient if (*i*) $N_{\mathrm{b}}^{\mathrm{SVLO}} \ll N_{\mathrm{b}}^{\mathrm{FV}}$ and (*ii*) when the desired precision is achieved with a number of unoccupied states that, when added to the number of LO, is smaller than the number of unoccupied states required to achieve the same precision with the conventional SV method ($N_{\mathrm{unocc}}^{(\mathrm{SVLO})} + N_{\mathrm{LO}} < N_{\mathrm{unocc}}^{(\mathrm{SV})}$).

6.3 Dirac type local orbitals

The LO that can be employed as explicit SV basis functions in Eq. 6.1 can be of different types. The first consists of LO defined in Eq. 3.9-3.10, which we will refer to as SR-LO, since the radial functions are solutions of the radial SR Schrödinger equation. The second is referred to as Dirac-type LO since at least one of the radial functions is the solution of the radial Dirac equation. This accounts for the correct asymptotic behavior of the $p_{1/2}$ orbitals at the atomic nuclei. In the case of Dirac-type LO, U_μ in Eq. 3.9 is defined as the following linear combination:

$$U_\mu^{\mathrm{Dirac}}(r_\alpha) = \sum_\xi a_{\mu\xi} u^{v}_{\alpha\xi jl}(r_\alpha; \varepsilon_{\alpha\xi jl}), \tag{6.5}$$

where the radial functions and the energy parameters are j-resolved. Depending on the purpose of the LO, the values of j may be different or the same for different radial functions. In `exciting`, the total angular momentum, j, of the Dirac-type radial functions is controlled by k, which is defined as

$$k = (l - j)(2j + 1). \tag{6.6}$$

Overall, the relativistic effects are included only by modifying the radial functions, while the spherical harmonics in Eq. 3.9 remain fixed. This is particularly convenient in terms of implementation, but also provides flexibility, by allowing the inclusion of one or more LO with the desired total angular momentum, going beyond what has been done before [215]. The same approach is used in Ref. [184]; more information can also be found in the bachelor thesis of Hannah Kleine [216] and in Ref. [212].

6.4 Computational details

The set of five materials for testing the performance of the SVLO method includes systems with different electronic characters, dimensionality, atomic species, stoichiometry, and degree of SOC. For all of them, the convergence behavior of the SV and SVLO methods is carefully monitored, and the effect of Dirac-type LO is investigated. To carry out this analysis, the NP treatment from Ref. [184] is used as a reference. SR calculations serve to evaluate the magnitude of the SOC effects. PBE is the xc functional adopted. SR and SOC effects of valence and semi-core states are treated with ZORA [133, 134]. Core states are computed by using the 4-component Dirac equation.

For all materials, the experimental lattice constants and atomic positions are used (see Table 6.1). This table also lists the MT radii, the dimensionless parameters $R_{\mathrm{MT}}^{\mathrm{min}} G_{\mathrm{max}}$ and the $\boldsymbol{k}$-meshes. They are chosen to meet a numerical precision of 10^{-2} eV/atom for the total energies and of 10^{-2} eV for the energy gaps. The size of the FV basis functions

(APW+LO) is given for each material in Table 6.2 together with the number of occupied states treated as valence/semi-core states (N_{occ}).

Table 6.1: Space group, lattice constants, and convergence parameters used in the calculations. The structural parameters are taken from the experimental references. Among the convergence parameters, there are $R_{\text{MT}}^{\text{min}}G_{\text{max}}$, from which G_{max} can be accessed, R_{MT} for all species, and the $\boldsymbol{k}$-mesh. For MoS_2, the first MT radius corresponds to Mo and the second to S.

Material	Xe	MoS_2	PbI_2	CsPbI_3	Bi_2Te_3
Space group	Fm3-m	P-6m2	P-3m1	Pnma	R-3m
a [Å]	6.20	3.16	4.56	8.86	10.44
b [Å]	6.20	3.16	4.56	8.57	10.44
c [Å]	6.20	15.88	6.99	12.47	10.44
Ref.	[217], [201]	[218]	[219]	[220]	[221]
$R_{\text{MT}}^{\text{min}}G_{\text{max}}$	8	8	8	9	10
R_{MT} [a_0]	3.00	2.30/2.05	2.90	2.90	2.80
$\boldsymbol{k}$-mesh	4×4×4	6×6×1	6×6×4	3×3×2	6×6×6

Table 6.2: Basis-set sizes: N_{APW} is the number of APW, and N_{LO} ($N_{\text{LO}}^{1/2}$) is the number of LO functions for calculations without (with) Dirac-type LO. The last column shows the number of occupied valence states N_{occ}.

Material	N_{APW}	N_{LO}	$N_{\text{LO}}^{1/2}$	N_{occ}
Xe	138	26	38	13
MoS_2	939	35	-	13
PbI_2	318	73	109	33
CsPbI_3	3236	496	736	228
Bi_2Te_3	895	141	201	57

In the case of Bi_2Te_3, the band gap moves away from high-symmetry points when considering SOC. To determine the position and the magnitude of the band gap, an additional iteration with a 48×48×48 $\boldsymbol{k}$-mesh is performed on top of the self-consistent NP calculation. The $\boldsymbol{k}$ points thus determined are then included in the band structure path from which the final values are extracted.

All input and output files are available in the NOMAD Repository [222] at the following link `https://doi.org/10.17172/NOMAD/2023.06.06-1`.

6.5 Results

The first part of the results focuses on the performance of the SVLO method compared to the conventional SV. In this part, the Dirac-type LO are omitted since they are the focus of the second part. To distinguish between the sets of LO used in the two cases, the first set is denoted as p and the second as $p_{1/2}$. During this work, the impact of $p_{3/2}$-type LO was also examined. However, since their effect was of the order of 10^{-2} eV or less, they are not included in the further analysis. In MoS_2, where the VBM and the conduction band minimum (CBm) exhibit dominant d character [223], the influence of $d_{3/2}$ and $d_{5/2}$-type LO was also found to be negligible.

6.5.1 Performance of the SVLO method

For all investigated materials, we examine the convergence behavior of total energy and the band gap with respect to the "reduced" number of basis functions, which is defined for the SV and the SVLO methods as:

$$\tilde{N}_{\mathrm{b}}^{\mathrm{SV(LO)}} = \begin{cases} N_{\mathrm{unocc}}^{\mathrm{(SV)}} & \mathrm{SV} \\ N_{\mathrm{unocc}}^{\mathrm{(SVLO)}} + N_{\mathrm{LO}} & \mathrm{SVLO.} \end{cases} \tag{6.7}$$

These numbers differ from the total number of SV(LO) basis functions (Eq. 3.34-6.3) by the number of the occupied states, which does not change when using the same core-valence distribution. Since the number of LO basis functions is also fixed (see Table 6.2), the increase in $\tilde{N}_{\mathrm{b}}^{\mathrm{SV(LO)}}$ only corresponds to an increase in the number of unoccupied bands. As the number of unoccupied states in Eq. 6.7 is different for the two methods, we distinguish them by the superscripts (SV) and (SVLO). The results are plotted in Fig. 6.2. In the rest of the chapter, we will refer to $\tilde{N}_{\mathrm{b}}^{\mathrm{SV(LO)}}$ as the number of basis functions. The same analysis is also performed for selected SOC splittings, the only exception being Bi_2Te_3 for which we analyze the transition energy between the highest VB and the lowest CB at Γ (E_Γ).

The energy gaps computed with and without SOC and the SOC splittings are collected in Tables 6.3 and 6.4, respectively. The results with SOC include both calculations with pure SR-LO and with LO sets including Dirac-type LO. Also in Fig. 6.3-6.9 the band structures are plotted for both LO sets.

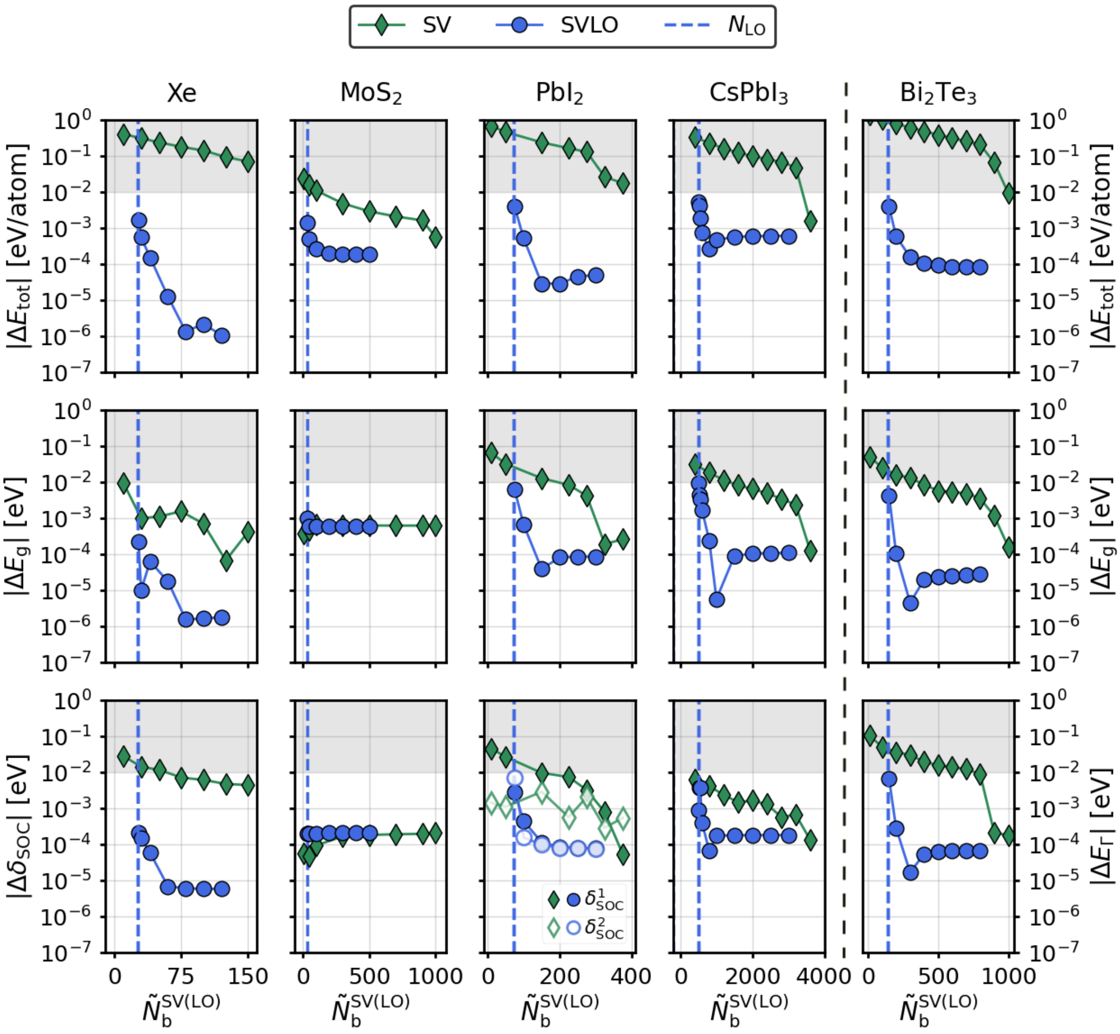

Figure 6.2: Convergence behavior of the total energy (E_{tot}) and several band energies with respect to the number of basis functions used in the SV(LO) methods ($\tilde{N}^{\mathrm{SV(LO)}}$), employing the p-set of LO. For all materials, the convergence is studied for the band gap E_{g} and selected SOC splitting δ_{SOC}, the only exception being Bi$_2$Te$_3$, where the convergence is studied for E_Γ instead of δ_{SOC}. For PbI$_2$, the energy difference δ^1_{SOC} is also considered (here the SOC splitting is named δ^2_{SOC}). The selected SOC splittings are indicated in the band structure plots (Figs. 6.3-6.7). The y-axes show the energy differences with the NP values as reference. Note the logarithmic scale. The vertical lines indicate the number of LO basis functions (p-set). The gray shaded areas serve to highlight the points that are within the target precision (10^{-2} eV/atom for the total energy and 10^{-2} eV for the other quantities). The values used to generate the plots are collected in Tables C.1-C.5.

Table 6.3: Energy gaps (E_g) in eV of the considered materials computed with the SVLO method for different sets of LO. For comparison, SR results are shown. Note that in Bi_2Te_3, SOC changes not only the magnitude of the gap but also the position of the VBM and the CBm. Both are again altered when Dirac-type LO are considered.

Method	E_g				
	Xe	MoS_2	PbI_2	$CsPbI_3$	Bi_2Te_3
SR	6.22	1.78	2.20	1.64	0.25 ($\Gamma \rightarrow \Gamma$)
SVLO (p)	5.79	1.71	1.66	0.82	0.10 (B→B)
SVLO ($p_{1/2}$)	5.79	-	1.40	0.55	0.03 (D→C)

Table 6.4: SOC splittings (δ_SOC) in eV computed with the SVLO method for the p and the $p_{1/2}$ sets of LO. For Bi_2Te_3 the transition energy between the highest VB and the lowest CB at Γ (E_Γ) is shown instead. The SR results are shown only for δ^1_SOC of PbI_2 and E_Γ, the first in fact is not a proper SOC splitting.

Method	δ_SOC					E_Γ
	Xe	MoS_2	PbI_2 (δ^1_SOC)	PbI_2 (δ^2_SOC)	$CsPbI_3$	Bi_2Te_3
SR	-	-	0.94	-	-	0.25
SVLO (p)	1.30	0.15	1.25	0.63	0.71	0.58
SVLO ($p_{1/2}$)	1.40	-	1.45	0.68	0.76	0.69

Xe

Xenon is a material with a wide band gap and significant SOC effects, i.e., the band gap closes by 0.43 eV due to the splitting of the triple degenerate (disregarding spin) VBM into a single state and a double-degenerate state by about 1.30 eV (Fig. 6.3). Analyzing the convergence behavior of the total energy, it can be observed that the values computed by the SVLO method remain within a few 10^{-3} eV/atom when using a number of basis functions comparable to the number of LO basis functions (i.e. 26). A convergent value of the order of 10^{-6} eV/atom is achieved with only about 80 basis functions. In contrast, the SV method requires all available FV states to reach only $\sim 7 \times 10^{-2}$ eV/atom. For both the energy gap and the SOC splitting, the SVLO method already achieves an accuracy of the order of 10^{-4} eV with a number of basis functions comparable to the number of LO functions; with about 80 basis functions it is two orders of magnitude better. In contrast, using all available FV-KS eigenstates, SV converges only within 10^{-3} eV and 10^{-2} eV for the energy gap and the SOC splitting, respectively. For production calculations, a precision of 10^{-2} eV/atom for the total energy and 10^{-2} eV for energy gaps and SOC splittings is often aimed for. Considering this target, the advantage of the SVLO method is significant, in particular for the total energy. On the other hand,

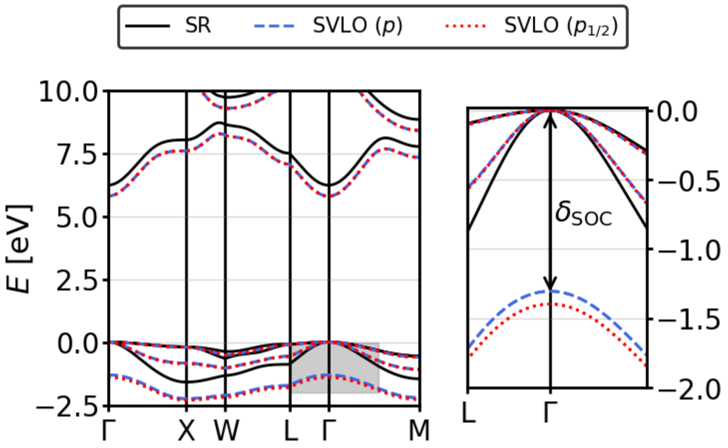

Figure 6.3: Xenon band structure computed with different methods and LO sets. The right panel shows the zoom into the gray region where the SOC spitting occurs (δ_{SOC}). The VBM is set to 0.

the SV method performs better than SVLO for reaching the target energy gap because the number of basis functions needed is smaller than the number of LO. The SV requires about 75 empty bands for the SOC splitting within the target precision.

This analysis shows that the SV and the SVLO methods do not converge to the same value. This may seem counterintuitive, since if all available FV KS states are used as basis functions, the two methods should be equivalent. The reason can be found in the implementation of the SV method in the `exciting` code: while the APW basis set size can be different at different $\boldsymbol{k}$-points, in the SV method, the number of available KS states is enforced to be the same at all $\boldsymbol{k}$-points and corresponds to the smallest APW basis set. To prove this, in Fig. 6.4 we show the same analysis as for Xenon in Fig. 6.2, but for calculations performed using a single $\boldsymbol{k}$-point. In this case, the SV and SVLO methods achieve the same precision, i.e. about 10^{-6} eV, for all analyzed properties.

MoS$_2$

MoS$_2$ is a transition metal dichalcogenide (TMDC) and, being a candidate for many applications in optoelectronics [224, 225, 226, 227, 228, 229], one of the most studied 2D materials. SOC is responsible for the formation of valley excitons, which makes it suitable for spintronic applications [230, 231]. A reduction of its energy gap by only 0.07 eV is caused by the SOC splitting of the VBM at K (Fig. 6.5). Although quite small, *i.e.* 0.15 eV, it is fundamental, since being considered or not can change the gap from direct to indirect or *vice-versa* [210]. For example, when computing the gap in the PBE

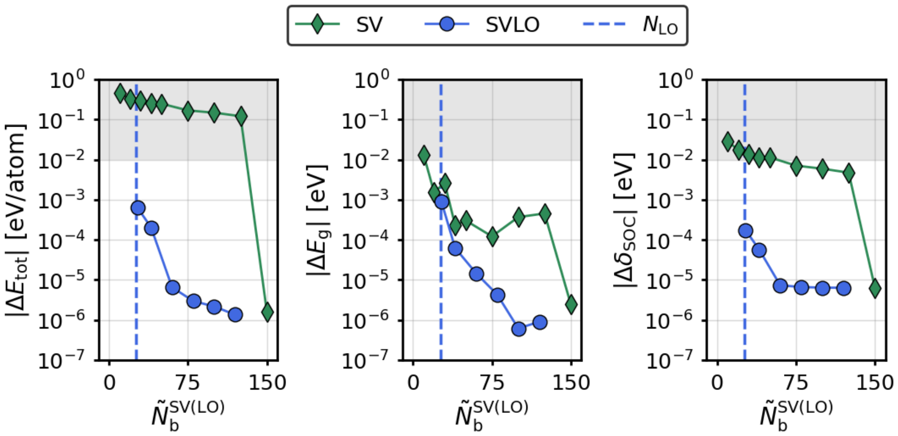

Figure 6.4: Same as Fig. 6.2 for Xe and for calculations with 1 $\boldsymbol{k}$-point. The data used for the plots are in Table C.6.

geometry, an unphysical band gap between the high symmetry points Γ → K is predicted with PBE and LDA without SOC. When SOC is included the correct direct gap is obtained [232, 210]. On the other hand, in Ref. [210] we show that for the geometry optimized with HSE, G_0W_0@LDA predicts the correct direct band gap at K, which becomes between Q → K when SOC is considered. This happens because at Q the lowest CB also splits (this splitting is not analyzed here). The splitting at the VBM is also crucial for the optical spectra [233, 234, 231]. Regarding the convergence behavior, in Fig. 6.2 a small improvement of the SVLO method over the SV method is observed for the total energy, i.e. the SVLO method achieves a precision of the order of 10^{-3} with about 40 basis functions, while the SV does not go below 10^{-2} eV/atom for the same number of basis functions. For the energy gap and the SOC splitting, the two methods are comparable, reaching a precision of about 10^{-4} eV with only a few basis functions.

PbI_2

PbI_2 is a semiconductor with hexagonal symmetry, which is mainly used for X-ray and γ-ray detectors [235, 236, 237, 238]. It is the precursor of lead-iodide based HaP that are the focus of this work. Like in these materials, the SOC effects in PbI_2 are massive: The calculations performed for the p-set of LO show that the band gap is reduced by 0.54 eV when SOC is applied, and the two-fold degenerate (disregarding spin) second CB splits by δ^2_{SOC}= 0.63 eV (Fig. 6.6). In addition, the distance between the CBm and the second CB, which we refer to as δ^1_{SOC} for convenience, increases by 0.31 eV. In this case, the

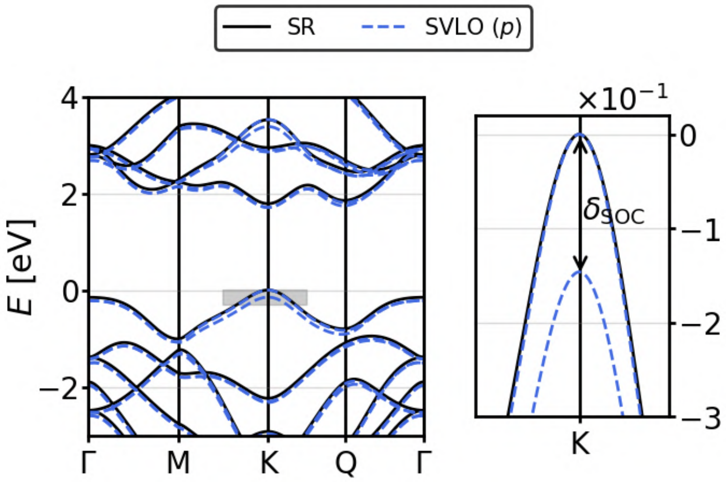

Figure 6.5: Band structure of MoS_2 with and without SOC. The SOC is computed using the SVLO method and with SR LO. The SOC splitting is highlighted in the right panel and the Fermi energy is at 0 eV.

advantages of the SVLO method over SV are significant: With a number of basis functions comparable to the number of LO functions (i.e. 73), the SVLO method achieves the target precision for all quantities considered. In contrast, the SV method needs basically all empty states (i.e. ~375) to reach the target precision for the total energy, ~225 empty bands for the energy gap, and ~150 for δ^1_{SOC}. For δ^2_{SOC} only ~10 empty states are necessary. Both approaches eventually converge to comparable precision. The only exception is the total energy, for which the SV method converges to a precision of the order of 10^{-2} eV/atom and the SVLO method converges to a precision of the order of 10^{-5} eV/atom.

$CsPbI_3$

$CsPbI_3$ is a widely studied inorganic HaP which, together with PbI_2, is one of the materials discussed in Chapter 7. Here, it is considered in its orthorhombic phase (γ-phase), which contains 20 atoms. It is the largest system studied in this chapter (see Table 6.2). It consists of three heavy elements that lead to massive SOC effects: The band gap decreases from 1.64 eV to 0.82 eV, and two-fold degenerate (disregarding spin) CBm undergoes a splitting of 0.71 eV (Fig. 6.7). Although SV and SVLO converge to a comparable precision, the computational effort required for the two approaches is remarkably different. For example, considering the total energy, the SV method needs nearly all available KS basis functions (i.e. ~3600) to achieve convergence, while the SVLO converges with only a few unoccupied KS bands in addition to the 496 LO functions. In

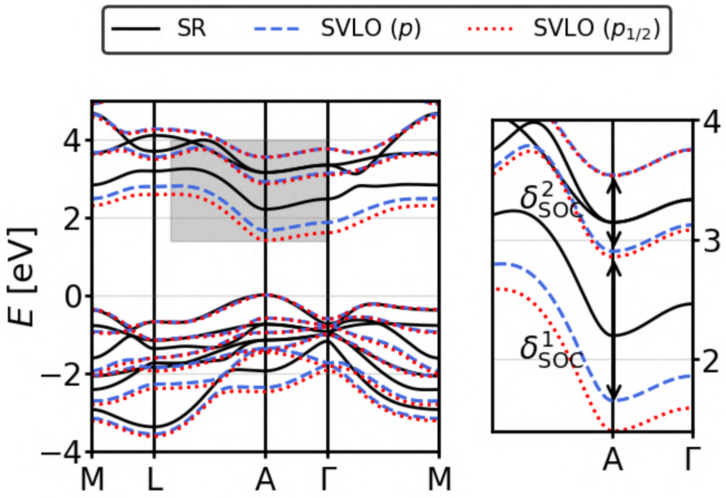

Figure 6.6: Same as Fig. 6.3, but for PbI_2. On the right, both δ^1_{SOC} and δ^2_{SOC} are shown.

this case, the computational cost of the SV method is worse than that of the NP treatment: As discussed in Section 3.4.2, due to the initial FV step, the SV procedure scales as $(N_b^{\mathrm{FV}})^3 + (2N_b^{\mathrm{SV}})^3$. Here $N_b^{\mathrm{FV}} \approx N_b^{\mathrm{SV}}$, so SV scales as $9(N_b^{\mathrm{FV}})^3$, while the NP method scales as $8(N_b^{\mathrm{FV}})^3$ (see Section 3.4.1). In contrast, the SVLO Hamiltonian has a size of $\sim 1500 \times 1500$ (considering also the 228 occupied states), so the diagonalization of the FV step is the computationally most expensive part of the calculation (FV Hamiltonian size of $\sim 3800 \times 3800$). Moreover, by comparing the time to solve the FV and SVLO eigenvalue problems, with the time to solve the NP eigenvalue problem we observed an improvement in computational time of a factor of 3.6.

Considering the other quantities, SV achieves the target precision for the energy gap with about twice the number of basis functions compared to the SVLO method, and for the SOC splitting with a comparable amount.

Bi_2Te_3

Bi_2Te_3, is a topological insulator with a single Dirac cone at Γ [239, 240]. It is known as an efficient thermoelectric material [214, 241]. At the DFT level, strong SOC effects shift the fundamental band gap from Γ to off-symmetry points, which are located in the mirror plane of the first BZ, i.e. the red plane in Fig. 6.8. The same figure also shows the atomic structure.

The VBM and CBm positions are highly sensitive to the structural details and the choice

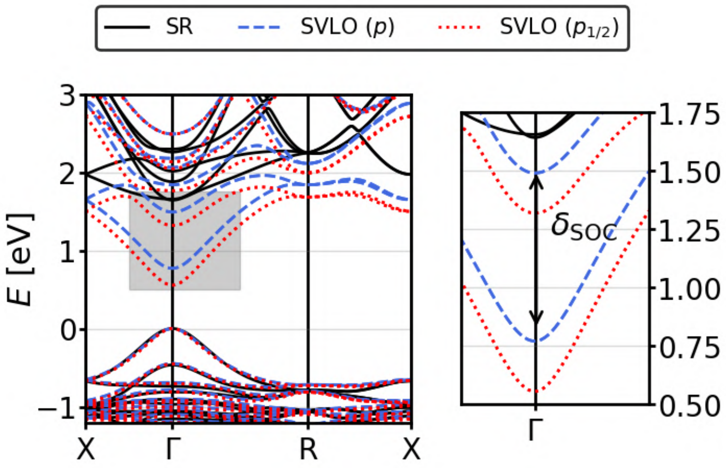

Figure 6.7: Same as Fig. 6.3 but for CsPbI$_3$.

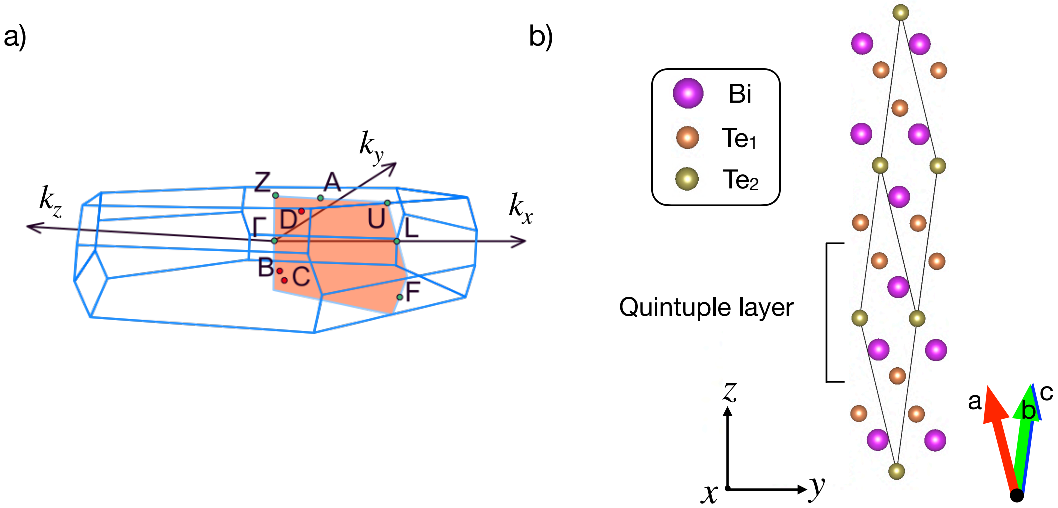

Figure 6.8: a) Brillouin zone of the rhombohedral Bi$_2$Te$_3$ structure shown on the right. The mirror plane containing the out-of-symmetry points where the band gap is located when SOC is considered is indicated in red. All the reciprocal space points displayed are used in the band structure of the Bi$_2$Te$_3$ in Fig. 6.9. b) Crystal structure with R-3m symmetry formed by Bi (purple) and two chemically non-equivalent Te atoms (Te$_1$ orange, Te$_2$ gold). The quintuple layer composed of Te-Bi-Te-Bi-Te sheets repeating along the z-direction is highlighted.

of the xc functional, hence controversial results exist in the literature. For an overview of this diversity, see Ref. [242]. When using more accurate methods, such as the G_0W_0 approximation, the discrepancies even increase [243, 189]. Because of all these aspects, Bi_2Te_3 is particularly computationally challenging.

When considering SOC (without Dirac-type LO), the direct band gap at Γ of 0.25 eV is reduced by 0.15 eV and shifts to B=(0.67, 0.58, 0.58), which appears six-fold in the BZ. This result is comparable to those of Ref. [244] and Ref. [214]. In the former, a direct band gap of 0.13 eV at (0.667,0.571, 0.571) was found, while in the latter, the computed gap of 0.11 eV is indirect. However, the locations of the VBM, (0.652, 0.579, 0.579), and that of the CBm, (0.663, 0.568, 0.568), are very close to each other. The differences can be attributed to the use of different $\boldsymbol{k}$-grids and crystal structures: Here we use $a = 10.44$ Å and $\theta = 24.27^\circ$ [221], while Refs. [214, 244] use the experimental structure with $a = 10.48$ Å and $\theta = 24.16^\circ$.

From Fig. 6.2 it is evident that for Bi_2Te_3 the SVLO method has clear advantages over the conventional SV method. The latter reaches the target precision for the total energy only with basically all available FV KS states (i.e. ~1000). In contrast, SVLO requires a basis set size comparable to the number of LO (i.e. 141). The SVLO method reaches convergence, which is of the order of 10^{-4} eV/atom, with about 250 additional KS states. As for the other materials, the electronic structure obtained by SV reaches the targeted precision faster than the total energy, but it remains inferior to SVLO: For a precision of 10^{-2} eV, the gap needs about twice the number of SVLO basis functions (not including the occupied states); for E_Γ the basis-set size must be further doubled. Furthermore, the SVLO band gap converges to a precision of $\sim 10^{-5}$ eV, while the SV gap cannot go below 10^{-4} eV. Both methods reach a convergence of the order of 10^{-4} eV for E_Γ.

6.5.2 Effects of $p_{1/2}$ LO within the SVLO method

The focus of this section is to highlight the importance of Dirac-type LO and to investigate the efficiency of the SVLO method when including them as explicit basis functions. The results are generated by adding two $p_{1/2}$-type LO for each p state to the SR LO set. The p character gives rise to three degenerate basis functions for each LO (see Table 6.2). The convergence behavior of the SVLO method with the $p_{1/2}$- set of LO is collected in Fig. 6.10, where the SVLO(p) results are shown for direct comparison. The band gaps and SOC splittings are given in Table 6.3 and 6.4, respectively, also for SVLO($p_{1/2}$). MoS_2 is

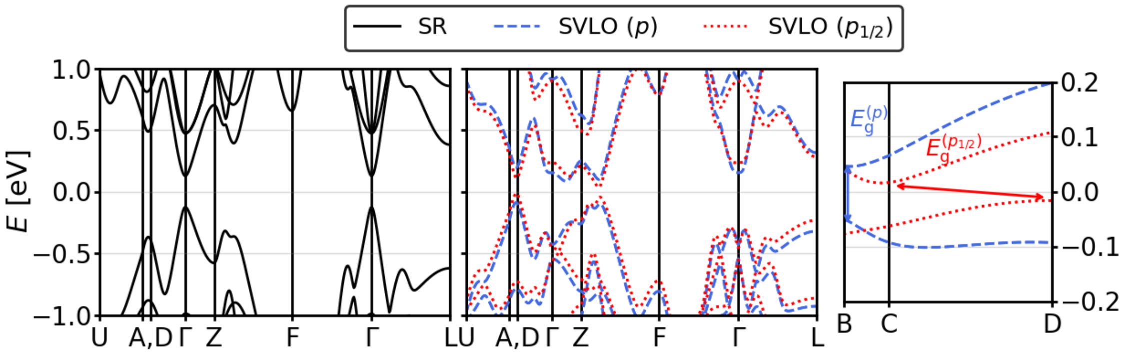

Figure 6.9: Band structures of Bi$_2$Te3 computed with and without SOC. The SOC results are obtained using the SVLO method with different LO sets. The plot on the left (middle), shows the SR (SVLO) band structure along the path including the high symmetry points U (0.823,0.339, 0.339), Z (0.5,0.5,0.5), F (0.5,0.5,0.0), L (0.5,0.0,0.0), and Γ. The coordinates of the points A, B, C, and D are given in the text. The panel on the right zooms into the region of the band edges and shows the direct (indirect) band gap computed with p ($p_{1/2}$). The zero energy is at the center of the band gap.

not discussed, since the effects of Dirac-type LO were found to be negligible.

Xe

In Xenon, the Dirac-type LO turn out to be significant for the SOC splitting, which increases by 0.1 eV. In contrast, their effect on the energy gap is negligible (see Fig. 6.3). All the analyzed quantities reach the targeted precision with a few empty states in addition to the LO basis functions (in this case, they are only 12 more with respect to the p-set). The convergence behavior of the energy gap and the SOC splitting is comparable to that of the SVLO method with SR LO. However, in contrast to the p-set, where convergence within 10^{-6} eV/atom can be reached, the $p_{1/2}$-set only reaches values of $\sim 10^{-4}$ eV/atom. We attribute this finding to the different species files used.

PbI$_2$

For this material, $p_{1/2}$-type LO are crucial for an accurate description of the electronic structure. Here four of them have been added for each species, for a total of 36 LO basis functions (see Table 6.2). They reduce the energy gap by 0.26 eV and increase δ^1_{SOC} by 0.20 eV and δ^2_{SOC} by 0.05 eV. The convergence behavior with $p_{1/2}$-type LO is overall comparable to that with SR LO. Note that the two curves appear to be shifted by these 36 additional basis functions. Although this number is considerable for such a system,

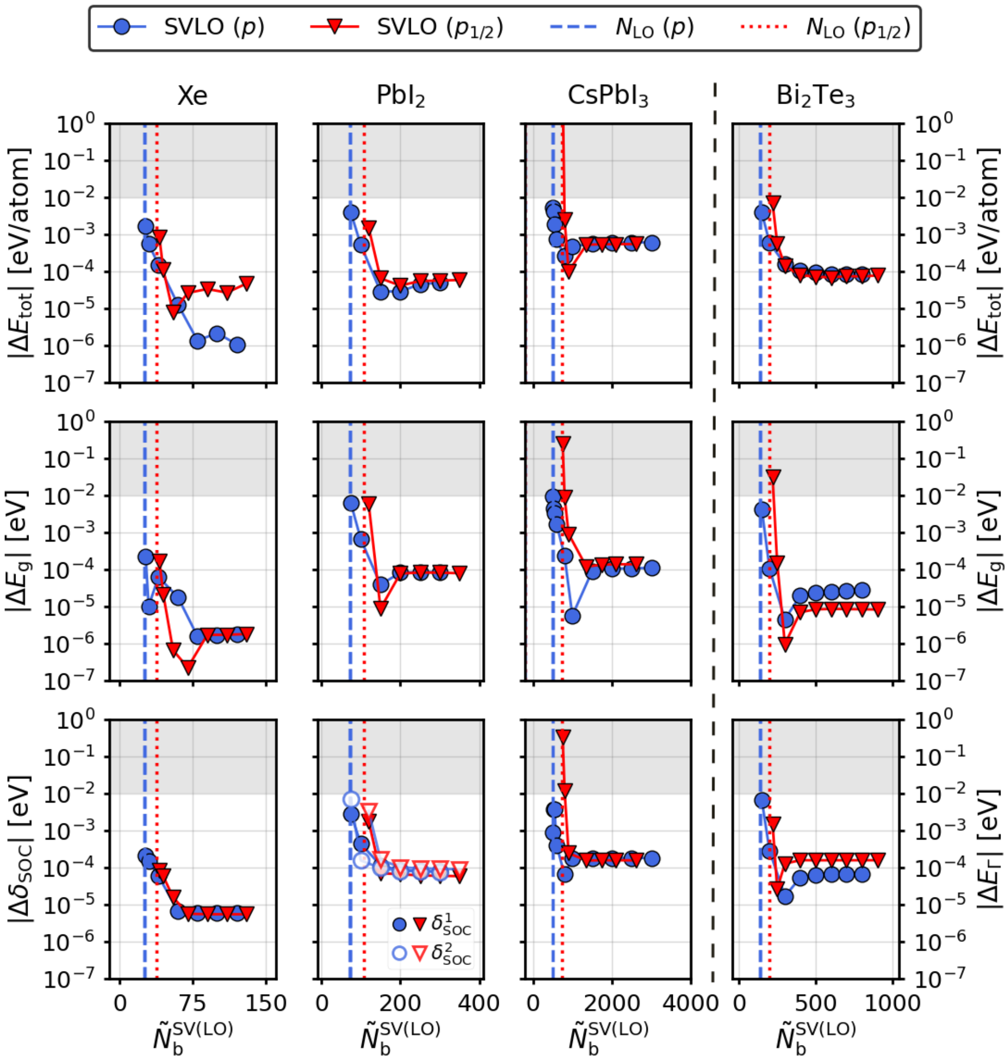

Figure 6.10: Comparison between the convergence behavior of the SVLO method when employing the p-set (blue symbols) and the $p_{1/2}$-set (red symbols) of LO. The figure utilizes the same design as Fig. 6.2. The values used to generate the plots are collected in Tables C.1-C.5.

the method behaves the same and is highly efficient compared to SV.

CsPbI$_3$

As expected, also in CsPbI$_3$, Dirac-type LO are essential to describe the SOC effects properly. Adding a total of 240 LO reduces the gap by 0.27 eV and increases the SOC splitting by 0.05 eV (Fig. 6.7). In terms of computational resources, the additional number of LO is a tiny overhead for the system size (i.e. 3236 APW and 736 LO functions). The convergence behavior of the SVLO method with SR and Dirac-type LO is comparable.

$\mathbf{Bi_2Te_3}$

While in the examples discussed above, the Dirac-type LO cause rigid shifts of some bands, in Bi_2Te_3 their inclusion leads to major changes in the whole band structure (see Fig. 6.9). By adding the $p_{1/2}$-type LO for a total of 60 basis functions, the gap becomes indirect and reduces to 0.03 eV. In the right panel of Fig. 6.9, one can observe that the VB is lowered at B and raised at D=(0.52, 0.35, 0.35), which is the new VBM location. The CB is not altered at B but is lowered at C=(0.65, 0.54, 0.54). This is the approximate location of the CBm. Note that the resolution is limited by the $48{\times}48{\times}48$ $\boldsymbol{k}$-mesh. Points C and D are six-fold degenerate. D is located between Γ and A=(0.64, 0.43, 0.43), the latter being located on the path between Z and U (Fig. 6.8). C and B are near Z → F. The band gaps obtained by Larson [245] and Huang and coworkers [244] when including $p_{1/2}$-type LO are 0.05 eV and 0.07 eV, respectively. The position of the band extrema differs slightly between the three works; ours agrees better with that of Larson [245]. One thing that does not change with the addition of Dirac-type LO is the hump at Γ that appears when SOC is included. This feature is a consequence of the band-inversion characteristic of Bi_2Te_3[239, 242]. Interestingly, unlike similar topological insulators, the hump is maintained in spinor *GW* calculations, even those that include the off-diagonal elements of the self-energy, although the band dispersion is strongly altered [189]. Again, the convergence behavior is comparable to that of the SVLO method with SR LO.

6.6 Related topics

As mentioned above, the large number of unoccupied states needed in the SV procedure also limits the performance of calculations that use DFT results as a starting point. In the context of hybrid functionals and G_0W_0, the problem arises when the NL quantities require a number of occupied states that is much smaller than the number of unoccupied states essential for the SV step. This computational overhead did not hamper the calculations for the materials studied in this thesis.

The case of BSE is different. As part of this work, we tested the implementation of BSE with SOC, in order to use it for the calculation of optical spectra of HaP. The tests performed on MoS_2 are shown in Appendix C.2.1 and show an enormous rise in computational time when SOC is considered, which gets notably worse as the number of unoccupied states increases. Since only a few empty states are necessary to accurately compute SOC effects in TMDC, such calculations are still feasible [231]. This is currently not the case for HaP. These tests also serve as a starting point for extending the SVLO method to the BSE. The Appendix C.3 contains more information about the current status of the extension of the SVLO in BSE.

6.7 Conclusions

The results presented in this chapter show that the SVLO method in combination with Dirac-type LO, allows us to obtain fast convergence and highly precise results, e.g. band gaps on the order of 10^{-4} eV or even better. Band energies and total energies can be obtained within a target precision of 10^{-2} eV or 10^{-2} eV/atom, respectively, with a number of basis functions that is comparable to the number of occupied states plus the LO functions. The use of the SVLO method is most efficient when the SOC effects are strong. In these cases, the contributions of $p_{1/2}$-type LO are also found to be significant. The overall gain of our method becomes more pronounced as the system size increases. This work contributes to obtaining highly accurate electronic properties at the DFT level, which can also be used as a starting point for higher-level methods.

Note that the work discussed in Chapters 6 and part of the work in 7) was carried out prior to the implementation of the SVLO method and the Dirac-type LO. For this reason, these parts and also Ref. [208] do not use them. Furthermore, the method is not yet implemented for ground-state calculations with hybrid functionals and G_0W_0 calculations. Such enhancements would be essential to obtain accurate results for many materials, including HaP.

PART III

APPLICATIONS

CHAPTER 7

Electronic structure of 3D lead-iodide perovskites: impact of functionals

In this chapter, we present the work on 3D HaP, which has been published in Ref. [35]. The goal is to find the best methodology, in terms of accuracy and computational effort, for calculating the energy gaps of 3D lead-iodide perovskite compounds. The hybrid functionals PBE0 and HSE are at the center of the investigation. Emphasis is placed on tuning methods to determine their optimal parameters and on their performance as starting points for G_0W_0 calculations. SOC effects are considered. An extensive study is carried out on PbI_2, which is the precursor of lead-iodide perovskites. HSE tuned with the *density-based mixing method* is found to be the most suitable choice to obtain energy gaps comparable with one-shot *GW* results. In the absence of tuning methods, HSE proved to be a good starting point for these calculations. The results obtained for PbI_2 are shown to be transferable to $CsPbI_3$, and the same behavior is expected for the entire family of 3D lead-iodide perovskites. The discussion closely follows that in Ref. [35].

7.1 Introduction

The complexity of HaP (see Chapter 1) raises the need to find accurate yet computationally efficient computational approaches with high predictive power. The lack of predictive power in the calculation of the band gap of PbI_2 is highlighted in Fig. 7.1. The

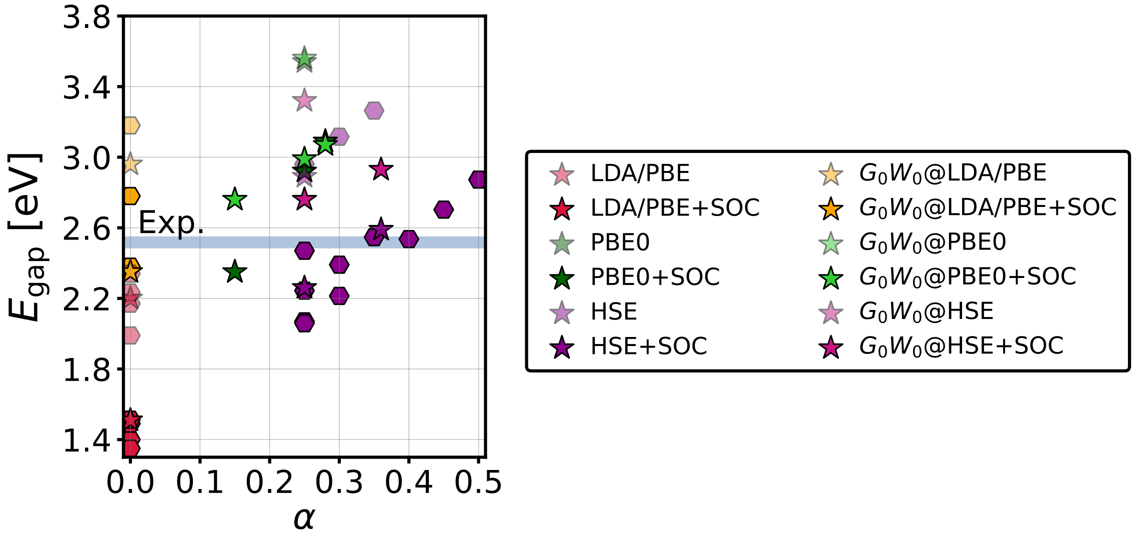

Figure 7.1: Energy gaps of PbI_2 computed with different methodologies, plotted as a function of the mixing parameter α. The results include calculations performed with semi-local and hybrid functionals as well as G_0W_0 calculations with different starting points. The darker symbols indicate the inclusion of SOC effects. The light blue region indicates the range of experimental values (Refs. [246, 247]). The **`exciting`** results are marked with stars, and the others are collected from the literature [248, 249, 250, 251, 252, 253, 254]. See Fig. D.1 for more details about the references.

collected values, which include values from literature [248, 249, 250, 251, 252, 253, 254] as well as our calculations, are spread over a ~ 2 eV range that is far from being acceptable. The collection includes results that consider SOC, which significantly lowers the gap [255]. The calculations performed with LDA and PBE underestimate the gap by ~ 1 eV when SOC is included. On the x-axis is the mixing parameter α of the hybrid functionals PBE0 and HSE. For these methods, as well as for the G_0W_0 results, several points are within the experimental region or only a few ten meV above or below. A similar scenario is expected for HaP.

In the context of finding a reliable method for calculating the electronic structure of HaP, there are other works in the literature. Among them, some use HSE [256, 257] or explore methods to tune the parameters of the hybrid functionals [258, 259]. Others utilize the more expensive GWA [260, 261, 38, 36]. Here, we aim to provide insight into the performance of different methods, e.g. DFT and G_0W_0, and determine an *ab initio* procedure to accurately compute the band gaps of lead-iodide perovskites and their precursor PbI_2. In particular, we apply the *ab initio* DDH and DM methods (Section 2.2.3.3), to find an optimal and transferable mixing parameter α for the two functionals. Furthermore, we investigate the dependence of G_0W_0 on different parameterizations used for the DFT starting points. PbI_2 is used as a testbed for the most expensive calculations. An important aspect of this study is the transferability of the methods from PbI_2 to the perovskite systems.

The computational details are given in Appendix D.2. All input and output files are available in the NOMAD Repository [222] and can be downloaded from the following link `https://doi.org/10.17172/NOMAD/2021.10.26-1`.

7.2 Systems under investigation

Among the systems studied are $CsPbI_3$ in its orthorhombic (γ-phase) and cubic (α-phase) phases, cubic $MAPbI_3$ (α-phase), and bulk PbI_2 (Fig. 7.2). The symmetry groups of γ-$CsPbI_3$ and PbI_2 are Pnma and P-3m1 (also listed in Table 6.1), that of α-$CsPbI_3$ and α-$MAPbI_3$ is Pm-3m. These four materials can be used to study various aspects, such as the role of the organic/inorganic cation and that of the crystalline structure. Overall, it is known that the states in the proximity of the band gap come from the Pb and I ions [262], while the cation has only an indirect influence on them, mainly stabilizing the crystalline structure [9]. This justifies the use of the precursor PbI_2 as a testbed. In addition, it is known that the higher symmetry of the α-phase (high temperature phase) of HaP is obtained as the average of the octahedral tilts. Therefore, for a good theoretical description without the explicit consideration of dynamical effects, it is convenient to consider the less symmetric γ-phase for comparison with experimental data [263, 220]. The α-$CsPbI_3$ and α-$MAPbI_3$ are only used to investigate the effects of the crystal symmetry and the A-cation (i.e. Cs or MA). For simplicity, we will refer to the group of perovskite systems investigated as $APbI_3$.

7.3 Results and discussion

7.3.1 Electronic structure of $APbI_3$ and PbI_2

In this section, the electronic structure of $APbI_3$ and PbI_2 is investigated using DFT and G_0W_0 for the default hybrid functional parameters ($\alpha = 0.25$ and $\omega = 0.11\ a_0^{-1}$).

PBE results and SOC effects

In Table 7.1, the fundamental band gaps computed with PBE and PBE+SOC are given. As

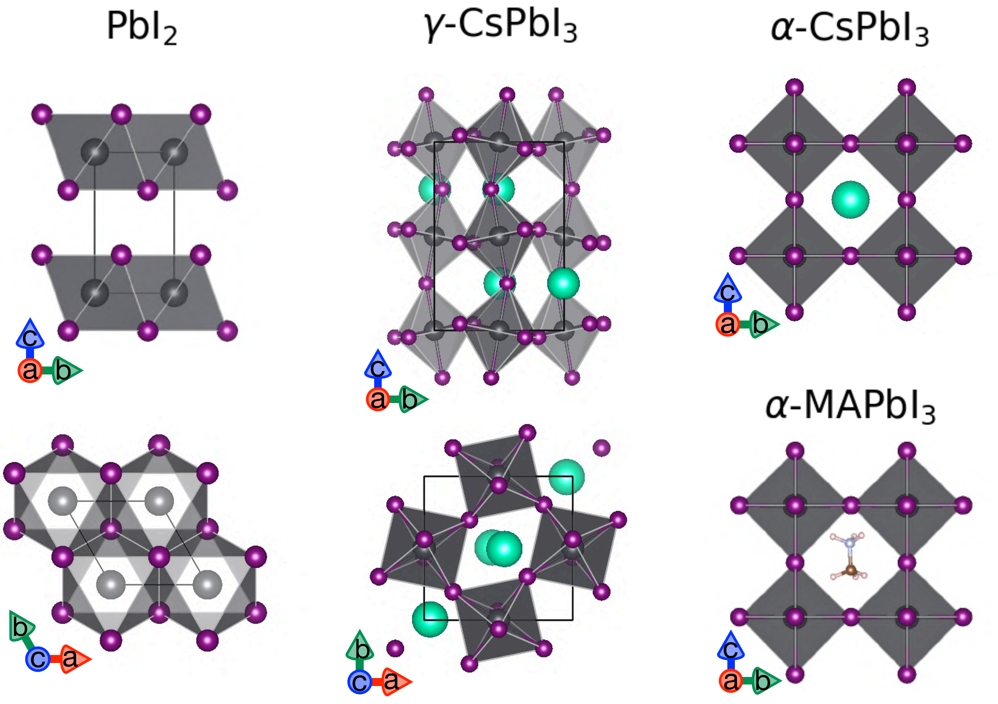

Figure 7.2: Unit cells of PbI_2, γ-$CsPbI_3$, α-$CsPbI_3$ and α-$MAPbI_3$. Note that two orientations are shown for PbI_2 and γ-$CsPbI_3$.

discussed in Chapter 6, PbI_2 and γ-$CsPbI_3$ have massive SOC effects. Due to the presence of lead and iodine, the same is expected for α-$CsPbI_3$ and α-$MAPbI_3$. Indeed, the band gap reduction due to SOC ranges from 0.69 eV in PbI_2 to 1.13 eV in α-$CsPbI_3$.

At the time of performing these calculations, the Dirac-type LO were not yet implemented in the **`exciting`** code and are therefore not included here. They have characteristics that cannot be reproduced by SR LO. In addition, without their inclusion, the LO sets cannot reach full convergence, and thus the PBE+SOC values in Table 7.1 differ from those in Table 6.3, even from those considering only SR LO. Note that they are obtained with different species files. In the present case, the values are much closer to the $p_{1/2}$ results: The gaps of PbI_2 and γ-$CsPbI_3$ are 110 meV and 80 meV larger, respectively. In Table 6.3, the difference between the p and $p_{1/2}$ sets was 260 meV and 270 meV for PbI_2 and γ-$CsPbI_3$, respectively. The better agreement observed here is partly due to the treatment of the semi-core states as core states, for which the 4-component Dirac equation is solved, whereas in the p-set of Table 6.3 some of the semi-core states were treated as valence states.

Table 7.1: Band gaps in eV of PbI_2, γ-$CsPbI_3$, α-$CsPbI_3$, and α-$MAPbI_3$, calculated with different functionals and G_0W_0 with different starting points. Results include calculations with and without SOC.

	PbI_2	γ-$CsPbI_3$	α-$CsPbI_3$	α-$MAPbI_3$
Exp.	$2.55^{a)}$, $2.485^{b)}$	$1.73^{c)}$,$1.67^{d)}$	-	$1.69^{e)}$
PBE	2.20	1.58	1.31	1.35
PBE+SOC	1.51	0.63	0.18	0.28
PBE0	3.54	2.75	2.32	-
PBE0+SOC	2.92	1.86	1.27	-
HSE	2.89	2.13	1.75	-
HSE+SOC	2.26	1.25	0.70	-
G_0W_0@PBE	2.96	2.17	1.98	-
G_0W_0@PBE+SOC	2.35	1.32	0.94	-
G_0W_0@PBE0	3.56	2.84	-	-
G_0W_0@PBE0+SOC	2.99	1.99	-	-
G_0W_0@HSE	3.32	2.54	-	-
G_0W_0@HSE+SOC	2.76	1.72	-	-

$^{a)}$ Ref. [246] $^{b)}$ Ref. [247] $^{c)}$ Refs. [264, 265] $^{d)}$ Ref. [266] $^{e)}$ Ref. [267]

The band gaps collected in Table 7.1 clearly show their sensitivity to the crystal symmetry, and thus to the octahedral tilts. Indeed, the band gap of γ-$CsPbI_3$ with (without) SOC is 0.45 eV (0.27 eV) larger than that of α-$CsPbI_3$, while that of α-$MAPbI_3$ is only 0.10 eV (0.04 eV) larger. Considering that there is a difference of ~0.01 Å between the Pb-I bond in the α-$CsPbI_3$ and α-$MAPbI_3$ structures, these results also show that the cation (Cs^+ or MA) has a less critical effect on the gap.

The band structures of the four systems are shown in Fig. 7.3. The minimal difference between the two cubic structures is also evident from the bands. Their energy gap is located at R, and the CBm (disregarding spin), which is triple degenerate, splits into a single and a double degenerate state when SOC is considered. Also in $CsPbI_3$ the CBm splits, resulting in the reduction of the gap. Instead in PbI_2, as discussed in Chapter 6, the splitting occurs in the second empty band. In the γ-phase, SOC is also responsible for modifying the order of the unoccupied states at Γ. These results confirm that SOC is of critical importance. Because of this, SOC is always considered in the following discussion, unless otherwise specified.

In the atom-resolved DOS in Fig. 7.4 it can be observed that in all four materials, the VBM is dominated by iodine states and the CBm mainly by lead states, with iodine also contributing significantly. In addition, the contributions of the organic/inorganic cations

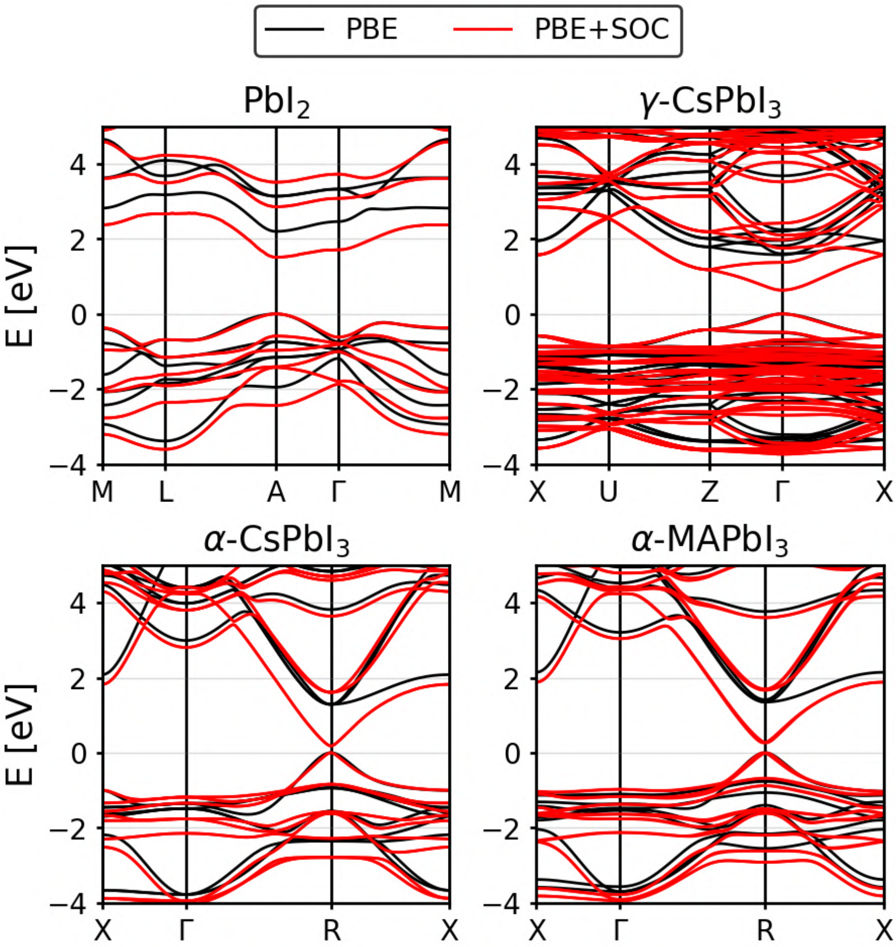

Figure 7.3: Band structures PbI_2 (upper left), γ-$CsPbI_3$ (upper right), α-$CsPbI_3$ (lower left) and α-$MAPbI_3$, plotted along selected high-symmetry paths. The black lines correspond to PBE and the red lines to PBE+SOC calculations. The zero energy matches the VBM.

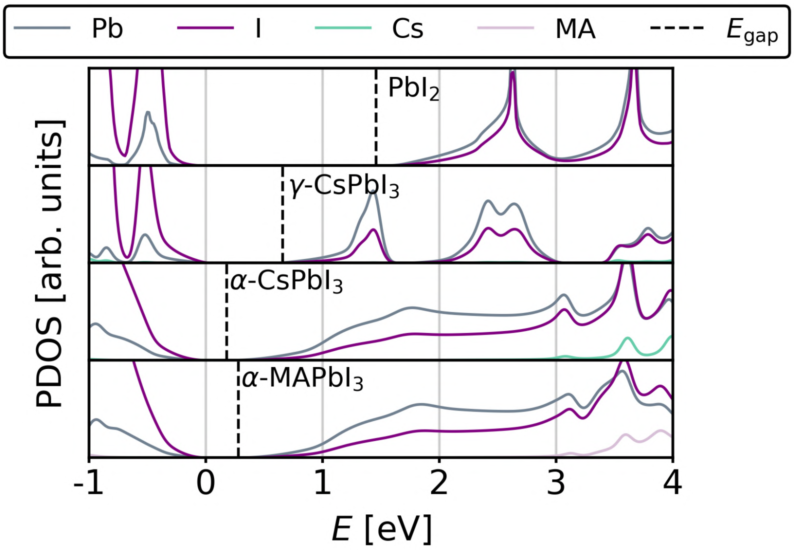

Figure 7.4: Atom-resolved density of states of the four systems computed with PBE+SOC. In the case of α-$MAPbI_3$, the DOS is resolved for the entire MA molecule. The VBM are aligned at 0 eV and the vertical dashed lines indicate the band gap.

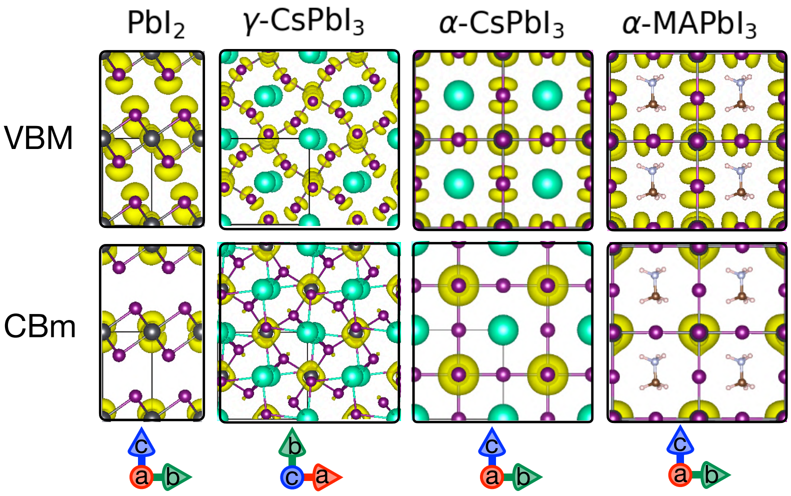

Figure 7.5: KS states of the four materials at the VBM and CBm.

are located in regions far from the gap. The KS wave functions in Fig. 7.5 confirm that the main contribution at the VBM (CBm) comes from iodine (lead) and have p-character. Note that in the CBm of the $APbI_3$ system, the orbitals do not display the typical p-orbital shape but rather that of relativistic $p_{1/2}$ states [268]. This is a consequence of the splitting due to SOC. As an additional proof of the p-character of the orbitals at the VBM and CBm, Fig. D.2 shows the orbital-resolved DOS. This analysis emphasizes a similar composition of the band-edge states in PbI_2 and $APbI_3$, which justifies the use of PbI_2 as a testbed for exploring different methodologies. Moreover, since the A cation has only little effect on the gap, that of $MAPbI_3$ is not evaluated by other methods.

Hybrid functionals and one-shot *GW*

Considering the gaps computed with PBE0, HSE, and G_0W_0 on top of different DFT starting points, i.e. PBE, PBE0, and HSE, it can be observed that the effect of SOC is massive with all methods (Table 7.1). The amount by which SOC lowers the gaps varies within 0.15 eV comparing all the methods. In particular, in PbI_2 the reduction ranges from 0.56 eV to 0.69 eV, in γ-$CsPbI_3$ from 0.82 eV to 0.95 eV and in α-$CsPbI_3$ from 1.04 eV to 1.13 eV.

The results for α-$CsPbI_3$ support the choice of using the γ-phase for comparison with experiment. Even using G_0W_0@PBE+SOC, the experimental gap is underestimated by a huge amount, i.e. 0.73 eV (44%). In the case of γ-$CsPbI_3$, the underestimation amounts to 0.35 eV (21%). Comparing all the methods in combination with SOC, G_0W_0@HSE is considered the best, with a value of 1.72 eV, which lies within the experimental range. Furthermore, PBE0 overestimates the gap by only 0.13 eV (7%), while HSE underestimates it by 0.42 eV (25%). G_0W_0@PBE0 overestimates it slightly more than PBE0, i.e. by 0.26 eV (15%).

For PbI_2, the gap of 2.35 eV obtained by G_0W_0@PBE is closest to experiment, thus underestimating the experimental gap by 0.135 eV (5%). HSE and G_0W_0@HSE also perform well with values that are only 0.225 eV (9%) too low and 0.21 eV (8%) too high, respectively. The overestimation of PBE0 amounts to 0.37 eV (14%). Again, the difference between PBE0 and G_0W_0@PBE0 is minimal, i.e. G_0W_0@PBE0 overestimates the gap by additional 0.07 eV. It should be emphasized that the comparison between experimental and calculated values is subject to some uncertainties due to, for example, the crystal structure, the presence of defects or thermal effects, and the SOC treatment. Moreover, the gap does not include the zero point renormalization energy due to electron-phonon coupling [269, 270]. Note that the focus of this work is also on the comparison between different computational methods. For example, from Fig. 7.6, where the energy gaps from Table 7.1 are plotted as a function α, it is clear that there is a similar trend in the two materials. These observations provide a first evidence of the transferability of the methods within the materials under investigation.

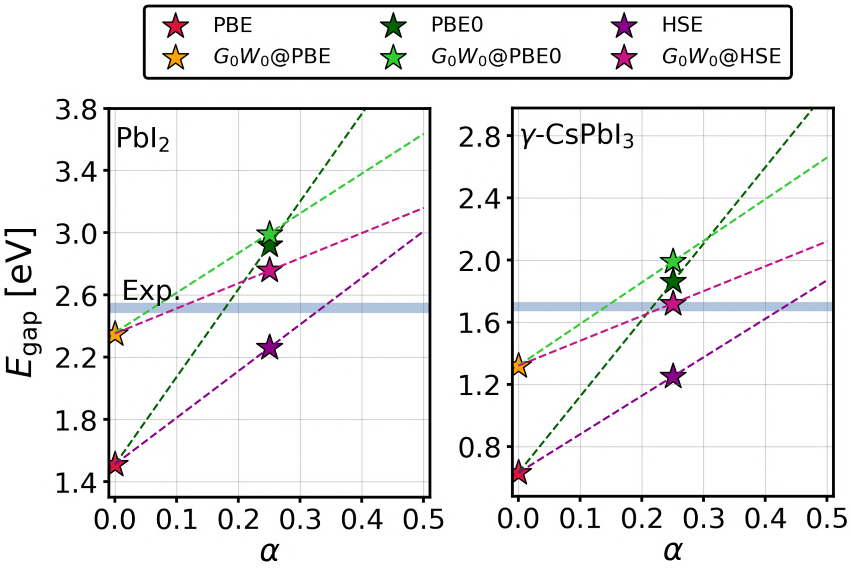

Figure 7.6: Energy gaps of PbI_2 (left) and γ-$CsPbI_3$ (right) evaluated with different methods and plotted as a function of α. The values are those from Table D.1 which include SOC. The dashed lines show the linear behavior of the gaps as α increases.

In summary, G_0W_0@HSE appears overall to perform well for both materials. However, it is computationally highly demanding, which leads us to explore methods to tune the parameters of PBE0 and HSE to avoid *GW* calculations on top.

7.3.2 Mixing parameters for PBE0 and HSE

This section is dedicated to the performance of the DDH and the DM methods for tuning the mixing parameters of PBE0 and HSE when applied to $APbI_3$ and PbI_2.

Dielectric dependent hybrid method

The key quantity of the DDH method is the electronic dielectric constant ε_∞. The RPA on top of PBE and including LFE gives a good estimate for this, as discussed in Section 2.2.3.3. For HaP and their precursors, where SOC effects are crucial for describing their electronic properties, it is important to investigate the effect of SOC also in the dielectric response. However, since RPA calculations with SOC are computationally highly demanding for complex materials such as HaP, we have mimicked the SOC effect with a scissors operator, taking the difference between the energy gaps obtained with PBE+SOC and PBE as the scissors shift. This may be seen as a rough approximation, since it only takes into account the closure of the gap without considering the other effects on the band structure. To justify the use of the scissors shift within the DDH method, we first test its validity within the IPA. In particular, we compare the dielectric constants, the mixing parameters obtained with the DDH method, and the corresponding band gaps obtained by PBE+SOC and PBE+scissors. The results are shown in Table 7.2. For PbI_2, the dielectric constants computed with the two starting points differ only by an amount small enough to lead to the same value for the optimized mixing parameter and thus for the energy gap. In the HaP, on the other hand, the use of a scissors shift leads to a larger change in the dielectric constant, but the differences in the mixing parameter α and in the energy gaps remain small for all the HaP, i.e., α being 0.01 larger when SOC is explicitly considered and the gap increases within 0.05 eV for both γ-$CsPbI_3$ and α-$CsPbI_3$. Thus, it can be concluded that the scissors operator is legitimate for the determination of the mixing parameter. Our analysis also shows that SOC is important for the DDH method: The gaps obtained using IPA@PBE are about 0.12-0.17 eV larger than that obtained using IPA@PBE+SOC.

For PbI_2, the energy gap obtained with PBE0-DDH, using RPA@PBE+scissors to evaluate the dielectric response, is equal to that computed with G_0W_0@PBE (5% lower than the experimental references) and thus improves over PBE0 (overestimation of 14%). Also for γ-$CsPbI_3$, the gap obtained with PBE0-DDH is comparable to that of G_0W_0@PBE, the difference being within 0.05 eV. In this case, however, PBE0 performs better, overestimating the gap by only 7%, while PBE0-DDH overestimates it by 18%.

Also in this case the effect of the cation on the dielectric response (RPA@PBE+scissors) and thus on the mixing parameter, is sufficiently small. Interestingly, the structure also has only a small effect on it, in fact the mixing parameter ranges from 0.12 for α-$CsPbI_3$ to 0.15 for PbI_2 and γ-$CsPbI_3$. Using the mixing parameter obtained for PbI_2, i.e. α=0.15, for the $APbI_3$ systems, it can be observed that there is no difference for γ-$CsPbI_3$, since PBE0-DDH leads to the same mixing parameter, while for α-$CsPbI_3$ the gap increases by only 0.13 eV compared to that obtained by applying PBE0-DDH (see Table 7.2). For α-$MAPbI_3$, an even smaller change of the gap is expected, since the obtained mixing parameter is closer to that of PbI_2.

Density-based mixing method

First, the effect of SOC on $\bar{g}$ is studied and found to be negligible (Table 7.3). This can be explained by the fact that the main effect of SOC is in the conduction bands.

Table 7.2: Dielectric constants, ε_∞, mixing parameters obtained by the DDH method ($\alpha = 1/\epsilon_\infty$), and corresponding PBE0 and GW@PBE0 gaps (in eV) obtained from different methods. The values marked by $^\perp$ are explicitly computed with the procedure described in Section D.2, all the other values result from the linear fits shown in Fig. D.3.

Material	Method	ε_∞	α	PBE0(α)	G_0W_0@PBE0(α)
PbI_2	IPA@PBE	7.31	0.14	2.30	2.71
	IPA@PBE+SOC	8.27	0.12	2.18	2.66
	IPA@PBE+scissors	8.46	0.12	2.18	2.66
	RPA@PBE	5.74	0.17	2.47	2.79
	RPA@PBE+scissors	6.88	0.15	$2.35^\perp$	$2.76^\perp$
γ-$CsPbI_3$	IPA@PBE	6.02	0.17	1.47	1.82
	IPA@PBE+SOC	7.10	0.14	1.32	1.73
	IPA@PBE+scissors	7.69	0.13	1.27	1.70
	RPA@PBE	5.13	0.19	1.56	1.88
	RPA@PBE+scissors	6.46	0.15	1.37	1.76
α-$CsPbI_3$	IPA@PBE	6.43	0.15	0.83	-
	IPA@PBE+SOC	9.07	0.11	0.66	-
	IPA@PBE+scissors	9.77	0.10	0.62	-
	RPA@PBE	5.57	0.18	0.96	-
	RPA@PBE+scissors	8.38	0.12	0.70	-
α-$MAPbI_3$	IPA@PBE	6.35	0.16	-	-
	IPA@PBE+SOC	8.23	0.12	-	-
	IPA@PBE+scissors	9.10	0.11	-	-
	RPA@PBE	5.48	0.18	-	-
	RPA@PBE+scissors	7.78	0.13	-	-

Overall, the $\bar{g}$ value varies within a range of 0.166 $a_0^{-1/2}$ for PbI_2 and 0.186 $a_0^{-1/2}$ for α-$MAPbI_3$. Using Eq. 2.34 (2.35) for computing the mixing parameter of PBE0 (HSE), leads to α ranging from 0.28 to 0.30 (from 0.36 to 0.38). Note that this time the organic/inorganic cation has a slightly larger influence on the mixing parameter than the crystal structure, i.e. the difference between α-$CsPbI_3$ and α-$MAPbI_3$ is larger than between α-$CsPbI_3$ and γ-$CsPbI_3$. The reason is that the organic/inorganic cation influences the electron density even when its states are far from the Fermi level. Still, the difference is small enough to conclude that the A cation does not have a major influence on the DM method. Moreover, the variation of the DM mixing parameters within the four materials is only 0.02, which translates into an error in the gap of up to about 0.1 eV when using the PbI_2 mixing parameters for the $APbI_3$ compounds.

Considering PbI_2 and γ-$CsPbI_3$, the DM method applied to PBE0 (PBE0-DM) leads to a

Table 7.3: The first row shows the value of $\bar{g}$ computed from the PBE or PBE+SOC (value in parenthesis) electron density. The rest of the table is divided into two parts. The first one shows the mixing parameters obtained with the PBE0-DM method and the corresponding DFT and G_0W_0 gaps in eV using PBE0. The second part shows the same for HSE. The band gap values marked by $^{\perp}$ are explicitly computed while the others are obtained from the linear fits shown in Fig. D.3.

	PbI$_2$	γ-CsPbI$_3$	α-CsPbI$_3$	α-MAPbI$_3$
$\bar{g}$ [a$_0^{-1/2}$]	1.166 (")	1.176 (")	1.168 (1.167)	1.187 (1.186)
$\alpha^{\mathrm{DM}}_{\mathrm{PBE0}}$	0.28	0.29	0.28	0.30
PBE0-DM	$3.09^{\perp}$	2.05	1.40	-
G_0W_0@PBE0-DM	$3.07^{\perp}$	2.09	-	-
$\alpha^{\mathrm{DM}}_{\mathrm{HSE}}$	0.36	0.37	0.36	0.38
HSE-DM	$2.59^{\perp}$	1.54	0.93	-
G_0W_0@PBE0-DM	$2.93^{\perp}$	1.91	-	-

larger overestimation of the gap compared to PBE0. This is expected since the PBE0-DM α value is larger than α=0.25 and PBE0 already overestimates the gap. In contrast, its combination with HSE (HSE-DM) improves over HSE for the gaps of both materials: The HSE-DM gap of PbI$_2$ is only 0.04 eV (1.6%) larger than the experimental counterpart. In the case of γ-CsPbI$_3$, the deviation from experiment is slightly larger (underestimation of 0.13 eV, i.e. 8%) but it is second only to G_0W_0@HSE (value lying in the experimental range) and is comparable to PBE0, which overestimates the experimental gap by the same amount.

To the best of our knowledge, the work in Ref. [35] is the first where the DM method was applied to HaP.

7.3.3 Screening parameter ω and G_0W_0 calculations

This section starts with the analysis of the impact of the HSE screening parameter ω on the band gap of PbI$_2$. To recall, HSE satisfies two limits: first, for ω=0, it coincides with PBE0, second, for $\omega \to \infty$ it becomes equivalent to PBE (see Eqs. 2.31 and 2.32). Moreover, regardless of the value of ω, for $\alpha \to 0$, PBE is recovered. This property is better seen in the left panel of Fig. 7.7, where the band gaps from Tables 7.1, 7.2, and 7.2, are plotted as a function of α. The figure also shows how the gap changes for values of ω going from 0 a_0^{-1} (PBE0) to 0.11 a_0^{-1} (HSE) for increasing values of α. The left panel of Fig. 7.8 displays the dependence of the gap on ω more explicitly, for selected values of α, i.e. 0.25 and those obtained by the DDH and DM methods. The α dependence gets less steep as ω increases. This is consistent with the definition of HSE, since for

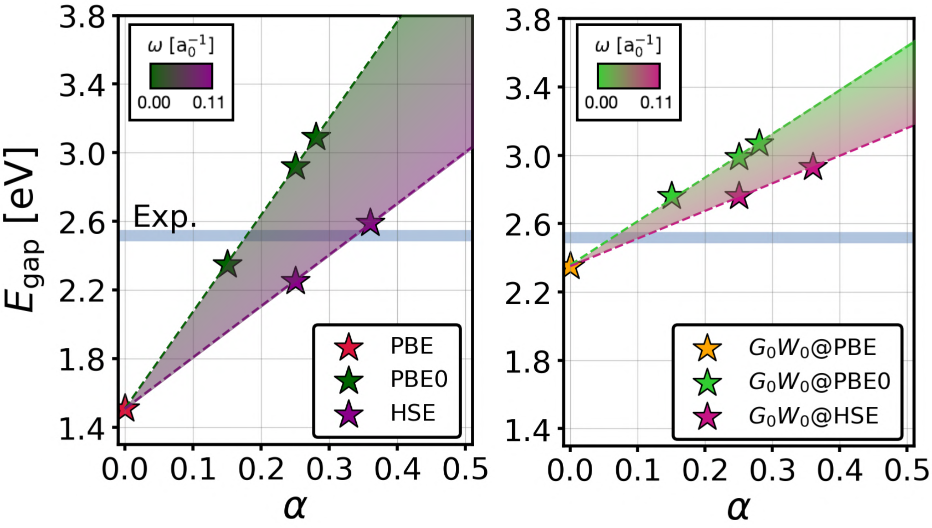

Figure 7.7: The left panel shows the PBE0 and HSE gaps plotted against α. The markers correspond to the values evaluated with the default mixing parameter, $\alpha = 0.25$ and those obtained with the DDH and DM methods. The area between the lines, showing the linear increase of the gap with α, illustrates the changes in the gap due to different screening parameters. The right panel displays the same for G_0W_0 using PBE0 and HSE as starting points.

infinite omega, all curves asymptotically approach the PBE value. By combining the results shown in Figs 7.7-7.8, we obtained the color map in the left panel of Fig. 7.9, which encodes the energy gaps as a function of α and ω. Note that the same band gap values can be obtained for different combinations of α and ω. In particular, to obtain the same gap, as α increases, ω should also increase.

In the right panel of Figs. 7.7, 7.8, and 7.9 the same analysis is performed, but for G_0W_0 using the DFT results on the left panels as a starting point. As expected, the changes in α and ω also affect the G_0W_0 gaps. In Fig. 7.7, where the gaps from Tables 7.1, 7.2, and 7.2 are plotted as a function of α, it can be observed that also at the G_0W_0 level the gap increases linearly with increasing α, but in a narrower range compared to PBE0 and HSE. Also for ω (Fig. 7.8) the trend is similar to that observed at the DFT level, but the range is smaller. In fact, in this case, for $\omega \to \infty$, the gaps should asymptotically approach the G_0W_0@PBE result, which is only 0.60 eV lower than that computed with G_0W_0@PBE0 (for $\alpha = 0.25$), while the difference between the gaps of PBE and PBE0 reaches 1.41 eV. The color map in Fig. 7.9 displays a trend similar to the one observed for the DFT results. However, while on the DFT side, the gap changes in a range between 1.2 and 4.4 eV, on the G_0W_0 side, it changes only between 2.2 and 3.8 eV. Nevertheless, the dependence on

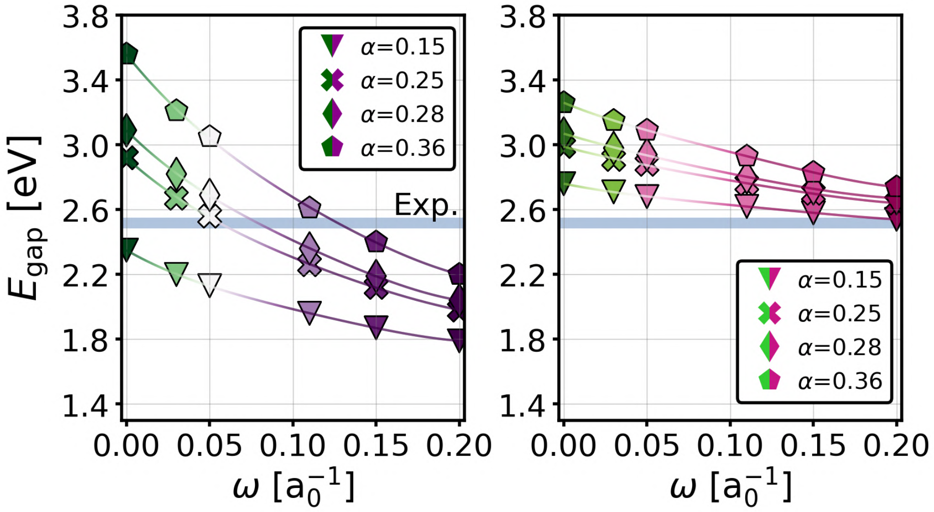

Figure 7.8: Band gap of PbI_2 evaluated with HSE (left panel) or G_0W_0@HSE (right panel) plotted as a function of *omega*, for selected α.

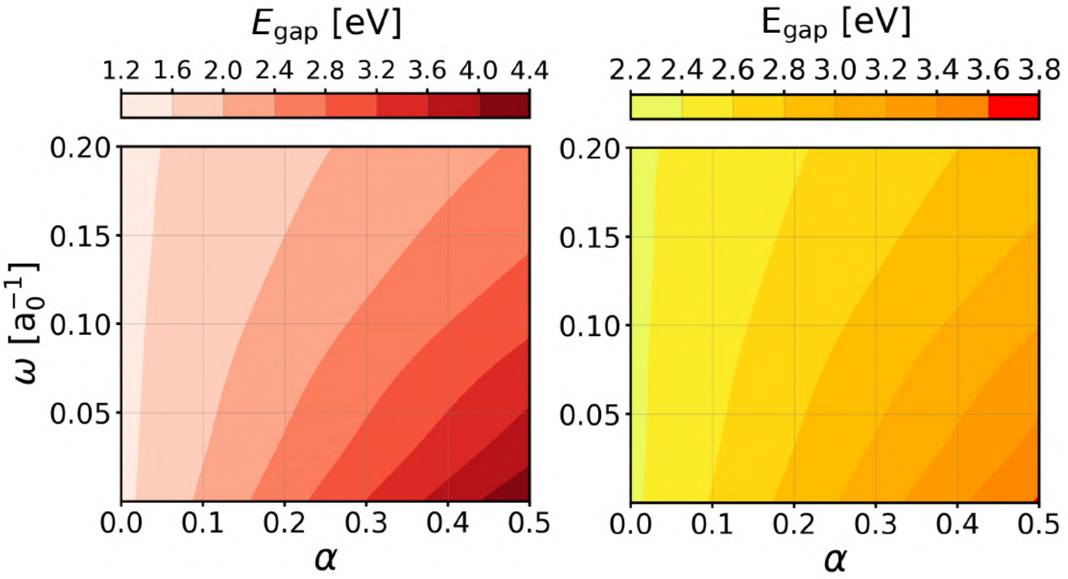

Figure 7.9: Color map visualizing the effect of the parameters α and ω on the band gap of PbI_2 at the DFT level (right panel) and the G_0W_0 level (left panel).

the parameterization of the DFT starting point is significant.

7.4 Conclusions

In this chapter, we have accomplished a systematic investigation of the performance of several methods within DFT and MBPT to compute the band gaps of PbI_2 and $APbI_3$. We have verified that the A cations have a minor influence on the band gap and that SOC effects are enormous. G_0W_0@HSE performs well for both PbI_2 and γ-$CsPbI_3$, but is computationally expensive. PBE0-DDH yields gaps that are comparable to those of G_0W_0@PBE, but for γ-$CsPbI_3$, the method is still far from the quality of G_0W_0@HSE. The HSE-DM method gives the best overall estimate of the energy gap, with a performance comparable to that of G_0W_0@HSE. It should be noted that the evaluation of α using $\bar{g}$ also presents certain challenges as discussed in Appendix B.2. For the four investigated materials, both DDH and DM lead to mixing parameters varying within 0.03. This result allows the use of the parameters tuned for PbI_2 for all the $APbI_3$ compounds within an error of 0.13 eV. This means that the atomic species Pb and I, which characterize the band gap region, also have larger effects on the screening parameter and on $\bar{g}$ than the crystalline structure and the (in)organic cation. This reflects the fact that the band gap region is dominated by p-Pb and p-I states, which also explains the analogous behavior of the method for PbI_2 and $APbI_3$. The dependence of the PbI_2 energy gap on α and ω shows that their impact is significant both at the DFT and at the G_0W_0 level. The results listed above suggest that the findings for this material can be transferred to the study of the other $APbI_3$ compounds. It would be interesting to verify whether the similarities between the methods observed for the 3D lead-iodide compounds and their precursor are also valid for the 2D systems, and whether the observed transferability would occur in HaP with different compositions.

PbI_2, as a small system with strong SOC effects, has proven to be a perfect material for testing and exploring different methodologies. In this respect, in Ref. [271], it was used as a test case to investigate how the spectral fingerprint can be used as a descriptor for the DOS [272] to measure how different functionals impact the results.

CHAPTER 8

Optoelectronic properties of 2D HaP evaluated by replacing the organic molecule with Cs

2D HaP with the formula $(RNH_3)_2(A)_{n-1}BX_{3n+1}$ can easily reach unit cells of the order of several hundred atoms due to the size of the spacer (RNH_3), the tilting of the octahedra, and the number of organic layers (n). Therefore, simulating these systems with high-accuracy methods can easily become computationally prohibitive. In 3D HaP, it is common to reduce the computational effort by focusing on purely inorganic compounds. In this chapter, we show that under certain conditions, also in 2D HaP, the electronic structure in the energy region around the band gap can be largely reproduced by purely inorganic systems. In particular, we show that this is the case when the BA molecule in BA_2PbI_4 is substituted by a Cs atom, if its position is carefully chosen. We start with the model system BA_2PbI_4, consisting of only 39 atoms. In this case, we also investigate to what extent the analogous Cs system can reproduce the optical properties of BA_2PbI_4. In the second part of this chapter, we apply the same procedure to compute the electronic structure and the effective masses of the two metastable phases of BA_2PbI_4 with the hybrid functional HSE, as published in Ref. [208]. This study proposes an approach to evaluate the opto-electronic properties of 2D HaP with reduced computational cost, enabling calculations with hybrid functionals. Furthermore, this approach can provide insight into the effects of different structural components, such as the type of organic spacer, the octahedra tilts, the distance between the inorganic layers and their number (n), on the electronic and optical properties of 2D HaP.

8.1 Introduction

As for 3D HaP, it is a common practice to employ purely inorganic systems, such as Cs_2PbI_4, to investigate the fundamental properties of the class of 2D HaP [40, 41, 42, 43, 44, 45, 46]. It is, however, less common to use structures with Cs substitution to investigate the properties of reference hybrid systems. An example in this direction is Ref. [273], where the effect of Pb-I layers on the electronic structure of the low-temperature (LT) phase of BA_2PbI_4 near the gap was investigated by substituting the BA molecule with Cs, placing it at the nitrogen position. In this work, no other possible positions were considered. Here, we focus on the role of the Cs position in the optoelectronic properties of the organic-inorganic compound. Moreover, we want to determine to which extent the reduced Cs system can mimic its counterpart.

This work is performed on the BA_2PbI_4 system, which is smaller than other typical 2D HaP. BA_2PbI_4 consists of a single layer of PbI_6 octahedra separated by butylammonium ($BA{=}C_4H_9NH_3^+$) as shown in Fig. 8.1. BA is a polar ionic molecule consisting of a hydrocarbon chain of four single-bonded carbon atoms linked to the positively charged NH_3 group. The NH_3 group is located near the perovskite layer in the center of the cavity formed by four Pb-I octahedra. In nature, it exists in two meta-stable phases [274], both orthorhombic, which we will refer to as the LT and high-temperature (HT) phases. The phase transition is around 256-274 K [274]. With increasing temperature, the tilting of the octahedra decreases, and the orientation of the BA molecule changes [274]: Considering the parallelogram formed by the in-plane I atoms, the ammonium group is located near the obtuse angle of the parallelogram in the LT phase and near the acute angle in the HT phase. The optical band gaps of these materials are about 2.4-2.6 eV, and the exciton binding energies vary between 400 and 500 meV [208].

The chapter is structured in two parts. In the first part, the electronic and optical properties of artificial tetragonal phases of BA_2PbI_4 are investigated. The unit cell of these tetragonal structures contains only 39 atoms, while the real orthorhombic ones contains 156 atoms. Replacing BA with Cs reduces the unit cell to only 7 atoms. Due to this small size, this system is perfectly suited as a test case to investigate how and to what extent the system with Cs can imitate the properties of the BA_2PbI_4 system. In the second part, the same approach is used to investigate the electronic properties of the LT and HT phases of BA_2PbI_4. This work was done in collaboration with the groups of Prof. Alexey Chernikov, Prof. David A. Egger, and Prof. Henry J. Snaith within the priority program

SPP2196, supported by the German Research Foundation, and led to a publication [208]. The goal was to investigate the optical properties at the phase transition. Moreover, we wanted to understand from a theoretical point of view if the Wannier model [275] is valid for excitons in 2D HaP, and if there is a relationship between the total exciton mass and the exciton diffusion, as commonly expected.

All computational details are collected in Appendix E. The input and output files are published on the NOMAD Repository at the link `https://doi.org/10.17172/NOMAD/2025.01.11-2`.

8.2 Cs substitution in BA_2PbI_4 tetragonal phase

8.2.1 Properties of the tetragonal BA_2PbI_4 systems

Structure of the model systems The tetragonal BA_2PbI_4 system is used as test case to evaluate to what extent the substitution of the BA molecule with Cs can be considered a valid approximation. Two tetragonal structures were constructed for this study. Avogadro [276] was employed for the construction of the BA molecule. To build up the layered structure of non-tilted corner-sharing Pb-I octahedra, the layer distance was chosen to be equal to that of LT-BA_2PbI_4 ($d_{\text{layer}} = 13.117$ Å) [274]. To obtain the Pb-I distance, we optimized the experimental 3D α-$CsPbI_3$ structure [277] with FHI-aims [278, 279] employing the PBE functional. The so-determined Pb-I distance ($d_{I-Pb} = 3.189$ Å) was used for both the in-plane and the out-of-plane iodine atoms, i.e., iodine bound to a single Pb atom (Fig. 8.1). Then we inserted the BA molecules into the Pb-I skeleton and employed FHI-aims to optimize the structure of the hybrid system. During the relaxation, the inorganic part was kept fixed. The relaxation of the molecule was performed with different functionals. In particular, we used BLYP, which is often used for molecular systems, and PBE with the Tkatchenko and Scheffler van der Waals (VDW) correction [280], which is often employed for hybrid systems such as BA_2PbI_4. The two structures are shown in Fig. 8.1, where one can notice the different positions of the molecules. It can be seen from both the front and the top view that in the structure optimized with BLYP, the ammonium group is placed almost at the center of the cavity formed by the octahedra, and the C-N bond is oriented perpendicular to the inorganic layer. Conversely, in the structure resulting from PBE+VDW, the ammonium group is oriented towards the Pb atom, and the C-N bond is no longer oriented perpendicular to the inorganic layer. In the following, we will refer to the two structures as BA-BLYP and BA-PBE+VDW, respectively, to distinguish between them.

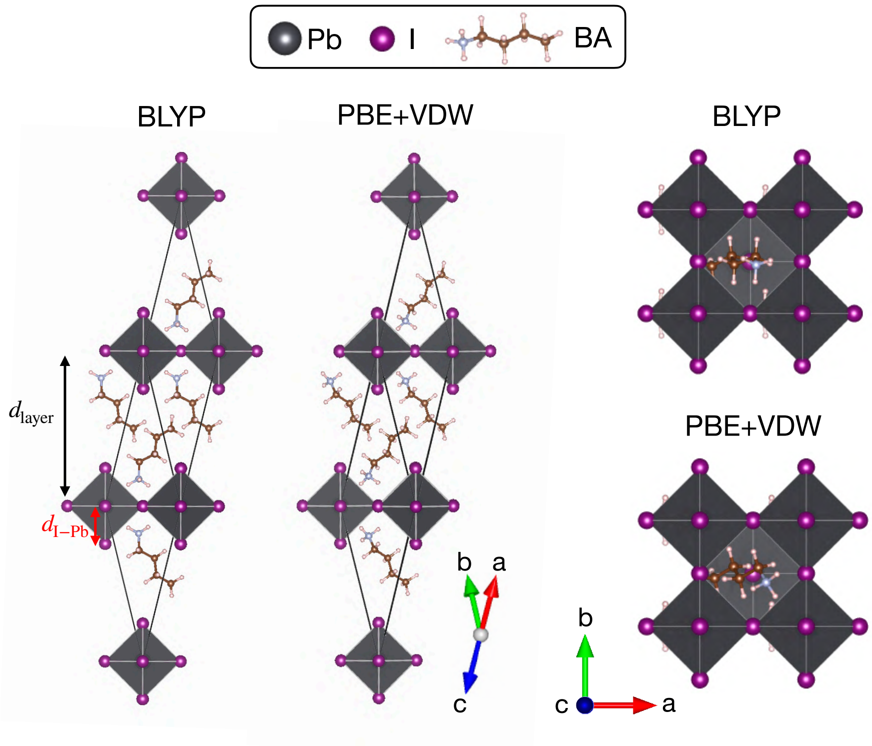

Figure 8.1: Geometries of the tetragonal BA_2PbI_4 structure as obtained by BLYP and PBE+VDW by relaxing the organic molecules (BLYP or PBE+VDW). In the left panels, the conventional primitive cells are displayed, and the system is oriented parallel to the layer of the Pb-I octahedra. The right panels show the top view, oriented perpendicular to the inorganic layer. Here, the 78-atom cells are shown for better visualization.

Electronic properties

The different orientations of the molecules also cause differences in the electronic structure, but as can be seen in Figs. 8.2 and 8.3, the overall picture remains the same. For example, both structures have a direct band gap at X and a weak dispersion along the X-P path, as a consequence of the quantum-well nature of this material [282, 46]. Moreover, both exhibit large SOC effects that reduce the energy gap by about 0.70-0.80 eV.

At the PBE level, the different orientations of the molecules lead to differences in the energy gap of only 0.05 eV (Table 8.1). On the other hand, the differences in the band dispersion are significant, especially for the highest VB: In the BA-BLYP structure, its energy between X and Γ (X and S) spans a range of $\Delta E^{\text{v}}_{\text{X}\Gamma} = -0.37$ eV ($\Delta E^{\text{v}}_{\text{XS}} = -0.21$ eV),

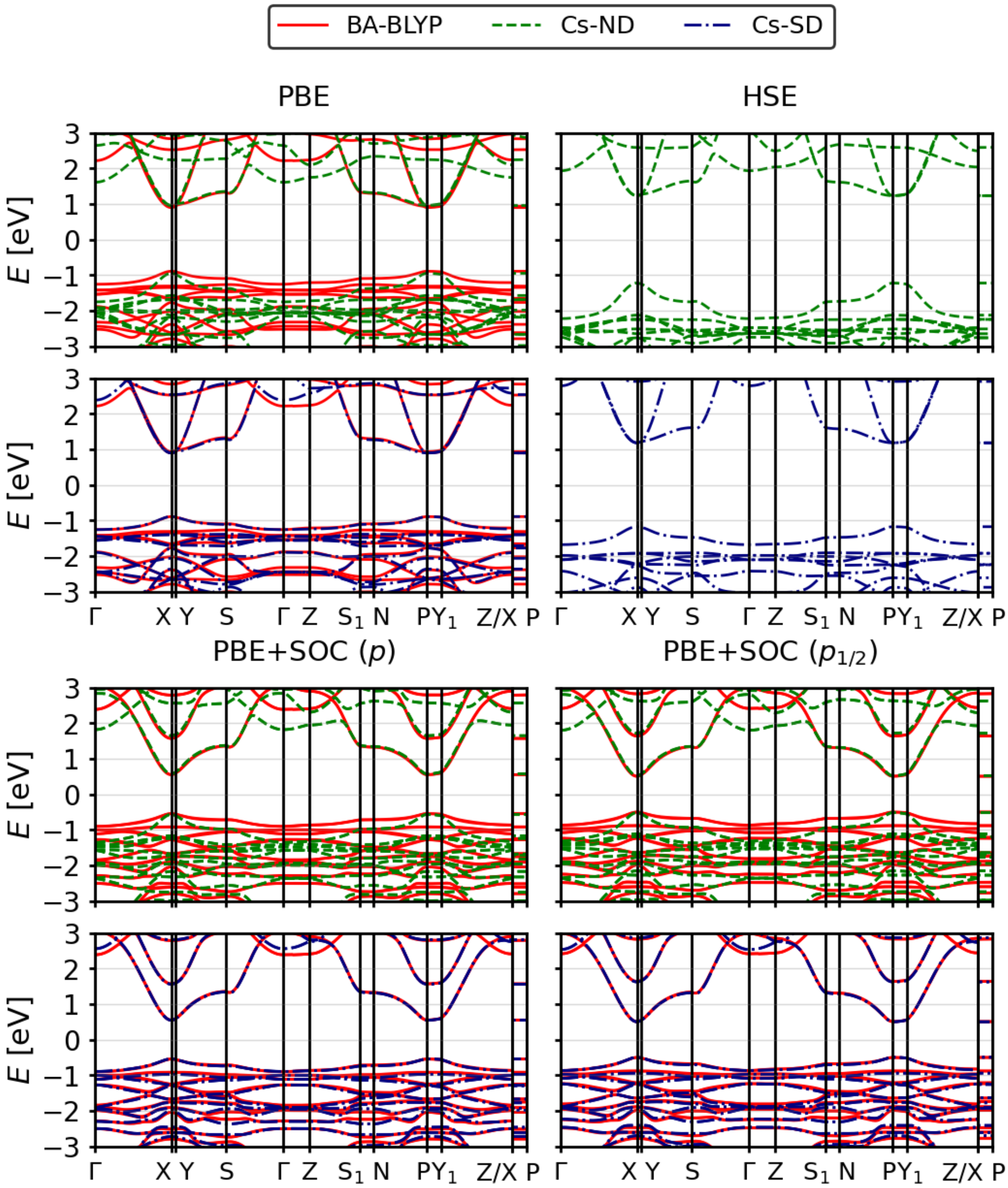

Figure 8.2: Band structure of the BA-BLYP geometry compared to two geometries where the BA molecule is replaced by Cs, i.e. Cs-ND (ND="no displacement") and Cs-SD (SD="straight displacement"). The Cs geometries are shown in Fig. 8.6. The bands are plotted along the standard reciprocal-space paths of the body-centered tetragonal structure [281] and are computed with different functionals (PBE and HSE) and excluding (top panels) and including SOC effects (bottom panels). The latter are distinguished by the type of LO sets used, i.e. the p-set in the left panels and the $p_{1/2}$-set in the right panels. The zero energy is aligned with the Fermi energy.

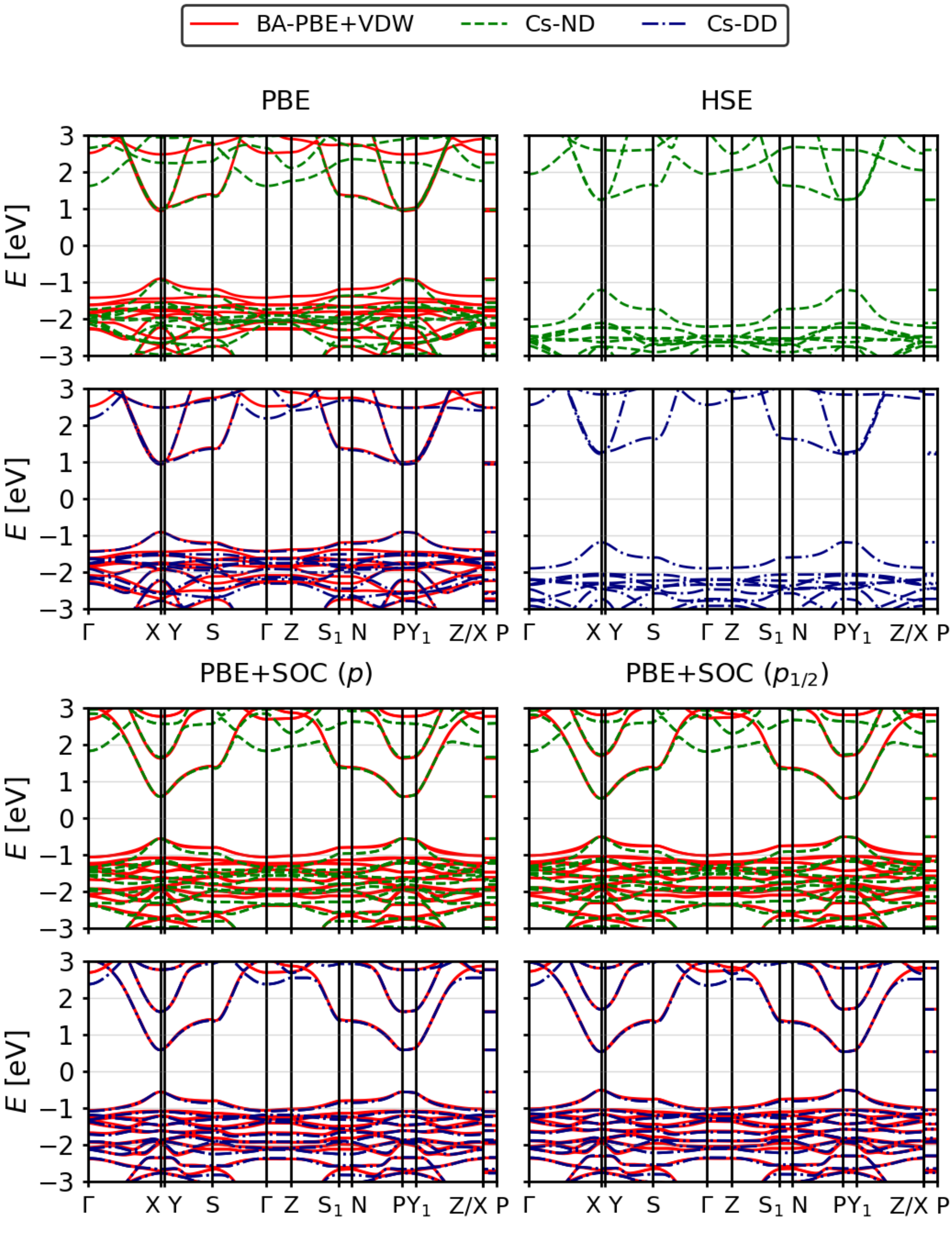

Figure 8.3: Band structure of the BA-PBE+VDW geometry compared with geometries where Cs replaces BA, i.e. Cs-ND and Cs-DD (DD="diagonal displacement"). As in Fig. 8.2, the bands are computed with different functionals and with and without SOC and, in the case of SOC, for two LO sets.

while in BA-PBE+VDW, this is $\Delta E^{\mathrm{v}}_{\mathrm{X}\Gamma} = -0.52$ eV ($\Delta E^{\mathrm{v}}_{\mathrm{XS}} = -0.29$ eV). This difference also shows up in the effective hole masses (Table 8.2), where the absolute value of the mean between $m_{h,\mathrm{X}\to\Gamma}$ and $m_{h,\mathrm{X}\to\mathrm{Y}}$ of the BA-BLYP geometry is 0.13 m_0 higher than that of the BA-PBE+VDW geometry. Concerning the lowest conduction band, below 2 eV, there is good agreement between the two structures, where the values for $\Delta E^{\mathrm{c}}_{\mathrm{XS}}$ differ by only 0.03 eV, and the effective electron masses m_e are essentially the same. Comparing instead $\Delta E^{\mathrm{c}}_{\mathrm{X}\Gamma}$, where the energy at Γ is above 2 eV, the difference between the two structure amounts to 0.26 eV. The reason is that the lowest CB at Γ has a dominant contribution from BA (Figure E.1). The two structures also exhibit differences in the DOS (Fig. 8.4): The peak in the BA-BLYP structure at -1.5 eV, while in the BA-PBE+VDW structure, it is broader and shows some splitting. The peak at 2.86 eV in the BA-BLYP geometry is shifted in the BA-PBE+VDW geometry by 0.16 eV towards lower energies and is slightly narrower.

A similar behavior is observed when considering SOC (both with SR and Dirac-type LO). Before taking a closer look at the SOC effects in the two systems, here we discuss the differences between the two sets of LO used. The differences between these results are relatively small, compared with the examples discussed in Chapter 6 for the systems containing Pb and I. For example, the energy gap of the BA-BLYP structure is 0.09 eV higher for the case without Dirca-type LO and is slightly higher (0.10 eV) in the case of the BA-PBE+VDW structure (Table 8.1). The energy differences $\Delta E^{\mathrm{v}}_{\mathrm{X}\Gamma}$ and $\Delta E^{\mathrm{v}}_{\mathrm{XS}}$ are comparable, while $\Delta E^{\mathrm{c}}_{\mathrm{X}\Gamma}$ and $\Delta E^{\mathrm{c}}_{\mathrm{XS}}$ vary within 0.07 eV, being larger when Dirac-type LO are used. The difference in the band structure is subtle on the energy scale considered. On the other hand, when looking at the DOS, which is sensitive to small differences in the electronic structure, a few differences stand out, especially in the peak height of the valence states. The differences in the effective masses are also negligible. The better agreement observed here is explained by the use of a different set of SR LO (the Dirac set is the same) than in Chapter 6. Here, there are no LO for semi-core states which are treated as core states. This better agreement suggests that $p_{1/2}$ LO are fundamental for the basis set for HaP systems.

The main effects of SOC are the reduction of the gap and the splitting of the CBm. Considering the calculations with the $p_{1/2}$ LO set, the energy gaps of the BA-BLYP and BA-PBE+VDW structures decrease by 0.78 eV and 0.80 eV, respectively (see Table 8.1), and the SOC splittings at X are 1.13 eV (BA-BLYP) and 1.16 eV (BA-PBE+VDW). Also $\Delta E^{\mathrm{c}}_{\mathrm{X}\Gamma}$

Table 8.1: Energy gaps (E_g), SOC splittings at X (δ_SOC), and energy differences between the highest VB and lowest CB at selected high-symmetry points (all in eV), i.e., $\Delta E^\mathrm{v}_\mathrm{X\Gamma}$ and $\Delta E^\mathrm{v}_\mathrm{XS}$ where v stands for valence ($\Delta E^\mathrm{c}_\mathrm{X\Gamma}$ and $\Delta E^\mathrm{c}_\mathrm{XS}$ where c stands for conduction). They are obtained by subtracting the eigenvalue at Γ or S from that at X, e.g., $\Delta E^\mathrm{v}_\mathrm{X\Gamma} = E^\mathrm{v}_\mathrm{X} - E^\mathrm{v}_\Gamma$. The results are shown for the five systems studied and for calculations performed with PBE and HSE, with and without SOC, and, in the case of SOC, for two LO sets.

Structure	E_g	δ_SOC	$\Delta E^\mathrm{v}_\mathrm{X\Gamma}$	$\Delta E^\mathrm{v}_\mathrm{XS}$	$\Delta E^\mathrm{c}_\mathrm{X\Gamma}$	$\Delta E^\mathrm{c}_\mathrm{XS}$
			PBE			
BA-BLYP	1.79	-	-0.37	-0.21	1.32	0.43
BA-PBE+VDW	1.84	-	-0.52	-0.29	1.58	0.46
Cs-ND	1.91	-	-0.80	-0.44	0.65	0.40
Cs-SD	1.79	-	-0.37	-0.22	1.49	0.40
Cs-DD	1.84	-	-0.53	-0.33	1.25	0.42
			PBE+SOC (p)			
BA-BLYP	1.09	1.02	-0.36	-0.17	1.84	0.80
BA-PBE+VDW	1.14	1.04	-0.50	-0.24	2.11	0.83
Cs-ND	1.14	1.08	-0.79	-0.42	1.25	0.80
Cs-SD	1.09	1.01	-0.35	-0.20	2.01	0.79
Cs-DD	1.14	1.04	-0.53	-0.30	1.79	0.80
			PBE+SOC ($p_{1/2}$)			
BA-BLYP	1.01	1.13	-0.37	-0.18	1.91	0.83
BA-PBE+VDW	1.04	1.16	-0.51	-0.25	2.19	0.86
Cs-ND	1.04	1.19	-0.80	-0.42	1.28	0.82
Cs-SD	1.00	1.12	-0.37	-0.21	2.03	0.82
Cs-DD	1.04	1.16	-0.54	-0.31	1.81	0.83
			HSE			
Cs-ND	2.45	-	-1.00	-0.53	0.70	0.42
Cs-SD	2.36	-	-0.51	-0.31	1.60	0.43
Cs-DD	2.40	-	-0.71	-0.42	1.34	0.45

Table 8.2: Effective hole (m_h) and electron masses (m_e) in m_0 along X → Γ and X → Y. The results are shown for all cases considered in Table 8.1.

Structure	$m_{\mathrm{h,X\to\Gamma}}$	$m_{\mathrm{h,X\to Y}}$	$m_{\mathrm{e,X\to\Gamma}}$	$m_{\mathrm{e,X\to Y}}$
PBE				
BA-BLYP	-0.37	-0.38	0.17	0.17
BA-PBE+VDW	-0.25	-0.25	0.17	0.16
Cs-ND	-0.20	-0.20	0.16	0.17
Cs-SD	-0.40	-0.39	0.17	0.17
Cs-DD	-0.26	-0.25	0.17	0.14
PBE+SOC (p)				
BA-BLYP	-0.38	-0.41	0.15	0.15
BA-PBE+VDW	-0.26	-0.28	0.15	0.15
Cs-ND	-0.18	-0.18	0.13	0.12
Cs-SD	-0.38	-0.38	0.14	0.14
Cs-DD	-0.24	-0.24	0.14	0.13
PBE+SOC ($p_{1/2}$)				
BA-BLYP	-0.37	-0.39	0.15	0.15
BA-PBE+VDW	-0.25	-0.27	0.14	0.15
Cs-ND	-0.17	-0.17	0.12	0.12
Cs-SD	-0.35	-0.34	0.13	0.13
Cs-DD	-0.23	-0.22	0.13	0.13
HSE				
Cs-ND	-0.21	-0.21	0.16	0.17
Cs-SD	-0.35	-0.35	0.17	0.18
Cs-DD	-0.26	-0.25	0.17	0.15

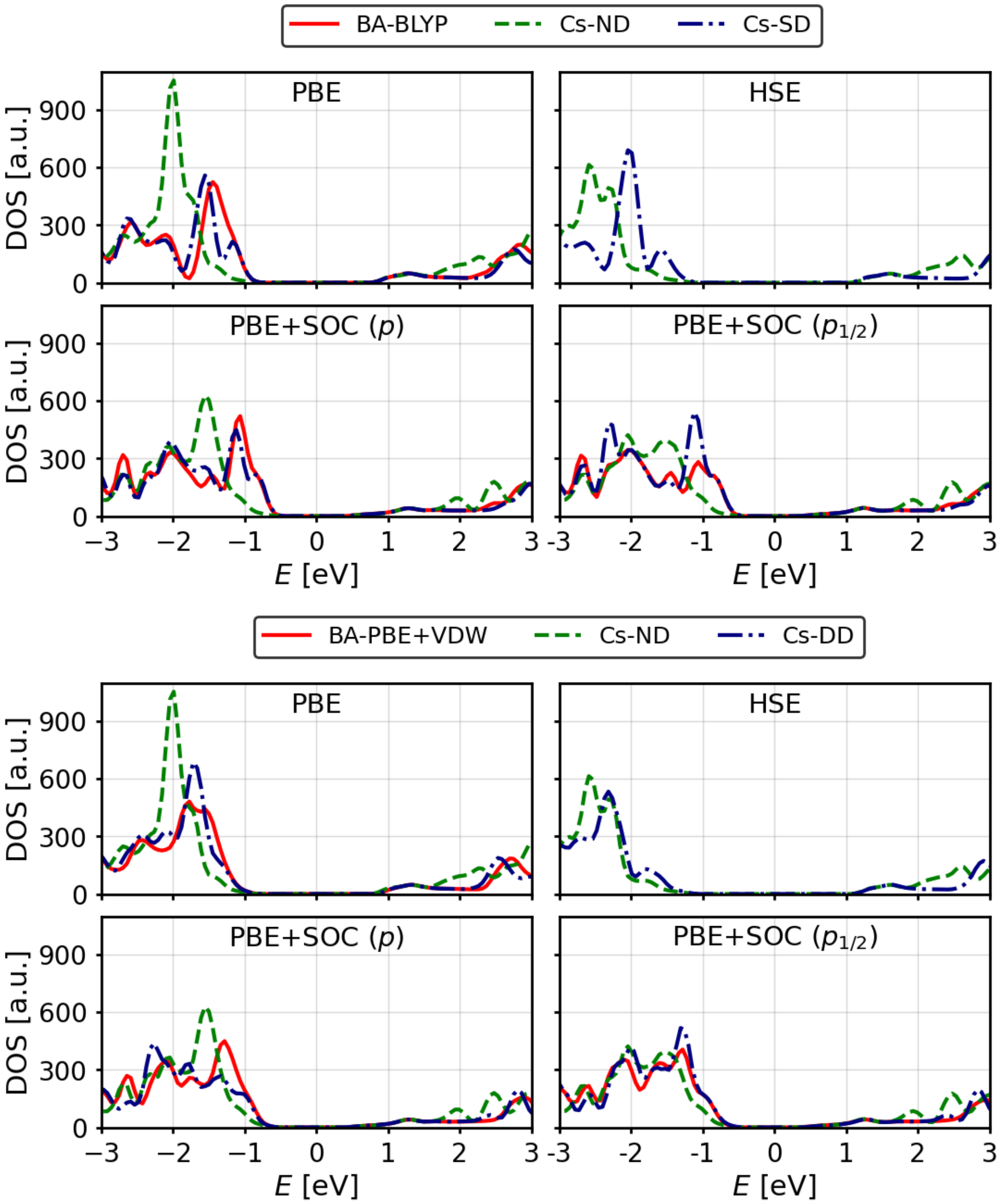

Figure 8.4: DOS of BA_2PbI_4 and Cs_2PbI_4, evaluated with different functionals (PBE and HSE) and with or without SOC effects. In the case of SOC, the DOS is shown for both the LO p-set (left panels) and the $p_{1/2}$-set (right panels). In the top panels, the DOS of the BA-BLYP system is compared with that of the Cs-ND and Cs-SD systems, while in the bottom panels, the comparison is made between the BA-PBE+VDW and the Cs-ND and Cs-DD systems. The Fermi energy is located at 0 eV.

and ΔE^c_{XS} show the large SOC effects on the conduction band: in both structures, $\Delta E^c_{\mathrm{X\Gamma}}$ increases by $\sim$ 0.60 eV and ΔE^c_{XS} by 0.40 eV. On the other hand, the differences in the effective masses are small (within 0.03 $\mathrm{m_0}$), even for the conduction band. Comparing the two structures, the difference in band gap decreases to 0.03 eV when SOC is taken into account. The major differences are found for $\Delta E^c_{\mathrm{X\Gamma}}$ and the dispersion of the highest VB, which is evident from the effective hole masses as well as from $\Delta E^v_{\mathrm{X\Gamma}}$ and ΔE^v_{XS}.

Optical properties

The differences between the two structures observed in the electronic properties are also reflected in the optical spectra computed within the IPA and shown in Fig. 8.5. Due to the organic spacer, the systems are not symmetric in the planes parallel to the octahedral layer, so the parallel component of the optical spectra ($\varepsilon_{\parallel}$) was obtained by computing the average of its two in-plane components. Overall, $\varepsilon_{\parallel}$ is characterized by two peaks, the first of which is of lower intensity. In the BA-BLYP structure, it has lower oscillator strength than that of the BA-PBE+VDW structure, and its maximum is red-shifted by 0.17 eV. The second peaks in the two structures are comparable in position and intensity. The perpendicular component ($\varepsilon_{\perp}$) is characterized by a small hump in front of the main peak. In the BA-BLYP geometry, this hump is more pronounced, and its maximum is at 2.55 eV, while in the BA-PBE+VDW geometry, it is at 2.75 eV. The shape of the main peak is broader in the BA-PBE+VDW structure, and the maximum is less high compared to the BA-BLYP case.

On the other hand, when comparing the dielectric constants (Table 8.3), the difference between the two systems is minimal: ϵ_{∞}, obtained by averaging the three components $\epsilon_{\infty,i}$, where $i = x, y$ or z, the two values are within 0.02. The difference in the individual components is slightly larger, i.e. within 0.07. While $\epsilon_{\infty,x}$ and $\epsilon_{\infty,y}$ of the BA-PBE+VDW geometry are larger than those of the BA-BLYP geometry, $\epsilon_{\infty,z}$ is smaller.

8.2.2 Tretagonal structure with Cs replacement

When replacing the BA molecule with Cs, it is important to put Cs close to the organic layer in order to neutralize its charge. Otherwise, the system becomes metallic [273]. In addition, since the BA-BLYP and BA-PBE+VDW structures have non-negligible differences in the optoelectronic properties, one can expect that the position of the Cs atom also influences the properties of the material. In the following, we will analyze three

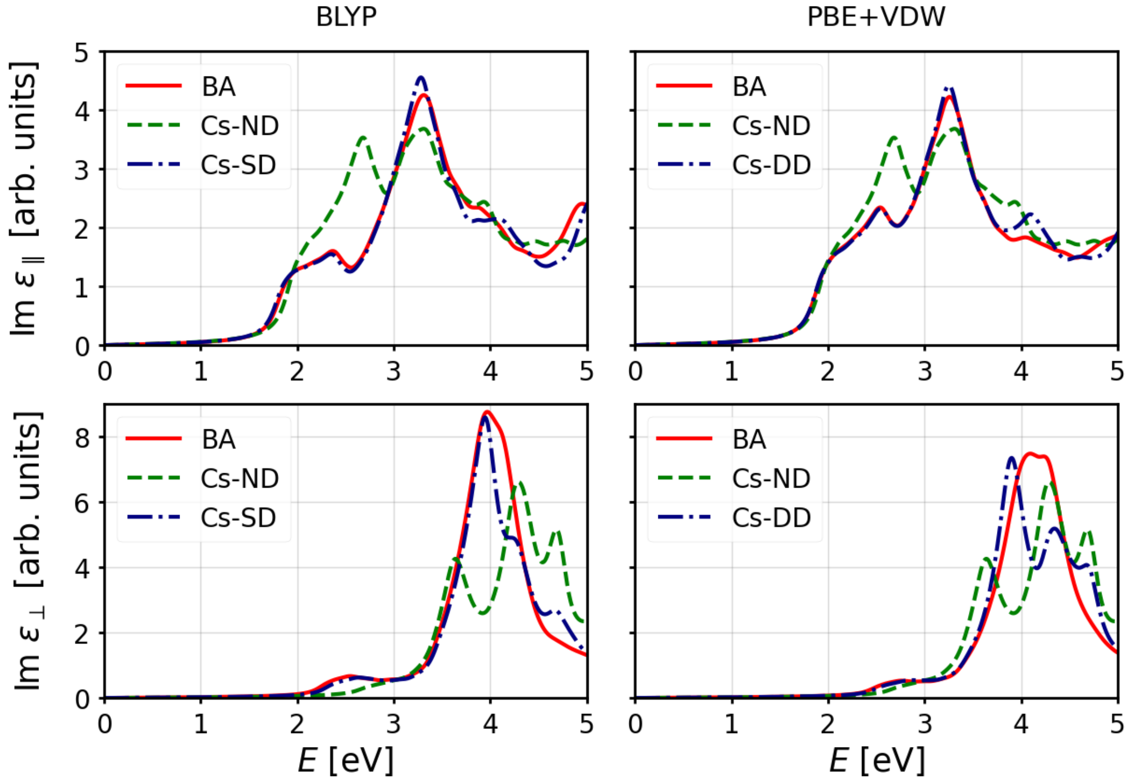

Figure 8.5: Parallel (top panels) and perpendicular (bottom panels) components of the imaginary part of the dielectric tensor of the tetragonal phase of BA_2PbI_4 and Cs_2PbI_4, computed with the IPA based on the PBE results. The left panels show the comparison between the spectra of the BA-BLYP, Cs-ND and Cs-SD structures, the right panels show the same for the BA-PBE+SOC, Cs-ND and Cs-DD structures.

Table 8.3: Dielectric constants at infinite frequency computed with the RPA, i.e. including local-field effects, based on the PBE electronic structure. ϵ_∞ is computed as the average of the three cartesian components.

Structure	$\varepsilon_{\infty,x}$	$\varepsilon_{\infty,y}$	$\varepsilon_{\infty,z}$	ε_∞
BA-BLYP	3.70	3.55	3.02	3.42
BA-PBE+VDW	3.75	3.62	2.95	3.44
Cs-ND	3.38	3.38	2.13	2.96
Cs-SD	3.25	3.25	2.04	2.85
Cs-DD	3.30	3.30	2.06	2.89

structures that differ in the Cs positions, which we have labeled ND for “no displacement”, SD for “straight displacement”, and DD for “diagonal displacement” (Fig. 8.6).

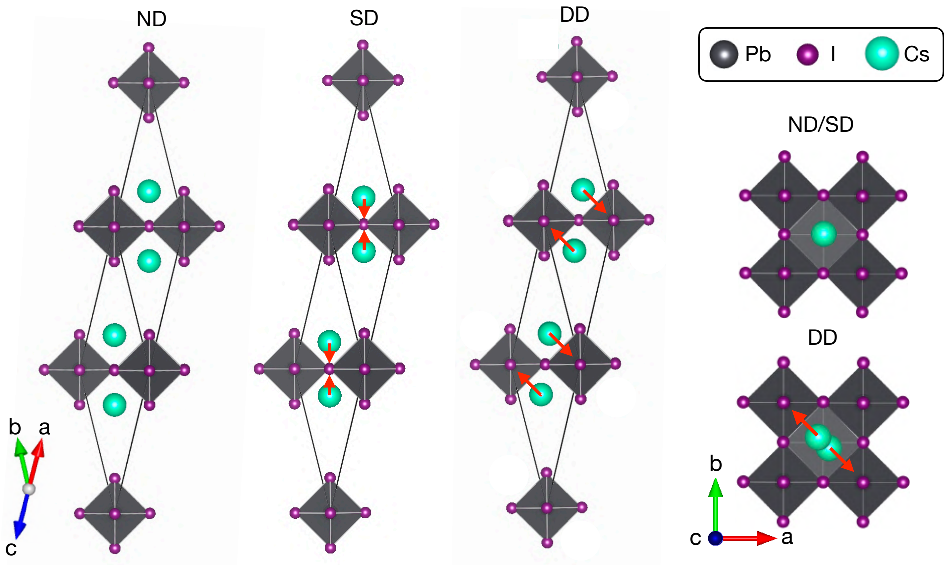

Figure 8.6: Cs_2PbI_4 structures distinguished by different Cs configurations (ND=“no displacement", SD=“straight displacement", DD=“diagonal displacement"). The left panels show the systems-oriented parallel to the octahedra layer, and the right panels show them oriented perpendicular to it. The red arrows indicate the direction of the displacement of the Cs atoms.

Configuration without displacement

In the ND configuration, the Cs atom is placed in the plane formed by the out-of-plane iodine atoms, exactly in the center of the cavity formed by the Pb-I octahedra (Fig. 8.6). This position corresponds to the one that Cs would have if the $CsPbI_3$ 3D cubic structure were sliced into layers without any additional structural changes, as the name implies. This configuration is good enough to neutralize the organic layer but shows some major differences in the electronic structure and optical properties of both the BA-BLYP and BA-PBE+VDW geometries.

As visible in the band structures without SOC in Fig. 8.2-8.3, the dispersion of the highest VB of the Cs-ND structure is much higher than that of the systems with the BA molecule. In fact, $\Delta E^{v}_{X\Gamma}$ is -0.80 eV, while in the BA-BLYP and BA-PBE+VDW geometries, it is -0.37 eV and -0.52 eV, respectively (see Table 8.1). The same holds for ΔE^{v}_{XY}, which is -0.44 eV, in the Cs system, while being -0.21 eV and -0.29 eV, in the BA-BLYP and BA-PBE+VDW geometries, respectively. This also is reflected in the effective hole masses (see Table 8.2): The absolute value of their mean is 0.18 m_0 (0.05 m_0) lower than that of BA-BLYP (BA-PBE+VDW). There is also a difference in the band gap, but it is less pronounced: The PBE gap of Cs-ND is 0.12 eV (0.07 eV) larger than that of BA-BLYP (BA-PBE+VDW). Comparing the two BA geometries, the differences in the CBm are minor (see ΔE^{c}_{XS} and the effective electron masses in Tables 8.1 and 8.2). Nevertheless, the deviation of the electronic structure of Cs-ND from the BA systems remains significant as can be seen from the DOS in Fig. 8.4. When SOC is taken into account (with both the SR and the Dirac LO sets), similar differences can be observed between the Cs-ND and the two BA structures. Considering the case with $p_{1/2}$-LO, the largest deviation is observed for the effective masses: the absolute value of the mean of the effective hole masses is 0.21 m_0 (0.09 m_0) smaller than that of BA-BLYP (BA-PBE+VDW), while the absolute value of the mean of the effective electron masses is 0.03 m_0 smaller than that of both BA systems. The differences between the gaps of the three geometries are slightly smaller for PBE+SOC ($p_{1/3}$): The gap of Cs-ND is equal to that of the BA-PBE+VDW structure and 0.03 eV larger than that of the BA-BLYP structure. The SOC splitting of 1.19 eV is slightly bigger than in both BA structures.

Differently from the BA systems, the structures with Cs are symmetric in the components parallel to the layer of the Pb-I octahedra, so the parallel component of the IPA spectra is $\varepsilon_{\parallel} = \varepsilon_x = \varepsilon_y$. In the ND configuration, $\varepsilon_{\parallel}$ shows two peaks of comparable intensity, in contrast to the BA structures, where the first peak has a significantly lower intensity. Additionally, the first peak is blue-shifted by 0.31 eV (0.14 eV) compared to that of the BA-BLYP (BA-PBE+VDW) geometry. For the perpendicular component ($\varepsilon_{\perp}$), the differences are even larger: The single peak observed for the BA structures splits into three peaks in the Cs-ND structure, and the initial hump appears as a tail of the first peak. The dielectric constant ϵ_{∞}, is 0.46 (0.48) lower than that of the BA-BLYP (BA-PBE+VDW) geometry. The largest difference is in the z component, which in Cs-ND decreases by 0.89 (0.82) with respect to that of BA-BLYP (BA-PBE+VDW). The decrease observed for the x and y components varies between 0.18 and 0.37 compared to both BA systems. These results already show that the composition has a greater influence on the dielectric response of the material than the electronic structure. In addition, even though the perpendicular response is the one most affected by the type of organic/inorganic cation, there is also an effect on the response parallel to the octahedra layers.

Straight-displacement configuration

To achieve a better agreement between the BA reference systems and that with the Cs substitution, we explored other configurations by displacing the Cs atom from its ND configuration. We started by displacing it in a straight line perpendicular to the Pb-I octahedra layer (SD), both toward this layer and in the opposite direction. We found that by applying an SD of 0.75 Å towards the layer, the electronic properties of BA-BLYP can be reproduced. In particular, the band gap, both with and without SOC, and the SOC splitting, are reproduced within an accuracy of 0.01 eV (Table 8.1). The only significant deviation is observed for $\Delta E^{c}_{X\Gamma}$, which in Cs-SD is about 0.12-0.17 eV higher than that of BA-BLYP (this range includes results with and without SOC). This is expected since the conduction band at Γ is dominated by the organic/inorganic cation (see Fig. E.1). However, it is interesting to note that the difference between the two systems is strongly reduced compared to the case of Cs-ND, where $\Delta E^{c}_{X\Gamma}$ was about 0.59-0.67 lower than in BA-BLYP. For the effective masses, the accuracy is within 0.03 m_0 without SOC and with SOC for SR-type LO, and within 0.05 m_0 with SOC for Dirac-type LO. In the energy range from -3 to 3 eV displayed in Fig. 8.2, the whole band structure shows excellent agreement with that of the BA-BLYP system. The main differences appear below -2 eV and above 2 eV, where BA/Cs have dominant contributions to the bands (Fig. E.1). When SOC is considered, the good agreement extends to the range -2.5 and 2.5 eV. Even if the curves do not perfectly overlap, there is also an improvement in the DOS in comparison to the Cs-ND system, especially if considering the peak positions. The excellent agreement is also reflected in the IPA spectra (Fig. 8.5), where both the parallel and the perpendicular components of BA-BLYP and Cs-SD nearly overlap up to about 4 eV. Regarding the dielectric constant, again one can observe that the composition is more important than the electronic structure, since ϵ_∞ is only 0.11 smaller than that of Cs-SD, while it is 0.57 smaller than that of BA-BLYP.

Diagonal-displacement configuration

For the BA-PBE+VDW geometry, the SD did not lead to the desired result. As discussed in Section 8.2.1, the ammonium group in this geometry points in the direction of the Pb atom, therefore, we displaced Cs in this direction, which is diagonal with respect to the octahedra layer. We found that by such diagonal displacement of 0.73 Å from the ND case (Fig. 8.6), the desired agreement can be reached: The band gap, with and without

SOC, and the SOC splitting are the same for the BA-PBE+VDW and the Cs-DD structures. All energy differences, except for $\Delta E^{\mathrm{c}}_{\mathrm{X}\Gamma}$, which is up to 0.38 eV smaller in Cs-DD, are within 0.06 eV. The effective masses are within 0.05 m_0. The worse agreement is found for the effective hole masses along the X→Y path for the PBE+SOC calculation with the $p_{1/2}$ set of LO (see Table 8.2). These variations are similar to those observed when comparing BA-BLYP with Cs-SD. For the electronic structure (Figs. 8.2-8.4) and the IPA spectra (Fig. 8.5), the agreement is also comparable. The dielectric constant, which is not far from that of the other Cs systems, shows a similar trend when comparing Cs-SD with Cs-DD and BA-BLYP with BA-PBE+VDW: ϵ_∞ for the Cs-DD is 0.04 larger compared to the Cs-SD systems and that of BA-PBE+VDW is 0.02 larger than that of BA-BLYP. The parallel response, obtained by averaging the x and y components, is 0.05 (0.06) larger in the Cs-DD (BA-PBE+VDW) than in Cs-SD (BA-BLYP) case. On the other hand, the z components of Cs-SD and Cs-DD differ by only 0.02, with Cs-DD being larger, while the difference between BA-BLYP and BA-PBE+VDW is 0.07, with BA-BLYP having the larger value.

HSE results

Using HSE opens the gap for all analyzed systems by a comparable amount; i.e. 0.54 eV for Cs-ND, 0.57 eV for Cs-SD, and 0.56 eV for Cs-DD. Additionally, it causes a non-negligible increase of $\Delta E^{\mathrm{v}}_{\mathrm{X}\Gamma}$, $\Delta E^{\mathrm{v}}_{\mathrm{XS}}$, and $\Delta E^{\mathrm{c}}_{\mathrm{X}\Gamma}$, while the variation of $\Delta E^{\mathrm{c}}_{\mathrm{XS}}$ is within 0.03 eV. In particular, $\Delta E^{\mathrm{v}}_{\mathrm{X}\Gamma}$ increases in the order of 0.14-0.20 eV, $\Delta E^{\mathrm{v}}_{\mathrm{XS}}$ of 0.09 eV for all the three systems, and $\Delta E^{\mathrm{c}}_{\mathrm{X}\Gamma}$ between 0.05 and 0.11 eV. The variation on $\Delta E^{\mathrm{c}}_{\mathrm{XS}}$ is within 0.03 eV. The increase of the valence band curvature due to HSE is also visible in the band structure in Figs. 8.2 and 8.3. Additionally, the second-highest valence band is slightly further away from the highest valence bands. This is reflected in the DOS (Fig. 8.4), which shows some major differences in the valence region close to the gap. Finally, the effective masses are within 0.01 m_0, the only exceptions being the effective hole masses of Cs-SD, which decrease by about 0.05 m_0. Despite some significant differences, the trends between the three structures observed at the PBE level remain the same.

8.2.3 Discussion

In this study, we have shown that the position of the Cs atom is very important to accurately mimic the properties of the original $\mathrm{BA_2PbI_4}$ systems. By carefully selecting it, the electronic structure of the organic-inorganic system (evaluated with or without SOC) can be reproduced by the inorganic system, which is computationally more affordable. The same is observed for the IPA spectra. On the other hand, the dielectric constant turns out to be more sensitive to the composition than to the position of the organic/inorganic cation, and the variations in ϵ_∞ are only within 0.59. This opens up the possibility that, at least for the BA system, the computationally convenient Cs system could be used for a preliminary investigation of the optical properties of the system at the BSE level and thus for the evaluation of quantities such as excitonic binding energies.

In 2D HaP, a way for tuning the binding energy is by properly choosing the organic spacer [283, 284, 25, 285, 286]. This analysis could be used to investigate to which extent the dielectric constant and exciton binding energies are affected by structural properties. These can be the chemical environment generated by the organic spacer, the distance between the octahedra layers determined by the choice of organic spacer, or the tilting of the octahedra due to the interaction of the organic and inorganic components of the systems.

8.3 LT and HT phase of BA_2PbI_4

The aim of this section is to investigate the electronic properties of the LT and HT phases of BA_2PbI_4 using various functionals. In this context, the substitution of the BA molecule with Cs, as explored above for the tetragonal structures, comes into play. In order to choose a good position for Cs, both types of systems are studied at the PBE level, while only the systems with the Cs replacement are studied with higher-level theory.

8.3.1 Atomic structures

The structures used in this study were optimized by Xiangzhou Zhu for the work in Ref. [208]. Details of the optimization are given in Ref. [208].

Figure 8.7 shows the optimized unit cells of the LT and HT phases of BA_2PbI_4, and Table 8.4 lists the lattice constants and the angles used to determine the size of the octahedra tilts. The results follow the expected trend: With increasing temperature, the tilting of the octahedra decreases, the distance between the layers increases, and the ammonium group, which in the LT phase is located near the obtuse angle of the parallelogram formed by the in-plane I-atoms, moves to the vicinity of the acute angle [274].

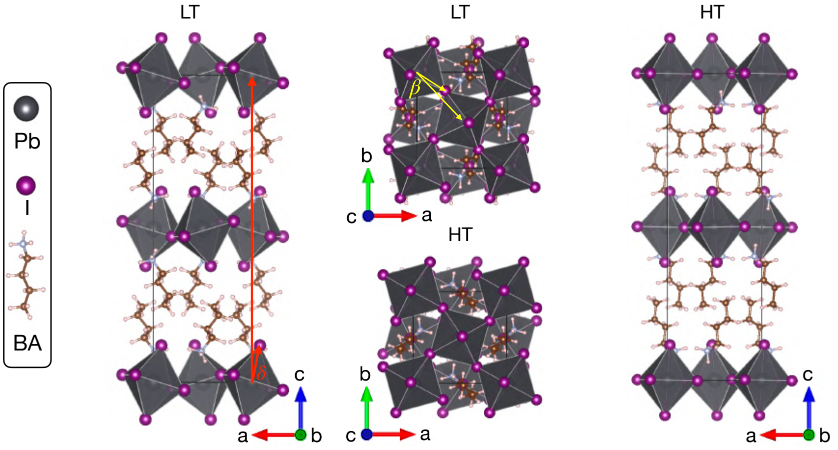

Figure 8.7: Lateral view and top view of the optimized LT and HT structures of BA_2PbI_4. In the LT structure the out-of-plane angle δ=(Pb-Pb-I) and the in-plane angle β=(Pb-Pb-I), which characterize the octahedra tilts, are highlighted.

Table 8.4: Lattice parameters and out-of-plane (δ) and in-plane (β) angles used to classify the size of the octahedra tilts [40]. The angles δ and β are displayed in Fig. 8.7.

Structure	a [Å]	b [Å]	c [Å]	δ [°]	β [°]
LT	8.35846	8.97096	26.14232	12.8178	17.6451
HT	8.69557	8.53095	28.28355	4.2086	15.4469

8.3.2 Electronic structure from PBE

BA_2PbI_4 systems

Both the LT and HT systems have a direct band gap at Γ and a flat band along the path from Γ to Z (Fig. 8.8). At the PBE level, the energy gap of the LT phase is 0.11 eV higher than that of the HT phase (Table 8.5). This finding is consistent with what is usually observed in 3D HaP systems, i.e., that the band gap increases with the increase of the octahedra tilts. When SOC is included, the two lowest conduction bands (each doubly degenerate excluding spin), which are very close in energy without SOC, move further apart. More specifically, without SOC, these two bands are 0.23 eV apart in the LT phase and 0.06 eV apart in the HT phase. When SOC is applied, these differences increase by 0.76 eV and 1.02 eV in the LT and HT phase, respectively. This results in a 0.63 eV (0.76 eV) reduction of the band gap of the LT (HT) phase, and the difference between the gaps of the two structures increases to 0.24 eV (Fig. 8.9). Note that the results in Table 8.5 include VDW effects in addition to SOC. The former should, however, not affect the electronic structure.

Table 8.5: Energy gap (E_g) and effective hole (electron) masses m_h (m_e) of the LT and HT phases of BA_2PbI_4. The results include calculations performed for the pristine system (BA cation) and systems with Cs replacement, using PBE and HSE, including and excluding SOC effects. For some of them, MLWF have been used for the band structure calculation. The label $^{\perp}$ indicates the calculations performed by Xiangzhou Zhu, which include also the Tkatchenko-Scheffler method to account for VDW effects.

Cation	Functional	MLWF	E_g [eV]	m_h [m$_0$]	m_e [m$_0$]
		LT			
BA	PBE	No	2.25	-0.39	0.25
BA$^{\perp}$	PBE+SOC	No	1.62	-0.39	0.25
Cs	PBE	No	2.27	-0.39	0.26
Cs	PBE	Yes	2.27	-0.41	0.28
Cs	PBE+SOC	No	1.62	-0.38	0.25
Cs	HSE	Yes	2.88	-0.37	0.25
		HT			
BA	PBE	No	2.14	-0.24	0.23
BA$^{\perp}$	PBE+SOC	No	1.38	-0.24	0.19
Cs	PBE	No	2.16	-0.25	0.24
Cs	PBE	Yes	2.16	-0.26	0.25
Cs	PBE+SOC	No	1.42	-0.24	0.19
Cs	HSE	Yes	2.75	-0.24	0.23

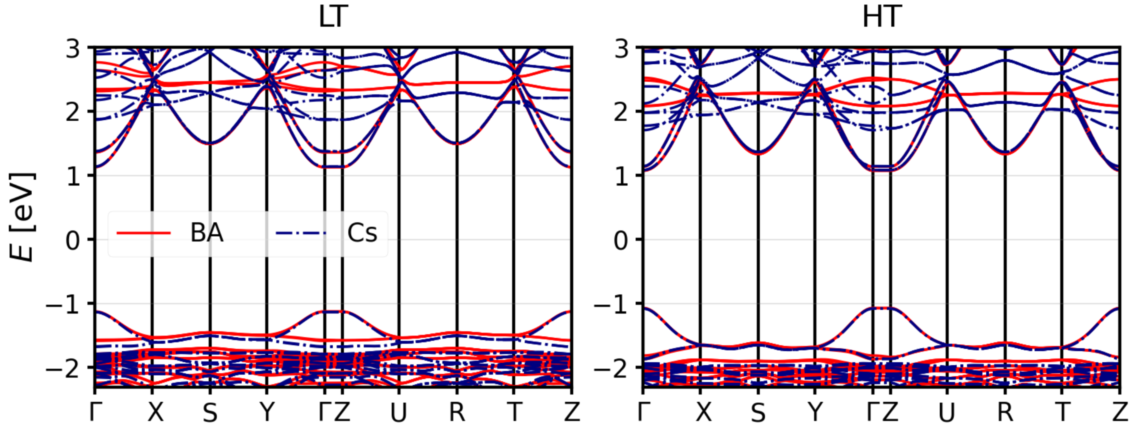

Figure 8.8: Comparison of the PBE band structures of the LT (left panel) and HT (right panel) phases of BA_2PbI_4 and those of with Cs-replacement. The Fermi energy is at 0 eV.

The effective masses in Table 8.5 are calculated by averaging the x and y components, which are evaluated along Γ → X and Γ → Y, respectively. The LT effective hole mass is 0.15 m$_0$ larger than that of the HT phase, while the effective electron mass is only 0.02

m_0 larger. By analyzing the effects of SOC in the two structures, it can be observed that the differences to the cases without SOC are negligible, except for the effective electron mass of the HT phase, which decreases by 0.04 m_0. This reduction leads to an increase in the deviation between the two phases by 0.06 m_0. The reason for this is that without SOC, the two lower conduction bands of the HT phase show an intersection around Γ (Fig. 8.9), which leads to effective masses that are significantly different in the Γ → X and Γ → Y directions, i.e., $m_{e,x} = 0.29$ m_0 and $m_{e,y} = 0.17$ m_0. When SOC is applied, the two bands split by 1.08 eV, and the effective masses in the two directions become comparable (see results for Cs in Table E.4).

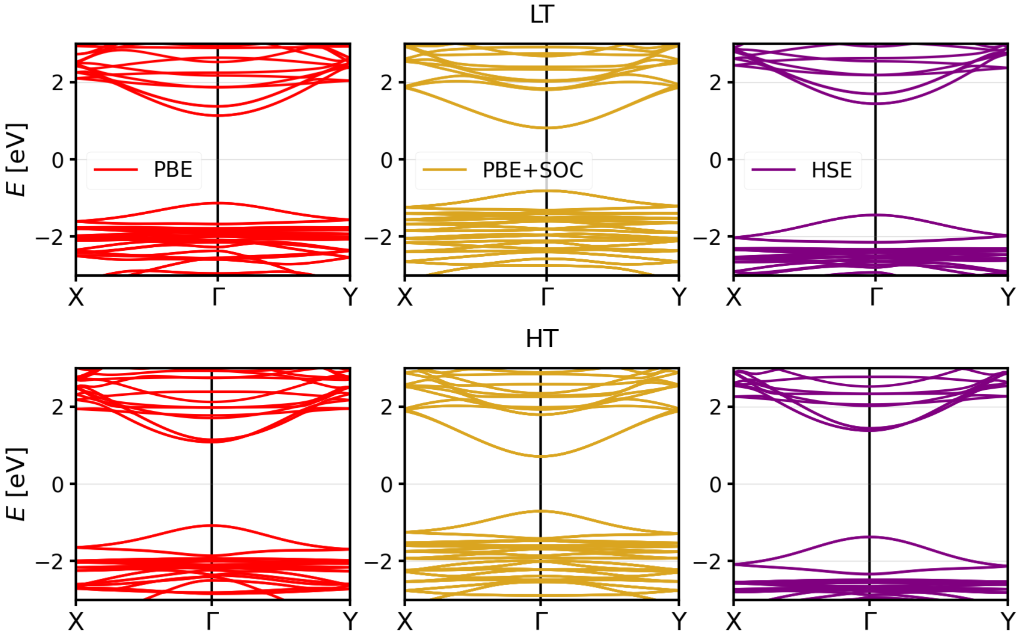

Figure 8.9: Band structure of the LT (top panels) and HT (bottom panels) phases computed for the Cs system along the path used to evaluate the effective masses, i.e., X → Γ → Y with X = (0.5, 0.0, 0.0) and Y = (0.0, 0.5, 0.0). The panels on the left show the PBE results, those in the middle include SOC, and those on the right are obtained by HSE excluding SOC and employing the Wannier interpolation method. The 0 energy is aligned with the Fermi level.

Cs_2PbI_4 systems

For the LT phase, the position of the Cs atoms in the *xy*- plane are obtained to be in the center of the parallelogram formed by the Pb atoms. The *z* coordinate is 0.13Å away from the plane formed by the out-of-plane I atoms in the direction opposite to the layer of the Pb-I octhaedra (Fig. 8.10). In the HT phase, the Cs atom is in the center of the

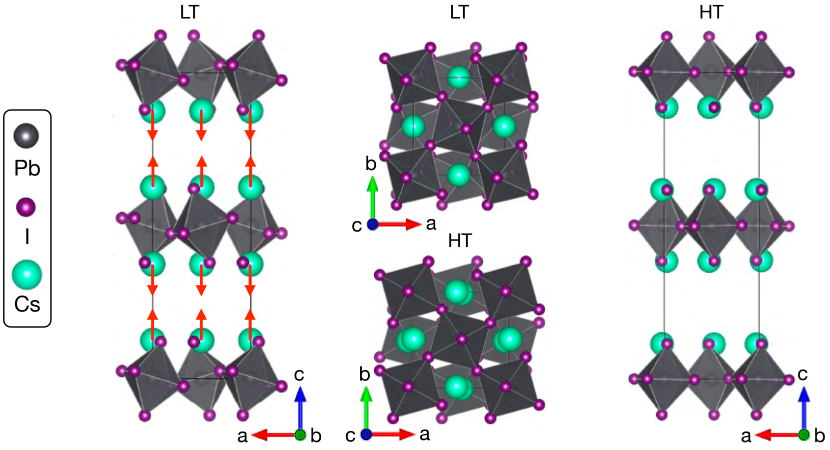

Figure 8.10: Side and top views of the LT and HT phases of BA_2PbI_4 with Cs replacing the BA molecule. The red arrows in the side view of the LT structure illustrate the direction of the Cs displacements.

parallelogram formed by the out-of-plane I atoms. Note that these systems are very complex, and it cannot be excluded that other structures may give comparable results.

In Fig. 8.8, it can observed that in the LT phase, the band structure of the system with the Cs substitution is basically identical to that of the reference system in the energy range from -1.5 eV to 1.8 eV. A small deviation is observed for the band around -1.5 eV, which, notably, is perfectly described by the HT-Cs system in the HT phase. In fact, in the HT system, the agreement is very good in the range between -2.0 eV and 1.5 eV. Comparing the energy gaps and the effective masses of the systems with the Cs substitution with those of the BA_2PbI_4 systems, good agreement is found: In the PBE results, the differences in energy gaps is within 0.02 eV for both phases, while the PBE+SOC calculations show differences below 0.01 eV for the LT-phase and below 0.04 eV for the HT-phase. The differences in the effective masses are within 0.01 m_0 for both systems, for both PBE and PBE+SOC results.

8.3.3 Electronic structure from HSE

For the HSE calculations, Wannier interpolation is employed to compute band structures (Section 3.7). The $\boldsymbol{k}$-mesh convergence to construct the MLWF and then compute the band structure from which the effective masses are evaluated, is slower than that of the default method used for the PBE calculations. Therefore, in order to obtain results with a precision comparable to that of the PBE and PBE+SOC cases, we had to increase the $\boldsymbol{k}$-mesh. We have chosen it to reproduce the PBE Cs_2PbI_4 effective masses values with a precision of 0.02 m_0 (Tables 8.5-E.5) but small enough to permit HSE calculations for such large systems.

The main effect of the HSE functional is the band-gap opening, which increases by about 0.60 eV in both the LT and HT phases compared to the PBE results, leading to a an increase of only 0.02 eV in the band-gap difference between the LT and HT phases (i.e. the difference is 0.13 eV, Table 8.5). As observed for the tetragonal systems, the curvature of the highest valence bands increases slightly, and for the path shown in Fig 8.9 a small gap forms between the second and the third highest valence bands. In the energy range considered, the conduction bands appear rigidly shifted, and even the intersection of the two lowest conduction bands around Γ in the HT phase is preserved. The trend for the effective masses is maintained: The difference in the effective masses is only within 0.02 m_0 (for comparison we used the PBE effective masses evaluated by Wannier interpolation).

The results obtained at the PBE and HSE level are in good agreement with what is expected when analyzing the properties of the HT and LT phases: A smaller out-of-plane distortion angle (δ) of the HT phase (Table 8.4) corresponds to a smaller band gap [40] and lighter effective carrier masses [287].

In Ref. [208], we reported an experimental optical gap that shows an abrupt shift towards lower energies (120 meV) at about 270 K, i.e., the phase transition temperature. On the other hand, the binding energy, which is in the range of 400-500 meV, increases as the temperature increases but does not change across the phase transition, i.e. about E_v = 480 meV. Moreover, we found comparable diffusion coefficients between the LT and HT [208]. Comparing the experimental with the theoretical results, the energy differences between the optical gap of the two phases, is in agreement with what we observe at the PBE and HSE level, i.e., a difference between the gap of the two phases of 110 meV and 130 meV, respectively. When including SOC, which we know being fundamental, the trend is maintained but the difference increases to 240 meV. Instead, for the binding energy and the diffusion, the results show that the models typically used for semiconductors, such as the Wannier model [275] and the semi-classical band-like propagation, respectively, cannot explain the results of the 2D HaP. In fact, in the Wannier model, the binding energy scales with the reduced effective mass $\mu = m_\mathrm{h} m_\mathrm{e} / (m_\mathrm{h} + m_\mathrm{e})$. Considering SOC, $\mu = 0.15\ m_0$ in LT and $\mu = 0.11\ m_0$ in HT, a significant reduction of the binding energy should have been observed at the phase transition if the Wannier model was valid. Similarly, in the semi-classical band-like propagation model, the diffusion coefficient scales as the inverse of the total exciton mass $M_\mathrm{X} = m_\mathrm{h} + m_\mathrm{e}$, being the other quantity comparable; in this case, we would expect a change by a factor of 1.5.

8.4 Conclusions

In this chapter, we have shown that by replacing the BA molecule with a Cs atom, the 2D HaP' electronic structure in the region around the band gap can be accurately reproduced if Cs is properly placed. This allows for the study of this material with more computationally demanding functionals such as HSE. We have shown that the effect of HSE is mainly in the opening of the gap, while its effect on the effective masses is minimal. Moreover, the differences between the electronic properties of different structures do not change significantly when HSE is employed. For the optical properties, things get more complicated: For the IPA spectra, still good agreement is found. However, if one wants to evaluate excitonic properties such as binding energies, the chemical environment has a significant influence, since it determines the dielectric screening. As shown for the tetragonal case, the dielectric constants of systems with the same composition are very similar, even if they have quite different effective masses.

CHAPTER 9

Conclusions and Outlooks

This work presents a comprehensive study of electronic excitations in 3D and 2D HaP, combined with the implementation of the HSE hybrid functionals in the `exciting` code and the presentation of a novel, efficient and accurate methodology to compute SOC effects. All these pieces of work have been highly relevant to achieve the results for 3D and 2D HaP presented here.

Among the most significant results, we found that HSE with a mixing parameter of $\alpha = 0.36$ obtained by applying the DM method [106], is the best in terms of accuracy and computational effort to predict band gaps of 3D lead-iodide based perovskites. The band gap thus evaluated gives results comparable to the *state-of-the-art* single shot *GW* method using HSE as starting point, which supports our conclusion. Moreover, with this analysis, we could underline the transferability of the methodology from the easy-to-compute PbI_2 precursor to complex hybrid structures like $APbI_3$. A further step forward would be to verify the performance of the DM method for 2D compounds. However, due to their layered structure, it would first be necessary to implement the DM method for interfaces [123].

From the investigation of 2D compounds, we found that many properties of the hybrid systems, such as the band gap, the effective masses at the VBM and CBm, the electronic structure near the Fermi level, and the optical spectra evaluated in the IPA, can be well described by simplified systems where Cs replace the organic molecule if it is carefully placed. We have tested this for BA_2PbI_4 and can expect a similar result for other 2D HaP of the Ruddlesden-Popper type. Using this approach, we were able to compute the band gap and the effective masses of the LT and HT phases of BA_2PbI_4 with the functional HSE, and we showed that the main effect of HSE is to open the gap, while the effect on the effective masses is negligible. Moreover, the differences between the two phases remain the same, since HSE has a comparable effect on both structures.

By comparing the hybrid systems with their counterparts with Cs as a replacement for the organic spacer, we found that the dielectric environment due to the type of spacer (BA or Cs) has less of an effect on the dielectric constant than that of the Pb-I octahedral configuration. For example for the five systems analyzed, differentiated by the type of spacer and its position, we obtained dielectric constants ranging from 2.85 to 3.44. By applying this approach to other systems, it will be possible to determine the effect of the single structural component, e.g., type of spacer, distance between octhaedral layers, octhaedral tilt and number of octaedral in the inorganic layers, on the dielectric constant, which strongly influences the excitonic properties of 2D HaP systems.

As emphasized in different parts of the manuscripts, these achievements serve as starting points for many projects initiated by the group. Among these, it is worth mentioning the implementation of real-time time-dependent DFT with hybrid functionals, realized by Antonio Cillis, the extension of the hybrid functionals code to magnetic systems, recently started by Fabian Nemitz, the realization of a model for the *density-based mixing* method based on `exciting` results, done by Jessica Richter, and the development of the SVLO method in the BSE framework, which is now primarily carried out by Seokhyun Hong.

Advances in the code, such as the implementation of the HSE functional, the combination of SOC with hybrid functionals, and G_0W_0 on top of the HSE starting point, allowed us to determine that the G_0W_0@HSE is best in computing the band gap of several semiconductors such as $LaIO_3$ [209], PbI_2, 3D lead-based HaP [35], and MoS_2 [210].

APPENDICES

APPENDIX A

Supporting materials for Chapter 4

A.1 Computational details

Table A.1 summarizes the parameters used for the test in Section 4.2.2. The parameters have been chosen so that the transition energies between the highest VB and the lowest CB of Table 4.1 are within a precision of ~10-20 meV. When computing the MLWF for the calculation of the band structures (Fig. 4.5) and the DOS (Fig. 4.6), the $\boldsymbol{k}$ mesh had to be increased for some materials. In particular, for C we used an 8x8x8 $\boldsymbol{k}$-mesh for PBE and HSE, and for GaAs and Ar, we employed a 12x12x12 and 6x6x6 $\boldsymbol{k}$-mesh, respectively, for all the three functionals.

The input and output data related to the computations of Chapters 4-5 are collected in the NOMAD Repository [222] at the link `https://doi.org/10.17172/NOMAD/2025.01.02-1`.

A.2 Comparison of PBE and PBE0 calculations with literature

Here we compare the PBE and PBE0 results given in Table 4.2.2 with those from Ref. [205]. Zavickis and co-workers implemented the adaptive compressed exchange method for the PBE0 functional in the **`exciting`** code[1]. To validate their implementation, they computed the same set of transition energies as those listed in Table 4.1 using PBE and

---

[1] This implementation is not yet released.

Table A.1: Computational parameters used for the tests in Sections 4.2.2 and 4.2.4.

:

xc functional	Si			C		
	$\boldsymbol{k}$-mesh	$R_{\mathrm{MT}}G_{\mathrm{max}}$	N_{unocc}	$\boldsymbol{k}$-mesh	$R_{\mathrm{MT}}G_{\mathrm{max}}$	N_{unocc}
PBE	6x6x6		-	6x6x6		-
PBE0	8x8x8	7	200	10x10x10	7	60
HSE	6x6x6			6x6x6		
xc-functional	GaAs			MgO		
	$\boldsymbol{k}$-mesh	$R_{\mathrm{MT}}G_{\mathrm{max}}$	N_{unocc}	$\boldsymbol{k}$-mesh	$R_{\mathrm{MT}}G_{\mathrm{max}}$	N_{unocc}
PBE	6x6x6		-	6x6x6		-
PBE0	12x12x12	7	140	8x8x8	8	300
HSE	6x6x6			6x6x6		
xc-functional	NaCl			Ar		
	$\boldsymbol{k}$-mesh	$R_{\mathrm{MT}}G_{\mathrm{max}}$	N_{unocc}	$\boldsymbol{k}$-mesh	$R_{\mathrm{MT}}G_{\mathrm{max}}$	N_{unocc}
PBE	4x4x4		-			-
PBE0	6x6x6	8	300	4x4x4	6	150
HSE	4x4x4					

PBE0. The values can be found in Table II of Ref. [205]. The authors claim a precision of 1 meV. Compared to our results, the differences are within 20-30 meV. The only exception is NaCl, for which, however, the lattice constants employed are different (we used $a = 5.64$ Å and they used $a = 5.59$ Å). Since Zavickis's results for NaCl are in very good agreement with VASP results (Table 4.1), the discrepancy observed between our results and VASP, for which we do not know the lattice constant, could have the same reason (see discussion in Section 4.2.2).

A.3 k-points convergence of $E_{\Gamma\rightarrow\mathrm{X}}$ and $E_{\Gamma\rightarrow\mathrm{L}}$

In Fig. 4.7, the convergence behavior of the transition energies between the highest VB and the lowest CB at Γ with respect to the number of $\boldsymbol{k}$-points are plotted for PBE, PBE0, and HSE. In Figs. A.1 and A.2, the same is shown for the transition energies $E_{\Gamma\rightarrow\mathrm{X}}$ and $E_{\Gamma\rightarrow\mathrm{L}}$, respectively. Ar is excluded. Overall, the same behavior is observed: the $\boldsymbol{k}$-points convergence of PBE0 is slower than that of HSE, which is closer to that of PBE. For all materials, for PBE and HSE, a precision of 10 meV is reached when using the same number of $\boldsymbol{k}$-points. PBE0 always requires a larger grid. All the values used for the plot in Figs. 4.7, A.1 and A.2 are listed in Table A.2.

Table A.2: Values of E_{Γ}, $E_{\Gamma\to\mathrm{K}}$ and $E_{\Gamma\to\mathrm{L}}$ used in Figs. 4.7, A.1 and A.2.

	PBE			PBE0			HSE		
Si									
$\boldsymbol{k}$-mesh	E_{Γ}	$E_{\Gamma\to\mathrm{K}}$	$E_{\Gamma\to\mathrm{L}}$	E_{Γ}	$E_{\Gamma\to\mathrm{K}}$	$E_{\Gamma\to L}$	E_{Γ}	$E_{\Gamma\to\mathrm{K}}$	$E_{\Gamma\to\mathrm{L}}$
4x4x4	2.543	0.702	1.534	4.087	2.075	3.025	3.352	1.350	2.294
6x6x6	2.558	0.716	1.539	4.010	1.992	2.922	3.328	1.317	2.248
8x8x8	2.561	0.719	1.540	3.984	1.967	2.890	3.324	1.311	2.240
10x10x10	2.561	0.720	1.541	3.975	1.958	2.879	3.323	1.310	2.238
C									
$\boldsymbol{k}$-mesh	E_{Γ}	$E_{\Gamma\to\mathrm{K}}$	$E_{\Gamma\to\mathrm{L}}$	E_{Γ}	$E_{\Gamma\to\mathrm{K}}$	$E_{\Gamma\to\mathrm{L}}$	E_{Γ}	$E_{\Gamma\to\mathrm{K}}$	$E_{\Gamma\to\mathrm{L}}$
4x4x4	2.543	0.702	1.534	4.087	2.075	3.025	3.352	1.350	2.294
6x6x6	2.558	0.716	1.539	4.010	1.992	2.922	3.328	1.317	2.248
8x8x8	2.561	0.719	1.540	3.984	1.967	2.890	3.324	1.311	2.240
10x10x10	2.561	0.720	1.541	3.975	1.958	2.879	3.323	1.310	2.238
GaAs									
$\boldsymbol{k}$-mesh	E_{Γ}	$E_{\Gamma\to\mathrm{K}}$	$E_{\Gamma\to\mathrm{L}}$	E_{Γ}	$E_{\Gamma\to\mathrm{K}}$	$E_{\Gamma\to\mathrm{L}}$	E_{Γ}	$E_{\Gamma\to\mathrm{K}}$	$E_{\Gamma\to\mathrm{L}}$
6x6x6	0.539	1.460	1.009	2.061	2.687	2.407	1.439	2.027	1.761
8x8x8	0.541	1.464	1.012	2.008	2.664	2.371	1.428	2.024	1.754
10x10x10	0.542	1.465	1.013	1.983	2.654	2.356	1.424	2.022	1.752
12x12x12	0.542	1.466	1.013	1.970	2.649	2.349	1.424	2.022	1.752
14x14x14	0.542	1.466	1.013	1.963	2.646	2.345	1.423	2.022	1.752
MgO									
$\boldsymbol{k}$-mesh	E_{Γ}	$E_{\Gamma\to\mathrm{K}}$	$E_{\Gamma\to\mathrm{L}}$	E_{Γ}	$E_{\Gamma\to\mathrm{K}}$	$E_{\Gamma\to\mathrm{L}}$	E_{Γ}	$E_{\Gamma\to\mathrm{K}}$	$E_{\Gamma\to\mathrm{L}}$
4x4x4	4.734	9.130	7.905	7.285	11.666	10.482	6.508	10.892	9.705
6x6x6	4.741	9.141	7.914	7.248	11.651	10.463	6.492	10.889	9.698
8x8x8	4.742	9.142	7.915	7.238	11.646	10.457	6.491	10.889	9.698
10x10x10	4.742	9.142	7.915	7.234	11.644	10.455	6.491	10.889	9.698
NaCl									
$\boldsymbol{k}$-mesh	E_{Γ}	$E_{\Gamma\to\mathrm{K}}$	$E_{\Gamma\to\mathrm{L}}$	E_{Γ}	$E_{\Gamma\to\mathrm{K}}$	$E_{\Gamma\to\mathrm{L}}$	E_{Γ}	$E_{\Gamma\to\mathrm{K}}$	$E_{\Gamma\to\mathrm{L}}$
4x4x4	5.116	7.526	7.270	7.272	9.826	9.412	6.529	9.058	8.665
6x6x6	5.117	7.528	7.271	7.258	9.818	9.403	6.528	9.057	8.664
8x8x8	5.117	7.528	7.271	7.256	9.816	9.401	6.528	9.057	8.664
10x10x10	5.117	7.528	7.271	7.255	9.816	9.401	6.528	9.058	8.664
Ar									
$\boldsymbol{k}$-mesh	E_{Γ}	$E_{\Gamma\to\mathrm{K}}$	$E_{\Gamma\to\mathrm{L}}$	E_{Γ}	$E_{\Gamma\to\mathrm{K}}$	$E_{\Gamma\to\mathrm{L}}$	E_{Γ}	$E_{\Gamma\to\mathrm{K}}$	$E_{\Gamma\to\mathrm{L}}$
4x4x4	8.702	-	-	11.146	-	-	10.366	-	-
6x6x6	8.702	-	-	11.142	-	-	10.366	-	-
8x8x8	8.702	-	-	11.141	-	-	10.366	-	-
10x10x10	8.702	-	-	11.140	-	-	10.366	-	-

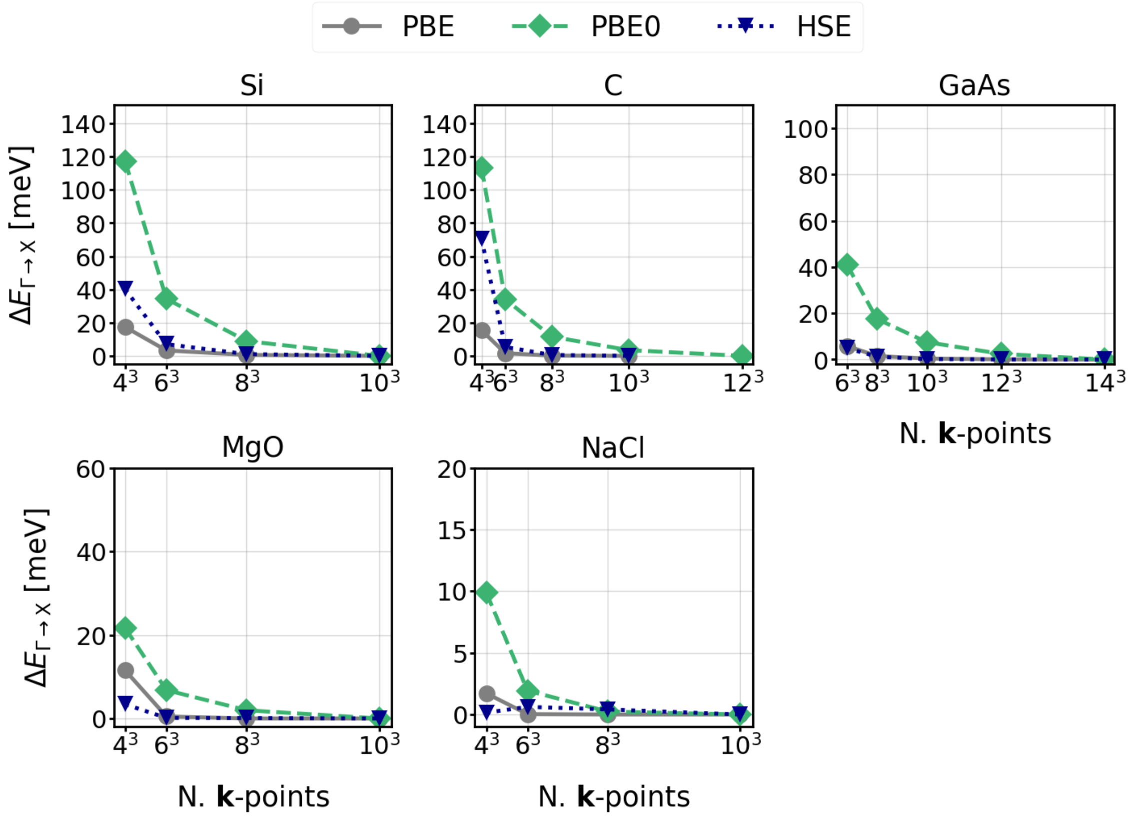

Figure A.1: Convergence behavior of $E_{\Gamma\rightarrow X}$ with respect to the $\boldsymbol{k}$-mesh for PBE, PBE0, and HSE.

A.4 Supporting data for the singular term of screened Coulomb potential

In Table A.3, the values used in Fig. 4.8, are summarized. They include results evaluated with different methods for the singular term, $\boldsymbol{k}$-meshes, and screening parameters. For Si, GaAs, and Ar the calculations were performed with the parameters shown in Table A.1, while for PbI_2 the parameters are summarized in Table B.1.

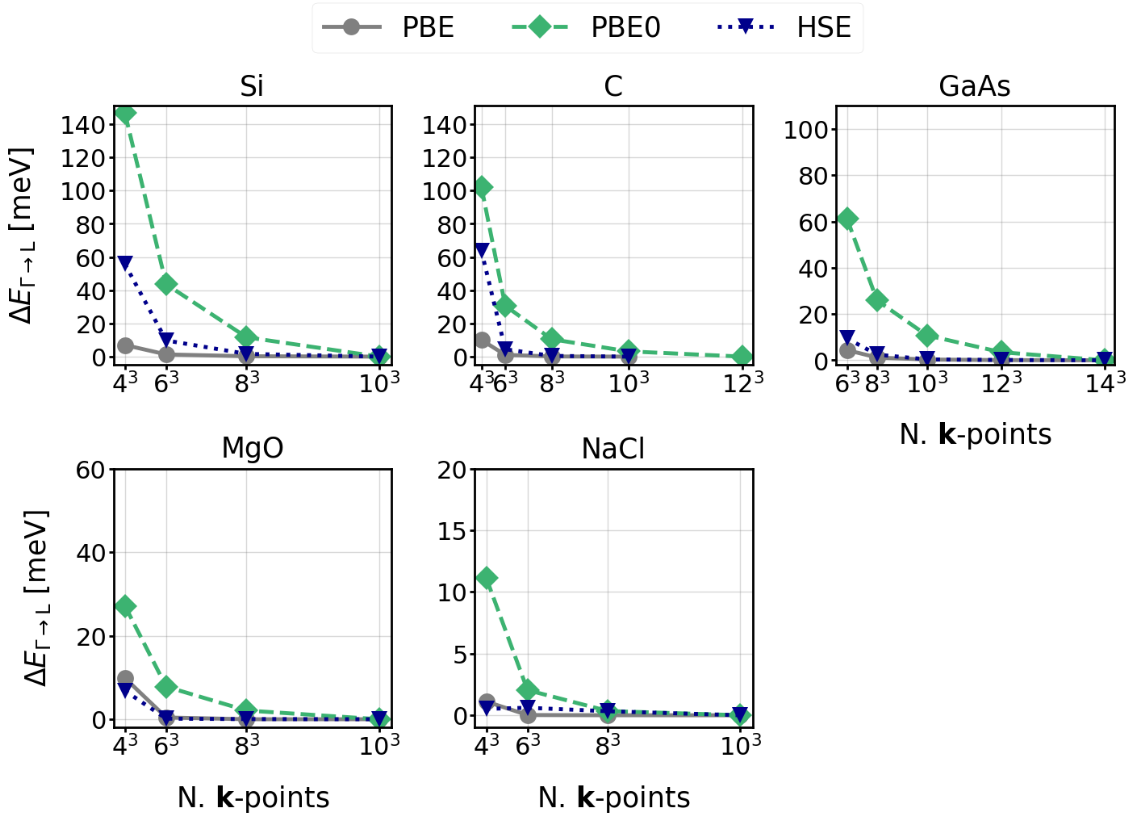

Figure A.2: Convergence behavior of $E_{\Gamma\to L}$ with respect to the $\boldsymbol{k}$-meshes for PBE, PBE0, and HSE.

Table A.3: E_Γ for Si and GaAs and E_g for Ar and PbI_2 computed with HSE for different $\boldsymbol{k}$-meshes, screening parameters ω, and treatment of the singular term (all values in eV). For $\omega = 0$ a_0^{-1} the values are those of PBE0. These data are used in Fig. 4.8.

Si

ω [a_0^{-1}]	Taylor expansion			Exact treatment		
	4x4x4	6x6x6	8x8x8	4x4x4	6x6x6	8x8x8
0.00 (PBE0)	4.078	4.000	3.976	4.078	4.000	3.976
0.03	4.696	3.900	3.763	3.745	3.702	3.705
0.05	3.818	3.628	3.609	3.606	3.593	3.600
0.11 (HSE)	3.342	3.319	3.315	3.330	3.317	3.314
0.15	3.189	3.176	3.174	3.185	3.176	3.174
0.20	3.044	3.040	3.040	3.043	3.040	3.040

GaAs

ω [a_0^{-1}]	Taylor expansion			Exact treatment		
	4x4x4	6x6x6	8x8x8	4x4x4	6x6x6	8x8x8
0.00 (PBE0)	2.098	2.074	2.020	2.098	2.074	2.020
0.03	2.730	1.977	1.834	1.907	1.809	1.785
0.05	1.948	1.732	1.694	1.768	1.703	1.686
0.11 (HSE)	1.407	1.452	1.440	1.494	1.451	1.439
0.15	1.355	1.322	1.313	1.352	1.321	1.313
0.20	1.210	1.190	1.184	1.208	1.190	1.184

Ar

ω [a_0^{-1}]	Taylor expansion			Exact treatment		
	4x4x4	6x6x6	8x8x8	4x4x4	6x6x6	8x8x8
0.00 (PBE0)	11.138	11.134	11.134	11.138	11.134	11.134
0.03	11.877	11.064	10.932	10.807	10.837	10.865
0.05	10.910	10.764	10.759	10.666	10.723	10.748
0.11 (HSE)	10.359	10.359	10.360	10.344	10.357	10.359
0.15	10.133	10.134	10.135	10.129	10.133	10.134
0.20	9.895	9.896	9.896	9.893	9.895	9.896

PbI_2

ω [a_0^{-1}]	Taylor expansion			Exact treatment		
	3x3x2	6x6x4	9x9x6	3x3x2	6x6x4	9x9x6
0.00 (PBE0)	3.605	3.541	3.533	3.605	3.541	3.533
0.03	4.413	3.366	3.329	3.308	3.296	3.318
0.05	3.419	3.198	3.197	3.166	3.187	3.195
0.11 (HSE)	2.901	2.894	2.896	2.886	2.894	2.896
0.15	2.754	2.752	2.752	2.749	2.752	2.752
0.20	2.620	2.621	2.621	2.619	2.621	2.621

APPENDIX B

Supporting materials for Chapter 5

B.1 Convergence parameters for HYB+SOC calculations

Table B.1 summarizes the parameters used for testing the HYB+SOC implementation. For Si, the parameters are those listed in Table A.1, and the number of unoccupied states in SOC calculations is 100.

Table B.1: Computational parameters used to test the HYB+SOC implementation.

xc-functional	$\boldsymbol{k}$-mesh	$R_{\mathrm{MT}}G_{\mathrm{max}}$	N_{unocc}	N_{unocc} (SOC)
		Xe		
PBE	4x4x4	8	-	120
PBE0	6x6x6		80	
HSE	4x4x4			
		MoS_2		
PBE	6x6x1	7	-	200
PBE0	12x12x1		200	
HSE	6x6x1			
		PbI_2		
PBE	3x3x2	8	-	350
PBE0	9x9x6		250	
HSE	3x3x2			

B.2 Density-based mixing method in `exciting`

Equation 2.34 (Eq. 2.35) shows the relation proposed in Ref. [106] to compute the mixing parameter of PBE0 (HSE) knowing $\bar{g}$. It is obtained by fitting the mixing parameter for which PBE0 (HSE) gives the experimental gap, i.e. $\alpha_{\text{opt}}^{\text{PBE0}}$ ($\alpha_{\text{opt}}^{\text{HSE}}$), to $\bar{g}$. Due to the differences between $\bar{g}$ in **exciting** and VASP (see Section 5.2), it is expected that doing the same with **exciting** data might produce different fits. Considering the following models

$$\alpha_{\text{PBE0}} = a + b\bar{g} \quad \text{and} \quad \alpha_{\text{HSE}} = a + b\bar{g}^4, \tag{B.1}$$

We analyze how a and b change when using the two sets of data. The $\bar{g}$ values are given in Table 5.2, the optimal mixing parameters in Table B.2. The latter are evaluated by taking advantage of the linear behavior of the energy gaps of PBE0 and HSE with respect to the mixing parameter. More details about it are given at the end of this section.

Table B.2: Optimal mixing parameters of PBE0 and HSE. Those of **exciting** are obtained following the procedure described at the end of this section. VASP data were kindly shared by the authors of Ref. [106].

Material	**exciting**		VASP	
	$\alpha_{\text{opt}}^{\text{PBE0}}$	$\alpha_{\text{opt}}^{\text{HSE}}$	$\alpha_{\text{opt}}^{\text{PBE0}}$	$\alpha_{\text{opt}}^{\text{HSE}}$
Si	0.1219	0.2631	0.1238	0.2516
C	0.1740	0.2897	0.1737	0.2813
GaAs	0.1699	0.2686	0.1668	0.2632
MgO	0.3111	0.4443	0.3064	0.4262
Ar	0.5647	0.8305	0.5710	0.8198
Xe	0.4691	0.7600	0.4779	0.7643
LiF	0.4060	0.5375	0.4083	0.5351
ZnO	0.2669	0.3771	0.2691	0.3697

Figure B.1 compares the curves obtained by fitting Eq. B.1 with **exciting** and VASP data, and Table B.3 shows the parameters a and b. For both PBE0 and HSE, the **exciting** fit is almost rigidly shifted downward compared to VASP. The reason is that the $\bar{g}$ values computed with **exciting** are, except for Ar, larger than those computed with VASP, while the agreement for the optimal mixing parameters is excellent (the RMSE of the **exciting** results with respect to those of VASP for $\alpha_{\text{opt}}^{\text{PBE0}}$ is only 0.004 and that of $\alpha_{\text{opt}}^{\text{HSE}}$ is only 0.009). It is important to note that the parameters are fitted to a subset of the data, therefore also the VASP results differ from the values proposed in Ref. [106] and given in Eqs. 2.34 and 2.35. The differences between the two codes are on the second decimal digit for all parameters except for a of PBE0, where it is on the first decimal digit.

Our results confirm that it is advisable to remodel Eqs. 2.34 and 2.35 according to the code employed. We note that Jessica Richter worked on finding the best DM model for **`exciting`** in her bachelor's thesis [122].

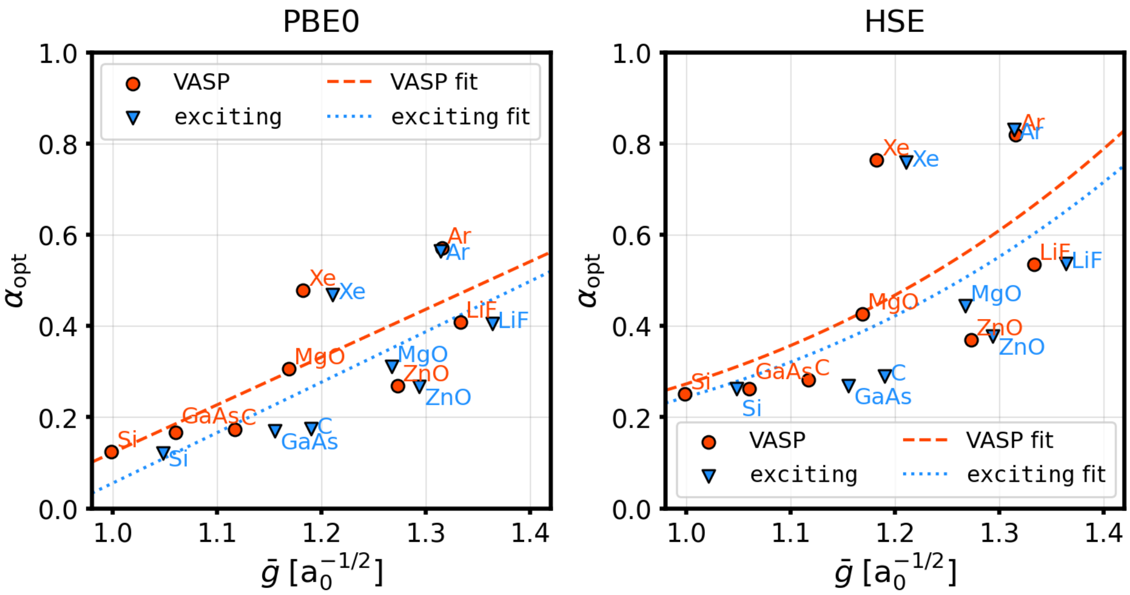

Figure B.1: Optimal mixing parameters versus $\bar{g}$ for PBE0 (left) and HSE (right). The lines are obtained by fitting the **`exciting`** and VASP data to Eq. B.1. The values are provided in Table 5.2.

Table B.3: Parameters a and b of Eq. B.1 obtained by fitting the **`exciting`** and VASP data given in Tables 5.2 and B.2. The last two columns are the parameters of the DM model as proposed in Ref. [106].

Functional	**`exciting`**		VASP		Ref. [106]	
	a	b	a	b	a	b
PBE0	-1.0499	1.1056	-0.9240	1.0465	-1.00778	1.10507
HSE	0.0783	0.1657	0.0919	0.1812	0.121983	0.130711

Evaluation of α_{opt}

The optimal mixing parameters of PBE0 (HSE), shown in Table B.2, are determined from the intersection of the experimental values and the linear fits computed using the PBE, PBE0 (HSE) energy gaps, as shown in Fig. B.2. The equation fitted is $E_g = m\alpha + b'$, and the parameters m and b' computed for the different materials are summarized in Table B.4. The fits are computed employing the `polyfit` function of `Numpy`. α_{opt} is then obtained for each material as

$$\alpha_{\text{opt}} = \frac{E_{\text{g}}^{\text{exp}} - b'}{m}, \tag{B.2}$$

where $E_{\text{g}}^{\text{exp}}$ is the experimental value given in Table 5.3.

This method is justified by the linear behavior of the PBE0 and HSE energy gaps with respect to α (see Fig. D.3). In Ref. [106], the authors used the same idea, but included gaps for other α to get more precise results.

Table B.4: Fitting parameters of $E_{\text{g}} = m\alpha + b'$.

Material	PBE0		HSE	
	m	b'	m	b'
Si	4.8348	0.5804	2.2412	0.5804
C	7.6600	4.1473	4.6008	4.1473
GaAs	5.7696	0.5399	3.6492	0.5399
MgO	9.9304	4.7402	6.9536	4.7402
Ar	9.7328	8.7043	6.6176	8.7043
Xe	7.6264	6.2221	4.7076	6.2221
LiF	12.3364	9.1908	9.3196	9.1908
ZnO	9.4152	0.9272	6.6640	0.9272

B.3 Performance of the new parallelization and memory distribution

New MPI scheme

Figure B.3 shows an example of the performance of the new MPI parallelization scheme described in Section 5.3. For these tests, we used PbI_2 and a $3 \times 3 \times 2$ $\boldsymbol{k}$-mesh. Due to the crystal symmetry, this corresponds to 6 reduced $\boldsymbol{k}$-points which, when multiplied by the 18 $\boldsymbol{q}$-points, form 108 $\boldsymbol{k}$-$\boldsymbol{q}$ pairs. In Fig. B.3, it can be seen that the evaluation of the NL potential (Eq. 3.29) scales remarkably well with the number of MPI processes. In contrast, the inner SCF cycle does not gain any additional speedup after 6 MPI processes, since it is parallelized over the 6 reduced $\boldsymbol{k}$-points. In addition, it does not reach the optimal speedup. When many MPI processes are used, the time spent evaluating the NL potential becomes of the same order as the time spent in the inner SCF cycle. Because of

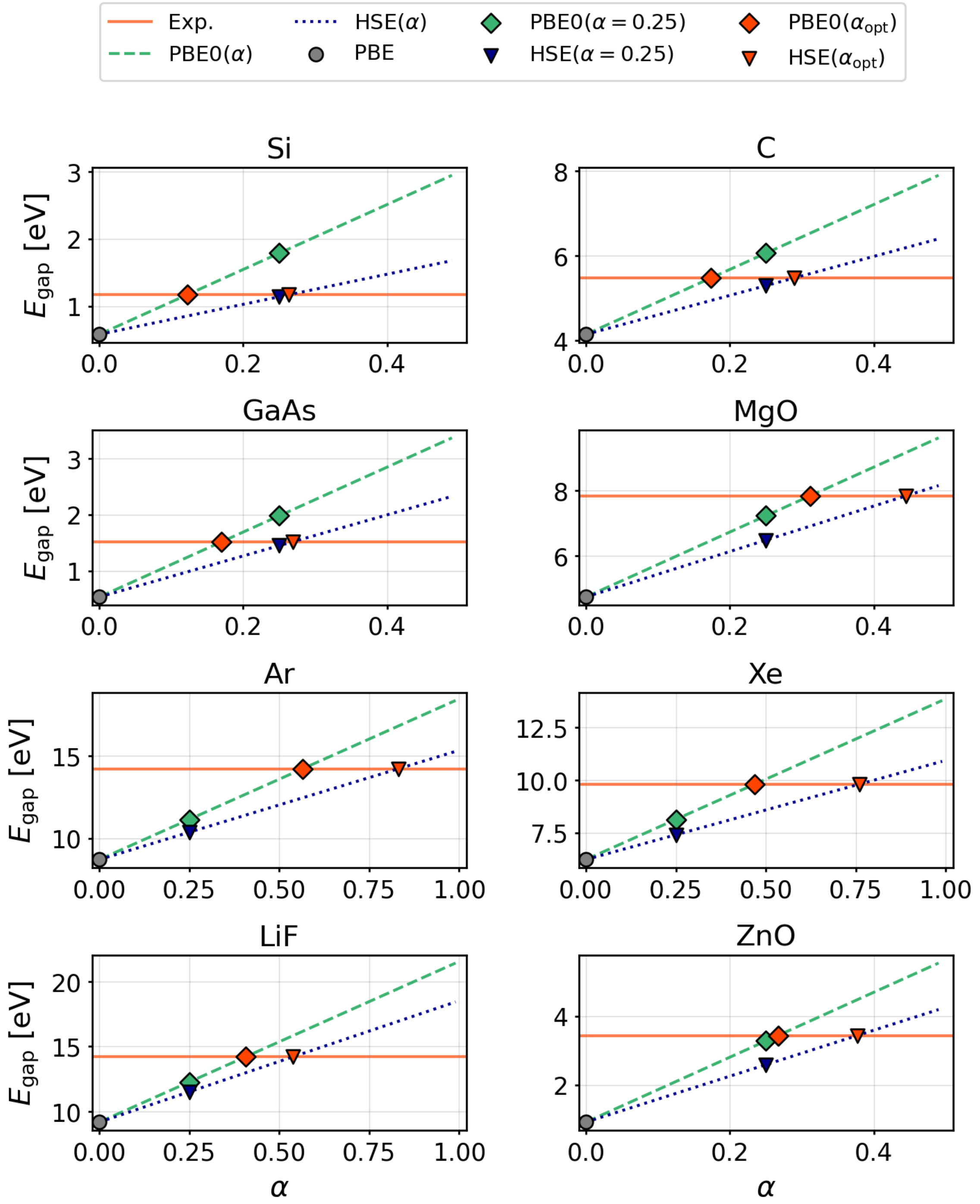

Figure B.2: Intersections (orange diamonds) of the linear fits (PBE0(α) and HSE(α)) with the experimental gap (orange line). The other symbols show the PBE, PBE0 and HSE gaps used to generate the fits.

this, even though the NL potential scales very well with the number of MPI processes, the total time deviates from the optimal speed up beyond 18 processes[1]. The gain compared to the scheme implemented up to the `exciting` version Nitrogen is significant, e.g., for the system under study, a maximum of 6 MPI processes was possible, while, with the new scheme, the speedup is considerable up to 36 MPI processes.

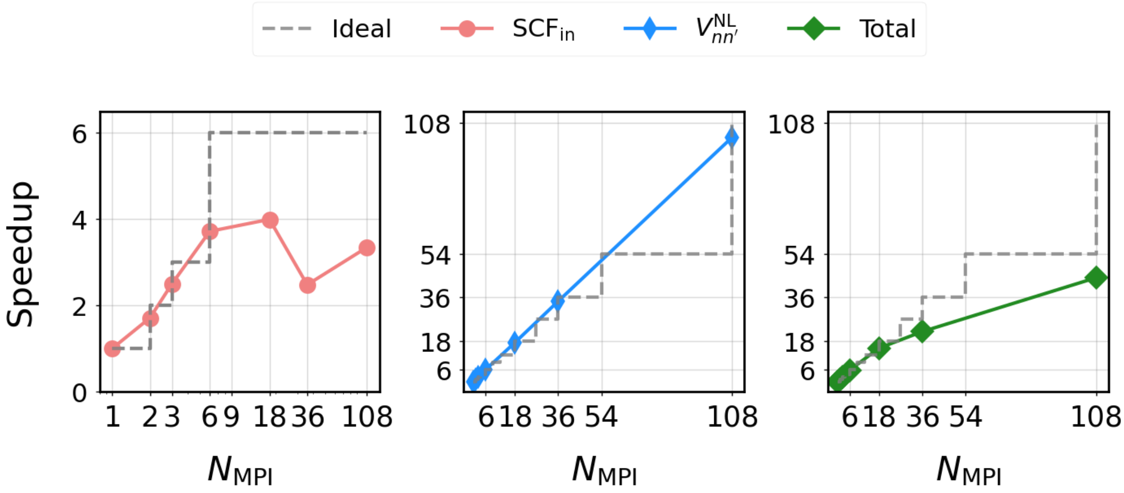

Figure B.3: Speedups when increasing the number of MPI processes for a single inner SCF step (left panel), the calculation of the NL potential (middle panel), and the sum of the two (right panel). The sum is computed by considering 10 inner SCF steps. The ideal speedup is shown as a step curve, since we considered the divisibility of the number of reduced $\boldsymbol{k}$-points (left panel) or $\boldsymbol{k}$-$\boldsymbol{q}$ pairs by the number of MPI processes. Note that the scale of the x-axis on the plot on the left is different from the others. The data used for the plots are listed in Table B.5.

The speedup depends on the parameters and system size. In addition, the number of open multi-processing (OMP) threads used is important to obtain the excellent speedup of the NL potential shown in Fig. B.3. For the data plotted in Fig. B.3 and collected in Table B.5), we used 2 OMP processes.

Memory distribution

In Table B.6, we show the performance of the block distribution given by Eq. 5.3 for PbI_2. The number of occupied states is 151. It can be seen that up to 5 blocks of size 32 there is no noticeable slowdown. With 10 blocks of size 16, the slowdown is 8%, and with 76

---

[1] The total time is calculated by considering 10 steps for the inner cycle. The reason is that initially, the cycle requires approximately 20 steps while getting closer to the convergence the inner SCF steps reduces up to 2.

Table B.5: Time in s spent by `exciting` for computing the inner SCF cycle, the NL potential ($V^{\text{NL}}_{nn'}$), and the sum of both for different MPI settings (first column). The second and the third columns show the number of serial calculations for the NL potentials and the inner SCF cycle, respectively. These numbers are used for the ideal speedup in Fig. B.3.

N_{MPI}	$N_{V^{\text{NL}}_{nn'}}$	$N_{\text{SCF}_{\text{in}}}$	SCF_{in} [s]	$V^{NL}_{nn'}$ [s]	Total [s]
1	108	6	28.82 x 10	6185.60	6473.80
2	54	3	16.87 x 10	3088.08	3256.78
3	36	2	11.53 x 10	2058.70	2174.00
6	18	1	7.76 x 10	1021.93	1099.53
18	6	1	7.22 x 10	361.21	433.41
36	3	1	11.64 x 10	180.38	296.78
108	1	1	8.62 x 10	60.60	146.80

Table B.6: Time in s spent evaluating the NL potential (Eq. 5.3) for different block sizes (S_{b}) and the corresponding number of blocks (N_{blk}). The maximum block size for these tests is 151.

S_{b}	2	4	8	16	32	64	128	All
N_{blk}	76	38	19	10	5	3	2	1
Time [s]	173.44	130.17	107.67	101.94	94.74	94.66	94.74	94.78

blocks of size 2 it is 83%. These tests show that the current block distribution can help in running calculations with medium-large size systems, but must be used with caution.

APPENDIX C

Supporting materials for Chapter 6

C.1 Convergence with the SV(LO) basis

Tables C.1-C.5 contain all the data used to generate the plots in Figs. 6.2 and 6.10. Table C.6 shows the data of Xenon, obtained by using a single $\boldsymbol{k}$-point (Fig. 6.4). In all tables, the results are shown for the p-set of LO with the NP, SV, and SVLO methods, and the $p_{1/2}$ set with NP and SVLO. The only exception is MoS_2, for which only the p-set was used. The number of basis functions (second column) omits the number of occupied states. In the case of SVLO, the number of unoccupied states (first number) is distinguished from that of the LO functions, which is added to it. The numbers of occupied states and LO are given for all materials in Table 6.2.

Table C.1: Total energy (E_{tot}), energy gap (E_{g}), and SOC splitting (δ_{SOC}) computed for Xenon using different methods (NP, SV, or SVLO) and LO sets (p or $p_{1/2}$-set). For the SV and the SVLO methods, the quantities are given for different numbers of basis functions (excluding valence states). Note that for the SVLO method, this number is given by the sum of the unoccupied states plus the number of LO (26 for the p-set and 38 for the $p_{1/2}$-set). These numbers are given in the column $\tilde{N}_{\mathrm{b}}^{\mathrm{SV(LO)}}$.

	$\tilde{N}_{\mathrm{b}}^{\mathrm{SV(LO)}}$	E_{tot} [eV/atom]	E_{g} [eV]	δ_{SOC} [eV]
NP(p)	-	-202730.7184313	5.7879208	1.3055232
SV(p)	10	-202730.3095063	5.7783156	1.2769067
	30	-202730.4062343	5.7869169	1.2912677
	50	-202730.4782035	5.7890398	1.2937172
	75	-202730.5377842	5.7894778	1.2983198
	100	-202730.5759566	5.7886224	1.2993532
	125	-202730.6241395	5.7878534	1.3007338
	150	-202730.6478028	5.7875029	1.3010581
SVLO(p)	1+26	-202730.7166988	5.7881449	1.3053154
	4+26	-202730.7178754	5.7879106	1.3053765
	14+26	-202730.7182767	5.7878575	1.3054641
	34+26	-202730.7184185	5.7879029	1.3055163
	54+26	-202730.7184299	5.7879193	1.3055171
	74+26	-202730.7184291	5.7879225	1.3055173
	94+26	-202730.7184302	5.7879226	1.3055173
NP($p_{1/2}$)	-	-202732.9993302	5.7852006	1.3981448
SVLO($p_{1/2}$)	3+38	-202732.9984926	5.7853723	1.3980594
	7+38	-202732.9992186	5.7852218	1.3980864
	17+38	-202732.9993223	5.7852013	1.3981290
	32+38	-202732.9993038	5.7852008	1.3981392
	52+38	-202732.9993640	5.7852023	1.3981393
	72+38	-202732.9993033	5.7852023	1.3981393
	92+38	-202732.9993773	5.7852024	1.3981393

Table C.2: Same as Table C.1 but for MoS_2. In this case, the values are shown only for the *p*-set, which consists of 35 SR-LO basis functions.

	$\tilde{N}_{\mathrm{b}}^{\mathrm{SV(LO)}}$	E_{tot} [eV/atom]	E_{g} [eV]	δ_{SOC} [eV]
NP(p)	-	-43974.4011292	1.7065039	0.1461521
SV(p)	10	-43974.3768537	1.7061232	0.1460952
	50	-43974.3848232	1.7060410	0.1461051
	100	-43974.3899940	1.7058386	0.1462460
	300	-43974.3962433	1.7058671	0.1463189
	500	-43974.3981974	1.7058720	0.1463354
	700	-43974.3990143	1.7058767	0.1463443
	900	-43974.3994864	1.7058761	0.1463493
	1000	-43974.4005639	1.7058859	0.1463602
SVLO(p)	1+35	-43974.3996929	1.7075050	0.1459476
	15+35	-43974.4006170	1.7059036	0.1463524
	65+35	-43974.4008640	1.7059017	0.1463533
	165+35	-43974.4009266	1.7058941	0.1463586
	265+35	-43974.4009363	1.7058927	0.1463592
	365+35	-43974.4009389	1.7058930	0.1463592
	465+35	-43974.4009363	1.7058927	0.1463592

Table C.3: Same as Table C.1 but for $\mathrm{PbI_2}$. In this case, two band energies are considered, i.e. δ^1_{SOC} and δ^2_{SOC}. The number of LO basis functions is 73 for the p-set and 109 for the $p_{1/2}$-set.

	$\tilde{N}_{\mathrm{b}}^{\mathrm{SV(LO)}}$	E_{tot} [eV/atom]	E_{g} [eV]	δ^1_{SOC} [eV]	δ^2_{SOC} [eV]
NP(p)	-	-318975.7100574	1.6561961	1.2455577	0.6349072
SV(p)	10	-318975.0317084	1.7218586	1.1994620	0.6334524
	50	-318975.2444289	1.6887372	1.2184964	0.6338019
	150	-318975.4706126	1.6690999	1.2358823	0.6320013
	225	-318975.5451264	1.6646409	1.2380798	0.6343337
	275	-318975.5796278	1.6604174	1.2423138	0.6328403
	325	-318975.6836043	1.6563895	1.2447716	0.6346157
	375	-318975.6923155	1.6559352	1.2455031	0.6343601
SVLO(p)	2+73	-318975.7060990	1.6624219	1.2484202	0.6276334
	27+73	-318975.7095340	1.6568620	1.2451116	0.6347504
	77+73	-318975.7100283	1.6561570	1.2454427	0.6348095
	127+73	-318975.7100864	1.6561137	1.2454727	0.6348256
	177+73	-318975.7101027	1.6561097	1.2454760	0.6348270
	227+73	-318975.7101072	1.6561107	1.2454795	0.6348299
NP($p_{1/2}$)	-	-318980.3914764	1.4029338	1.4527091	0.6766162
SVLO($p_{1/2}$)	11+109	-318980.3899317	1.4089155	1.4508910	0.6732336
	41+109	-318980.3914111	1.4029249	1.4526387	0.6764507
	91+109	-318980.3915181	1.4028554	1.4526423	0.6765145
	141+109	-318980.3915317	1.4028506	1.4526477	0.6765200
	191+109	-318980.3915335	1.4028513	1.4526488	0.6765230
	241+109	-318980.3915354	1.4028539	1.4526502	0.6765262

Table C.4: Same as Table C.1 but for $CsPbI_3$. The LO functions are 496 for the p-set and 736 for the $p_{1/2}$-set.

	$\tilde{N}_{\mathrm{b}}^{\mathrm{SV(LO)}}$	E_{tot} [eV/atom]	E_{g} [eV]	δ_{SOC} [eV]
NP(p)	-	-272525.7528487	0.8188481	0.7116576
SV(p)	400	-272525.4168929	0.8502164	0.7051896
	800	-272525.5242269	0.8372910	0.7074759
	1200	-272525.5891968	0.8304168	0.7092983
	1600	-272525.6282682	0.8270865	0.7101675
	2000	-272525.6535109	0.8253852	0.7100035
	2400	-272525.6711180	0.8238125	0.7103545
	2800	-272525.6836992	0.8223107	0.7110815
	3200	-272525.7046669	0.8212167	0.7109856
	3600	-272525.7512759	0.8187217	0.7115233
SVLO(p)	14+496	-272525.7475357	0.8283473	0.7125708
	24+496	-272525.7487031	0.8232515	0.7154901
	54+496	-272525.7509848	0.8221416	0.7154602
	104+496	-272525.7521059	0.8205546	0.7112537
	304+496	-272525.7531100	0.8190900	0.7115917
	504+496	-272525.7533195	0.8188538	0.7114820
	1004+496	-272525.7534215	0.8187570	0.7114782
	1504+496	-272525.7534487	0.8187435	0.7114755
	2004+496	-272525.7534583	0.8187393	0.7114758
	2504+496	-272525.7534623	0.8187380	0.7114758
NP($p_{1/2}$)	-	-272530.1075084	0.5544823	0.7635506
SVLO($p_{1/2}$)	18+736	-272519.8886461	0.3002558	0.4338434
	68+736	-272530.1050005	0.5636588	0.7754658
	168+736	-272530.1076087	0.5554034	0.7633039
	618+736	-272530.1080373	0.5543631	0.7633948
	1000+736	-272530.1080536	0.5543462	0.7633924
	1368+736	-272530.1080577	0.5543435	0.7633929
	1868+736	-272530.1080591	0.5543429	0.7633930

Table C.5: Same as Table C.1 but for Bi_2Te_3. Additionally, the last column shows the transition between the highest VB and the lowest CB at Γ. The number of LO is 141 for the p-set and 201 for the $p_{1/2}$-set.

	$\tilde{N}_{\mathrm{b}}^{\mathrm{SV(LO)}}$	E_{tot} [eV/atom]	E_{g} [eV]	E_{Γ} [eV]
NP(p)	-	-345874.2277445	0.0969901	0.5833215
SV(p)	10	-345872.8154972	0.1484337	0.4784063
	100	-345873.1835964	0.1225359	0.5323564
	200	-345873.4417410	0.1131084	0.5466970
	300	-345873.6130383	0.1101241	0.5530490
	400	-345873.7411789	0.1055931	0.5635106
	500	-345873.8403959	0.1028060	0.5677149
	600	-345873.9163739	0.1024370	0.5694921
	700	-345873.9674230	0.1018667	0.5708503
	800	-345874.0189059	0.1005487	0.5744046
	900	-345874.1618984	0.0981572	0.5831072
	1000	-345874.2182782	0.0971516	0.5831423
SVLO(p)	9+141	-345874.2238261	0.1012970	0.5766531
	59+141	-345874.2271453	0.0970968	0.5830319
	159+141	-345874.2275878	0.0969855	0.5833383
	259+141	-345874.2276379	0.0969704	0.5833756
	359+141	-345874.2276515	0.0969660	0.5833836
	459+141	-345874.2276580	0.0969646	0.5833871
	559+141	-345874.2276585	0.0969630	0.5833883
	659+141	-345874.2276607	0.0969624	0.5833887
NP($p_{1/2}$)	-	-345878.7493217	0.0328684	0.6942499
SVLO($p_{1/2}$)	19+201	-345878.7422718	0.0647076	0.6957863
	49+201	-345878.7487443	0.0330188	0.6942767
	99+201	-345878.7491808	0.0328674	0.6943781
	199+201	-345878.7492423	0.0328613	0.6944088
	299+201	-345878.7492488	0.0328599	0.6944082
	399+201	-345878.7492526	0.0328597	0.6944079
	499+201	-345878.7492461	0.0328598	0.6944083
	599+201	-345878.7492483	0.0328599	0.6944084
	699+201	-345878.7492434	0.0328600	0.6944085

Table C.6: Same as Table C.1 but for calculations using only 1 $\boldsymbol{k}$-point. The results are only for the $\boldsymbol{p}$-set of LO.

	$\tilde{N}_{\mathrm{b}}^{\mathrm{SV(LO)}}$	E_{tot} [eV/atom]	E_{g} [eV]	δ_{SOC} [eV]
NP($\boldsymbol{p}$)	-	-202726.8086661	1.2535970	4.9337268
SV($\boldsymbol{p}$)	10	-202726.3561106	1.2252635	4.9202733
	20	-202726.4748029	1.2358945	4.9321943
	30	-202726.5162238	1.2395446	4.9310958
	40	-202726.5574618	1.2420396	4.9334954
	50	-202726.5610099	1.2422004	4.9334224
	75	-202726.6400679	1.2465071	4.9338487
	100	-202726.6606814	1.2476568	4.9340955
	125	-202726.6875134	1.2488586	4.9341824
	150	-202726.8086645	1.2535906	4.9337292
SVLO($\boldsymbol{p}$)	1+26	-202726.8080277	1.2534212	4.9328332
	14+26	-202726.8084618	1.2535399	4.9336643
	34+26	-202726.8086596	1.2535896	4.9337414
	54+26	-202726.8086631	1.2535903	4.9337311
	74+26	-202726.8086639	1.2535905	4.9337274
	94+26	-202726.8086648	1.2535906	4.9337277

C.2 Tests of BSE with SOC in `exciting`

C.2.1 BSE+SOC validation

To test the implementation of SOC for the BSE method, we use the MoS_2 monolayer. The implementation was done by Christian Vorwerk. For comparison, we use the work of Marsili and co-workers [234]. Between these and our calculations, there are, however, a few differences, e.g. the crystal structure and the BSE starting point. While in Ref. [234] G_0W_0 results are used, we use PBE eigenenergies.[1]. This choice is justified by the fact that in MoS_2 the SOC effects are not strongly dependent on the crystal structure and on the method used to compute the electronic structure [210, 234]. Additionally, these results serve only as a test.

When including SOC, as discussed in Section 6.5.1, the VBM at K splits by 0.15 eV (Fig. 6.5 and Table 6.4). This splitting is also reflected in the optical spectra, where the single peak observed for calculations without SOC (A′) splits into two separate peaks (A and B), which are 133 meV apart (Table C.7 and Fig. C.1). In addition, the A (B) peak is preceded by a dark peak referred to as "A dark" ("B dark"). The peak positions are listed in Table C.8. In Fig. C.2, visualizing the bright excitons corresponding to the peaks A′, A and B, the connection between the SOC splitting at K observed in the electronic structure and the splitting of the first peak in the optical spectra becomes clear.

Table C.7: Binding energies computed from SR calculations (E_b^SR), from calculations including SOC ($E_\mathrm{b}^\mathrm{SOC}$), and binding energy differences between the two cases ($\Delta E_\mathrm{b} = E_\mathrm{b}^\mathrm{SR} - E_\mathrm{b}^\mathrm{SOC}$). In the last column, there is the energy difference between the peaks A and B. The values from Ref. [234] are those obtained with the perturbative treatment of SOC for the GW-BSE approach.

	E_b^SR [meV]	$E_\mathrm{b}^\mathrm{SOC}$ [meV]	ΔE_b [meV]	A-B [meV]
`exciting`	381	384	-3	133
Ref. [234]	679	673	6	140

By comparing the results obtained with `exciting` with those of Ref. [234], good agreement can be observed regarding the A-B distance (Table C.7), the spectral shape, as well as the alternation of dark and bright excitations. Regarding the binding energy, the difference to Ref. [234] is significant for both the results with SOC and without SOC.

---

[1] Computational details: The atomic structure, the parameters and functionals used for the ground-state calculation are the same as in Ref. [288]. For the BSE calculation, a 33x33x1 $\boldsymbol{k}$-grid and $\boldsymbol{q}$-grid are employed, the cutoff for the LFE is set to `gqmax=2`, and the Lorentzian broadening to 0.00183 Ha. The spectra include excitations only coming from the 2 highest VB and the two lowest CB (disregarding spin).

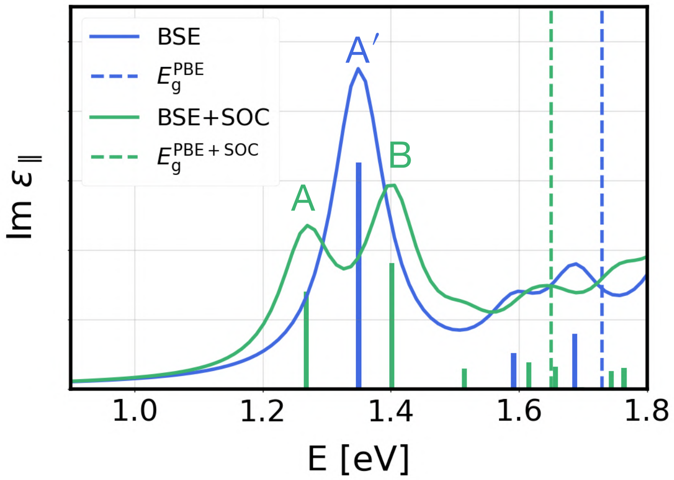

Figure C.1: Optical spectra of MoS_2 for excitations between the 2 highest VB and the 2 lowest CB (disregarding spin) computed with and without SOC. The vertical solids lines are the oscillation strength of the excitations, and the dashed lines are the energy gaps computed with PBE and PBE+SOC.

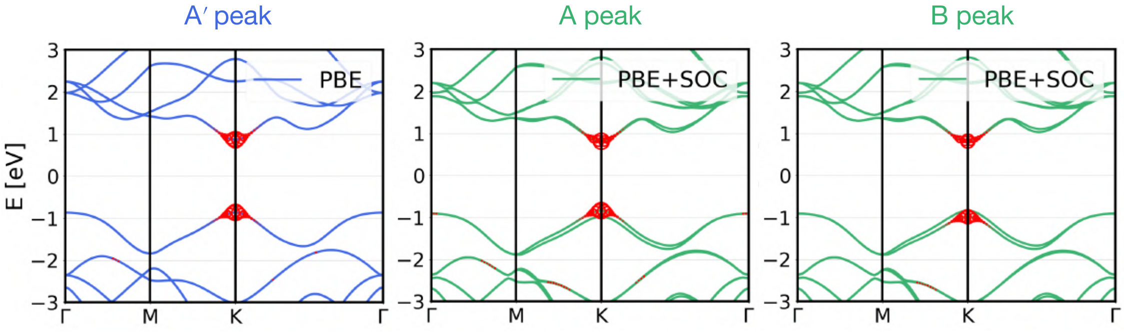

Figure C.2: Reciprocal space representation of the excitons corresponding to the peaks A′ (BSE omitting SOC), A, and B (the latter two including SOC).

However, the difference in binding energies ($\Delta E_\mathrm{b} = E_\mathrm{b}^\mathrm{nSOC} - E_\mathrm{b}^\mathrm{SOC}$) is comparable to that of Ref. [234]: Even if one value is positive and the other is negative, the difference between the two is only 9 meV. Moreover, the difference between the perturbative and the full SOC treatment in Ref. [234] is much larger ($E_\mathrm{b}^\mathrm{pert}$=673 meV $E_\mathrm{b}^\mathrm{full}$=691 meV). This discrepancy is independent of the implementation of BSE+SOC. We attribute it in part to the lack of a Coulomb cutoff in the evaluation of the screening, which is important in low-dimensional systems to speed up the $\boldsymbol{k}$-point convergence and reduce the amount of vacuum needed. Ben Alex implemented this method for G_0W_0 and BSE calculations in his master thesis [289] after this preliminary work presented here. He showed that,

Table C.8: Time spent on BSE+SOC calculations for an increasing number of unoccupied states. For comparison, the first row shows the case without SOC (SR) using N_{unocc}=100. The other rows show the peak positions with respect to the energy gap. The A′ peak, obtained for BSE without SOC, is shown in the column of the A peak. Up to 40 unoccupied states ($\mathrm{N}_{\text{unocc}}$), the peak positions are not well determined. Therefore, no values are included for these cases. All calculations are performed with 8 nodes and 4 MPI processes per node each one employing 4 CPUs.

N_{unocc}	Time	A dark [meV]	A [meV]	B dark [meV]	B [meV]
SR (100)	2 h 26 m	-	381 (A′)	-	
10	8 h 53 m	-			
20	11 h 50 m	-			
30	13 h 46 m	-			
40	15 h 48 m	-			
50	18 h 21 m	-402	-384	-257	-251
60	21 h 43 m	-402	-384	-257	-251
100	34 h 21 m	-402	-384	-257	-251

without the Coulomb cutoff, a binding energy value comparable to that of Table C.7 (SR) is obtained when using a 33x33x1 $\boldsymbol{k}$- and $\boldsymbol{q}$-mesh. On the other hand, when including the Coulomb cutoff, for the same $\boldsymbol{k}$- and $\boldsymbol{q}$-grid, the binding energy is 0.47 eV, which is in closer agreement with the result from Ref. [234].

C.2.2 Efficiency of the BSE+SOC implementation

Another important aspect of the BSE+SOC implementation is the increase in computational time due to the inclusion of SOC. The time also increases with the number of unoccupied states. In Table C.8, these results are collected. Including SOC with only 10 empty states quadruples the computational time, and with 100, it is 14 times higher. Up to 50 empty states, the calculations are not stable. Therefore, the code needs approximately 7.5 times longer than calculations without SOC. This clearly shows that for $\mathrm{CsPbI_3}$, which is about 4 times larger than $\mathrm{MoS_2}$ (see Table 6.2), and which needs approximately 1600 empty states for reaching a band gap precision of 10^{-2} (Table C.4), BSE calculations including SOC are not feasible with this code version.

As a side note, these tests served as a starting point for the implementation of the many-body theory of valley-selective circular dichroism and valley excitons based on the BSE, implemented by Max Schebeck and used in Ref. [231].

C.3 Extension of the SVLO method to optical spectra

The aim is to extend the SVLO method to BSE to enable the calculation of optical spectra of complex materials, where SOC is important. This implementation is not yet complete, but in this section, we want to show the work done so far and the steps needed to complete the project. The project was started in collaboration with Sven Lubeck and Keith Gilmore, and is now continued within the master thesis of Seokhyun Hong.

Two main modifications have been identified within the TDA, namely the evaluation of the momentum and plane-wave matrix elements. Beyond the TDA, additional changes would be required [290]. More information about the definition of these quantities can be found in Ref. [290].

As explained in Section 3.6, the BSE is obtained by the sum of three terms. The evaluation of the momentum matrix elements is sufficient for computing the diagonal term, and therefore to obtain the IPA spectra. Contrarily, for computing RPA or BSE spectra, also the plane-wave matrix elements must be evaluated. Here, we only show the modifications that we applied to the momentum matrix elements. Subsequently, the implementation is validated using LiF and $\mathrm{PbI_2}$. A similar idea should be applied to the plane-wave matrix elements.

Momentum matrix elements

Omitting SOC, the momentum matrix elements are evaluated as:

$$\begin{aligned} P^j_{nn'\boldsymbol{k}} = \langle n\boldsymbol{k}|\, i\nabla_j \,|n'\boldsymbol{k}\rangle = &\sum_{\boldsymbol{G}'\boldsymbol{G}''} c^{\boldsymbol{k}*}_{n\boldsymbol{G}'} c^{\boldsymbol{k}}_{n'\boldsymbol{G}''} P^j_{\boldsymbol{G}'\boldsymbol{G}''\boldsymbol{k}} + \sum_{\boldsymbol{G}'\mu''} c^{\boldsymbol{k}*}_{n\boldsymbol{G}'} c^{\boldsymbol{k}}_{n'\mu''} P^j_{\boldsymbol{G}'\mu''\boldsymbol{k}} \\ &+ \sum_{\mu'\boldsymbol{G}''} c^{\boldsymbol{k}*}_{n\mu'} c^{\boldsymbol{k}}_{n'\boldsymbol{G}''} P^j_{\mu'\boldsymbol{G}''\boldsymbol{k}} + \sum_{\mu'\mu''} c^{\boldsymbol{k}*}_{n\mu'} c^{\boldsymbol{k}}_{n'\mu''} P^j_{\mu'\mu''\boldsymbol{k}}, \end{aligned} \tag{C.1}$$

where j is the direction of the incoming light. $c^{\boldsymbol{k}}_{n'\boldsymbol{G}'}$ and $c^{\boldsymbol{k}}_{n'\mu'}$ are the coefficients of the APW and LO basis functions, respectively (Eq. 3.8), and $P^j_{\boldsymbol{G}'\boldsymbol{G}''}$, $P^j_{\boldsymbol{G}'\mu''\boldsymbol{k}}$, $P^j_{\mu'\boldsymbol{G}''\boldsymbol{k}}$, and $P^j_{\mu'\mu''\boldsymbol{k}}$ are the APW-APW, APW-LO, LO-APW, LO-LO momentum matrix elements, respectively:

$$P^j_{\boldsymbol{G}'\boldsymbol{G}''\boldsymbol{k}} = \langle \phi^{\mathrm{APW}}_{\boldsymbol{G}'+\boldsymbol{k}}(\boldsymbol{r})|\, - i\nabla_j \,|\phi^{\mathrm{APW}}_{\boldsymbol{G}''+\boldsymbol{k}}(\boldsymbol{r})\rangle\,; \tag{C.2}$$

$$P^j_{\boldsymbol{G}'\mu''\boldsymbol{k}} = \langle \phi^{\mathrm{APW}}_{\boldsymbol{G}+\boldsymbol{k}}(\boldsymbol{r})|\, - i\nabla_j \,|\phi_{\mu''}(\boldsymbol{r})\rangle\,; \tag{C.3}$$

$$P^j_{\mu'\boldsymbol{G}''\boldsymbol{k}} = \langle \phi_{\mu'}(\boldsymbol{r})|\, - i\nabla_j \,|\phi^{\mathrm{APW}}_{\boldsymbol{G}''+\boldsymbol{k}}(\boldsymbol{r})\rangle\,; \tag{C.4}$$

$$P^{j}_{\mu'\mu''\boldsymbol{k}} = \langle \phi_{\mu'}(\boldsymbol{r})| - i\nabla_j \, |\phi_{\mu''}(\boldsymbol{r})\rangle . \tag{C.5}$$

When SOC is considered, the momentum matrix elements become

$$P^{j,\mathrm{SV}}_{ab\boldsymbol{k}} = \sum_{\sigma'=1}^{2} \sum_{\sigma''=1}^{2} \sum_{n'=1}^{N_{\mathrm{b}}^{\mathrm{SV}}} \sum_{n''=1}^{N_{\mathrm{b}}^{\mathrm{SV}}} C^{\boldsymbol{k}*}_{an'\sigma'} C^{\boldsymbol{k}}_{bn''\sigma''} P^{j}_{n'n''\boldsymbol{k}}, \tag{C.6}$$

where a and b are the SV band indices, $C^{\boldsymbol{k}}_{an'\sigma'}$ are the SV coefficients used in Eq. 3.33, and $N_{\mathrm{b}}^{\mathrm{SV}} = N_{\mathrm{occ}} + N_{\mathrm{unocc}}^{(\mathrm{SV})}$. $P^{j}_{n'n''\boldsymbol{k}}$ is defined in Eq. C.1. Within the SVLO method, Eq. C.6 is rewritten as:

$$P^{j,\mathrm{SVLO}}_{ab\boldsymbol{k}} = \sum_{\sigma'=1}^{2} \sum_{\sigma''=1}^{2} \sum_{n'=1}^{N_{\mathrm{b}}^{\mathrm{SVLO}}} \sum_{n'=1}^{N_{\mathrm{b}}^{\mathrm{SVLO}}} C^{\boldsymbol{k}}_{an'\sigma'} C^{\boldsymbol{k}}_{bn''\sigma''} \bar{P}^{j}_{n'n''\boldsymbol{k}}. \tag{C.7}$$

This time, the sum over n, n'' goes up to $N_{\mathrm{b}}^{\mathrm{SVLO}} = N_{\mathrm{occ}} + N_{\mathrm{unocc}}^{(\mathrm{SVLO})} + N_{\mathrm{LO}}$, and $\bar{P}^{j}_{n'n''\boldsymbol{k}}$ is defined as

$$\bar{P}^{j}_{n'n''\boldsymbol{k}} = \begin{cases} \sum_{\boldsymbol{G}'\boldsymbol{G}''} c^{\boldsymbol{k}*}_{n\boldsymbol{G}'} c^{\boldsymbol{k}}_{n'\boldsymbol{G}''} P^{j}_{\boldsymbol{G}'\boldsymbol{G}''\boldsymbol{k}} & 1 \leq n', n'' \leq N_{\mathrm{b}}^{\mathrm{SV}}; \\ \sum_{\boldsymbol{G}'\mu''} c^{\boldsymbol{k}*}_{n\boldsymbol{G}'} P^{j}_{\boldsymbol{G}'\mu''\boldsymbol{k}} & 1 \leq n' \leq N_{\mathrm{b}}^{\mathrm{SV}},\ N_{\mathrm{b}}^{\mathrm{SV}} + 1 \leq n'' \leq N_{\mathrm{b}}^{\mathrm{SV}} + N_{\mathrm{LO}}; \\ \sum_{\mu'\boldsymbol{G}''} c^{\boldsymbol{k}}_{n'\boldsymbol{G}''} P^{j}_{\mu'\boldsymbol{G}''\boldsymbol{k}} & N_{\mathrm{b}}^{\mathrm{SV}} + 1 \leq n' \leq N_{\mathrm{b}}^{\mathrm{SV}} + N_{\mathrm{LO}},\ 1 \leq n'' \leq N_{\mathrm{b}}^{\mathrm{SV}}; \\ \sum_{\mu'\mu''} P^{j}_{\mu'\mu''\boldsymbol{k}} & N_{\mathrm{b}}^{\mathrm{SV}} + 1 \leq n', n'' \leq N_{\mathrm{b}}^{\mathrm{SV}} + N_{\mathrm{LO}}. \end{cases} \tag{C.8}$$

In this case, $\bar{P}^{j}_{n'n''\boldsymbol{k}}$ is defined differently, depending on which representation the states n', n'' fall into, i.e. modified FV KS (Eq. 6.2 or LO functions. The coefficients associated to the LO are set to one.

Validation of IPA spectra

To validate the implementation of the SVLO momentum matrix elements just discussed, we show here the optical spectra of LiF and PbI$_2$ computed within the IPA picture as implemented in the BSE approach[2]. In LiF the influence of SOC is negligible and no differences should be observed in the spectra for calculations with and without SOC. In fact, in the top panel of Fig. C.3 all spectra coincide. Only a few empty states are needed

---

[2] Computational details: These calculations are for testing purposes only, therefore the results do not need to be fully converged with respect to all computational parameters. For both materials, the calculations are performed with `gqmax=2.5`, and a Lorentzian broadening of 0.007 Ha. In the case of LiF, a $6 \times 6 \times 6$ $\boldsymbol{k}$- and $\boldsymbol{q}$-grid are employed; all occupied states and 5 unoccupied states (disregarding spin) are considered. In the case of PbI$_2$, we used a $4 \times 4 \times 2$ $\boldsymbol{k}$- and $\boldsymbol{q}$-grid, and transition between the last 5 occupied states and the first 10 unoccupied states (disregarding spin)

to converge the SV spectra as evident from the bottom-right panel. This means that, in this case, the SVLO method (bottom-left panel Fig. C.3), where we use 50 LO functions in addition to the unoccupied states, is computationally less efficient .

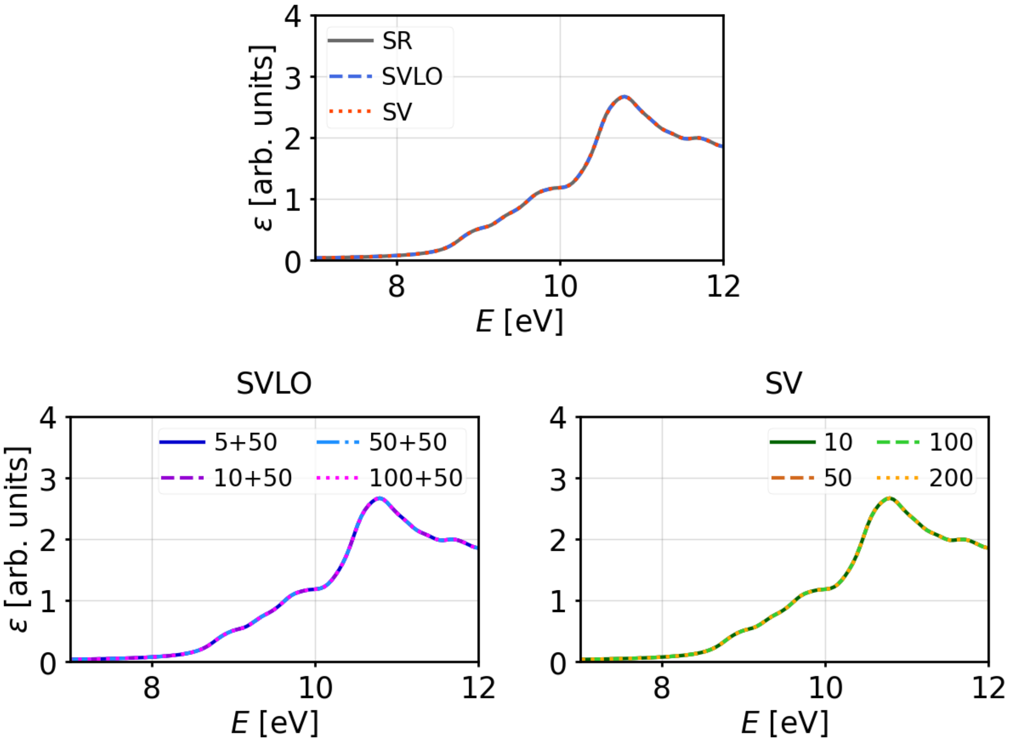

Figure C.3: Optical spectra of LiF within the IPA picture. In the top panel, the spectra computed without SOC (SR) and with SOC are compared. The bottom panels show the convergence of the spectra with respect to the reduced number of basis functions ($\tilde{N}_{\mathrm{b}}^{\mathrm{SV(LO)}}$) for the SVLO (left panel) and the SV method (right panel). The number of LO is 50.

In PbI_2, on the other hand, we know that the SOC effects are significant. The in-plane and out-of-plane optical spectra, computed with and without SOC show major differences (Fig. C.4, top panels), but the spectra computed with the SVLO and the SV methods overlap. In this case, a slower convergence is observed in the SV case, requiring $N_{\mathrm{b}}^{\mathrm{SV}} \sim 400$, while the SVLO spectrum converges with 16 empty bands and 54 LO.

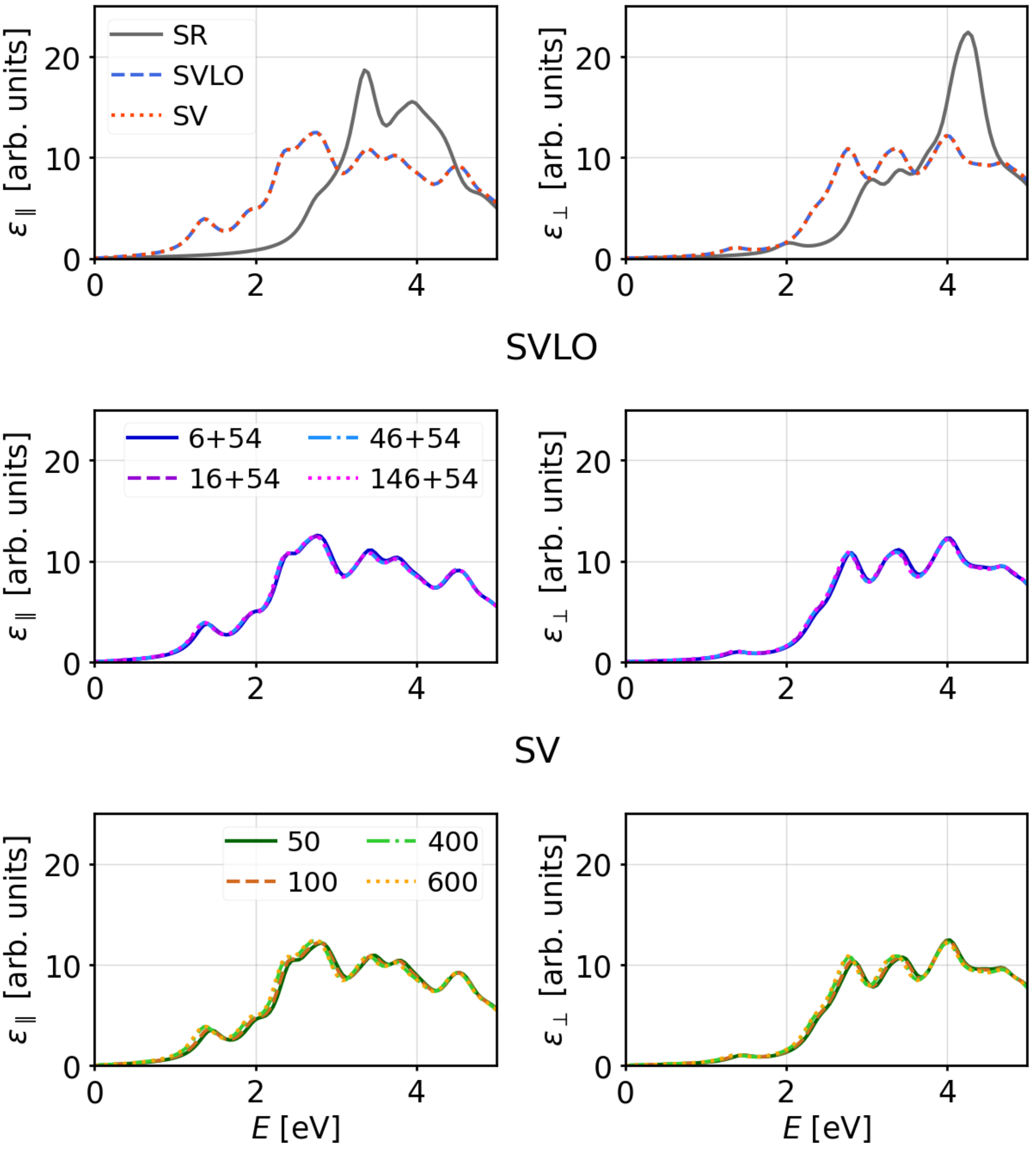

Figure C.4: In-plane ($\varepsilon_\parallel$) and out-of-plane ($\varepsilon_\perp$) components of the optical spectra of PbI_2 in the IPA. The top panels show the SR sepctra compared with th SVLO and SV spectra converged with respect to the number of basis functions. The middle panels show the convergence of the SVLO spectra with respect to $\tilde{N}_b^{\mathrm{SVLO}}$, where the number of LO is 54. The bottom panels show the same for the SV method.

APPENDIX D

Supporting material for Chapter 7

D.1 Literature data of PbI_2 band gaps

Figure 7.1 shows the PbI_2 band gap calculated with different methods within DFT and MBPT and with or without SOC. Some results are obtained with `exciting`, others are taken from the literature. In Fig. D.1, we provide the information on the references from which the data are taken.

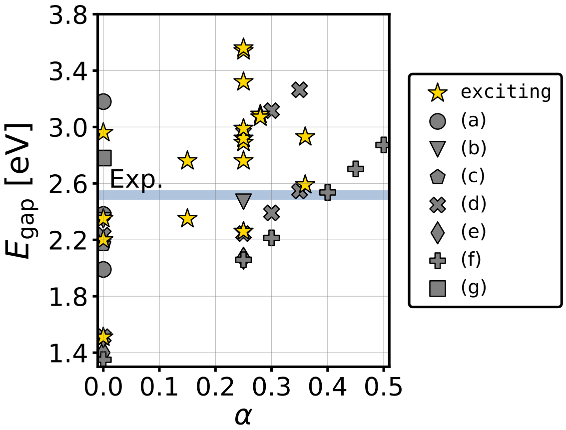

Figure D.1: Band gap of PbI_2 computed with various methods (see Fig. 7.1). The stars indicate the **`exciting`** results, the other data come from the literature, i.e. (a) [248], (b) [249], (c) [250], (d) [251], (e) [252], (f) [253], (g) [254].

D.2 Computational details

All calculations are performed using `exciting`. Details about the methods and the `exciting` code are given in Chapters 2 and 3, respectively. Calculations with the HSE functionals use the implementations described in Chapter 4.

For γ-CsPbI$_3$, α-CsPbI$_3$, and PbI$_2$, we employed the experimentally determined lattice parameters and atomic positions [220, 277, 219]. For α-MAPbI$_3$, we adopted the structure from Ref. [291], in which the hydrogen atoms that cannot be resolved by x-ray were added manually, and then the whole MA molecule was relaxed. The positions of the Pb and we atoms are from Ref. [292].

The parameters determining the number of APW basis functions and the $\boldsymbol{k}$-mesh employed are displayed in Tables D.1 and D.2, respectively. In the DFT calculations, the chosen settings for $R_{\mathrm{MT}}G_{\mathrm{max}}$ and the $\boldsymbol{k}$-mesh guarantee a numerical precision of the band gap within 20 meV for PbI$_2$, α-CsPbI$_3$, and α-MAPbI$_3$ and within 50 meV for γ-CsPbI$_3$. For the G_0W_0 gaps we used 100 meV as the convergence criterion. Also for this set of materials, the convergence of the energy gaps with the $\boldsymbol{k}$-mesh turned out to be slower for PBE0 compared to PBE and HSE (see Section 4.2.3). Nevertheless, in the investigation of the effect of the screening parameter ω carried out for PbI$_2$, we used the same grid for both PBE0 and HSE, i.e. 6x6x4. For these calculations we employed the *Exact* method to compute the screened Coulomb potential in the limit $\boldsymbol{G} + \boldsymbol{q} \to 0$ (see Section 4.2.4). In the G_0W_0 calculations, the correlation part of the self-energy is evaluated using the double Gauss–Legendre quadrature with 32 frequency points along the imaginary axis. The Pade approximantion is used for the analytical continuation to the real axis.

Table D.1: Computational parameters, i.e., G_{max}, $R_{\mathrm{MT}}G_{\mathrm{max}}$, and R_{MT}, for the studied systems.

		$R_{\mathrm{MT}}G_{\mathrm{max}}$					
		Pb	I	Cs	C	N	H
Material	G_{max} [a_0^{-1}]\\R_{MT} [a_0]	2.9	2.9	2.9	1.1	1.0	0.9
PbI$_2$	2.76	8	8	-	-	-	-
γ-CsPbI$_3$	2.07	6	6	6	-	-	-
α-CsPbI$_3$	2.41	7	7	7	-	-	-
α-MAPbI$_3$	3.55	10.3	10.3	-	3.9	3.5	3.2

SOC is treated within the ZORA [133, 134] and the SV scheme (Section 3.4.2). Details of the calculation of SOC with hybrid functionals and G_0W_0 can be found in Sections 5.1 and

Table D.2: $\boldsymbol{k}$-meshes used for the different materials and methods. For the G_0W_0 calculations, the same meshes are used as for their DFT starting points. The last column shows the $\boldsymbol{k}$-meshes used for the calculation of the dielectric screening, with and without SOC.

	PBE	PBE0	HSE	ε_∞ (SOC)
PbI_2	3x3x2	6x6x4	6x6x4	6x6x4 (6x6x4)
γ-$CsPbI_3$	2x2x1	3x3x2	2x2x1	6x6x4 (6x6x4)
α-$CsPbI_3$	4x4x4	6x6x6	4x4x4	10x10x10 (16x16x16)
α-$MAPbI_3$	4x4x4	-	-	10x10x10 (16x16x16)

3.5, respectively. For reaching the desired precision for the set of considered materials, the SV treatment requires almost all available KS functions. This number is significantly higher than that required to converge the hybrid and G_0W_0 calculations. In order, to maintain the same level of precision with and without SOC, the number of empty states required for SOC is used in all DFT and G_0W_0 calculations, i.e., 300 for PbI_2, 1000 for γ-$CsPbI_3$, 460 α-$CsPbI_3$, and 1000 for α-$MAPbI_3$.

To apply the DDH method, the dielectric constant ϵ_∞, must be determined first. It is calculated using both the IPA and the RPA (with LFE) on top of the PBE results. The $\boldsymbol{k}$-mesh and, in the RPA also the cutoff for the LFE and the number of unoccupied states, have been chosen so that the mixing parameter α is determined within a precision of $5 \cdot 10^{-3}$. The $\boldsymbol{k}$-meshes are given in Table D.2, the LFE cutoff (gqmax) is set to 2, and the number of unoccupied states is 10 for PbI_2, 20 for α-$CsPbI_3$, and α-$MAPbI_3$ and 100 for γ-$CsPbI_3$. The parameter $\bar{g}$ of the DM method (Section 5.2) is computed from the PBE electron density, using the computational parameters in Tables D.1 and D.2. This ensures that the α values are within $5 \cdot 10^{-3}$.

D.3 Orbital-resolved density of states

This section, as well as Secs. D.4 and D.5 closely follow the Supporting Information of Ref. [35]. They are reported here for convenience.

Figure D.2 shows the orbital-resolved DOS for each atomic species computed with PBE including SOC. In all systems, the top of the VB is dominated by I-p orbitals, with significant contributions also from Pb-s states. The bottom of the CB consists mainly of Pb-p states.

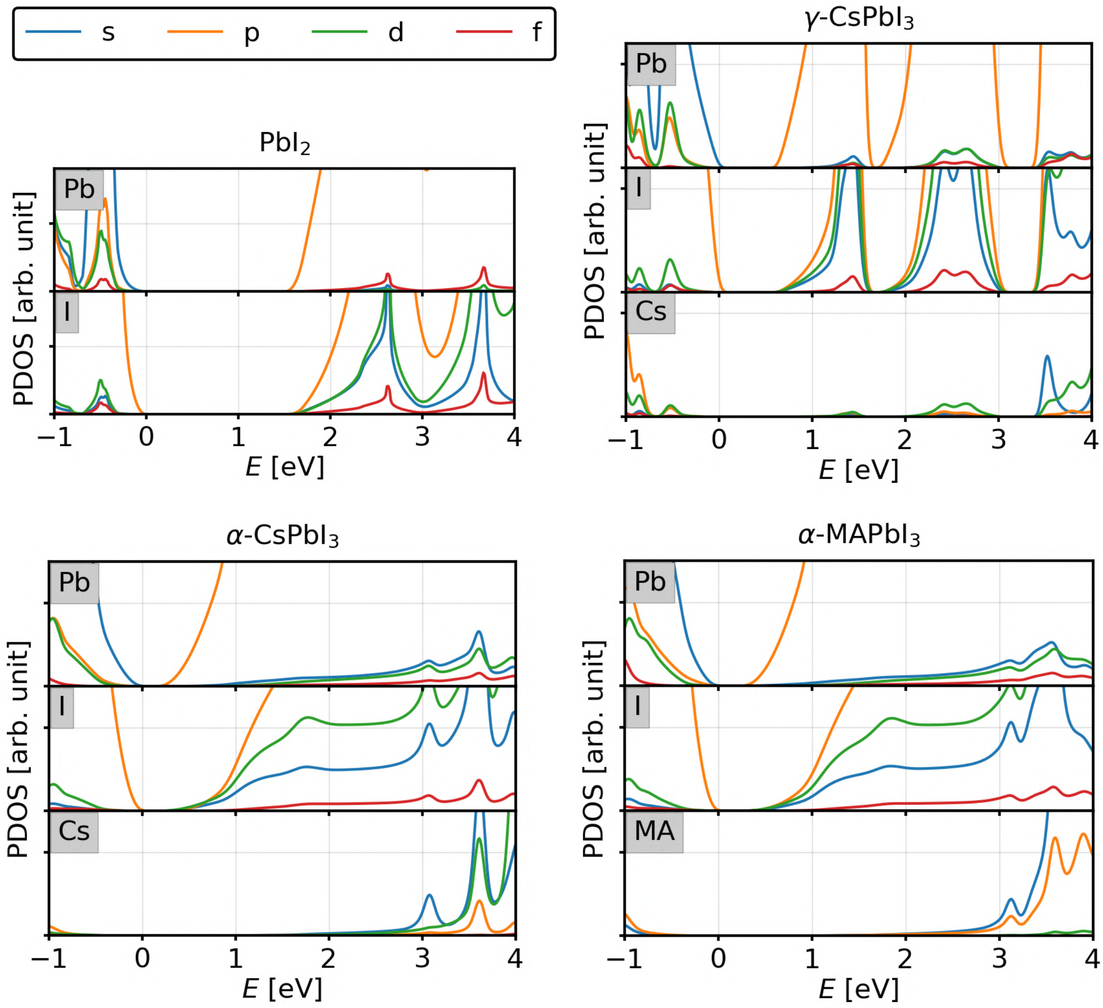

Figure D.2: Orbital-resolved DOS of PbI_2, γ-$CsPbI_3$, α-$CsPbI_3$, and α-$MAPbI_3$. For α-$MAPbI_3$, it is plotted for Pb, I, and MA. The partial density of states (PDOS) of the latter is obtained by summing up the contributions coming from H, N, and C.

D.4 Extrapolation of band gaps

As discussed in Chapter 7 and Section B.2, the band gaps computed with PBE0 and HSE vary linearly with the mixing parameter α. The same is observed for G_0W_0@PBE0 and G_0W_0@HSE. In Chapter 7, we made use of this feature, to evaluate the band gaps corresponding to the DDH and the DM mixing parameters shown in Tables 7.2 and 7.3. The linear fits are shown in Figure D.3. In the case of PbI_2, the band gaps corresponding to $\alpha = 0.15, 0.25, 0.28,$ and 0.36 have been computed explicitly.

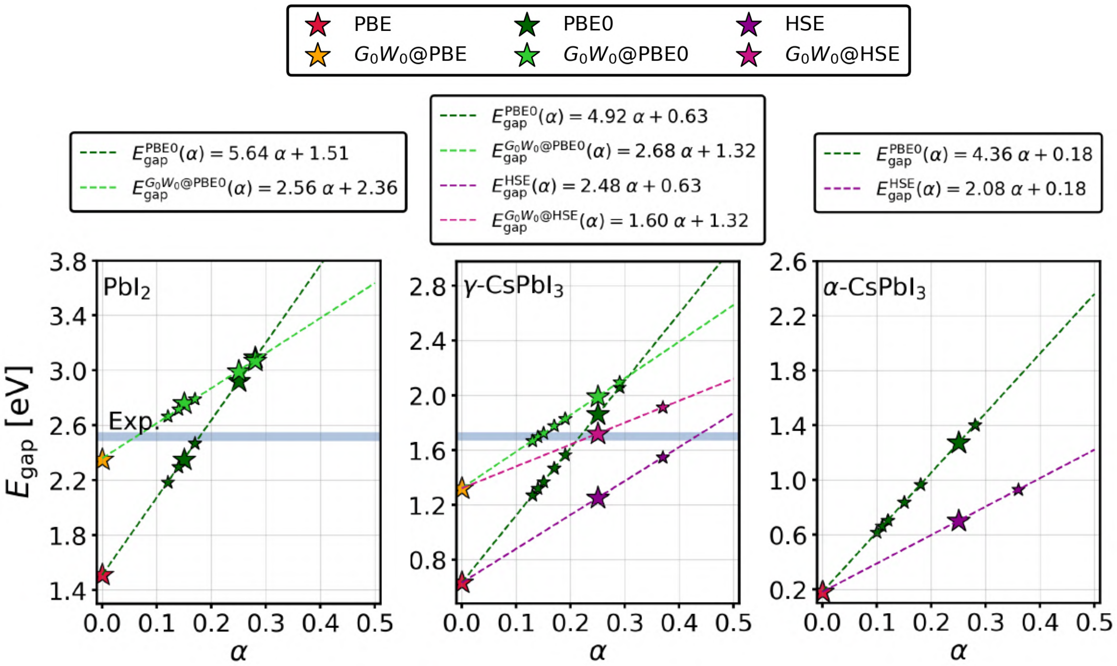

Figure D.3: Band gaps of PbI_2, γ-$CsPbI_3$, and α-$CsPbI_3$ from PBE0 and HSE as well as G_0W_0@PBE0 and G_0W_0@PBE0 for different values of α. The dashed lines indicate the fits obtained using the data depicted by the big stars. The small stars are the gaps evaluated from the fits.

D.5 Energy gaps of PbI_2 for different values of α and ω

For the sake of completeness, in Table D.3 we report the energy gaps plotted in Fig. 7.8.

Table D.3: Energy gaps of PbI_2 (in eV) calculated with PBE0 and HSE, for different combinations of α and ω. The second part of the table shows the same for G_0W_0@PBE0 and G_0W_0@HSE.

	ω [a_0^{-1}]	α			
		0.15	0.25	0.28	0.36
PBE0	0	2.35	2.92	3.09	3.56
HSE	0.03	2.20	2.67	2.82	3.21
	0.05	2.13	2.56	2.69	3.05
	0.11	1.96	2.26	2.36	2.61
	0.15	1.87	2.12	2.19	2.40
	0.20	1.79	1.98	2.04	2.20
G_0W_0@PBE0	0	2.76	2.99	3.07	3.26
G_0W_0@HSE	0.03	2.71	2.91	2.98	3.15
	0.05	2.68	2.88	2.94	3.09
	0.11	2.62	2.76	2.80	2.93
	0.15	2.58	2.70	2.73	2.83
	0.20	2.54	2.64	2.67	2.74

APPENDIX E

Supporting material for Chapter 8

E.1 BA_2PbI_4 tertragonal phase

E.1.1 Computational details

Structure relaxation

For the structure relaxation of both the 3D α-$CsPbI_3$ structure and the tetragonal BA_2PbI_4 systems, we used FHI-aims [278, 279]. In the case of the α-$CsPbI_3$ systems, we used the experimental structure from Ref. [277] as a starting point and relaxed the cell with the Broyden–Fletcher–Goldfarb–Shanno (BFGS) algorithm up to maximum residual force components of 5×10^{-3} eV/Å. The angles were kept fixed during relaxation. We employed tight settings for the species and selected a $6 \times 6 \times 6$ $\boldsymbol{k}$-mesh, aiming for a precision of 1x10^{-3} Å of the lattice constants.

The tetragonal BA_2PbI_4 system has the same I-Pb distance as the relaxed α-$CsPbI_3$ structure, and the distance between the layers is equal to that of the LT-BA_2PbI_4 phase [274]. The BA molecule initially constructed with Avogadro [276], was inserted in the Pb-I skeleton and then relaxed employing BLYP and PBE+VDW. The VDW effects were evaluated by the Tkatchenko-Scheffler method [280]. The relaxation was performed on the tetragonal unit cell of 78 atoms. Also in this case, we used the BFGS algorithm and chose a maximum of 5×10^{-3} eV/Å as the convergence criterion for the forces. Again we used tight settings for the species, and for the $\boldsymbol{k}$ points we chose an $8 \times 8 \times 2$ grid.

Table E.1: G_{max}, $R_{\mathrm{MT}}G_{\mathrm{max}}$ and R_{MT} values used for the BA_2PbI_4 and Cs_2PbI_4 systems. Since $R_{\mathrm{MT}}G_{\mathrm{max}}$ depends on the sphere size, individual values are provided.

		$R_{\mathrm{MT}}G_{\mathrm{max}}$					
		Pb	I	Cs	C	N	H
Material	G_{max} $[a_0^{-1}]\backslash R_{\mathrm{MT}}$ $[a_0]$	2.9	2.9	2.9	1.0	1.0	0.9
BA_2PbI_4	3.33	9.66	9.66	-	3.33	3.33	3.00
Cs_2PbI_4	2.76	8	8	8	-	-	-

After having the two tetragonal structures with 78 atoms relaxed with BLYP and PBE+VDW, we used the `exciting` extension of the Python library Pymatgen to obtain the primitive cell with 39 atoms. Since the output was not provided in the conventional primitive unit cell, we determined it following the guidelines in Ref. [281] for the body-centered tetragonal cell. This also gave me the reciprocal space path for calculating the band structure.

Electronic structure calculations with `exciting`

For the calculation of the electronic and optical properties, we employed the `exciting` code. SOC effects are evaluated using the SVLO method and are treated within ZORA [133, 134]. The convergence parameters were chosen to achieve a precision of the energy gap of $\sim 1 \times 10^{-2}$ eV. The $\boldsymbol{k}$-grid is $6 \times 6 \times 6$ for all PBE and HSE calculations. In Table E.1, $R_{\mathrm{MT}}G_{\mathrm{max}}$ and R_{MT} are listed for all elements. Additionally, G_{max}, which is determined from the product $R_{\mathrm{MT}}^{\mathrm{min}}G_{\mathrm{max}}$. Table E.2 displays the number of unoccupied states needed for SOC and HSE calculations and the number of LO used. In fact, two sets of LO were adopted for the SOC treatment, one containing only SR-type LO (p-set) and the other containing also Dirca-type LO for the elements Pb, I, and Cs ($p_{1/2}$-set). The $p_{1/2}$-sets have 99 LO more for the BA_2PbI_4 systems and 131 LO more for the Cs_2PbI_4 systems. These additional LO are a mix of SR and Dirac-type LO, since the two sets have a different core- and valence-state partitioning. Finally, the HSE band structure and DOS are evaluated by employing MLWF.

Effective masses

We computed the effective masses along different reciprocal space paths by making use of the following definition:

$$m^* = \hbar^2 \left[\frac{\partial^2 E_n(\boldsymbol{k})}{\partial^2 \boldsymbol{k}} \bigg|_{\boldsymbol{k}=\boldsymbol{k}_0} \right]^{-1} = \lim_{\delta k \to 0} \hbar^2 \left[\frac{E_n(\boldsymbol{k}_0 + 2\delta \boldsymbol{k}) + E_n(\boldsymbol{k}_0) - 2E_n(\boldsymbol{k}_0 + \delta \boldsymbol{k})}{\delta \boldsymbol{k}^2} \right]^{-1}, \quad \text{(E.1)}$$

Table E.2: Number of LO (N_{LO}) and number of unoccupied states (N_{unocc}) for the calculations performed on the tetragonal phases of BA_2PbI_4 and Cs_2PbI_4. N_{LO} depends on the material and the type of LO used. N_{unocc} is a convergence parameter for HSE and SOC+PBE calculations. SOC is evaluated using the SVLO method.

Cation	Functional	SOC	N_{LO}	N_{unocc}
BA	PBE	No	238	-
		SVLO (p)		30
		SVLO ($p_{1/2}$)	337	
Cs	PBE	No	126	-
		SVLO (p)		100
		SVLO ($p_{1/2}$)	257	50
	HSE	No	126	1100

where $E_n(\boldsymbol{k})$ is the energy of the band with index n at $\boldsymbol{k}$, $\boldsymbol{k}_0$ is the reciprocal-space point where the (local) maximum/minimum is located, and $\delta\boldsymbol{k}$ is the distance between $\boldsymbol{k}_0$ and a sufficiently close $\boldsymbol{k}$-point of the mesh. In the case of the tetragonal BA_2PbI_4 and Cs_2PbI_4 structures, we computed the effective masses at X along the paths X → Γ and X → Y, and we used a spacing of $|\delta\boldsymbol{k}| \approx 5 \times 10^{-3}\text{Å}^{-1}$. To remove the numerical noise, we fitted the energy values around X in the parabolic regime to compute the second derivative.

Optical properties

The spectra in Fig. 8.5 are computed using the IPA with a broadening of $\sim$ 0.1 eV. To obtain convergent optical spectra, we employed the double-grid method [293] with an $18 \times 18 \times 18$ $\boldsymbol{k}$-mesh in each calculation. Since the hybrid systems are non-symmetric in the x and y directions, the parallel components are obtained by averaging the spectra computed for the x and y polarizations.

To evaluate the dielectric response we computed ϵ_∞ using the RPA on top of the PBE calculations and including LFE. The parameter governing the LFE is chosen to be `gqmax=2`. For these calculations, a 8×8×8 $\boldsymbol{k}$-mesh and 100 empty states are used. These parameters ensure a precision of 0.05.

E.1.2 Species-resolved band structure and DOS

In Fig. E.1, the species-resolved band structures and DOS of the BA-BLYP and Cs-SD systems are plotted. For a better comparison, the sum over the species C, H and N, as contained in BA, is shown. The main contribution in the VBM comes from the I atoms, for the CBm, it is mainly from the Pb atoms, but the I atoms also have a non-negligible contribution. The BA and Cs cations contribute in regions farther away from the band gap: In the valence states, the main contributions of the cation (BA or Cs) are around -1.5 eV, in the conduction states, they are above 2 eV. More specifically, from the band structure it can be observed that in the conduction bands the organic/inorganic cations have a dominant contribution in the first conduction band around the points Γ and Z.

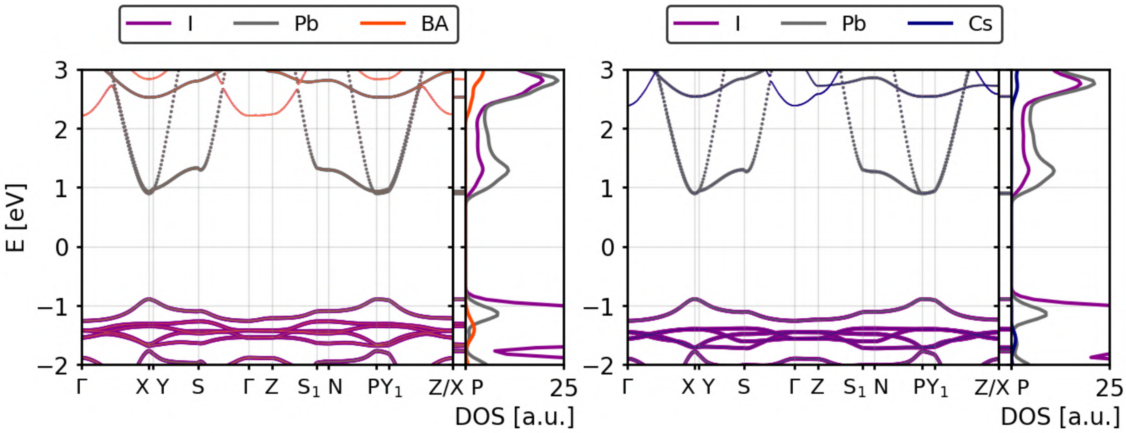

Figure E.1: Species-resolved band structure and DOS of BA-BLYP (left) and Cs-ND (right) systems. In the case of the BA cation (upper left panel), the contributions of the H, C, and N atoms are summed up.

E.2 LT and HT phases of BA_2PbI_4: Computational details

The structural relaxation of the LT and HT phases of BA_2PbI_4 was performed by Xiangzhou Zhu using VASP [203], starting from the experimentally determined structures of Ref. [274]. VASP was also used by Xiangzhou Zhu to evaluate the band gaps and effective masses computed with PBE+SOC marked by $^{\perp}$ in Table 8.5. For more information about the computational details, we refer to the Supporting Information of Ref. [208].

For my calculations, we employed `exciting`. The computational parameters, such as $R_{\mathrm{MT}}G_{\mathrm{max}}$, the $\boldsymbol{k}$-mesh, and the number of unoccupied states important for PBE+SOC and HSE calculations, are listed in Table E.3. They were chosen to achieve a precision for the band gap of 2×10^{-2} eV and for the effective masses of 0.02 m_0. The SOC effects were evaluated with the standard SV method since the SVLO method was not yet fully implemented at the time of the calculations.

Table E.3: Computational parameters such as $R_{\mathrm{MT}}G_{\mathrm{max}}$, G_{max}, $\boldsymbol{k}$-mesh, and the number of unoccupied states (N_{unocc}) employed in the calculations of the HT and LT phases of BA_2PbI_4. The muffin-tin radii are the same as for the tetragonal systems (see Table E.1).

Phase	Cation	Functional	MLWF	$\boldsymbol{k}$-mesh	$R_{\mathrm{MT}}G_{\mathrm{max}}$	G_{max}	N_{unocc}
LT/HT	BA	PBE	No	3×3×1	3	3.33	-
LT	Cs	PBE	No	3×3×1	6.9	2.38	-
			Yes	4×4×1			-
		PBE+SOC	No	3×3×1			3100
		HSE	Yes	4×4×1			2200
HT	Cs	PBE	No	3×3×1	6.4	2.20	-
			Yes	4×4×1			-
		PBE+SOC	No	3×3×1			2700
		HSE	Yes	4×4×1			1800

To compute the effective masses, we used the approach described in Section E.1.1, but on the bands along $\Gamma \rightarrow X$ and $\Gamma \rightarrow Y$ employing a spacing of $|\delta \boldsymbol{k}| \approx 0.01$Å^{-1}. The hole and effective electron masses in Table 8.5 are obtained by averaging the effective masses along the two paths. For completeness, their values are listed in Table E.4. In the case of the HSE functional, we employed the MLWF to evaluate the band structure along the $\Gamma \rightarrow$ X and $\Gamma \rightarrow$ Y paths (Fig. 8.9). For these systems, the interpolation method based on the MLWF converges slower than the standard approach, and thus a denser $\boldsymbol{k}$-mesh is needed. For a direct comparison, we have tested the two methods at the PBE level. The results are collected in Table E.5. It can be observed that by using the $4 \times 4 \times 1$ grid chosen for the HSE calculations, the effective masses can be reproduced with a precision of ~0.02 m_0. Larger grids are not computationally feasible with HSE.

Table E.4: Effective hole and electron masses computed from the paths $\Gamma \rightarrow$ X ($m_{\text{h},x}$ and $m_{\text{e},x}$) and $\Gamma \rightarrow$ Y ($m_{\text{h},y}$ and $m_{\text{e},y}$). Their average gives the effective masses in Table 8.5.

Cation	Functional	MLWF	$m_{\text{h},x}$ [m$_0$]	$m_{\text{h},y}$ [m$_0$]	$m_{\text{e},x}$ [m$_0$]	$m_{\text{e},y}$ [m$_0$]
			LT			
BA	PBE	No	-0.396	-0.386	0.241	0.266
Cs	PBE	No	-0.398	-0.388	0.248	0.270
Cs	PBE	Yes	-0.385	-0.380	0.257	0.235
Cs	PBE	Yes	-0.417	-0.412	0.272	0.292
Cs	PBE+SOC	No	-0.385	-0.380	0.257	0.235
Cs	HSE	Yes	-0.374	-0.369	0.247	0.260
			HT			
BA	PBE	No	-0.244	-0.233	0.294	0.174
Cs	PBE	No	-0.256	-0.241	0.296	0.180
Cs	PBE	Yes	-0.271	-0.255	0.304	0.199
Cs	PBE+SOC	No	-0.243	-0.228	0.189	0.185
Cs	HSE	Yes	-0.250	-0.238	0.275	0.184

Table E.5: Convergence tests to evaluate the optimal $\boldsymbol{k}$-mesh to be employed for computing effective masses. All calculations are performed with PBE. Those that do not employ MLWF serve as a reference. The hole (electron) masses $m_{\text{h},x}$ ($m_{\text{e},x}$) are computed from the path $\Gamma \rightarrow$ X, while $m_{\text{h},y}$ ($m_{\text{e},y}$) are computed from the path $\Gamma \rightarrow$ Y. m_{h} (m_{e}) are calculated as the average of the two.

MLWF	$\boldsymbol{k}$-mesh	$m_{\text{h},x}$ [m$_0$]	$m_{\text{h},y}$ [m$_0$]	m_{h} [m$_0$]	$m_{\text{e},x}$ [m$_0$]	$m_{\text{e},y}$ [m$_0$]	m_{e} [m$_0$]
				LT			
No	3×3×1	-0.398	-0.388	-0.393	0.248	0.270	0.259
Yes	3×3×1	-0.429	-0.424	-0.427	0.276	0.277	0.277
	4×4×1	-0.417	-0.412	-0.414	0.272	0.292	0.282
	4×4×2	-0.417	-0.412	-0.414	0.267	0.274	0.270
	5×5×1	-0.412	-0.400	-0.406	0.251	0.268	0.260
				HT			
No	3×3×1	-0.256	-0.241	-0.249	0.296	0.180	0.238
Yes	3×3×1	-0.291	-0.274	-0.283	0.320	0.230	0.275
	4×4×1	-0.271	-0.255	-0.263	0.304	0.199	0.251
	4×4×2	-0.271	-0.255	-0.263	0.284	0.195	0.240
	5×5×1	-0.260	-0.246	-0.253	0.307	0.183	0.245

References

[1] J. Burschka, N. Pellet, S.-J. Moon, R. Humphry-Baker, P. Gao, M. K. Nazeeruddin, and M. Grätzel, Sequential deposition as a route to high-performance perovskite-sensitized solar cells. Nature **499**, 316-319 (2013).

[2] M. A. Green, E. D. Dunlop, M. Yoshita, N. Kopidakis, K. Bothe, G. Siefer, D. Hinken, M. Rauer, J. Hohl-Ebinger, and X. Hao, Solar cell efficiency tables (version 64). Progress in Photovoltaics: Research and Applications **32**, 425-441 (2024).

[3] Nrel best research-cell efficiency chart, https://www.nrel.gov/pv/cell-efficiency.html, last accessed: November 28, 2024.

[4] S. D. Stranks, G. E. Eperon, G. Grancini, C. Menelaou, M. J. P. Alcocer, T. Leijtens, L. M. Herz, A. Petrozza, and H. J. Snaith, Electron-hole diffusion lengths exceeding 1 micrometer in an organometal trihalide perovskite absorber. Science **342**, 341-344 (2013).

[5] M. B. Johnston and L. M. Herz, Hybrid perovskites for photovoltaics: Charge-carrier recombination, diffusion, and radiative efficiencies. Accounts of Chemical Research **49**, 146-154 (2016).

[6] K. X. Steirer, P. Schulz, G. Teeter, V. Stevanovic, M. Yang, K. Zhu, and J. J. Berry, Defect tolerance in methylammonium lead triiodide perovskite. ACS Energy Letters **1**, 360-366 (2016).

[7] D. A. Valverde-Chávez, C. S. Ponseca, C. C. Stoumpos, A. Yartsev, M. G. Kanatzidis, V. Sundström, and D. G. Cooke, Intrinsic femtosecond charge generation dynamics in single crystal $CH_3NH_3PbI_3$. Energy & Environmental Science **8**, 3700-3707 (2015).

[8] S. Tao, I. Schmidt, G. Brocks, J. Jiang, I. Tranca, K. Meerholz, and S. Olthof, Absolute energy level positions in tin- and lead-based halide perovskites. Nature Communications **10**, 2560 (2019).

[9] L. Schmidt-Mende, V. Dyakonov, S. Olthof, F. Ünlü, K. M. T. Lê, S. Mathur, A. D. Karabanov, D. C. Lupascu, L. M. Herz, A. Hinderhofer, F. Schreiber, A. Chernikov,

D. A. Egger, O. Shargaieva, C. Cocchi, E. Unger, M. Saliba, M. M. Byranvand, M. Kroll, F. Nehm, K. Leo, A. Redinger, J. Höcker, T. Kirchartz, J. Warby, E. Gutierrez-Partida, D. Neher, M. Stolterfoht, U. Würfel, M. Unmüssig, J. Herterich, C. Baretzky, J. Mohanraj, M. Thelakkat, C. Maheu, W. Jaegermann, T. Mayer, J. Rieger, T. Fauster, D. Niesner, F. Yang, S. Albrecht, T. Riedl, A. Fakharuddin, M. Vasilopoulou, Y. Vaynzof, D. Moia, J. Maier, M. Franckevičius, V. Gulbinas, R. A. Kerner, L. Zhao, B. P. Rand, N. Glück, T. Bein, F. Matteocci, L. A. Castriotta, A. Di Carlo, M. Scheffler, and C. Draxl, Roadmap on organic–inorganic hybrid perovskite semiconductors and devices. APL Materials **9**, 109202 (2021).

[10] S. D. Stranks and H. J. Snaith, Metal-halide perovskites for photovoltaic and light-emitting devices. Nature Nanotechnology **10**, 391-402 (2015).

[11] Q. Lin, A. Armin, D. M. Lyons, P. L. Burn, and P. Meredith, Low noise, IR-blind organohalide perovskite photodiodes for visible light detection and imaging. Advanced Materials **27**, 2060-2064 (2015).

[12] L. Dou, Y. M. Yang, J. You, Z. Hong, W.-H. Chang, G. Li, and Y. Yang, Solution-processed hybrid perovskite photodetectors with high detectivity. Nature Communications **5**, 5404 (2014).

[13] G. Xing, N. Mathews, S. S. Lim, N. Yantara, X. Liu, D. Sabba, M. Grätzel, S. Mhaisalkar, and T. C. Sum, Low-temperature solution-processed wavelength-tunable perovskites for lasing. Nature Materials **13**, 476-480 (2014).

[14] C. Qin, A. S. D. Sandanayaka, C. Zhao, T. Matsushima, D. Zhang, T. Fujihara, and C. Adachi, Stable room-temperature continuous-wave lasing in quasi-2D perovskite films. Nature **585**, 53-57 (2020).

[15] V. M. Goldschmidt, Die Gesetze der Krystallochemie. Naturwissenschaften **14**, 477-485 (1926).

[16] C. J. Bartel, C. Sutton, B. R. Goldsmith, R. Ouyang, C. B. Musgrave, L. M. Ghiringhelli, and M. Scheffler, New tolerance factor to predict the stability of perovskite oxides and halides. Science Advances **5**, eaav0693 (2019).

[17] I. C. Smith, E. T. Hoke, D. Solis-Ibarra, M. D. McGehee, and H. I. Karunadasa, A layered hybrid perovskite solar-cell absorber with enhanced moisture stability. Angewandte Chemie International Edition **53**, 11232-11235 (2014).

[18] D. H. Cao, C. C. Stoumpos, O. K. Farha, J. T. Hupp, and M. G. Kanatzidis, 2D homologous perovskites as light-absorbing materials for solar cell applications. Journal of the American Chemical Society **137**, 7843-7850 (2015).

[19] G. Grancini, C. Roldán-Carmona, I. Zimmermann, E. Mosconi, X. Lee, D. Martineau, S. Narbey, F. Oswald, F. De Angelis, M. Grätzel, and M. K. Nazeeruddin,

One-year stable perovskite solar cells by 2D/3D interface engineering. Nature Communications **8**, 15684 (2017).

[20] T. L. Leung, I. Ahmad, A. A. Syed, A. M. C. Ng, J. Popović, and A. B. Djurišić, Stability of 2D and quasi-2D perovskite materials and devices. Communications Materials **3**, 63 (2022).

[21] C. C. Stoumpos, D. H. Cao, D. J. Clark, J. Young, J. M. Rondinelli, J. I. Jang, J. T. Hupp, and M. G. Kanatzidis, Ruddlesden–Popper hybrid lead iodide perovskite 2D homologous semiconductors. Chemistry of Materials **28**, 2852-2867 (2016).

[22] T. Kataoka, T. Kondo, R. Ito, S. Sasaki, K. Uchida, and N. Miura, Magneto-optical study on excitonic spectra in $(C_6H_{13}NH_3)_2PbI_4$. Physical Review B **47**, 2010 (1993).

[23] T. Ishihara, Optical properties of PbI-based perovskite structures. Journal of Luminescence **60-61**, 269-274 (1994).

[24] O. Yaffe, A. Chernikov, Z. M. Norman, Y. Zhong, A. Velauthapillai, A. van der Zande, J. S. Owen, and T. F. Heinz, Excitons in ultrathin organic-inorganic perovskite crystals. Physical Review B **92**, 045414 (2015).

[25] X. Li, J. M. Hoffman, and M. G. Kanatzidis, The 2D halide perovskite rulebook: How the spacer influences everything from the structure to optoelectronic device efficiency. Chemical Reviews **121**, 2230-2291 (2021).

[26] Y. Gao, X. Dong, and Y. Liu, Recent progress of layered perovskite solar cells incorporating aromatic spacers. Nano-micro Letters **15**, 169 (2023).

[27] C. R. Kagan, D. B. Mitzi, and C. D. Dimitrakopoulos, Organic-inorganic hybrid materials as semiconducting channels in thin-film field-effect transistors. Science **286**, 945-947 (1999).

[28] T. Ishihara, J. Takahashi, and T. Goto, Exciton state in two-dimensional perovskite semiconductor $(C_{10}H_{21}NH_3)_2PbI_4$. Solid State Communications **69**, 933-936 (1989).

[29] N. Wang, L. Cheng, R. Ge, S. Zhang, Y. Miao, W. Zou, C. Yi, Y. Sun, Y. Cao, R. Yang, Y. Wei, Q. Guo, Y. Ke, M. Yu, Y. Jin, Y. Liu, Q. Ding, D. Di, L. Yang, G. Xing, H. Tian, C. Jin, F. Gao, R. H. Friend, J. Wang, and W. Huang, Perovskite light-emitting diodes based on solution-processed self-organized multiple quantum wells. Nature Photonics **10**, 699-704 (2016).

[30] K. Shibuya, M. Koshimizu, Y. Takeoka, and K. Asai, Scintillation properties of $(C_6H_{13}NH_3)_2PbI_4$: Exciton luminescence of an organic/inorganic multiple quantum well structure compound induced by 2.0 MeV protons. Nuclear Instruments and Methods in Physics Research Section B: Beam Interactions with Materials and Atoms **194**, 207-212 (2002).

[31] L. Li, Z. Sun, P. Wang, W. Hu, S. Wang, C. Ji, M. Hong, and J. Luo, Tailored engineering of an unusual $(C_4H_9NH_3)_2(CH_3NH_3)_2Pb_3Br_{10}$ two-dimensional multilayered perovskite ferroelectric for a high-performance photodetector. Angewandte Chemie International Edition **56**, 12150 (2017).

[32] A. V. Krukau, O. A. Vydrov, A. F. Izmaylov, and G. E. Scuseria, Influence of the exchange screening parameter on the performance of screened hybrid functionals. The Journal of Chemical Physics **125**, 224106 (2006).

[33] D. Nabok, A. Gulans, and C. Draxl, Accurate all-electron G_0W_0 quasiparticle energies employing the full-potential augmented plane-wave method. Physical Review B **94**, 035118 (2016).

[34] A. Gulans, A. Kozhevnikov, and C. Draxl, Microhartree precision in density functional theory calculations. Physical Review B **97**, 161105(R) (2018).

[35] C. Vona, D. Nabok, and C. Draxl, Electronic structure of (organic-)inorganic metal halide perovskites: The dilemma of choosing the right functional. Advanced Theory and Simulations **5**, 2100496 (2022).

[36] J. Wiktor, U. Rothlisberger, and A. Pasquarello, Predictive determination of band gaps of inorganic halide perovskites. The Journal of Physical Chemistry Letters **8**, 5507–5512 (2017).

[37] Y. Li and K. Yang, High-throughput computational design of organic–inorganic hybrid halide semiconductors beyond perovskites for optoelectronics. Energy & Environmental Science **12**, 2233-2243 (2019).

[38] L. Leppert, T. Rangel, and J. B. Neaton, Towards predictive band gaps for halide perovskites: Lessons from one-shot and eigenvalue self-consistent GW. Physical Review Materials **3**, 103803 (2019).

[39] H. Wang, A. Tal, T. Bischoff, P. Gono, and A. Pasquarello, Accurate and efficient band-gap predictions for metal halide perovskites at finite temperature. npj Computational Materials **8**, 237 (2022).

[40] L. Pedesseau, D. Sapori, B. Traore, R. Robles, H.-H. Fang, M. A. Loi, H. Tsai, W. Nie, J.-C. Blancon, A. Neukirch, S. Tretiak, A. D. Mohite, C. Katan, J. Even, and M. Kepenekian, Advances and promises of layered halide hybrid perovskite semiconductors. ACS Nano **10**, 9776-9786 (2016).

[41] Y.-F. Ding, Q.-Q. Zhao, Z.-L. Yu, Y.-Q. Zhao, B. Liu, P.-B. He, H. Zhou, K. Li, S.-F. Yin, and M.-Q. Cai, Strong thickness-dependent quantum confinement in all-inorganic perovskite Cs_2PbI_4 with a Ruddlesden–Popper structure. Journal of Materials Chemistry C **7**, 7433-7441 (2019).

[42] J. Li, Q. Yu, Y. He, C. C. Stoumpos, G. Niu, G. G. Trimarchi, H. Guo, G. Dong, D. Wang, L. Wang, and M. G. Kanatzidis, $Cs_2PbI_2Cl_2$, all-inorganic two-

dimensional Ruddlesden–Popper mixed halide perovskite with optoelectronic response. Journal of the American Chemical Society **140**, 11085-11090 (2018).

[43] J.-C. Blancon, J. Even, C. C. Stoumpos, M. G. Kanatzidis, and A. D. Mohite, Semiconductor physics of organic-inorganic 2D halide perovskites. Nature Nanotechnology **15**, 969-985 (2020).

[44] B. Maurer, C. Vorwerk, and C. Draxl, Rashba and Dresselhaus effects in two-dimensional Pb-I-based perovskites. Physical Review Materials **105**, 155149 (2022).

[45] C.-S. Liao, B. Liu, J.-L. Yang, and M.-Q. Cai, Multi-functional application potential of Ruddlesden–Popper perovskite-based heterostructure $PtSe_2/Cs_2PbI_4$ with tunable electronic properties. Journal of Physics: Condensed Matter **35**, 115002 (2023).

[46] C. Quarti, G. Giorgi, C. Katan, J. Even, and M. Palummo, Exciton ground state fine structure and excited states landscape in layered halide perovskites from combined BSE simulations and symmetry analysis. Advanced Optical Materials **12**, 2202801 (2024).

[47] W. Kohn and L. J. Sham, Self-consistent equations including exchange and correlation effects. Physical Review **140**, A1133 (1965).

[48] P. Hohenberg and W. Kohn, Inhomogeneous electron gas. Physical Review **136**, B864 (1964).

[49] M. Levy, Universal variational functionals of electron densities, first-order density matrices, and natural spin-orbitals and solution of the v-representability problem. Proceedings of the National Academy of Sciences **76**, 6062-6065 (1979).

[50] A. Gulans, S. Kontur, C. Meisenbichler, D. Nabok, P. Pavone, S. Rigamonti, S. Sagmeister, U. Werner, and C. Draxl, exciting: A full-potential all-electron package implementing density-functional theory and many-body perturbation theory. Journal of Physics: Condensed Matter **26**, 363202 (2014).

[51] J. P. Perdew and M. Levy, Physical content of the exact Kohn-Sham orbital energies: Band gaps and derivative discontinuities. Physical Review Letters **51**, 1884 (1983).

[52] L. J. Sham and M. Schlüter, Density-functional theory of the energy gap. Physical Review Letters **51**, 1888 (1983).

[53] E. Engel and R. Dreizler, Density functional theory: An advanced course (Springer Nature, 2011).

[54] A. Seidl, A. Görling, P. Vogl, J. A. Majewski, and M. Levy, Generalized Kohn-Sham schemes and the band-gap problem. Physical Review B **53**, 3764 (1996).

[55] R. Garrick, A. Natan, T. Gould, and L. Kronik, Exact generalized Kohn-Sham theory for hybrid functionals. Physical Review X **10**, 021040 (2020).

[56] J. P. Perdew and K. Schmidt, Jacob's ladder of density functional approximations for the exchange-correlation energy. AIP Conference Proceedings **577**, 1-20 (2001).

[57] E. Brémond, M. Savarese, N. Q. Su, A. J. Pérez-Jiménez, X. Xu, J. C. Sancho-García, and C. Adamo, Benchmarking density functionals on structural parameters of small-/medium-sized organic molecules. Journal of Chemical Theory and Computation **12**, 459-465 (2016).

[58] G.-X. Zhang, A. M. Reilly, A. Tkatchenko, and M. Scheffler, Performance of various density-functional approximations for cohesive properties of 64 bulk solids. New Journal of Physics **20**, 063020 (2018).

[59] P. Borlido, T. Aull, A. W. Huran, F. Tran, M. A. L. Marques, and S. Botti, Large-scale benchmark of exchange–correlation functionals for the determination of electronic band gaps of solids. Journal of Chemical Theory and Computation **15**, 5069-5079 (2019).

[60] G. Santra and J. M. L. Martin, Some observations on the performance of the most recent exchange-correlation functionals for the large and chemically diverse GMTKN55 benchmark. AIP Conference Proceedings **2186**, 030004 (2019).

[61] R. M. Martin, Electronic structure: Basic theory and practical methods (Cambridge University Press, 2004).

[62] D. R. Hartree, The wave mechanics of an atom with a non-Coulomb central field. Part I. Theory and methods. Mathematical Proceedings of the Cambridge Philosophical Society **24**, 89-110 (1928).

[63] J. L. Bao, L. Gagliardi, and D. G. Truhlar, Self-interaction error in density functional theory: An appraisal. The Journal of Physical Chemistry Letters **9**, 2353-2358 (2018).

[64] J. P. Perdew and A. Zunger, Self-interaction correction to density-functional approximations for many-electron systems. Physical Review B **23**, 5048 (1981).

[65] J. P. Perdew and Y. Wang, Accurate and simple analytic representation of the electron-gas correlation energy. Physical Review B **45**, 13244 (1992).

[66] D. M. Ceperley and B. J. Alder, Ground state of the electron gas by a stochastic method. Physical Review Letters **45**, 566 (1980).

[67] G. Ortiz and P. Ballone, Correlation energy, structure factor, radial distribution function, and momentum distribution of the spin-polarized uniform electron gas. Physical Review B **50**, 1391 (1994).

[68] D. Ceperley, Ground state of the fermion one-component plasma: A Monte Carlo study in two and three dimensions. Physical Review B **18**, 3126 (1978).

[69] R. O. Jones and O. Gunnarsson, The density functional formalism, its applications and prospects. Reviews of Modern Physics **61**, 689 (1989).

[70] D. C. Langreth and M. J. Mehl, Beyond the local-density approximation in calculations of ground-state electronic properties. Physical Review B **28**, 1809 (1983).

[71] A. D. Becke, Correlation energy of an inhomogeneous electron gas: A coordinate-space model. The Journal of Chemical Physics **88**, 1053-1062 (1988).

[72] C. Lee, W. Yang, and R. G. Parr, Development of the Colle-Salvetti correlation-energy formula into a functional of the electron density. Physical Review B **37**, 785 (1988).

[73] J. P. Perdew, K. Burke, and M. Ernzerhof, Generalized gradient approximation made simple. Physical Review Letters **77**, 3865 (1996).

[74] J. P. Perdew, K. Burke, and M. Ernzerhof, Generalized gradient approximation made simple [Phys. Rev. Lett. 77, 3865 (1996)]. Physical Review Letters **78**, 1396 (1997).

[75] Y. Zhao and D. G. Truhlar, A new local density functional for main-group thermochemistry, transition metal bonding, thermochemical kinetics, and noncovalent interactions. The Journal of Chemical Physics **125**, 194101 (2006).

[76] A. D. Becke and E. R. Johnson, A simple effective potential for exchange. The Journal of Chemical Physics **124**, 221101 (2006).

[77] F. Tran and P. Blaha, Accurate band gaps of semiconductors and insulators with a semilocal exchange-correlation potential. Physical Review Letters **102**, 226401 (2009).

[78] J. Sun, A. Ruzsinszky, and J. P. Perdew, Strongly constrained and appropriately normed semilocal density functional. Physical Review Letters **115**, 036402 (2015).

[79] J. C. Womack, N. Mardirossian, M. Head-Gordon, and C.-K. Skylaris, Self-consistent implementation of meta-GGA functionals for the ONETEP linear-scaling electronic structure package. The Journal of Chemical Physics **145**, 204114 (2016).

[80] F. G. Eich and M. Hellgren, Derivative discontinuity and exchange-correlation potential of meta-GGAs in density-functional theory. The Journal of Chemical Physics **141**, 224107 (2014).

[81] T. Aschebrock and S. Kümmel, Ultranonlocality and accurate band gaps from a meta-generalized gradient approximation. Physical Review Research **1**, 033082 (2019).

[82] T. Lebeda, T. Aschebrock, J. Sun, L. Leppert, and S. Kümmel, Right band gaps for the right reason at low computational cost with a meta-GGA. Physical Review Materials **7**, 093803 (2023).

[83] A. D. Becke, A new mixing of Hartree-Fock and local density-functional theories. The Journal of Chemical Physics **98**, 1372–1377 (1993).

[84] V. Fock, Näherungsmethode zur Lösung des quantenmechanischen Mehrkörperproblems. Zeitschrift für Physik **61**, 126–148 (1930).

[85] W. Pauli, Über den Zusammenhang des Abschlusses der Elektronengruppen im Atom mit der Komplexstruktur der Spektren. Zeitschrift für Physik **31**, 765-783 (1925).

[86] J. Harris and R. O. Jones, The surface energy of a bounded electron gas. Journal of Physics F: Metal Physics **4**, 1170 (1974).

[87] O. Gunnarsson and B. I. Lundqvist, Exchange and correlation in atoms, molecules, and solids by the spin-density-functional formalism. Physical Review B **13**, 4274 (1976).

[88] J. Harris, Adiabatic-connection approach to Kohn-Sham theory. Physical Review A **29**, 1648 (1984).

[89] A. D. Becke, Density-functional thermochemistry. III. The role of exact exchange. The Journal of Chemical Physics **98**, 5648–5652 (1993).

[90] A. D. Becke, Density-functional thermochemistry. IV. A new dynamical correlation functional and implications for exact-exchange mixing. The Journal of Chemical Physics **104**, 1040–1046 (1996).

[91] C. Adamo and V. Barone, Toward reliable adiabatic connection models free from adjustable parameters. Chemical Physics Letters **274**, 242-250 (1997).

[92] C. Adamo and V. Barone, Implementation and validation of the Lacks-Gordon exchange functional in conventional density functional and adiabatic connection methods. Journal of Computational Chemistry **19**, 418-429 (1998).

[93] C. Adamo and V. Barone, Toward reliable density functional methods without adjustable parameters: The PBE0 model. The Journal of Chemical Physics **110**, 6158–6170 (1999).

[94] M. Ernzerhof and G. E. Scuseria, Assessment of the Perdew-Burke-Ernzerhof exchange-correlation functional. The Journal of Chemical Physics **110**, 5029–5036 (1999).

[95] J. Heyd, G. E. Scuseria, and M. Ernzerhof, Hybrid functionals based on a screened Coulomb potential. The Journal of Chemical Physics **118**, 8207–8215 (2003).

[96] J. Heyd, G. E. Scuseria, and M. Ernzerhof, Erratum: "Hybrid functionals based on a screened Coulomb potential" [J. Chem. Phys. 118, 8207-8215 (2003)]. The Journal of Chemical Physics **124**, 219906 (2006).

[97] M. Betzinger, C. Friedrich, and S. Blügel, Hybrid functionals within the all-electron FLAPW method: Implementation and applications of PBE0. Physical Review B **81**, 195117 (2010).

[98] M. Ernzerhof, Construction of the adiabatic connection. Chemical Physics Letters **263**, 499-506 (1996).

[99] M. Levy, N. H. March, and N. C. Handy, On the adiabatic connection method, and scaling of electron–electron interactions in the Thomas–Fermi limit. The Journal of Chemical Physics **104**, 1989-1992 (1996).

[100] K. Burke, M. Ernzerhof, and J. P. Perdew, The adiabatic connection method: A non-empirical hybrid. Chemical Physics Letters **265**, 115-120 (1997).

[101] P. Mori-Sánchez, A. J. Cohen, and W. Yang, Self-interaction-free exchange-correlation functional for thermochemistry and kinetics. The Journal of Chemical Physics **124**, 091102 (2006).

[102] S. Vuckovic, T. J. P. Irons, A. Savin, A. M. Teale, and P. Gori-Giorgi, Exchange–correlation functionals via local interpolation along the adiabatic connection. Journal of Chemical Theory and Computation **12**, 2598-2610 (2016).

[103] J. P. Perdew, M. Ernzerhof, and K. Burke, Rationale for mixing exact exchange with density functional approximations. The Journal of Chemical Physics **105**, 9982–9985 (1996).

[104] A. Görling and M. Levy, Hybrid schemes combining the Hartree–Fock method and density-functional theory: Underlying formalism and properties of correlation functionals. The Journal of Chemical Physics **106**, 2675-2680 (1997).

[105] A. Görling and M. Levy, Correlation-energy functional and its high-density limit obtained from a coupling-constant perturbation expansion. Physical Review B **47**, 13105 (1993).

[106] M. A. L. Marques, J. Vidal, M. J. T. Oliveira, L. Reining, and S. Botti, Density-based mixing parameter for hybrid functionals. Physical Review B **83**, 035119 (2011).

[107] P. Borlido, J. Schmidt, A. W. Huran, F. Tran, M. A. L. Marques, and S. Botti, Exchange-correlation functionals for band gaps of solids: Benchmark, reparametrization and machine learning. npj Computational Materials **6**, 96 (2020).

[108] A. Alkauskas, P. Broqvist, F. Devynck, and A. Pasquarello, Band offsets at semiconductor-oxide interfaces from hybrid density-functional calculations. Physical Review Letters **101**, 106802 (2008).

[109] D. Koller, P. Blaha, and F. Tran, Hybrid functionals for solids with an optimized Hartree–Fock mixing parameter. Journal of Physics: Condensed Matter **25**, 435503 (2013).

[110] J. H. Skone, M. Govoni, and G. Galli, Self-consistent hybrid functional for condensed systems. Physical Review B **89**, 195112 (2014).

[111] J. H. Skone, M. Govoni, and G. Galli, Nonempirical range-separated hybrid functionals for solids and molecules. Physical Review B **93**, 235106 (2016).

[112] W. Chen, G. Miceli, G.-M. Rignanese, and A. Pasquarello, Nonempirical dielectric-dependent hybrid functional with range separation for semiconductors and insulators. Physical Review Materials **2**, 073803 (2018).

[113] F. Gygi and A. Baldereschi, Quasiparticle energies in semiconductors: Self-energy correction to the local-density approximation. Physical Review Letters **62**, 2160 (1989).

[114] D. M. Bylander and L. Kleinman, Good semiconductor band gaps with a modified local-density approximation. Physical Review B **41**, 7868 (1990).

[115] E. Runge and E. K. U. Gross, Density-functional theory for time-dependent systems. Physical Review Letters **52**, 997 (1984).

[116] Y.-M. Byun, J. Sun, and C. A. Ullrich, Time-dependent density-functional theory for periodic solids: Assessment of excitonic exchange–correlation kernels. Electronic Structure **2**, 023002 (2020).

[117] J. Paier, M. Marsman, and G. Kresse, Dielectric properties and excitons for extended systems from hybrid functionals. Physical Review B **78**, 121201(R) (2008).

[118] P. Liu, C. Franchini, M. Marsman, and G. Kresse, Assessing model-dielectric-dependent hybrid functionals on the antiferromagnetic transition-metal monoxides MnO, FeO, CoO, and NiO. Journal of Physics: Condensed Matter **32**, 015502 (2020).

[119] C. Gutle, A. Savin, J. B. Krieger, and J. Chen, Correlation energy contributions from low-lying states to density functionals based on an electron gas with a gap. International Journal of Quantum Chemistry **75**, 885-888 (1999).

[120] J. Jaramillo, G. E. Scuseria, and M. Ernzerhof, Local hybrid functionals. The Journal of Chemical Physics **118**, 1068-1073 (2003).

[121] A. V. Krukau, G. E. Scuseria, J. P. Perdew, and A. Savin, Hybrid functionals with local range separation. The Journal of Chemical Physics **129**, 124103 (2008).

[122] J. Richter, Bachelor thesis (Humboldt-Universität zu Berlin, Mathematisch-Naturwissenschaftliche Fakultät, 2021).

[123] P. Borlido, M. A. L. Marques, and S. Botti, Local hybrid density functional for interfaces. Journal of Chemical Theory and Computation **14**, 939-947 (2018).

[124] A. K. Rajagopal, Linear-response functions in spin-density-functional theory. Physical Review B **17**, 2980 (1978).

[125] A. H. MacDonald and S. H. Vosko, A relativistic density functional formalism. Journal of Physics C: Solid State Physics **12**, 2977 (1979).

[126] A. K. Rajagopal and J. Callaway, Inhomogeneous electron gas. Physical Review B **7**, 1912 (1973).

[127] T. Saue and T. Helgaker, Four-component relativistic Kohn–Sham theory. Journal of Computational Chemistry **23**, 814-823 (2002).

[128] K. G. Dyall and K. Faegri, Introduction to Relativistic Quantum Chemistry (Oxford University Press, 2007).

[129] R. Zhao, Y. Zhang, Y. Xiao, and W. Liu, Exact two-component relativistic energy band theory and application. The Journal of Chemical Physics **144**, 044105 (2016).

[130] R. Zhao, V. W. Yu, K. Zhang, Y. Xiao, Y. Zhang, and V. Blum, Quasi-four-component method with numeric atom-centered orbitals for relativistic density functional simulations of molecules and solids. Physical Review B **103**, 245144 (2021).

[131] W. P. Huhn and V. Blum, One-hundred-three compound band-structure benchmark of post-self-consistent spin-orbit coupling treatments in density functional theory. Physical Review Materials **1**, 033803 (2017).

[132] D. D. Koelling and B. N. Harmon, A technique for relativistic spin-polarised calculations. Journal of Physics C: Solid State Physics **10**, 3107 (1977).

[133] E. van Lenthe, E. J. Baerends, and J. G. Snijders, Relativistic regular two-component Hamiltonians. The Journal of Chemical Physics **99**, 4597-4610 (1993).

[134] E. van Lenthe, E. J. Baerends, and J. G. Snijders, Relativistic total energy using regular approximations. The Journal of Chemical Physics **101**, 9783-9792 (1994).

[135] D. J. Griffiths and D. F. Schroeter, Introduction to quantum mechanics, 3rd ed. (Cambridge University Press, 2018).

[136] B. Bransden and C. Joachain, Physics of atoms and molecules, Pearson Education (Prentice Hall, 2003).

[137] M. Kim, J. Im, A. J. Freeman, J. Ihm, and H. Jin, Switchable $S = 1/2$ and $J = 1/2$ Rashba bands in ferroelectric halide perovskites. Proceedings of the National Academy of Sciences **111**, 6900-6904 (2014).

[138] F. Zheng, L. Z. Tan, S. Liu, and A. M. Rappe, Rashba spin–orbit coupling enhanced carrier lifetime in $CH_3NH_3PbI_3$. Nano Letters **15**, 7794-7800 (2015).

[139] M. Kepenekian, R. Robles, C. Katan, D. Sapori, L. Pedesseau, and J. Even, Rashba and Dresselhaus effects in hybrid organic–inorganic perovskites: From basics to devices. ACS Nano **9**, 11557-11567 (2015).

[140] T. Etienne, E. Mosconi, and F. De Angelis, Dynamical origin of the Rashba effect in organohalide lead perovskites: A key to suppressed carrier recombination in perovskite solar cells? The Journal of Physical Chemistry Letters **7**, 1638-1645 (2016).

[141] D. Niesner, M. Wilhelm, I. Levchuk, A. Osvet, S. Shrestha, M. Batentschuk, C. Brabec, and T. Fauster, Giant Rashba splitting in $CH_3NH_3PbBr_3$ organic-inorganic perovskite. Physical Review Letters **117**, 126401 (2016).

[142] E. Mosconi, T. Etienne, and F. De Angelis, Rashba band splitting in organohalide lead perovskites: Bulk and surface effects. The Journal of Physical Chemistry Letters **8**, 2247-2252 (2017).

[143] Y. Zhai, S. Baniya, C. Zhang, J. Li, P. Haney, C.-X. Sheng, E. Ehrenfreund, and Z. V. Vardeny, Giant Rashba splitting in 2D organic-inorganic halide perovskites measured by transient spectroscopies. Science Advances **3**, e1700704 (2017).

[144] S. McKechnie, J. M. Frost, D. Pashov, P. Azarhoosh, A. Walsh, and M. van Schilfgaarde, Dynamic symmetry breaking and spin splitting in metal halide perovskites. Physical Review B **98**, 085108 (2018).

[145] J. Yin, P. Maity, L. Xu, A. M. El-Zohry, H. Li, O. M. Bakr, J.-L. Brédas, and O. F. Mohammed, Layer-dependent Rashba band splitting in 2D hybrid perovskites. Chemistry of Materials **30**, 8538-8545 (2018).

[146] I.-H. Park, Q. Zhang, K. C. Kwon, Z. Zhu, W. Yu, K. Leng, D. Giovanni, H. S. Choi, I. Abdelwahab, Q.-H. Xu, T. C. Sum, and K. P. Loh, Ferroelectricity and Rashba effect in a two-dimensional Dion-Jacobson hybrid organic–inorganic perovskite. Journal of the American Chemical Society **141**, 15972-15976 (2019).

[147] S. B. Todd, D. B. Riley, A. Binai-Motlagh, C. Clegg, A. Ramachandran, S. A. March, J. M. Hoffman, I. G. Hill, C. C. Stoumpos, M. G. Kanatzidis, Z.-G. Yu, and K. C. Hall, Detection of Rashba spin splitting in 2D organic-inorganic perovskite via precessional carrier spin relaxation. APL Materials **7**, 081116 (2019).

[148] E. Lafalce, E. Amerling, Z.-G. Yu, P. C. Sercel, L. Whittaker-Brooks, and Z. V. Vardeny, Rashba splitting in organic–inorganic lead–halide perovskites revealed

through two-photon absorption spectroscopy. Nature Communications **13**, 483 (2022).

[149] G. Onida, L. Reining, and A. Rubio, Electronic excitations: Density-functional versus many-body Green's-function approaches. Reviews of Modern Physics **74**, 601 (2002).

[150] A. L. Fetter and J. D. Walecka, Quantum theory of many-particle systems (McGraw-Hill, Boston, 1971).

[151] E. K. U. Gross, E. Runge, and O. Heinonen, Many-particle theory (Adam Hilger, 1991).

[152] D. Golze, M. Dvorak, and P. Rinke, The *GW* compendium: A practical guide to theoretical photoemission spectroscopy. Frontiers in Chemistry **7**, 377 (2019).

[153] C. Friedrich and A. Schindlmayr, Many-body perturbation theory: The gw approximation, in Computational Nanoscience: Do It Yourself!, NIC Series, Vol. 31, edited by J. Grotendorst, S. Blügel, and D. Marx page 335–355.

[154] L. Hedin, New method for calculating the one-particle Green's function with application to the electron-gas problem. Physical Review **139**, A796 (1965).

[155] M. S. Hybertsen and S. G. Louie, First-principles theory of quasiparticles: Calculation of band gaps in semiconductors and insulators. Physical Review Letters **55**, 1418 (1985).

[156] R. W. Godby, M. Schlüter, and L. J. Sham, Accurate exchange-correlation potential for silicon and its discontinuity on addition of an electron. Physical Review Letters **56**, 2415 (1986).

[157] F. J. Dyson, The *S* matrix in quantum electrodynamics. Physical Review **75**, 1736 (1949).

[158] R. Martin, L. Reining, and D. Ceperley, Interacting electrons: Theory and computational approaches (Cambridge University Press, 2016).

[159] M. Rui Bacelar, W.-D. Schöne, R. Keyling, and W. Ekardt, Lifetime of excited electrons in transition metals. Physical Review B **66**, 153101 (2002).

[160] R. Laasner, G_0W_0 band structure of $CdWO_4$. Journal of Physics: Condensed Matter **26**, 125503 (2014).

[161] P. Rinke, A. Qteish, J. Neugebauer, C. Freysoldt, and M. Scheffler, Combining *GW* calculations with exact-exchange density-functional theory: An analysis of valence-band photoemission for compound semiconductors. New Journal of Physics **7**, 126 (2005).

[162] F. Fuchs, J. Furthmüller, F. Bechstedt, M. Shishkin, and G. Kresse, Quasiparticle band structure based on a generalized Kohn-Sham scheme. Physical Review B **76**, 115109 (2007).

[163] T. Körzdörfer and N. Marom, Strategy for finding a reliable starting point for G_0W_0 demonstrated for molecules. Physical Review B **86**, 041110(R) (2012).

[164] N. Marom, F. Caruso, X. Ren, O. T. Hofmann, T. Körzdörfer, J. R. Chelikowsky, A. Rubio, M. Scheffler, and P. Rinke, Benchmark of GW methods for azabenzenes. Physical Review B **86**, 245127 (2012).

[165] F. Bruneval and M. A. L. Marques, Benchmarking the starting points of the GW approximation for molecules. Journal of Chemical Theory and Computation **9**, 324-329 (2013).

[166] L. Gallandi and T. Körzdörfer, Long-range corrected DFT meets GW: Vibrationally resolved photoelectron spectra from first principles. Journal of Chemical Theory and Computation **11**, 5391-5400 (2015).

[167] L. Gallandi, N. Marom, P. Rinke, and T. Körzdörfer, Accurate ionization potentials and electron affinities of acceptor molecules II: Non-empirically tuned long-range corrected hybrid functionals. Journal of Chemical Theory and Computation **12**, 605-614 (2016).

[168] U. von Barth and B. Holm, Self-consistent GW_0 results for the electron gas: Fixed screened potential W_0 within the random-phase approximation. Physical Review B **54**, 8411 (1996).

[169] M. E. Casida, Generalization of the optimized-effective-potential model to include electron correlation: A variational derivation of the Sham-Schlüter equation for the exact exchange-correlation potential. Physical Review A **51**, 2005 (1995).

[170] M. van Schilfgaarde, T. Kotani, and S. Faleev, Quasiparticle self-consistent GW theory. Physical Review Letters **96**, 226402 (2006).

[171] T. Kotani, M. van Schilfgaarde, S. V. Faleev, and A. Chantis, Quasiparticle self-consistent GW method: A short summary. Journal of Physics: Condensed Matter **19**, 365236 (2007).

[172] E. E. Salpeter and H. A. Bethe, A relativistic equation for bound-state problems. Physical Review **84**, 1232 (1951).

[173] D. J. Singh, Planewaves, pseudopotentials, and the lapw method (Springer, 1993).

[174] J. C. Slater, Wave functions in a periodic potential. Physical Review **51**, 846 (1937).

[175] O. K. Andersen, Linear methods in band theory. Physical Review B **12**, 3060 (1975).

[176] P. M. Marcus, Variational methods in the computation of energy bands. International Journal of Quantum Chemistry **1**, 567-588 (1967).

[177] D. Singh, Ground-state properties of lanthanum: Treatment of extended-core states. Physical Review B **43**, 6388 (1991).

[178] E. Sjöstedt, L. Nordström, and D. Singh, An alternative way of linearizing the augmented plane-wave method. Solid State Communications **114**, 15-20 (2000).

[179] H. Jiang, R. I. Gómez-Abal, X.-Z. Li, C. Meisenbichler, C. Ambrosch-Draxl, and M. Scheffler, FHI-gap: A *GW* code based on the all-electron augmented plane wave method. Computer Physics Communications **184**, 348-366 (2013).

[180] E. Wimmer, H. Krakauer, M. Weinert, and A. J. Freeman, Full-potential self-consistent linearized-augmented-plane-wave method for calculating the electronic structure of molecules and surfaces: O_2 molecule. Physical Review B **24**, 864 (1981).

[181] F. Aryasetiawan and O. Gunnarsson, Product-basis method for calculating dielectric matrices. Physical Review B **49**, 16214 (1994).

[182] C. Friedrich, A. Schindlmayr, and S. Blügel, Efficient calculation of the Coulomb matrix and its expansion around $\mathbf{k} = \mathbf{0}$ within the FLAPW method. Computer Physics Communications **180**, 347-359 (2009).

[183] A. H. MacDonald, W. E. Picket, and D. D. Koelling, A linearised relativistic augmented-plane-wave method utilising approximate pure spin basis functions. Journal of Physics C: Solid State Physics **13**, 2675 (1980).

[184] A. Gulans and C. Draxl, Influence of spin-orbit coupling on chemical bonding (2022), arXiv:2204.02751 [cond-mat.mtrl-sci].

[185] R. W. Godby, M. Schlüter, and L. J. Sham, Self-energy operators and exchange-correlation potentials in semiconductors. Physical Review B **37**, 10159 (1988).

[186] H. Jiang and E. Engel, Random-phase-approximation-based correlation energy functionals: Benchmark results for atoms. The Journal of Chemical Physics **127**, 184108 (2007).

[187] H. J. Vidberg and J. W. Serene, Solving the Eliashberg equations by means of N-point Padé approximants. Journal of Low Temperature Physics **29**, 179-192 (1977).

[188] K.-H. Lee and K. J. Chang, Analytic continuation of the dynamic response function using an N-point Padé approximant. Physical Review B **54**, R8285(R) (1996).

[189] I. Aguilera, C. Friedrich, G. Bihlmayer, and S. Blügel, *GW* study of topological insulators Bi_2Se_3, Bi_2Te_3, and Sb_2Te_3: Beyond the perturbative one-shot approach. Physical Review B **88**, 045206 (2013).

[190] N. Marzari and D. Vanderbilt, Maximally localized generalized Wannier functions for composite energy bands. Physical Review B **56**, 12847 (1997).

[191] I. Souza, N. Marzari, and D. Vanderbilt, Maximally localized Wannier functions for entangled energy bands. Physical Review B **65**, 035109 (2001).

[192] S. Tillack, A. Gulans, and C. Draxl, Maximally localized Wannier functions within the (L)APW + LO method. Physical Review B **101**, 235102 (2020).

[193] M. Schlipf, M. Betzinger, C. Friedrich, M. Ležaić, and S. Blügel, HSE hybrid functional within the FLAPW method and its application to GdN. Physical Review B **84**, 125142 (2011).

[194] M. Schlipf, Heyd-Scuseria-Ernzerhof screened exchange hybrid functional for complex materials: all-electron implementation and application (Forschungszentrum Jülich GmbH, 2013).

[195] T. M. Henderson, B. G. Janesko, and G. E. Scuseria, Generalized gradient approximation model exchange holes for range-separated hybrids. The Journal of Chemical Physics **128**, 194105 (2008).

[196] J. Heyd and G. E. Scuseria, Assessment and validation of a screened Coulomb hybrid density functional. The Journal of Chemical Physics **120**, 7274-7280 (2004).

[197] M. Ernzerhof and J. P. Perdew, Generalized gradient approximation to the angle- and system-averaged exchange hole. The Journal of Chemical Physics **109**, 3313-3320 (1998).

[198] P. Giannozzi, S. Baroni, N. Bonini, M. Calandra, R. Car, C. Cavazzoni, D. Ceresoli, G. L. Chiarotti, M. Cococcioni, I. Dabo, A. D. Corso, S. de Gironcoli, S. Fabris, G. Fratesi, R. Gebauer, U. Gerstmann, C. Gougoussis, A. Kokalj, M. Lazzeri, L. Martin-Samos, N. Marzari, F. Mauri, R. Mazzarello, S. Paolini, A. Pasquarello, L. Paulatto, C. Sbraccia, S. Scandolo, G. Sclauzero, A. P. Seitsonen, A. Smogunov, P. Umari, and R. M. Wentzcovitch, QUANTUM ESPRESSO: a modular and open-source software project for quantum simulations of materials. Journal of Physics: Condensed Matter **21**, 395502 (2009).

[199] P. Giannozzi, O. Andreussi, T. Brumme, O. Bunau, M. B. Nardelli, M. Calandra, R. Car, C. Cavazzoni, D. Ceresoli, M. Cococcioni, N. Colonna, I. Carnimeo, A. D. Corso, S. de Gironcoli, P. Delugas, R. A. DiStasio, A. Ferretti, A. Floris, G. Fratesi, G. Fugallo, R. Gebauer, U. Gerstmann, F. Giustino, T. Gorni, J. Jia, M. Kawamura, H.-Y. Ko, A. Kokalj, E. KÃŒçÃŒkbenli, M. Lazzeri, M. Marsili, N. Marzari, F. Mauri, N. L. Nguyen, H.-V. Nguyen, A. O. de-la Roza, L. Paulatto, S. Poncé, D. Rocca, R. Sabatini, B. Santra, M. Schlipf, A. P. Seitsonen, A. Smogunov, I. Timrov, T. Thonhauser, P. Umari, N. Vast, X. Wu, and S. Baroni, Advanced capabilities for materials modelling with QUANTUM ESPRESSO. Journal of Physics: Condensed Matter **29**, 465901 (2017).

[200] Gnu general public license, version 3, `http://www.gnu.org/licenses/gpl.html` (2007).

[201] N. Ashcroft and N. Mermin, Solid state physics (Cengage Learning, 2011).

[202] J. A. Paier, M. Marsman, K. Hummer, G. Kresse, I. C. Gerber, and J. G. Ángyán, Screened hybrid density functionals applied to solids. The Journal of Chemical Physics **124**, 154709 (2006).

[203] G. Kresse and J. Furthmüller, Efficient iterative schemes for *ab initio* total-energy calculations using a plane-wave basis set. Physical Review B **54**, 11169 (1996).

[204] J. Paier, M. Marsman, K. Hummer, G. Kresse, I. C. Gerber, and J. G. Ángyán, Erratum: "Screened hybrid density functionals applied to solids" [J. Chem. Phys. 124, 154709 (2006)]. The Journal of Chemical Physics **125**, 249901 (2006).

[205] D. Zavickis, K. Kacars, J. b. a. Cīmurs, and A. Gulans, Adaptively compressed exchange in the linearized augmented plane wave formalism. Physical Review B **106**, 165101 (2022).

[206] M. Wang, G.-B. Liu, H. Guo, and Y. Yao, An efficient method for hybrid density functional calculation with spin–orbit coupling. Computer Physics Communications **224**, 90-97 (2018).

[207] J. E. Peralta, J. Heyd, G. E. Scuseria, and R. L. Martin, Spin-orbit splittings and energy band gaps calculated with the Heyd-Scuseria-Ernzerhof screened hybrid functional. Physical Review B **74**, 073101 (2006).

[208] J. D. Ziegler, K.-Q. Lin, B. Meisinger, X. Zhu, M. Kober-Czerny, P. K. Nayak, C. Vona, T. Taniguchi, K. Watanabe, C. Draxl, H. J. Snaith, J. M. Lupton, D. A. Egger, and A. Chernikov, Excitons at the phase transition of 2D hybrid perovskites. ACS Photonics **9**, 3609-3616 (2022).

[209] W. Aggoune, K. Irmscher, D. Nabok, C. Vona, S. Bin Anooz, Z. Galazka, M. Albrecht, and C. Draxl, Fingerprints of optical absorption in the perovskite $LaInO_3$: Insight from many-body theory and experiment. Physical Review B **103**, 115105 (2021).

[210] R. Rodrigues Pela, C. Vona, S. Lubeck, B. Alex, I. Gonzalez Oliva, and C. Draxl, Critical assessment of G_0W_0 calculations for 2D materials: the example of monolayer MoS_2. npj Computational Materials **10**, 77 (2024).

[211] A. Cillis, Master thesis (Humboldt-Universität zu Berlin, Mathematisch-Naturwissenschaftliche Fakultät, 2023).

[212] C. Vona, S. Lubeck, H. Kleine, A. Gulans, and C. Draxl, Accurate and efficient treatment of spin-orbit coupling via second variation employing local orbitals. Physical Review B **108**, 235161 (2023).

[213] L. Nordström, J. M. Wills, P. H. Andersson, P. Söderlind, and O. Eriksson, Spin-orbit coupling in the actinide elements: A critical evaluation of theoretical equilibrium volumes. Physical Review B **63**, 035103 (2000).

[214] T. J. Scheidemantel, C. Ambrosch-Draxl, T. Thonhauser, J. V. Badding, and J. O. Sofo, Transport coefficients from first-principles calculations. Physical Review B **68**, 125210 (2003).

[215] J. Kuneš, P. Novák, R. Schmid, P. Blaha, and K. Schwarz, Electronic structure of fcc Th: Spin-orbit calculation with $6p_{1/2}$ local orbital extension. Physical Review B **64**, 153102 (2001).

[216] H. Kleine, Bachelor thesis (Humboldt-Universität zu Berlin, Mathematisch-Naturwissenschaftliche Fakultät, 2021).

[217] R. W. G. Wyckoff, Crystal structures, 2nd ed. (Interscience, 1963).

[218] T. Böker, R. Severin, A. Müller, C. Janowitz, R. Manzke, D. Voß, P. Krüger, A. Mazur, and J. Pollmann, Band structure of MoS_2, $MoSe_2$, and $\alpha-MoTe_2$: Angle-resolved photoelectron spectroscopy and ab initio calculations. Physical Review B **64**, 235305 (2001).

[219] B. Palosz, The structure of PbI_2 polytypes 2H and 4H: A study of the 2H-4H transition. Journal of Physics: Condensed Matter **2**, 5285 (1990).

[220] R. J. Sutton, M. R. Filip, A. Abbas Haghighirad, N. Sakai, B. Wenger, F. Giustino, and H. J. Snaith, Cubic or orthorhombic? Revealing the crystal structure of metastable black-phase $CsPbI_3$ by theory and experiment. ACS Energy Letters **3**, 1787–1794 (2018).

[221] V. R. Akshay, M. V. Suneesh, and M. Vasundhara, Tailoring thermoelectric properties through structure and morphology in chemically synthesized n-type bismuth telluride nanostructures. Inorganic Chemistry **56**, 6264-6274 (2017).

[222] C. Draxl and M. Scheffler, The NOMAD laboratory: From data sharing to artificial intelligence. Journal of Physics: Materials **2**, 036001 (2019).

[223] E. Cappelluti, R. Roldán, J. A. Silva-Guillén, P. Ordejón, and F. Guinea, Tight-binding model and direct-gap/indirect-gap transition in single-layer and multilayer MoS_2. Physical Review B **88**, 075409 (2013).

[224] B. Radisavljevic, A. Radenovic, J. Brivio, V. Giacometti, and A. Kis, Single-layer MoS_2 transistors. Nature Nanotechnology **6**, 147-150 (2011).

[225] D. Lembke and A. Kis, Breakdown of high-performance monolayer MoS_2 transistors. ACS Nano **6**, 10070-10075 (2012).

[226] Z. Yin, H. Li, H. Li, L. Jiang, Y. Shi, Y. Sun, G. Lu, Q. Zhang, X. Chen, and H. Zhang, Single-layer MoS_2 phototransistors. ACS Nano **6**, 74-80 (2012).

[227] O. Lopez-Sanchez, D. Lembke, M. Kayci, A. Radenovic, and A. Kis, Ultrasensitive photodetectors based on monolayer MoS_2. Nature Nanotechnology **8**, 497-501 (2013).

[228] D.-S. Tsai, K.-K. Liu, D.-H. Lien, M.-L. Tsai, C.-F. Kang, C.-A. Lin, L.-J. Li, and J.-H. He, Few-layer MoS_2 with high broadband photogain and fast optical switching for use in harsh environments. ACS Nano **7**, 3905-3911 (2013).

[229] M. Bernardi, M. Palummo, and J. C. Grossman, Extraordinary sunlight absorption and one nanometer thick photovoltaics using two-dimensional monolayer materials. Nano Letters **13**, 3664-3670 (2013).

[230] E. C. Ahn, 2D materials for spintronic devices. npj 2D Materials and Applications **4**, 17 (2020).

[231] F. Caruso, M. Schebek, Y. Pan, C. Vona, and C. Draxl, Chirality of valley excitons in monolayer transition-metal dichalcogenides. The Journal of Physical Chemistry Letters **13**, 5894-5899 (2022).

[232] M. Pisarra, C. Díaz, and F. Martín, Theoretical study of structural and electronic properties of $2H$-phase transition metal dichalcogenides. Physical Review B **103**, 195416 (2021).

[233] D. Y. Qiu, F. H. da Jornada, and S. G. Louie, Screening and many-body effects in two-dimensional crystals: Monolayer MoS_2. Physical Review B **93**, 235435 (2016).

[234] M. Marsili, A. Molina-Sánchez, M. Palummo, D. Sangalli, and A. Marini, Spinorial formulation of the GW-BSE equations and spin properties of excitons in two-dimensional transition metal dichalcogenides. Physical Review B **103**, 155152 (2021).

[235] S. Roth and W. R. Willig, Lead iodide nuclear particle detectors. Applied Physics Letters **18**, 328-330 (1971).

[236] C. Manfredotti, R. Murri, A. Quirini, and L. Vasanelli, PbI_2 as nuclear particle detector. IEEE Transactions on Nuclear Science **24**, 126-128 (1977).

[237] J. C. Lund, K. S. Shah, F. Olschner, J. Zhang, L. Moy, S. Medrick, and M. R. Squillante, Recent progress in lead iodide X-ray spectrometer development. Nuclear Instruments and Methods in Physics Research Section A: Accelerators, Spectrometers, Detectors and Associated Equipment **322**, 464-466 (1992).

[238] K. S. Shah, F. Olschner, L. P. Moy, P. Bennett, M. Misra, J. Zhang, M. R. Squillante, and J. C. Lund, Lead iodide X-ray detection systems. Nuclear Instruments and Methods in Physics Research Section A: Accelerators, Spectrometers, Detectors and Associated Equipment **380**, 266-270 (1996).

[239] H. Zhang, C.-X. Liu, X.-L. Qi, X. Dai, Z. Fang, and S.-C. Zhang, Topological insulators in Bi_2Se_3, Bi_2Te_3 and Sb_2Te_3 with a single Dirac cone on the surface. Nature Physics **5**, 438-442 (2009).

[240] Y. L. Chen, J. G. Analytis, J.-H. Chu, Z. K. Liu, S.-K. Mo, X. L. Qi, H. J. Zhang, D. H. Lu, X. Dai, Z. Fang, S. C. Zhang, I. R. Fisher, Z. Hussain, and Z.-X. Shen, Experimental realization of a three-dimensional topological insulator, Bi_2Te_3. Science **325**, 178-181 (2009).

[241] H. Mamur, M. Bhuiyan, F. Korkmaz, and M. Nil, A review on bismuth telluride (Bi_2Te_3) nanostructure for thermoelectric applications. Renewable and Sustainable Energy Reviews **82**, 4159-4169 (2018).

[242] T. Fang, X. Li, C. Hu, Q. Zhang, J. Yang, W. Q. Zhang, X. B. Zhao, D. J. Singh, and T. J. Zhu, Complex band structures and lattice dynamics of Bi_2Te_3-based compounds and solid solutions. Advanced Functional Materials **29**, 1900677 (2019).

[243] E. Kioupakis, M. L. Tiago, and S. G. Louie, Quasiparticle electronic structure of bismuth telluride in the *GW* approximation. Physical Review B **82**, 245203 (2010).

[244] B.-L. Huang and M. Kaviany, Ab initio and molecular dynamics predictions for electron and phonon transport in bismuth telluride. Physical Review B **77**, 125209 (2008).

[245] P. Larson, Effect of $p_{1/2}$ corrections in the electronic structure of Bi_2Te_3 compounds. Physical Review B **68**, 155121 (2003).

[246] C. Gähwiller and G. Harbeke, Excitonic effects in the electroreflectance of lead iodide. Physical Review **185**, 1141 (1969).

[247] R. Ahuja, H. Arwin, A. Ferreira Da Silva, C. Persson, J. M. Osorio-Guillén, J. Souza De Almeida, C. Moyses Araujo, E. Veje, N. Veissid, C. Y. An, I. Pepe, and B. Johansson, Electronic and optical properties of lead iodide. Journal of Applied Physics **92**, 7219-7224 (2002).

[248] A. S. Toulouse, B. P. Isaacoff, G. Shi, M. Matuchová, E. Kioupakis, and R. Merlin, Frenkel-like Wannier-Mott excitons in few-layer PbI_2. Physical Review B **91**, 165308 (2015).

[249] M. Zhou, W. Duan, Y. Chen, and A. Du, Single layer lead iodide: Computational exploration of structural, electronic and optical properties, strain induced band modulation and the role of spin-orbital-coupling. Nanoscale **7**, 15168-15174 (2015).

[250] L. Du, C. Wang, W. Xiong, S. Zhang, C. Xia, Z. Wei, J. Li, S. Tongay, F. Yang, X. Zhang, X. Liu, and Q. Liu, Perseverance of direct bandgap in multilayer 2D PbI_2 under an experimental strain up to 7.69%. 2D Materials **6**, 025014 (2019).

[251] C. Shen and G. Wang, Electronic and optical properties of bilayer PbI_2: A first-principles study. Journal of Physics D: Applied Physics **51**, 035301 (2018).

[252] M. Yagmurcukardes, F. M. Peeters, and H. Sahin, Electronic and vibrational properties of PbI_2: From bulk to monolayer. Physical Review B **98**, 085431 (2018).

[253] C. Borghesi, E. Radicchi, L. Belpassi, D. Meggiolaro, F. De Angelis, and F. Nunzi, The nature of the lead-iodine bond in PbI_2: A case study for the modelling of lead halide perovskites. Computational and Theoretical Chemistry **1164**, 112558 (2019).

[254] C. Shen and G. Wang, Excitonic effects on layer- and strain-dependent optoelectronic properties of PbI_2. Applied Surface Science **470**, 143-149 (2019).

[255] J. Even, L. Pedesseau, J. M. Jancu, and C. Katan, Importance of spin-orbit coupling in hybrid organic/inorganic perovskites for photovoltaic applications. The Journal of Physical Chemistry Letters **4**, 2999–3005 (2013).

[256] J. Feng and B. Xiao, Crystal structures, optical properties, and effective mass tensors of $CH_3NH_3PbX_3$ (X = I and Br) phases predicted from HSE06. The Journal of Physical Chemistry Letters **5**, 1278–1282 (2014).

[257] S. Kim, M. Lee, C. Hong, Y. Yoon, H. An, D. Lee, W. Jeong, D. Yoo, Y. Kang, Y. Youn, and S. Han, A band-gap database for semiconducting inorganic materials calculated with hybrid functional. Scientific Data **7**, 387 (2020).

[258] E. Menéndez-Proupin, P. Palacios, P. Wahnón, and J. C. Conesa, Self-consistent relativistic band structure of the $CH_3NH_3PbI_3$ perovskite. Physical Review B **90**, 045207 (2014).

[259] T. Bischoff, I. Reshetnyak, and A. Pasquarello, Adjustable potential probes for band-gap predictions of extended systems through nonempirical hybrid functionals. Physical Review B **99**, 201114(R) (2019).

[260] P. Umari, E. Mosconi, and F. De Angelis, Relativistic *GW* calculations on $CH_3NH_3PbI_3$ and $CH_3NH_3SnI_3$ perovskites for solar cell applications. Scientific Reports **4**, 4467 (2014).

[261] F. Brivio, K. T. Butler, A. Walsh, and M. van Schilfgaarde, Relativistic quasiparticle self-consistent electronic structure of hybrid halide perovskite photovoltaic absorbers. Physical Review B **89**, 155204 (2014).

[262] J. Endres, D. A. Egger, M. Kulbak, R. A. Kerner, L. Zhao, S. H. Silver, G. Hodes, B. P. Rand, D. Cahen, L. Kronik, and A. Kahn, Valence and conduction band densities of states of metal halide perovskites: A combined experimental–theoretical study. The Journal of Physical Chemistry Letters **7**, 2722-2729 (2016).

[263] J. Even, L. Pedesseau, C. Katan, M. Kepenekian, J.-S. Lauret, D. Sapori, and E. Deleporte, Solid-state physics perspective on hybrid perovskite semiconductors. The Journal of Physical Chemistry C **119**, 10161–10177 (2015).

[264] D. P. McMeekin, G. Sadoughi, W. Rehman, G. E. Eperon, M. Saliba, M. T. Hörantner, A. Haghighirad, N. Sakai, L. Korte, B. Rech, M. B. Johnston, L. M. Herz, and H. J. Snaith, A mixed-cation lead mixed-halide perovskite absorber for tandem solar cells. Science **351**, 151-155 (2016).

[265] G. E. Eperon, S. D. Stranks, C. Menelaou, M. B. Johnston, L. M. Herz, and H. J. Snaith, Formamidinium lead trihalide: A broadly tunable perovskite for efficient planar heterojunction solar cells. Energy & Environmental Science **7**, 982-988 (2014).

[266] R. K. Singh, R. Kumar, N. Jain, S. R. Dash, J. Singh, and A. Srivastava, Investigation of optical and dielectric properties of $CsPbI_3$ inorganic lead iodide perovskite thin film. Journal of the Taiwan Institute of Chemical Engineers **96**, 538-542 (2019).

[267] C. Quarti, E. Mosconi, J. M. Ball, V. D'Innocenzo, C. Tao, S. Pathak, H. J. Snaith, A. Petrozza, and F. De Angelis, Structural and optical properties of methylammonium lead iodide across the tetragonal to cubic phase transition: Implications for perovskite solar cells. Energy & Environmental Science **9**, 155-163 (2016).

[268] H. E. White, Pictorial representations of the Dirac electron cloud for hydrogen-like atoms. Physical Review **38**, 513 (1931).

[269] A. D. Wright, C. Verdi, R. L. Milot, G. E. Eperon, M. A. Pérez-Osorio, H. J. Snaith, F. Giustino, M. B. Johnston, and L. M. Herz, Electron-phonon coupling in hybrid lead halide perovskites. Nature Communications **7**, 11755 (2016).

[270] M. Zacharias, G. Volonakis, F. Giustino, and J. Even, Anharmonic electron-phonon coupling in ultrasoft and locally disordered perovskites. npj Computational Materials **9**, 153 (2023).

[271] M. Kuban, Š. Gabaj, W. Aggoune, C. Vona, S. Rigamonti, and C. Draxl, Similarity of materials and data-quality assessment by fingerprinting. MRS Bulletin **47**, 991-999 (2022).

[272] M. Kuban, S. Rigamonti, M. Scheidgen, and C. Draxl, Density-of-states similarity descriptor for unsupervised learning from materials data. Scientific Data **9**, 646 (2022).

[273] E. Manousakis, Towards understanding the electronic structure of the simpler members of two-dimensional halide-perovskites. Physical Review B **108**, 045130 (2023).

[274] D. G. Billing and A. Lemmerer, Synthesis, characterization and phase transitions in the inorganic–organic layered perovskite-type hybrids $[(C_nH_{2n+1}NH_3)_2PbI_4]$, $n = 4, 5$ and 6. Acta Crystallographica **B63**, 735–747 (2007).

[275] H. Haug and S. Koch, Quantum theory of the optical and electronic properties of semiconductors, G - Reference,Information and Interdisciplinary Subjects Series (World Scientific, 2004).

[276] M. D. Hanwell, D. E. Curtis, D. C. Lonie, T. Vandermeersch, E. Zurek, and G. R. Hutchison, Avogadro: An advanced semantic chemical editor, visualization, and analysis platform. Journal of Cheminformatics **4**, 17 (2012).

[277] D. M. Trots and S. V. Myagkota, High-temperature structural evolution of caesium and rubidium triiodoplumbates. Journal of Physics and Chemistry of Solids **69**, 2520-2526 (2008).

[278] V. Blum, R. Gehrke, F. Hanke, P. Havu, V. Havu, X. Ren, K. Reuter, and M. Scheffler, Ab initio molecular simulations with numeric atom-centered orbitals. Computer Physics Communications **180**, 2175-2196 (2009).

[279] X. Ren, P. Rinke, V. Blum, J. Wieferink, A. Tkatchenko, A. Sanfilippo, K. Reuter, and M. Scheffler, Resolution-of-identity approach to Hartree–Fock, hybrid density functionals, RPA, MP2 and *GW* with numeric atom-centered orbital basis functions. New Journal of Physics **14**, 053020 (2012).

[280] A. Tkatchenko and M. Scheffler, Accurate molecular van der Waals interactions from ground-state electron density and free-atom reference data. Physical Review Letters **102**, 073005 (2009).

[281] W. Setyawan and S. Curtarolo, High-throughput electronic band structure calculations: Challenges and tools. Computational Materials Science **49**, 299-312 (2010).

[282] J. Even, L. Pedesseau, M.-A. Dupertuis, J.-M. Jancu, and C. Katan, Electronic model for self-assembled hybrid organic/perovskite semiconductors: Reverse band edge electronic states ordering and spin-orbit coupling. Physical Review B **86**, 205301 (2012).

[283] J. Leveillee, C. Katan, J. Even, D. Ghosh, W. Nie, A. D. Mohite, S. Tretiak, A. Schleife, and A. J. Neukirch, Tuning electronic structure in layered hybrid perovskites with organic spacer substitution. Nano Letters **19**, 8732-8740 (2019).

[284] M. Madjet, G. Berdiyorov, and S. Ashhab, Effect of organic spacers on electronic, optical and transport properties of two-dimensional layered lead-halide perovskites. Computational Materials Science **169**, 109130 (2019).

[285] Z. Lu, X. Xu, Y. Gao, Z. Wu, A. Li, Z. Zhan, Y. Qu, Y. Cai, X. Huang, J. Huang, Z. Zhang, T. Luo, L. Peng, P. Liu, T. Shi, and W. Xie, The effect of spacer cations on

optoelectronic properties of two-dimensional perovskite based on first-principles calculations. Surfaces and Interfaces **34**, 102343 (2022).

[286] G. C. Fish, A. T. Terpstra, A. Dučinskas, M. Almalki, L. C. Carbone, L. Pfeifer, M. Grätzel, J.-E. Moser, and J. V. Milić, The impact of spacer size on charge transfer excitons in dion–jacobson and ruddlesden–popper layered hybrid perovskites. The Journal of Physical Chemistry Letters **14**, 6248-6254 (2023), pMID: 37390042.

[287] M. Dyksik, H. Duim, X. Zhu, Z. Yang, M. Gen, Y. Kohama, S. Adjokatse, D. K. Maude, M. A. Loi, D. A. Egger, M. Baranowski, and P. Plochocka, Broad tunability of carrier effective masses in two-dimensional halide perovskites. ACS Energy Letters **5**, 3609-3616 (2020).

[288] I. Gonzalez Oliva, F. Caruso, P. Pavone, and C. Draxl, Hybrid excitations at the interface between a MoS_2 monolayer and organic molecules: A first-principles study. Physical Review Materials **6**, 054004 (2022).

[289] B. Alex, Master thesis (Humboldt-Universität zu Berlin, Mathematisch-Naturwissenschaftliche Fakultät, 2024).

[290] C. Vorwerk, B. Aurich, C. Cocchi, and C. Draxl, Bethe–Salpeter equation for absorption and scattering spectroscopy: Implementation in the exciting code. Electronic Structure **1**, 037001 (2019).

[291] C. Vorwerk, C. Hartmann, C. Cocchi, G. Sadoughi, S. N. Habisreutinger, R. Félix, R. G. Wilks, H. J. Snaith, M. Bär, and C. Draxl, Exciton-dominated core-level absorption spectra of hybrid organic-inorganic lead halide perovskites. The Journal of Physical Chemistry Letters **9**, 1852–1858 (2018).

[292] C. C. Stoumpos, C. D. Malliakas, and M. G. Kanatzidis, Semiconducting tin and lead iodide perovskites with organic cations: Phase transitions, high mobilities, and near-infrared photoluminescent properties. Inorganic Chemistry **52**, 9019-9038 (2013).

[293] D. Kammerlander, S. Botti, M. A. L. Marques, A. Marini, and C. Attaccalite, Speeding up the solution of the Bethe-Salpeter equation by a double-grid method and Wannier interpolation. Physical Review B **86**, 125203 (2012)

List of Figures

List of Tables

Publication List

“Critical assessment of G_0W_0 calculations for 2D materials: the example of monolayer MoS_2”, R. Rodrigez Pela, C. Vona, S. Lubeck, B. Alex, I. Gonzalez Oliva, C. Draxl, *Npj Comput. Mater.* **10**, 77 (2024) DOI: `https://doi.org/10.1038/s41524-024-01253-2`

“Accurate and efficient treatment of spin-orbit coupling via second variation employing local orbitals”, C. Vona, S. Lubeck, H. Kleine, A. Gulans, and C. Draxl, *Phys. Rev. B* **108**, 235161 (2023) DOI: `https://doi.org/10.1103/PhysRevB.108.235161`.

“Excitons at the phase transition of 2D hybrid perovskites”, J. D. Ziegler, K. Lin, B. Meisinger, X. Zhu, M. Kober-Czerny, P. K. Nayak, C. Vona, T. Taniguchi, K. Watanabe, C. Draxl, H. J. Snaith, J. M. Lupton, D. A. Egger, and A. Chernikov, *ACS Photonics* **9**, 3609–3616 (2022) DOI: `https://doi.org/10.1021/acsphotonics.2c01035`.

“Similarity of materials and data-quality assessment by fingerprinting”, M. Kuban, Š. Gabaj, W. Aggoune, C. Vona, S. Rigamonti, C. Draxl, *MRS BULLETIN* **47**, 991–999 (2022) DOI: `https://doi.org/10.1557/s43577-022-00339-w`.

“Chirality of valley excitons in monolayer transition-metal dichalcogenides”, F. Caruso, M. Schebek, Y. Pan, C. Vona, and C. Draxl, *J. Phys. Chem. Lett.* **13**, 5894–5899 (2022). DOI: `https://doi.org/10.1021/acs.jpclett.2c01034`.

“Electronic Structure of (Organic-)Inorganic Metal Halide Perovskites: The Dilemma of Choosing the Right Functional”, C. Vona, D. Nabok, and C. Draxl, *Adv. Theory Simul.* **5**, 2100496 (2022). DOI: `https://doi.org/10.1002/adts.202100496`.

“Fingerprints of optical absorption in the perovskite $LaInO_3$: Insight from many-body theory and experiment”, W. Aggoune, K. Irmscher, D. Nabok, C. Vona, S. B. Anooz, Z. Galazka, M. Albrecht, and C. Draxl, *Phys. Rev. B* **103**, 115105 (2021). DOI: `https://doi.org/10.1103/PhysRevB.103.115105`.